Synthesis and Study of Quantum Kagome Magnets

David Boldrin

A thesis submitted for the degree of

Doctor of Philosophy in Chemistry

Department of Chemistry

University College London

September 9, 2015

I, David Boldrin confirm that the work presented in this thesis is my own. Where information has been derived from other sources, I confirm that this has been indicated in the thesis.

Acknowledgements

This thesis would never have been completed without the help, support and encouragement from numerous people, both during my studies and throughout my life. First and foremost, I could not have asked for a better supervisor in Andrew, who has helped me grow both as a scientist and, perhaps more importantly, as a person during my time at UCL. I am grateful now for the intense grilling sessions, although maybe not at the time, as it is now evident that you had my best interests at heart and I can't thank you enough for this: you will always be welcome at the bike/beer cafe! Similar thanks also go to other members of Andrew's group, past and present, particularly Eamonn Connolly, Ross Colman and Laura Fenner. You will be pleased to know that the invaluable lab skills that you taught me have improved both my results and my cooking/DIY!

The results presented here have all been achieved through collaborative work and so thanks must go to everyone who helped me with experiments, from minor things such as lending me some acetone to keeping an eye on a neutron diffraction experiment through the night. Particular mention to Björn Fåk who trained me in the dark arts of inelastic neutron scattering and patiently responded to countless idiotic questions from me. Thanks also to Manu Canavet, Jacques Ollivier and Ahmad Sultan for making me feel welcome during my time at the ILL and helping with experiments. For experiments at ISIS I spent a lot of time at WISH and those would never have worked without the tireless help of Pascal Manuel and Dmitry Khalyavin. Back at UCL, I'd like to thank Martin Vickers and Jeremy Cockcroft for their guidance in the use of the X-ray diffraction equipment and the time they generously gave explaining the fundamentals of diffraction. The SQUID and Raman experiments presented within were performed at UCL and only made possible with the help of Ian Watts and Steve Firth, respectively. In the lab, I'm very grateful to Andrea Sella for his help with glass-blowing, the high-vacuum equipment and his general infectious enthusiasm, whilst thanks to various members of lab 309 that have come and gone through my time for making it a fun place to work. Finally, I'd like to thank my eldest brother Paul Boldrin, who makes it into the 'work based acknowledgements' for many useful late night chemistry discussions!

Personally I would like to thank every single one of my family, my Mum, Dad, two brothers Paul and Tom and cat Schrödy, whom I all owe so much to; most importantly the pleasure of *not* making you read my thesis! To my friends, thanks for keeping me happy and sane throughout my Ph.D: I have met some special people that I will treasure for life. Whilst some friends have already been mentioned, the rest of you know who you are and don't get a mention because you won't even read this (or maybe this is the only page that you will read?!). Except Saraid, who gets a particular dedication for thinking it was a good idea to start a Ph.D. having watched me do one, no matter how *frustrated* I got! Despite the ridiculous number of words in this thesis, no number could describe how much you mean to me.

Contents

Publications

Spin dynamics in the $S = \frac{1}{2}$ quantum kagome compound vesignieite, $Cu_3Ba(VO_5H)_2$, R. H. Colman, F. Bert, D. Boldrin, A. D. Hillier, P. Manuel, P. Mendels, A. S. Wills, *Physical Review B.*, **83**, 180416(R), 2011

Ground state and intrinsic susceptibility of the kagome antiferromagnet vesignieite as seen by ^{51}V NMR, J. A. Quilliam, F. Bert, R. H. Colman, D. Boldrin, A. S. Wills, P. Mendels, *Physical Review B.*, **84**, 180401(R), 2011

Dzyaloshinsky-Moriya interaction in vesignieite: A route to freezing in a quantum kagome antiferromagnet, A. Zorko, F. Bert, A. Ozarowski, J. van Tol, D. Boldrin, A. S. Wills, P. Mendels, *Physical Review B.*, **88**, 144419, 2013

$SrCu_3V_2O_8(OH)_2$ – dynamic Jahn-Teller distortions and orbital frustration in a new $S = \frac{1}{2}$ kagome antiferromagnet, D. Boldrin, A. S. Wills, *Journal of Materials Chemistry C*, **3**, 4308–4315, 2015

Haydeeite: a $S = \frac{1}{2}$ kagome ferromagnet, D. Boldrin, B. Fåk, M. Enderle, S. Bieri, J. Ollivier, S. Rols, P. Manuel, A. S. Wills, *arXiv:1503.08023*, 2015

Chapter 1

Introduction

Magnetism has found countless essential applications since the use of lodestone (Fe_3O_4) by navigators in classical antiquity. For a long time it was thought to be a mystical force, for instance Thales of Miletus (585 B.C.) in ancient Greece believed lodestones were attracted due to their souls. Our ability to master magnetic properties of materials has led to significant technological advancements throughout human history, such as the use of the aforementioned lodestone in compasses. However, it is only relatively recently that a detailed microscopic understanding of magnetism has developed, particularly following the advent of quantum mechanics, leading to recent discoveries such as giant magnetoresistance (GMR) and magnetic resonance imaging (MRI), the former revolutionising computer data storage and the latter radiology. Further development in the field of magnetism has come from the study of geometrical frustration, where conflicting interactions give rise to novel classical or quantum states of great interest both theoretically and practically. Frustrated magnetism has strong connections with the fundamental physics of strongly correlated electronic systems and their associated properties such as superconductivity, spintronics, quantum Hall effects and topological insulators, putting it at the forefront of research in condensed matter.

Magnetic frustration occurs when superexchange interactions cannot be simultaneously satisfied and allows complex behaviour to emerge from qualitatively simple systems. Conventional Néel magnetic states are defined by a broken symmetry due to long-range order, however a typical consequence of magnetic frustration is persistent spin fluctuations as $T \rightarrow 0\,\mathrm{K}$, such as in the extensively studied classical ground states of the spin ice materials [1]. When quantum effects are large theory predicts the associated fluctuations inhibit long-range order in frustrated magnets and the system instead forms a new state of magnetism termed a quantum spin liquid (QSL) [2]. A QSL breaks no conventional spin or lattice symmetries and instead has a macroscopically degenerate ground state built from entangled, non-magnetic valence bond (VB) spin pairs [3]. The numerous, energetically equivalent VB configurations of the QSL ground state are entangled by quantum fluctuations and this novel situation allows several exciting properties to occur, namely fractional spin excitations (spinons) and macroscopic degeneracy. Moreover, the interest in these quantum states has been significantly boosted by the intimate connection between QSLs and high-T_C superconductivity as first proposed by Anderson [4]. Whilst QSLs in 1-dimensional systems are relatively familiar due to the symmetry restrictions of this model, experimental

evidence of a QSL in 2-dimensions remains elusive and is one of the frontiers of research in frustrated magnetism [5].

A corner-sharing triangular lattice of coupled $S = \frac{1}{2}$ Heisenberg spins, termed the $S = \frac{1}{2}$ kagome Heisenberg magnet (KHM), is the most promising model for hosting a QSL ground state [3]. Two of the best experimental realisations of the $S = \frac{1}{2}$ KHM, the Cu^{2+} d^9 based minerals volborthite [6], $Cu_3V_2O_7(OH)_2{\cdot}2H_2O$, and herbertsmithite [7], γ-$ZnCu_3(OH)_6Cl_2$, have recently evidenced hallmark QSL behaviour, such as persistent spin dynamics as $T \rightarrow 0\,\mathrm{K}$ and a continuum of low-energy spinon excitations, that adds further weight behind the potential of these materials [8, 9]. However, decoupling the magnetic response of structural imperfections inherent to real systems, such as impurity spins or lattice defects, from the intrinsic physics remains a major issue for experimentalists in the field and casts doubt on the true ground states of the studied materials. Thus, expanding our experimental library of $S = \frac{1}{2}$ KHMs is required as comparisons will help to determine true properties of the QSL and, moreover, further model systems will undoubtedly reveal unique ground states previously undiscovered.

This thesis details the synthesis and study of three different $S = \frac{1}{2}$ KHMs, vesignieite ($BaCu_3V_2O_8(OH)_2$), 'Sr-vesignieite' ($SrCu_3V_2O_8(OH)_2$) and haydeeite (α-$MgCu_3(OH)_6Cl_2$). 'Sr-vesignieite' is a previously unreported material and isolectronic Sr^{2+} analogue of the well studied mineral vesignieite [10]. Crystallographic studies presented in Chapter 5 reveal a trigonal structure that is consistent with the presence of dynamic Jahn-Teller fluctuations of the $S = \frac{1}{2}$ Cu^{2+} and highlight the importance of orbital contributions to the frustrated superexchange interactions. This structural model is also found in the parent mineral vesignieite, as shown by crystallographic studies in Chapter 6, and forces a revision of the previously predicted orbital order for this material which may prove crucial for understanding its magnetic properties [10, 11]. Moreover, Chapter 6 discusses the presence of dynamic Jahn-Teller effects for several other model $S = \frac{1}{2}$ KHMs, including volborthite, inferred from previously published structures [12]. Magnetic characterisation of vesignieite in Chapter 7 reveals antiferromagnetic spin-waves at low-T, clear evidence of a long-range ordered magnetic structure, and further analysis suggests a unique non-coplanar spin arrangement. In the final chapter, inelastic neutron scattering data collected on haydeeite are characteristic of an ordered ferromagnet, which is surprising considering its chemical and structural similarities to herbertsmithite, adding more variety to the magnetic properties found in these systems. These findings improve our understanding of both vesignieite and haydeeite, whilst 'Sr-vesignieite' adds another valuable model system to explore the physics of $S = \frac{1}{2}$ KHMs. Together, these studies reveal previously unobserved magnetic ground states that encourage further experimental and theoretical work in the field of frustrated magnetism.

Bibliography

[1] M. J. Harris, S. T. Bramwell, D. F. Mcmorrow, T. Zeiske and K. W. Godfrey, *Phys. Rev. Lett.*, 1997, **79**, 2554–2557.

[2] L. Balents, *Nature*, 2010, **464**, 199–208.

[3] C. Lacroix, P. Mendels and F. Mila, *Introduction to Frustrated Magnetism: Materials, Experiment, Theory*, Springer, New York, 2011.

[4] P. W. Anderson, *Science*, 1987, **235**, 1196–1198.

[5] B. Normand, *Contemp. Phys.*, 2009, **50**, 533–552.

[6] Z. Hiroi, M. Hanawa, N. Kobayashi, M. Nohara, H. Takagi, Y. Kato and M. Takigawa, *J. Phys. Soc. Japan*, 2001, **70**, 3377–3384.

[7] M. P. Shores, E. A. Nytko, B. M. Bartlett and D. G. Nocera, *J. Am. Chem. Soc.*, 2005, **127**, 13462–3.

[8] G. J. Nilsen, F. C. Coomer, M. A. de Vries, J. R. Stewart, P. P. Deen, A. Harrison and H. M. Rönnow, *Phys. Rev. B*, 2011, **84**, 172401.

[9] T.-H. Han, J. S. Helton, S. Chu, D. G. Nocera, J. A. Rodriguez-Rivera, C. Broholm and Y. S. Lee, *Nature*, 2012, **492**, 406–410.

[10] Y. Okamoto, H. Yoshida and Z. Hiroi, *J. Phys. Soc. Japan*, 2009, **78**, 033701.

[11] H. Yoshida, J.-I. Yamaura, M. Isobe, Y. Okamoto, G. J. Nilsen and Z. Hiroi, *Nat. Commun.*, 2012, **3**, 860.

[12] P. C. Burns and F. C. Hawthorne, *Can. Mineral.*, 1996, **34**, 1089–1105.

Chapter 2

Fundamental theories of magnetism

This chapter introduces the fundamentals of magnetism required to understand the research presented in this thesis. It begins with the atomic-level building block of magnetic behaviour, the magnetic moment, and its classical and quantum mechanical origins. From an understanding of how magnetic moments behave in isolation, the chapter builds a picture of their cooperative interactions in materials and how these lead to the macroscopic properties we observe of magnetic materials. The different magnetic interactions and local environments that occur in crystalline solids will be introduced before a discussion on some microscopic theoretical models of magnetism and the underlying importance of symmetry. The sources used in this chapter are [1, 2, 3, 4]

2.1 The magnetic moment

The fundamental building block of magnetism is the magnetic moment, which arises from the motion of charged particles and, in a classical sense, one can equate this with a current loop. For a current, *I*, whose loop covers the area $\mathbf{A}$, the associated magnetic moment, $\boldsymbol{\mu}$, lies normal to the plane of the current loop (Figure 2.1a) [2]. For a finite sized current loop, the magnetic moment is calculated by summing up many equal infinitesimal current loops of moment $\mathbf{d}\boldsymbol{\mu}$ and area $\mathbf{dA}$, and is given by:

$$\boldsymbol{\mu} = \int \mathbf{d}\boldsymbol{\mu} = I \int \mathbf{dA} \tag{2.1}$$

with SI units of $\mathrm{A\,m^2}$. This is analogous to an electric dipole where two magnetic monopoles are oppositely aligned along the vector $\mathbf{dA}$.

In addition to the motion of an electrical charge, for massive particles one must consider the orbital motion of mass and the associated angular momentum, for instance in the current loop just described. In such a case, the magnetic moment, $\boldsymbol{\mu}$, lies along the same direction as its angular momentum, $\mathbf{L}$, and is proportional to it. This relationship is given by:

$$\boldsymbol{\mu} = \gamma \mathbf{L} \tag{2.2}$$

where γ is the gyromagnetic ratio with SI units of $\mathrm{C\,kg^{-1}}$.

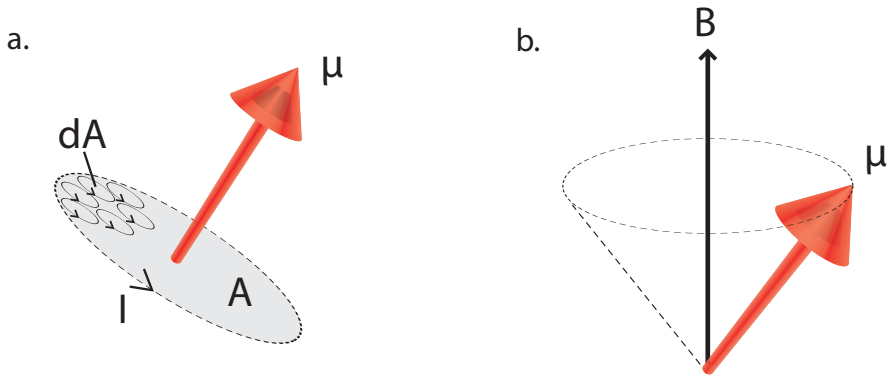

Figure 2.1: a. A magnetic moment, $\boldsymbol{\mu}$, can be equated with a current loop and lies normal to the surface of the area that it draws, **A**. For a finite size current loop, $\boldsymbol{\mu}$ is given by summing many infinitesimal equal current loops of area **dA**. **b.** In a magnetic field, **B**, a magnetic moment, $\boldsymbol{\mu}$, precesses around **B** due to its intrinsic angular momentum.

2.1.1 Precession in a magnetic field

The inherent angular momentum associated with a magnetic moment has important consequences on its behaviour in a magnetic field. Figure 2.1b illustrates a magnetic moment arising from a current loop, $\boldsymbol{\mu}$, in a magnetic field, **B**. In the absence of angular momentum, the torque on $\boldsymbol{\mu}$ would preferentially align it along **B**. However, due to the inherent angular momentum, the torque causes $\boldsymbol{\mu}$ to precess around **B**, analogous to a spinning top. The rate of precession, ω_{L}, is related to **B** again by the gyromegnetic ratio, γ:

$$\omega_{\mathrm{L}} = \gamma \mathbf{B} \tag{2.3}$$

where ω_{L} is termed the Larmor precession frequency. This fundamental relationship is beautifully demonstrated by the Einstein-de-Haas and Barnett effects where rotation is induced by magnetisation and vice-versa due to the conservation of angular momentum, respectively, and can be used to accurately determine γ [5].

The precession of magnetic moments around the magnetic field associated with an angular momentum is a crucial aspect of solid state magnetism. It underlies the fact that moments do not just uniformly align in materials but instead give rise to a wide variety of dynamic behaviour. We will now focus our attention on the magnetic moment associated with an electron, which gives rise to the vast majority of the magnetic properties discussed in this thesis.

2.2 Isolated electronic magnetic moments

In the majority of materials, the largest contributors to the magnetic properties are the electronic magnetic moments. The latter has two components: (i) that from *orbital* motion discussed in Section 2.1 and (ii) that from an intrinsic angular momentum known as electron *spin*. Both of these contributions are quantum mechanical in nature and, in fact, a classical treatment of electron magnetism will never predict a net magnetisation in the absence of an applied field [6].

2.2.1 Electronic angular momentum

The state of an electron can be described by four quantum numbers: the principal quantum number gives the energy level, *n*, the orbital and spin quantum numbers, *l* and *s*, correspond to the quantisation of the orbital and spin angular momenta, respectively, and the magnetic quantum number, m_l, which denotes the specific orbital subshell [2]. The magnitude of the orbital angular momentum is defined by $\sqrt{l(l+1)}\hbar$ where l can take integer values between 0 and $n-1$ corresponding to the subshell that the electron occupies. Along a fixed axis, the component of the orbital angular momentum is $m_l\hbar$, where m_l takes integer values between $-l$ and l and corresponds to the different orbitals within the subshell.

The spin quantum number of an electron, s, is equal to $\frac{1}{2}$. Along a fixed axis, the component of the spin angular momentum is $m_s\hbar$, where m_s can take values of $\frac{1}{2}$ or $-\frac{1}{2}$. Therefore, the only components of the spin angular momentum along a defined axis are $\frac{\hbar}{2}$ and $-\frac{\hbar}{2}$, which correspond to the commonly referred 'up' and 'down' spin states. Similarly to that for orbital angular momentum, the magnitude of the spin angular momentum is equal to $\sqrt{s(s+1)}\hbar$.

2.2.2 Total angular momentum

To calculate the total energy of an electron, both of these individual quantum numbers must be considered and combined. Spin and orbital angular momenta combine individually to give the total spin angular momentum, **S**, and total orbital angular momentum, **L** [2]. **S** has $(2S+1)$ combinations denoted by the quantum number m_s, which takes the values $-S, (-S+1), ..., S$ and the same applies for **L**. Therefore, in a many electron system, such as an atom or ion, the spin and orbital angular momenta of the electrons in the unfilled shells can combine in $(2L+1)(2S+1)$ ways. However, this picture is complicated by coupling of **L** and **S** *via* the spin-orbit interaction (SOI). Consequently, it is not **L** and **S** that are conserved as they are not accurate representations due to the SOI, but rather the total angular momentum, **J**.

The strength of the SOI determines the method used to calculate the total angular momentum for a many electron system. If the SOI is a weak perturbation, then **L** and **S** couple together according to $\mathbf{J} = \mathbf{L} + \mathbf{S}$. This scheme is known as Russell-Saunders or $\mathbf{L} \cdot \mathbf{S}$ coupling. If SOI is strong, which is the case for heavier atoms due to its Z^4 dependence on atomic number, then the individual orbital and spin angular momenta, s and l, couple together to form j, which subsequently combine to make $\mathbf{J} = \sum_i j_i$.

The total angular momentum, **J**, has a corresponding quantum number, J, which can take values from $|L-S|$ to $L+S$. In the absence of a SOI, these J values are degenerate, but with SOI the degeneracy is lifted to reveal the electronic fine structure. These levels can be further split to their constituent m_j values through the application of a magnetic field, where $m_\mathrm{J} = +J, J-1, ..., -J$, in a process known as Zeeman splitting [7]. Given the number of quantum numbers that define the electronic state, an immediate problem is how to determine which values are taken in the ground state.

2.2.3 Hund's rules

Three rules, termed Hund's rules, were developed to estimate the electronic ground state of an ion [8]. In order of decreasing importance, these are:

1. The state with the lowest energy has the largest value of the spin angular momentum, and so

multiplicity, $(2S + 1)$. This attempts to minimise Coulombic repulsion of electrons by placing them in separate orbitals.

2. For states with the same value of $(2S + 1)$, that with the largest value of the the orbital angular momentum, L, has the lowest energy. Again, this minimises Coulombic repulsion as, in a classical picture, electrons that precess in the same direction are more likely to avoid each other.

3. For a less than half-full shell the lowest energy value of J is $J = |L - S|$ whilst for a more than half-full shell it is instead $J = |L + S|$. Spin-orbit energy is minimised with this rule, although for the lighter elements it is negligible and therefore not strictly adhered to.

Whilst Hund's rules can be used to predict the electronic ground state of an ion, it gives no information on the energies of excited states and therefore how much these contribute to the magnetism. This is clear in the discrepancy between the predicted and experimental magnetic properties of the $4f$ Sm^{3+} and Eu^{3+} ions, where low lying excited states are populated and contribute to the magnetism [2]. For the rest of the $4f$ ions, the predicted magnetic properties from Hund's rules are in excellent agreement with experiment.

For the $3d$ transition metals, an important group of elements in many magnetic materials, the third rule often leads to incorrect predictions of their magnetic properties. The crystal field interaction of these ions is larger than the SOI, causing orbital quenching such that $L = 0$ and, therefore, $J = S$ is a much better approximation. This is still inadequate, as the SOI can still act as a small perturbation due to L not being totally quenched, *i.e.* $L \cong 0$. Therefore, Hund's rules often only act as a rough estimation for the $3d$ ions.

Having covered how electronic spin and orbital angular momentum gives rise to magnetic properties, we can now discuss how this appears in practice, such as how we define and quantify measured magnetic properties in materials.

2.2.4 The Bohr magneton

The magnitude of an atomic magnetic moment is tiny and therefore it is necessary to describe them in convenient units. From a simple picture of a single electron orbiting a lone proton, the size of the magnetic moment of the electron is given by:

$$\mu = -\frac{e\hbar}{2m_{\mathrm{e}}} \equiv -\mu_{\mathrm{B}} \tag{2.4}$$

where m_{e} is the electron mass, e is the elementary electron charge and μ_{B} is the Bohr magneton [4]. The Bohr magneton, in SI units, is equal to $9.274{\times}10^{-24}$ A m^2 which is roughly equal to the magnetic moment of an electron's spin and therefore is a convenient unit widely used in the field of magnetism.

2.2.5 Magnetic susceptibility

In any magnetic solid a vast number of individual atoms contribute to the overall magnetic properties. To make this quantity easy to handle, this can be defined as magnetic moment per unit volume or magnetisation, **M**. In many applications it is useful to know how **M** varies as a function of applied field, **H**, and this relationship is given by the magnetic susceptibility, χ:

$$\mathbf{M} = \chi\mathbf{H} \tag{2.5}$$

Care must be taken with the units of χ. Firstly, due to the original definition of **M**, χ from equation 2.5 is *per unit volume*. For all magnetic susceptibility data measured in this thesis the more commonly used *molar susceptibility* is calculated according to:

$$\chi_{\mathrm{mol}} = \frac{\chi M_{\mathrm{r}}}{m} \tag{2.6}$$

whereby M_{r} is the relative molecular mass of the material and m is the sample mass, or for χ_{mol} per magnetic ion in the formula unit:

$$\chi_{\mathrm{mol}} = \frac{\chi M_{\mathrm{r}}}{mn} \tag{2.7}$$

where n is the number of magnetic ions per formula unit. Secondly, due to the archaic history of magnetic materials research, SI units are rarely used for magnetic properties. Instead, electromagnetic units (emu) are used which originate from the centimetre-gram-second (cgs) variant of the metric system and differ slightly from SI units [9]. Consequently, χ_{mol} is often quoted with units emu mol^{-1} to indicate that SI units have not been used and a conversion factor is required to obtain them.

The sign of χ indicates whether a material is attracted or repelled by an applied magnetic field: if $\chi > 0$ the former occurs and the response is termed paramagnetism and if $\chi < 0$ the latter does and is called diamagnetism [3]. Thus, measurement of χ is often the first step in characterising a magnetic material as it gives an indication to the type of interactions. We will now discuss the origins of these responses and the additional information that can be extracted from χ.

2.2.6 Diamagnetism and paramagnetism

Diamagnetism arises due to the mutual repulsion between an applied magnetic field and the intrinsic fields in a material caused by orbiting electrons. Consequently, all materials show some degree of diamagnetism and the magnitude of this is proportional to the number of electrons [4]. However, diamagnetic contributions to χ are often weak compared to other forms of magnetism, such as paramagnetism. This latter effect reinforces applied magnetic fields due to the complimentary alignment of the electronic magnetic moment from unpaired electrons. This interaction is considerably stronger than diamagnetism, often an order of magnitude greater, and so is commonly ignored or treated as a weak perturbation [10]. As such, we will now concentrate on a detailed explanation of paramagnetism.

A classical treatment of paramagnetism ignores the fact that magnetic moments are quantized, which is effectively comparable to $J = \infty$, yet still leads to an accurate description of the temperature dependence of the magnetic susceptibility, χ [2]. To get there, we must first look at the average moment of a paramagnet that aligns along an applied field, **B**, in the z direction due to the torque provided by it and is given by the Langevin function, $L(y)$:

$$L(y) \equiv \coth(y) - \frac{1}{y} = \frac{\mu_z}{\mu} \tag{2.8}$$

where μ (μ_z) is the total magnetic moment (in the z direction) and $y = \mu B/k_{\mathrm{B}}T$. At small applied fields we find the Langevin function simplifies to $L(y) \approx \frac{y}{3}$, such that:

$$L(y) = \frac{\mu_z}{\mu} \approx \frac{y}{3} = \frac{\mu B}{3k_{\mathrm{B}}T} \tag{2.9}$$

The magnetic moment is related to the magnetisation from equation 2.5 by $M = n\mu_z = n\mu L(y)$, where n is the number of magnetic moments per unit volume. As we are in small fields, χ is also approximated by $\chi \approx \frac{\mu_0 M}{B}$, and therefore one can now define the temperature dependence of the magnetic susceptibility:

$$\chi = \frac{n\mu_0\mu^2}{3k_{\mathrm{B}}T} = \frac{C}{T} \tag{2.10}$$

where μ_0 is the permeability of free space and C is the Curie constant. From equation 2.10, it is evident that the magnetic susceptibility is inversely proportional to temperature. This relationship was defined by Pierre Curie and is known as the Curie law.

For any real system a quantum mechanical description of the paramagnetic magnetisation must be used. In such a system, the classical magnetic moments are replaced by quantum $J = \frac{1}{2}$ spins, so that $m_{\mathrm{J}} \pm \frac{1}{2}$ in an applied field and, consequently, the moment in the z direction can take only two possible values, $g_{\mathrm{J}}\mu_{\mathrm{B}}m_{\mathrm{J}}$ or $-g_{\mathrm{J}}\mu_{\mathrm{B}}m_{\mathrm{J}}$, where g_{J} is the Landé g-factor, the electronic equivalent of the gyromagnetic ratio. The Brillouin function, $\mathrm{B}_J(y)$, gives a general treatment of the paramagnetic magnetisation for any half integer value of J:

$$\mathrm{B}_J(y) = \frac{2J+1}{2J}\coth(\frac{2J+1}{2J}y) - \frac{1}{2J}\coth\frac{y}{2J} \tag{2.11}$$

where $y = g\mu_{\mathrm{B}}JB/k_{\mathrm{B}}T$. For a $J = \frac{1}{2}$ system the Brillouin function reduces to $\mathrm{B}_J(y) = \tanh(y)$, whilst at large J it becomes the Langevin function described in equation 2.8. For small y, *i.e.* small fields, $\mathrm{B}_J(y)$ simplifies to:

$$\mathrm{B}_J(y) = \frac{(J+1)y}{3J} \tag{2.12}$$

and analogously to the derivation of equation 2.10, *i.e.* with $M = ng_{\mathrm{J}}\mu_{\mathrm{B}}J\mathrm{B}_J(y)$, the magnetic susceptibility can be shown to be:

$$\chi = \frac{n\mu_0 g_{\mathrm{J}}^2\mu_{\mathrm{B}}^2 J(J+1)}{3k_{\mathrm{B}}T} = \frac{n\mu_0\mu_{\mathrm{eff}}^2}{3k_{\mathrm{B}}T} \tag{2.13}$$

which closely resembles the classical Curie law, but crucially now allows calculation of the effective moment, $\mu_{\mathrm{eff}} = g_{\mathrm{J}}\mu_{\mathrm{B}}\sqrt{J(J+1)}$, from measurement of χ.

With this understanding of how an isolated magnetic moment interacts with an applied magnetic field, we can now expand the discussion to how they interact in solids. This initially involves a discussion of their interactions with the local crystal environment before looking at how they interact with each other.

2.3 Magnetic moments in materials

The behaviour of an atom with its coordination environment is strongly dependent on its own electronic configuration as well as that of its neighbouring atoms. The majority of this thesis deals with magnetic materials consisting of first-row, $3d$ transition metals. Therefore, the discussion in this section will concentrate on the d-orbitals which host the lone electrons in these atoms or ions. How these interact with their local environment will be discussed first before turning to magnetic interactions, with particular emphasis on how the orbitals and local environment mediate them. Finally we look at the range of ordered magnetic structures that arise from these interactions and state the Curie-Weiss law which accurately predicts the temperature dependence of χ in many materials with magnetic interactions.

2.3.1 Crystal field environments

In an octahedral local environment, the five-fold degenerate d-orbitals are split into two classes with t_{2g} and e_g symmetry, whereby the g refers to an inversion centre that does not cause a change in sign (***g**erade*). Those with t_{2g} symmetry are triply degenerate and have labels d_{xy}, d_{xz} and d_{yz}, whilst those with e_g symmetry are doubly degenerate with labels $d_{x^2-y^2}$ and d_{z^2} (the latter is sometimes referred to as $d_{3z^2-r^2}$ particularly in the physics literature) [2].

Electrostatic interactions of the transition metal d orbitals with the local ligand orbitals is the underlying cause for the symmetry reduction in an octahedral local environment. The e_g orbitals have significant overlap with the ligand orbitals whilst the t_{2g} orbitals do not, therefore electrostatic repulsions raise the energy of the former and, to preserve the total energy, the latter are lowered in energy. The orbital energy diagram for an octahedral environment is represented in Figure 2.2a, but it is important to note that other local environments, such as a tetrahedra, cause different orbital splittings. The energy between the orbitals is known as the crystal field energy and is determined by several factors, for instance the degree of ligand-orbital overlap.

How the orbitals are occupied by electrons in each transition metal ion is dependent on crystal field and Coulombic, *i.e.* electron-electron repulsion, energies. If the crystal field energy is smaller than the Coulombic it is preferential for electrons to singly occupy orbitals, whereas for the opposite scenario it is energetically preferential for orbitals to be filled first. These competing energies are often of comparable magnitude leading to ground states that are not immediately obvious. However, on the positive side, it also leads to a rich variety of magnetic properties within the transition metal materials.

It is worth noting again that care must be taken when applying Hund's rules (Section 2.2.3) to $3d$ transition metal ions. The weak spin-orbit interaction may not fully quench the orbital angular momentum and states with $L \neq 0$ may contribute to the ground state. This is commonly found in Cu^{2+} containing materials and results in a slight raising of the Landé g-factor, g_J, above the spin-only value of 2 and a consequent increase of the effective moment, μ_{eff} [11, 12, 13].

2.3.2 The Jahn-Teller effect

Further lifting of the d-orbital degeneracy occurs in any nonlinear system with a spatially degenerate electronic ground state, known as the Jahn-Teller effect [14]. Such a system undergoes a geometric dis-

tortion to remove the degeneracy and lower the energy of the system. The effect is most pronounced in octahedral systems when the e_g orbitals are unevenly occupied, such as the d^9 Cu^{2+} ion, as a significant energy gain occurs from the distortion because these orbitals directly align with the ligands. Nevertheless, the effect also occurs with degeneracy in the t_{2g} orbitals or in tetrahedral geometry, but the resulting distortion is often much smaller as the energy loss involving the distortion is weaker.

In many materials the Jahn-Teller effect causes a static distortion and an accompanying symmetry lowering transition of the crystal structure. However, if there is no preferred distortion direction then a *dynamic* Jahn-Teller effect may occur whereby the system locally fluctuates between several distorted geometries [15]. For instance, in an octahedral d^9 system where the degeneracy arises from lone occupation of the d_{z^2} orbital, three energetically equivalent geometries are present with the orbital aligned along the x, y or z axes (Figure 2.2b). If the energetic barrier between these states is small on average then they are all equally occupied and the atom effectively retains the orbital degeneracy. Other ground states can occur through warping of the potential energy surface, such as two-fold orbital degeneracy whereby one distorted configuration lies at significantly higher energy than the rest. As we will see in Chapters 5, 6 and 7, the dynamic Jahn-Teller effect plays an important part in the physics of the materials studied in this thesis.

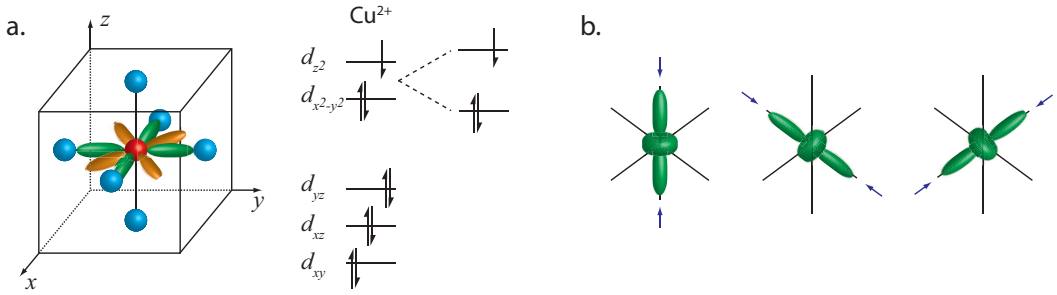

Figure 2.2: In an octahedral ligand field d-orbital degeneracy is lifted between those with e_g and t_{2g} symmetry, as the former point towards the ligands and the latter between them, as shown in **a.** with the d_{xy} (orange) and $d_{x^2-y^2}$ (green) orbitals. For a d^9 transition metal ion, such as Cu^{2+}, with a singly occupied d_{z^2} orbital the degeneracy is further lifted due to a process known as the Jahn-Teller effect. As the d_{z^2} orbital is raised in energy the bonds it is aligned along are shortened, forming a compressed octahedra as shown in **b.**. As the d_{z^2} can align along any pair of bonds, if the energetic barrier between these states is small, the system fluctuates between all three and is in a *dynamic* Jahn-Teller state.

Static Jahn-Teller transitions are usually induced in ions at low temperatures due to their inability to overcome the energy barriers between different states. However, this transition is not always constrained locally to individual ions. If a material contains Jahn-Teller ions that are neighbouring or closely coordinated then they may cooperatively distort throughout the crystal [16]. This is distinct from a static Jahn-Teller distortion, as the distortion of one ion necessarily requires every other ion to distort as well.

As we have seen, the local environment of a transition metal ion has interesting consequences for the relative d-orbital energies and therefore their electron occupation. In trying to understand the observed properties of real materials, knowledge of the orbitals energies and occupations is crucial as they play an

essential role in mediating magnetic interactions, as we will now discuss.

2.3.3 Magnetic interactions

Magnetic moments interact with each other *via* various means. The simplest of these is the dipolar interaction between two magnetic dipoles whose energy depends on their separation and degree of alignment. However this is generally several orders of magnitude smaller than other interactions and can be considered negligible in the majority of magnetic materials unless studied at temperatures below 1 K [2, 17].

The origin of the vast majority of magnetic properties in insulators lies in the exchange interaction. This is a purely quantum mechanical effect that arises due to the fact that when identical particles are exchanged their wavefunctions are subject to exchange symmetry [18]. For electrons, which are fermions, this exchange must be antisymmetric and the best understanding of this in a classical sense is due to electrostatic repulsion. The Hamiltonian for spin exchange is given by:

$$\hat{\mathcal{H}} = -2J\mathbf{S_1} \cdot \mathbf{S_2} \tag{2.14}$$

where J is the exchange term and $\mathbf{S_1}$ ($\mathbf{S_2}$) the spin of electron 1 (2). Expanding this to interactions between all spins in a material gives the Heisenberg Hamiltonian:

$$\hat{\mathcal{H}} = -2J\sum_{i>j}\mathbf{S_i} \cdot \mathbf{S_j} \tag{2.15}$$

Electronic exchange terms can occur within the same atom, between neighbouring atoms (direct exchange) or indirectly *via* an intermediate atom (superexchange). As the exchange interaction is relatively short-ranged and dependent on orbital overlap, direct exchange is often negligible in crystalline solids as there is little orbital overlap between neighbouring magnetic ions.

Superexchange is often the dominant term in the Hamiltonian of crystalline insulators due to better orbital overlap with neighbouring non-magnetic ligands [19]. In $3d$ transition metal oxides the superexchange pathway is often through a metal–oxygen–metal link, such as in Figure 2.3a, and the superexchange interaction lowers the kinetic energy of the system by allowing the magnetic electrons to delocalise across the whole bond through mixing with excited states. The kinetic term is heavily dependent on bond angle but favours antiferromagnetism at large angles until the ∠M–O–M angle approaches 90 °, and even then the ferromagnetic interaction is usually weak [20, 21]. Further neighbour superexchange can also occur *via* multiple mediating ligands and, although this is predictably weaker than shorter range interactions, it can define quite unexpected ground states when nearer-neighbour terms are competing, *i.e.* in frustrated magnets. Further neighbour superexchange is a common discussion point in this thesis.

One particularly relevant extension to this model is the inclusion of orbital exchange, which becomes important in systems with orbital degeneracy, as in the case with Jahn-Teller ions. This introduces a spatial aspect to the exchange, as orbitals have a spatial dependence, and the Hamiltonian becomes vastly more complicated and highly anisotropic [22]. The predicted ground states from these Hamiltonians can be very different to that of equation 2.15 and must be taken into consideration in magnetic

materials with orbital degeneracy.

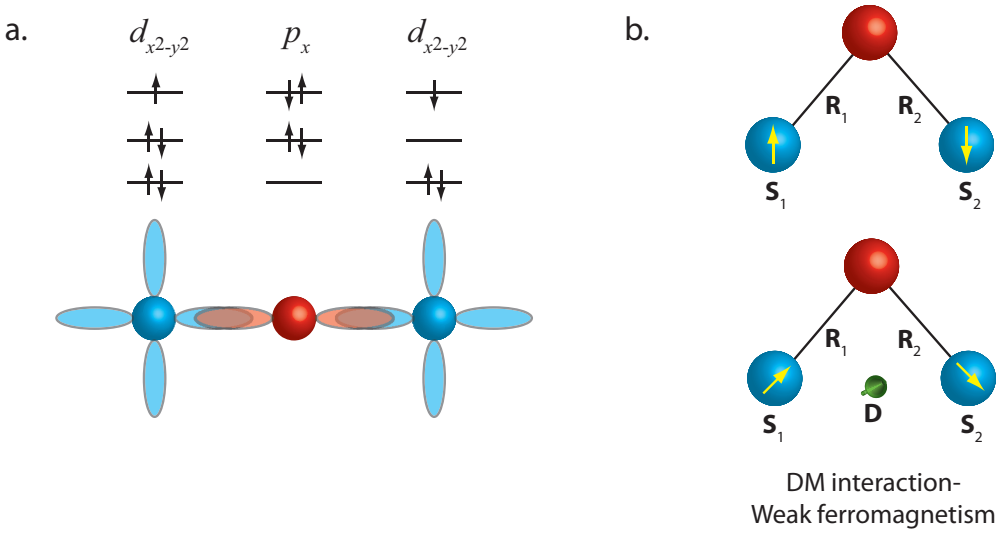

Figure 2.3: **a.** A schematic of antiferromagnetic superexchange between lone $d_{x^2-y^2}$ electrons on two $3d$ transition metals (blue) and the full p_x orbital of an oxygen ion (red). The kinetic energy of the system is lowered by delocalising the electrons across all three ions, as indicated by the three possible electronic states. Only one possible state exists for a ferromagnetic interaction due to the Pauli exclusion principle and consequently antiferromagnetism is energetically favourable in superexchange for the majority of M–O–M geometries. **b.** Antisymmetric exchange, or the Dzyaloshinskii-Moriya (DM) interaction, tries to align the spins at right-angles with each other perpendicular to the DM vector, which in this case lies out of the page. In antiferromagnets, this often introduces a ferromagnetic moment and is termed 'weak ferromagnetism'.

Thus far we have discussed exchange with respect to localised electrons, however itinerant electrons, for instance in metals, can also mediate exchange energy through what is termed the Ruderman-Kittel-Kasuya-Yosida (RKKY) interaction [23]. It arises from localised magnetic moments that polarise the conduction electrons which in turn couples to a neighbouring magnetic moment of distance r. Consequently the interaction is long-range and has an oscillatory dependence on r given by:

$$J_{\mathrm{RKKY}} \propto \frac{\cos(2k_{\mathrm{F}}r)}{r^3} \tag{2.16}$$

where k_{F} is the Fermi energy and J_{RKKY} can be either ferro- or antiferromagnetic.

The final form of exchange that will be discussed is antisymmetric exchange, also known as the Dzyaloshinskii-Moriya (DM) interaction [24]. The mechanism for this exchange arises from the spin-orbit interaction, whereby the exchange occurs between the spin-orbit excited state of an ion with the ground state of another. The DM Hamiltonian for two spins is given by:

$$\hat{\mathcal{H}}_{\mathrm{DM}} = \mathbf{D} \cdot \mathbf{S}_1 \times \mathbf{S}_2 \tag{2.17}$$

and the value of $\mathbf{D}$ is dependent on the symmetry of the central point between the two spins [25, 24]. When an inversion centre exists $\mathbf{D}$ vanishes, but otherwise it will lie perpendicular or parallel to the line connecting the two spins depending on the symmetry. If the exchange is mediated *via* a ligand, as in

superexchange, then **D** is defined by the vectors between all three ions [26]. The interaction introduces a component that forces $\mathbf{S}_1$ and $\mathbf{S}_2$ to lie at right angles to each other perpendicular to $\mathbf{D}$, as shown in Figure 2.3b, and therefore often leads to canted spin structures in antiferromagnets, *i.e.* weak ferromagnetism. The DM interaction can be a significant component of the Hamiltonian when the superexchange pathway does not possess inversion symmetry, *i.e.* if the angle between the three ions is $< 180\,^{\circ}$.

2.3.4 The Curie-Weiss law

The sign of the exchange parameter between two moments, J, discussed in the previous section determines whether the resulting magnetic interaction will be ferromagnetic or antiferromagnetic: for $J > 0$ it is ferro- whilst $J < 0$ it is antiferromagnetic. However, to define the magnetisation of a real material an approximation must be made on the field present at each magnetic site due to every other site in the lattice. This approximation is known as the Weiss molecular field and whilst theoretically incorrect it provides a convenient way of characterising magnetic materials [2, 27].

The temperature dependence of χ in a material with magnetic interactions, *i.e.* $J \neq 0$, is given by the Curie-Weiss law, an adaptation of the Curie law to include the Weiss molecular field. Incorporating the Weiss molecular field, whose strength is given by λ, into the Curie law is straightforward. First, the magnetic transition temperature must be defined with respect to the molecular field, commonly known as the Curie and Neél temperatures for ferromagnets and antiferromagnets, respectively. These are given by:

$$T_{\mathrm{C}} = \frac{g_{\mathrm{J}}\mu_{\mathrm{B}}(J+1)\lambda M_{\mathrm{sat}}}{3k_{\mathrm{B}}} \tag{2.18}$$

for the Curie temperature, and:

$$T_{\mathrm{N}} = \frac{g_{\mathrm{J}}\mu_{\mathrm{B}}(J+1)|\lambda| M_{\mathrm{sat}}}{3k_{\mathrm{B}}} \tag{2.19}$$

for the Néel temperature. Including the molecular field in the small field approximation of the Brillouin function, equation 2.12, it becomes:

$$\mathrm{B}_J(y) = \frac{M}{M_{\mathrm{sat}}} \approx \frac{(J+1)y}{3J} = \frac{g_{\mathrm{J}}\mu_{\mathrm{B}}(J+1)}{3k_{\mathrm{B}}T}\left(\frac{B+\lambda M}{T}\right) \tag{2.20}$$

Concentrating for now on the ferromagnetic susceptibility, by combining equations 2.18 and 2.20 we get:

$$\frac{M}{M_{\mathrm{sat}}} \approx \frac{T_{\mathrm{C}}}{\lambda M_{\mathrm{sat}}}\left(\frac{B+\lambda M}{T}\right) \tag{2.21}$$

which when combined with the small field approximation of the susceptibility, $\chi = \frac{\mu_0 M}{B}$, and rearranged gives the temperature dependence of the susceptibility of a magnet in the paramagnetic regime, known as the Curie-Weiss law:

$$\chi = \frac{\mu_0 M}{B} \propto \frac{C}{T - T_{\mathrm{C}}} \tag{2.22}$$

The same treatment for an antiferromagnet gives a similar result but with $-T_{\mathrm{C}}$ replaced by $+T_{\mathrm{N}}$. To resolve this issue, $-T_{\mathrm{C}}$ or $+T_{\mathrm{N}}$ is replaced by the Weiss constant, $-\theta_{\mathrm{W}}$, where positive values indicate ferromagnetic interactions and negative antiferromagnetic. Obviously, if no spin-spin correlations are present $\theta_{\mathrm{W}} = 0$ and we return to the Curie law (Equation 2.10). However, the opposite is not true: if $\theta_{\mathrm{W}} = 0$ it does not necessarily mean that no exchange interactions are present. For instance, competing ferro- and antiferromagnetic terms of equal magnitude will lead to this result due to the mean field approximation. This is of particular relevance in frustrated magnetism where two or more exchange terms compete and contribute to the mean field.

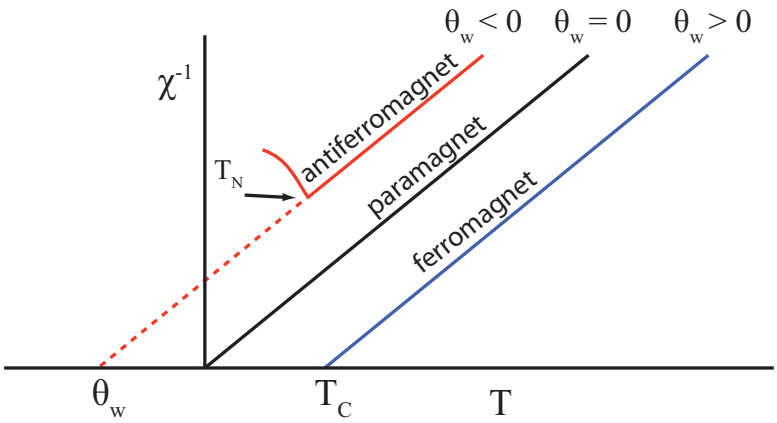

Figure 2.4: A schematic of χ^{-1} *vs.* T for a paramagnet, ferromagnet and antiferromagnet. In the paramagnetic regime of any material, the Curie-Weiss law states that χ^{-1} is linear in T and extrapolating the linear region to the x-axis gives the Weiss constant, θ_{W}. Negative θ_{W} values indicate antiferromagnetic interactions, whilst ferromagnetism causes a positive θ_{W}.

From the form of equation 2.22, it is evident that a plot of χ^{-1} *vs.* T is linear and a fit to this region gives the Curie constant, C, as the slope and the Weiss constant, θ_{W}, as the x-intercept (Figure 2.4). Thus, such a plot is a very powerful analytical technique for initial characterisation of a magnetic material. However, it is important to note that the mean field approximation breaks down close to the transition temperature due to large fluctuations in the magnetisation. Moreover, curvature in the paramagnetic regime of χ^{-1} may indicate the presence of short-range interactions. With these last two points in mind, care must be taken to choose the truly paramagnetic region of χ for this analysis.

2.4 Magnetic order and phase transitions

Spontaneous order is a fundamental phenomena of magnetic materials, and in condensed matter in general, that can give rise to permanent magnetisation and the variety of useful properties that can be developed from it. The phase transition between the disordered and ordered states can be 1^{st} or 2^{nd} order, although many are characterised by the latter, such as the paramagnetic $\Longleftrightarrow$ ferromagnetic, whose behaviour is well described by the theory developed by Landau [28, 29]. These involve a broken symmetry at the transition and, consequently, an additional parameter known as the order parameter is required to describe the low symmetry state, *i.e.* the spontaneous magnetisation. An interesting feature of 2^{nd} order

transitions is that universal behaviour close to the critical temperature is seen in many materials despite significant differences in their magnetic structure or interactions. This behaviour is a feature of universality theory and is not limited to magnetic phenomena, but characterises all phase transitions that involve symmetry breaking such as solid $\leftrightarrow$ liquid and superconducting $\leftrightarrow$ non-superconducting. The characteristic that is shared in universality theory is the critical exponent of the order parameter, which is defined solely by the dimensionality of the lattice and ordering degree of freedom. Conveniently, this means that exponents calculated for simple models apply also to much more complex systems. Before discussing how we can characterise magnetic phase transitions we will first look at the types of spontaneous order that can occur.

2.4.1 Ordered magnetic structures

The interactions discussed in Section 2.3.3 give rise to a wide variety of ordered magnetic structures shown in Figure 2.5. By far the most common are ferromagnetic and simple antiferromagnetic, where all the moments align in the same direction or neighbouring moments align antiparallel, respectively. Similar to antiferromagnets, in ferrimagnets the moment direction on neighbouring sites lie antiparallel but the moment size on the two sites also differs creating a net moment. Other structures include helical and spiral structures where the moment direction precesses around a circle or cone, respectively, usually due to further-neighbour exchange. In these latter structures, the magnetic unit cell or propagation vector may not be commensurate with the nuclear cell, in which case the magnetic structure is termed incommensurate. Introducing magnetic frustration further expands the types of magnetic structure possible: regular ferromagnetic or antiferromagnetic structures can become non-collinear or non-coplanar in the presence of competing interactions, despite having commensurate propagation vectors. An interesting feature of non-collinear or non-coplanar magnetic structures is that they can be chiral, which can lead to exotic properties such as multiferroicity [30].

Whilst the ordered structures in Figure 2.5 appear more symmetric than in a paramagnet where the spins are randomly aligned, the former actually has reduced rotational symmetry compared to the latter as a unique magnetisation direction has been chosen. The rotational symmetry cannot be broken gradually, *i.e.* it is either present or not, however predicting the transition point and the behaviour of the magnetisation below it is non-trivial. Both mean-field and microscopic models can be applied to analyse this behaviour however both have their advantages and disadvantages. Mean-field models do not model the behaviour close to the transition temperature very accurately, *i.e.* the critical region, as they ignore correlations and fluctuations in the order parameter [29]. Microscopic models can provide exact solutions to problems with specific spin and lattice dimensions, such as 1-dimensional systems, however they cannot for spins in 3-dimensions which best represent bulk materials [2].

2.4.2 Magnetic models

The Curie-Weiss law described in Section 2.3.4 is a mean-field model that describes the behaviour of a correlated magnet in the paramagnetic regime. Whilst an extremely useful tool experimentally as it gives an indication of the type and strength of interactions, it poorly models the behaviour of χ close to and below the transition temperature. Another mean-field approach of predicting magnetic behaviour

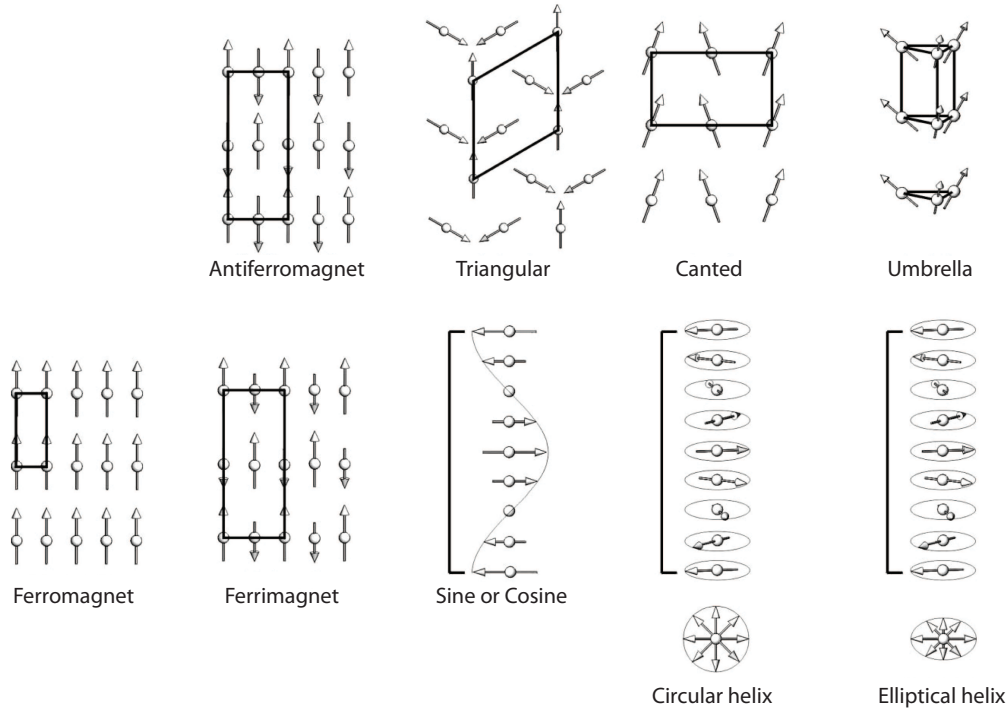

Figure 2.5: Different types of magnetic order arising from various exchange interactions. Taken from [31]

in the critical and ordered region comes from Landau theory which is based on a model where the free energy can be expanded as a power series in the order parameter [28, 29]. For a ferromagnet with a magnetisation, M, the power series expansion of the free energy in M is given by:

$$F(M) = F_0 + \alpha(T)M^2 + bM^4 \tag{2.23}$$

where F_0 and b are constants whilst $\alpha(T)$ is temperature dependent. The minimum in F is found when $dF/dM = 0$:

$$\frac{dF(M)}{dM} = 2\alpha(T)M + 4bM^3 = 0 \tag{2.24}$$

When $\alpha(T)$ becomes negative the symmetry of $F(M)$ changes dramatically from a single minimum at $M = 0$ to two minima with $M \neq 0$, as shown in Figure 2.6. By replacing $\alpha(T)$ with $\alpha(T - T_{\mathrm{C}})$ and solving equation 2.24, the solutions for M are:

$$M = 0 \quad \text{or} \quad M = \pm \left[\frac{\alpha(T_{\mathrm{C}} - T)}{2b} \right]^{\beta = \frac{1}{2}} \tag{2.25}$$

where $\beta = \frac{1}{2}$ is the critical exponent. For $T > T_{\mathrm{C}}$ the second condition is invalid so $M = 0$. However, for below T_{C} the first condition produces an unstable equilibrium and M becomes non-zero. It is also noteworthy that at $T = T_{\mathrm{C}}$ the minimum of $F(M)$ is very broad and M may take many values, hence the large fluctuations and poor performance of mean-field theories. Nevertheless, the critical exponent $\beta = \frac{1}{2}$ gives an excellent match of experimental $M(T)$ below T_{C}, except for temperatures extremely

close to the transition temperature. The precise value of the exponent found experimentally on a system with 3-dimensional lattice and spins is $\beta = 0.34$ [1].

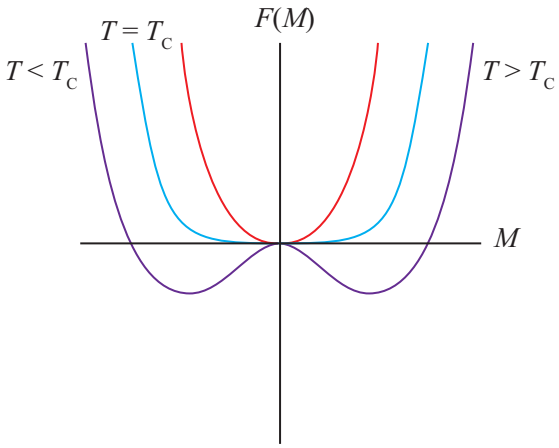

Figure 2.6: The free energy of a ferromagnet, $F(M)$, as a function of the magnetisation, M, as derived from Landau theory. Above the magnetic transition, T_{C}, no spontaneous magnetisation is present. As T_{C} is approached the well in $F(M)$ broadens due to fluctuations in M. Below T_{C} two minima in $F(M)$ appear which correspond to spontaneous magnetisation of values $\pm\left[\frac{a_0(T_{\mathrm{C}}-T)}{2b}\right]^{\frac{1}{2}}$ and signal the onset of a long-range ordered magnetic transition.

Microscopic models of magnetism are not necessarily restricted to mean-field approximations, however more detailed theory can be limited to small samples and are often not exactly solvable [32, 33]. Nevertheless, they offer insights into phase transitions unavailable from mean-field models and in many cases correctly predict behaviour observed experimentally. These models take account of the different interactions between spins but approximate with the dimensionality of the spin and the lattice. The most common spin models are in 1- and 3-dimensions, termed Ising and Heisenberg, respectively, and these will be discussed for various different lattice dimensions.

Calculations of the critical exponents from microscopic models can be performed through using the renormalisation group, which is a mathematical construct that takes advantages of the fact that exponents are unrelated to the microscopic interactions present in the system [32]. In fact, the exponents are determined by three things: (i) the spatial dimension, (ii) the symmetry of the order parameter and (iii) the symmetry and range of interactions.

In the Ising model the spins are 1-dimensional and constrained to lie along the z axis, *i.e.* up or down. The Hamiltonian then simplifies to:

$$\hat{\mathcal{H}} = -\sum_{\langle ij \rangle} J S_i^z S_j^z \tag{2.26}$$

These spins can be arranged on a lattice with dimension $d = 1, 2, 3, \ldots$. On a 1-dimensional lattice, *i.e.* a chain of spins, no magnetic ordering transition occurs as whilst the energy cost of flipping a spin is negligible, J, the entropy gain is massive. Therefore spin flipping occurs spontaneously at $T > 0\,\mathrm{K}$ and no long-range ordered state can occur. In a 2-dimensional lattice, the entropy and energy changes

related to flipping spins are of similar magnitude and scale with the size of the spin flipped region. These systems go through a magnetic ordering transition below some non-zero critical temperature.

The Heisenberg model describes spins as 3-dimensional vectors, so they can point in any direction in real space. Evidently, most real situations are best approximated by the Heisenberg model, however these can be difficult to solve exactly and so experimental and theoretical values of critical exponents can differ. For instance, the specific heat critical exponent varies from -0.12 to 0.1 from theory to experiment, respectively [1].

2.4.3 Representation theory and magnetic structures

The description of magnetic structures originally grew out of the field of crystallography and it therefore inherited many of the historical features of the latter, *i.e.* the space group formalism. However, problems with this approach arise when attempting to describe more complex magnetic structures with simple crystallographic symmetry operations. These limitations may be overcome by employing representational theory, where symmetry spaces are described using irreducible representations (irreps) [34]. These irreps span dimensions 1 through 6 and those of 2 and above cannot be converted directly into a space group description because they describe higher-order symmetry structures.

Combining representational analysis with Landau's theory of a second order phase transition provides an indispensable tool for analysing magnetic structures as Landau theory greatly limits the symmetries of the possible magnetic structures. This is evident from the common situation where a 2^{nd} order phase transition leads to a low symmetry structure described by only one irrep. Therefore, after determining the irreps of the magnetic structure from knowledge of the propagation vector and the crystallographic space group, use of Landau theory often restricts just one of these to be the correct solution [31].

To expand on this method we must first define the eigenfunctions of an electron travelling through a periodic crystal, termed a Bloch wave:

$$U_k(r) = u_k(0)e^{-2\pi i\mathbf{k}\cdot\mathbf{T}} \tag{2.27}$$

relating the initial electron position (0) to point r defined by the translation $\mathbf{T}$ and where $\mathbf{k}$ is the propagation vector. This relationship also applies for the propagation of a magnetic structure and by using ϕ_k to represent the basis vector that describes the magnetic moment, the total magnetisation, Φ, is given by the symmetry adapted linear combination (SALC) of these basis vectors:

$$\Phi_k(r) = \sum_{j,k} C_k^j \phi_k^j(0) e^{-2\pi i\mathbf{k}\cdot\mathbf{T}} \tag{2.28}$$

where C_k^j is the contribution of each basis vector, ϕ_k^j, to the SALC. To determine the basis vectors, the irreducible representations of the group of symmetry elements that leave $\mathbf{k}$ invariant, commonly known as the little group, $G_{\mathbf{k}}$, are required. The symmetry elements of $G_{\mathbf{k}}$ are then applied to each crystallographic magnetic site in the primitive unit cell to create the permutation representation, Γ_{perm}. In addition to Γ_{perm}, the moments themselves must be treated under the symmetry elements of $G_{\mathbf{k}}$ giving

the axial representation, Γ_{axial}. Care must be taken when calculating Γ_{axial} for magnetic moments as they are axial vectors and must be treated as such, *i.e.* inversion symmetry does not reverse the moment direction. With these, the magnetic representation, Γ_{mag}, can be calculated using:

$$\Gamma_{\mathrm{mag}} = \Gamma_{\mathrm{perm}} \times \Gamma_{\mathrm{axial}} \tag{2.29}$$

which can be decomposed into irreps of $G_{\mathbf{k}}$, such that:

$$\Gamma_{\mathrm{mag}} = \sum_{v} n\Gamma_{v} \tag{2.30}$$

where Γ_v are the irreps of $G_{\mathbf{k}}$. From these irreps the basis vectors, ϕ_v (Equation 2.28), can be projected and, along with the propagation vector, used to build the symmetry allowed magnetic structures. ϕ_v can have non-zero real and imaginary components, which together with the values of **k** leads to a complex range of potential magnetic structures.

2.4.4 Excitations

A further consequence of spontaneous symmetry breaking is the appearance of thermal excitations of the order parameter. In a crystalline solid these are lattice vibrations, quantised as phonons, whilst for a magnetic structure these are termed spin waves, quantised by magnons. Given the direct relationship to the ordered magnetic structure, measurement of spin waves is vital to our understanding of magnetic materials and is commonly done using inelastic neutron scattering. As we will see, characterisation of the spin wave dispersion relation enables the determination of the individual exchange parameters of a particular magnetic structure.

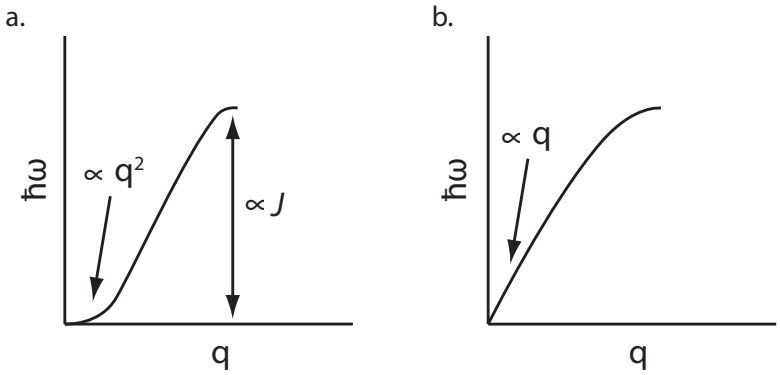

Figure 2.7: The spin wave dispersion relations for **a.** a ferromagnet and **b.** an antiferromagnet as observed in an inelastic neutron scattering experiment. The shape at low-q is a good fingerprint for distinguishing the origin of the interactions, whilst the amplitude of the spin wave is proportional to the exchange energy.

For an isotropic ferromagnet, the spin wave dispersion relation as a function of momentum and energy (q,ω) is derived from spin wave theory, based on the Heisenberg Hamiltonian (Equation 2.15), and is given by:

$$\hbar\omega = 4JS(1 - \cos(qa)) \tag{2.31}$$

where J is the exchange term and a is the magnetic unit cell lattice paramater. This dispersion is shown in Figure 2.7 and has two key features for an experimentalist: (i) the amplitude is equal to $8SJ$ and (ii) the low q region has a quadratic dispersion where $\hbar\omega \approx 2JSq^2a^2$. The former allows quick estimation of the size of the interactions, or vice-versa, whilst the latter is useful when compared against spin waves originating from an antiferromagnetic structure. For an antiferromagnet, the dispersion relation is a sine function, rather than cosine, and given by:

$$\hbar\omega = 4JS\sin(qa) \tag{2.32}$$

Figure 2.7 shows this dispersion, which at low q approximates to $\hbar\omega \approx 2JSqa$ and is therefore linear in these regions. The differences in the low q scattering for ferro- and antiferromagnets is a useful fingerprint for determining the origin of the spin waves in a neutron scattering experiment.

More complicated spin wave models can be calculated to allow extraction of exchange parameters between the different magnetic ions in the structure from experimental data. Whilst such calculations are beyond the scope of this thesis there are some important features that appear with complex models. It is noteworthy that the dispersion relations for simple ferro- and antiferromagnets have only a single acoustic branch, *i.e.* $\omega = 0$ when $q = 0$, however with increasing complexity of the model further branches appear. The number of branches is equal to the number of magnetic sites in the primitive unit cell and the additional branches will be optical, such that $\omega \neq 0$ when $q = 0$. The last chapter of this thesis, in particular, deals with inelastic neutron scattering data with multiple spin wave branches.

Bibliography

[1] P. M. Chaikin and T. C. Lubensky, *Principles of condensed matter physics*, Cambridge University Press, Cambridge, 7th edn., 1995.

[2] S. Blundell, *Magnetism in condensed matter*, Oxford University Press, Oxford, 2001.

[3] M. Getzlaff, *Fundamentals of Magnetism*, Springer, New York, 2008.

[4] J. Crangle, *Solid state magnetism*, Von Nostrand, 1991.

[5] G. G. Scott, *Rev. Mod. Phys.*, 1962, **34**, 102–111.

[6] J. H. Van Vleck, *Science*, 1978, **201**, 113–120.

[7] P. Zeeman, *Nature*, 1897, **55**, 357.

[8] F. Hund, *Zeitschrift für Phys.*, 1927, **40**, 742–764.

[9] L. H. Bennett, C. H. Page and L. J. Swartzendruber, *J. Res. Natl. Bur. Stand. (1934).*, 1978, **83**, 9–12.

[10] G. A. Bain and J. F. Berry, *J. Chem. Educ.*, 2008, **85**, 532.

[11] R. H. Colman, A. Sinclair and A. S. Wills, *Chem. Mater.*, 2010, **22**, 5774–5779.

[12] A. Zorko, S. Nellutla, J. van Tol, L. Brunel, F. Bert, F. Duc, J.-C. Trombe, M. de Vries, A. Harrison and P. Mendels, *Phys. Rev. Lett.*, 2008, **101**, 25–28.

[13] A. Zorko, F. Bert, A. Ozarowski, J. van Tol, D. Boldrin, A. S. Wills and P. Mendels, *Phys. Rev. B*, 2013, **88**, 144419.

[14] H. A. Jahn and E. Teller, *Proc. R. Soc. A Math. Phys. Eng. Sci.*, 1937, **161**, 220–235.

[15] M. C. M. O'Brien, *Proc. R. Soc. A Math. Phys. Eng. Sci.*, 1964, **281**, 323–339.

[16] G. A. Gehring and K. A. Gehring, *Rep. Prog. Phys.*, 1975, **38**, 1–89.

[17] S. T. Bramwell, M. J. Harris, B. C. den Hertog, M. J. P. Gingras, J. S. Gardner, D. F. McMorrow, A. R. Wildes, A. L. Cornelius, J. D. M. Champion, R. G. Melko and T. Fennell, *Phys. Rev. Lett.*, 2001, **87**, 047205.

[18] P. A. M. Dirac, *Proc. R. Soc. A Math. Phys. Eng. Sci.*, 1926, **112**, 661–677.

[19] P. W. Anderson, *Phys. Rev.*, 1950, **79**, 350–356.

[20] J. Kanamori, *J. Phys. Chem. Solids*, 1959, **10**, 87–98.

[21] Y. Mizuno, T. Tohyama and S. Maekawa, *Phys. Rev. B*, 1998, **57**, 5326–5335.

[22] K. I. Kugel' and D. I. Khomskii, *Sov. Phys. Usp.*, 1982, **25**, 231–254.

[23] M. A. Ruderman and C. Kittel, *Phys. Rev.*, 1954, **96**, 99–102.

[24] I. E. Dzyaloshinskii, *Sov. Phys. JETP*, 1964, **19**, 960–971.

[25] T. Moriya, *Phys. Rev.*, 1960, **120**, 91–98.

[26] F. Keffer, *Phys. Rev.*, 1962, **126**, 896–900.

[27] P. Weiss, *J. Phys. Theor. Appl.*, 1907, **6**, 661–690.

[28] L. Landau, *Zh. Eksp. Teor. Fiz.*, 1937, **7**, 19–32.

[29] L. Landau, *Ukr. J. Phys.*, 2008, **53**, 25–35.

[30] K. Wang, J.-M. Liu and Z. Ren, *Adv. Phys.*, 2009, **58**, 321–448.

[31] A. S. Wills, *J. Mater. Chem.*, 2005, **15**, 245.

[32] A. Pelissetto and E. Vicari, *Phys. Rep.*, 2002, **368**, 549–727.

[33] R. Guida and J. Zinn-Justin, *J. Phys. A. Math. Gen.*, 1998, **31**, 8103–8121.

[34] O. V. Kovalev, *Irreducible representations of the space groups*, Gordon and Breach, New York, 1965.

Chapter 3

Frustrated magnetism

The previous chapter introduces the relevant magnetic theory required to understand frustrated magnetism, the central theme of this thesis. In the following chapter, the discussion initially concentrates on the origins of classically frustrated magnetism on certain geometric structures. Quantum frustrated magnetism for small S is developed from this and the exotic ground states that can occur are described, such as quantum spin liquids, along with current experimental evidence for such states. The focus then moves to one particular model system predicted to host quantum spin liquids, the $S = \frac{1}{2}$ kagome Heisenberg magnet (KHM), which all the materials studied in this thesis are examples of. Theoretical and experimental work on the $S = \frac{1}{2}$ KHM is discussed in depth to allow understanding of, and give context to, the rest of the thesis.

3.1 Geometric frustration

In a classical Heisenberg nearest-neighbour antiferromagnet the sublattice magnetisation becomes non-zero at the Weiss temperature, *i.e.* $T_{\mathrm{N}} \approx \theta_{\mathrm{W}}$. The central concept of frustrated magnetism is that long-range magnetic order can be avoided by having a Hamiltonian where competing energies cannot be simultaneously minimised, leading to situations where $T_{\mathrm{N}} < \theta_{\mathrm{W}}$ [1]. Not only can frustration suppress T_{N}, it can lead to quite different ground states unobtainable in unfrustrated systems with exotic properties of interest at both a fundamental and functional level. Perhaps the most important of these properties is macroscopic ground state degeneracy, because whilst myriad exotic phenomena exist within the family of frustrated magnets the former is common to all.

Conveniently for experimentalists, magnetic frustration can be encouraged structurally through using magnetic lattices that are geometrically frustrated [1]. One of the simplest illustrations of this is on a single antiferromagnetic triangle with Ising spins, shown in Figure 3.1a. All three spins cannot simultaneously satisfy all their interactions and the ground state is two-fold degenerate. Further examples are found when further neighbour exchange is taken into account, for instance in the J_1–J_2 square lattice model (Figure 3.1b). If both exchange terms are antiferromagnetic, depending on the J_1/J_2 ratio one of the interactions cannot be satisfied. However, finding experimental models on a square lattice with the correct balance of exchange energies is rare and so the focus will return to periodic lattices based on triangular units.

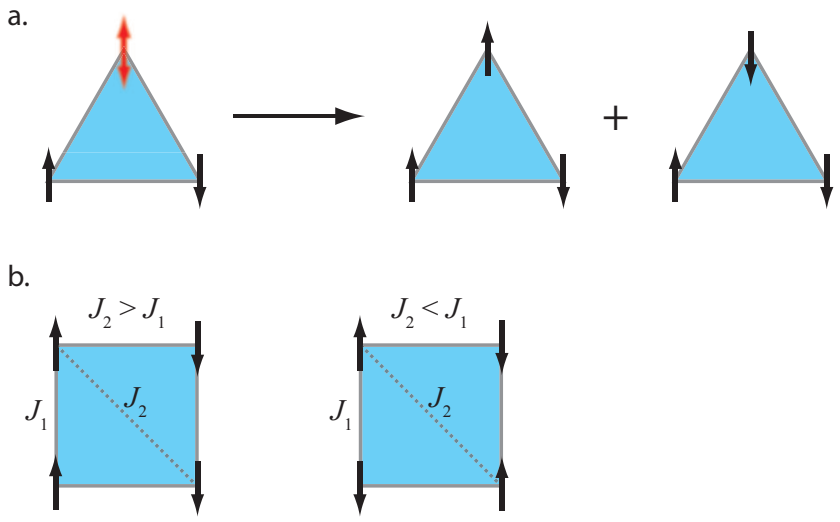

Figure 3.1: a. Antiferromagnetically coupled Ising spins arranged at the vertices of a triangle are two-fold degenerate. **b.** Antiferromagnetically coupled Ising spins on a square lattice. Depending on the J_1/J_2 ratio, the frustration can either arise along the side or through the diagonal of the square.

3.1.1 Triangular based lattices

Quantum spin disorder was predicted on triangular lattices several decades ago by Anderson in the context of resonating valence bond (RVB) theory and since then materials with triangular networks have attracted much research in search of this exotic state [2]. Several variations on the triangular lattice exist. The simplest is a lattice of edge-sharing equilateral triangles, shown in Figure 3.2a, although variations within this exist such as how the planes are stacked, the interplanar metal–metal bond length and the intraplanar metal–metal bond length. The majority of these materials belong to the delafossite or α-$NaFeO_2$ family of materials, with magnetic triangular layers separated along the stacking direction by diamagnetic transition metal or alkaline earth ions, respectively. Surprisingly, triangular magnets display a wide range of magnetic behaviour, from magnetic vortices in $NaCrO_2$ [3, 4] to spin and orbital frustration in $LiNiO_2$ [5] and spin liquid behaviour in $NiGa_2S_4$ [6].

Expanding the triangular lattice in three dimensions brings us to the pyrochlore lattice, where magnetic structures are built from stacked tetrahedrons (Figure 3.2b). As on a triangular unit, described earlier, an antiferromagnetically coupled tetrahedron possesses a similar set of degenerate ground states. One particularly intriguing pyrochlore family is the $A_2B_2O_7$ structure where the A-site is a trivalent rare-earth ion and the B-site is a tetravalent transition metal ion. Numerous examples of these exist with either the A- or B-site magnetic, or both, and studies into these have revealed a vast number of varied and exotic ground states. Perhaps the most famous of these is spin-ice, such as found in $Ho_2Ti_2O_7$, where the magnetic ground state consists of spins arranged in a 'two-in, two-out' structure on each tetrahedron: this is analogous to solid ice (H_2O) and holds a degeneracy [7, 8]. Due to the strongly localised f-electrons and large ($\sim 10\,\mu_B$) moment size, the dipolar interaction is of considerable magnitude to the exchange energy and has a large influence on the exotic ground state.

$Tb_2Ti_2O_7$ has received a lot of attention for showing a spin liquid ground state stable down to very low temperature, $T = 17\,\text{mK}$, despite antiferromagnetic correlations of $\Theta_\text{W} \sim 13\,\text{K}$ [9]. In addition to spin frustration, the material has a dynamic Jahn-Teller effect that adds further complexity to its ground state, showing that the magnetic properties are intricately linked to the lattice [10]. Confusingly, the isoelectronic Tb^{3+} pyrochlore, $Tb_2Sn_2O_7$, has very different properties, entering long-range magnetic order at $T = 0.87\,\text{K}$, but there is no definitive explanation why. Inelastic neutron scattering experiments suggest differences in the crystal field excitations, with the energies of the ground state and first excited state inverted, but the cause of this remains unknown [11].

Since Anderson's seminal paper on RVB theory the range of exotic magnetic ground states in triangular-based magnets has expanded considerably, along with our understanding of magnetic frustration. Even from this brief introduction, it is evident that these advancements are heavily reliant on progress in synthetic techniques and the discoveries of new materials with novel, geometrically frustrated lattices. As it turns out, edge-sharing triangular lattices do not offer the best opportunity to observe RVB physics [12] and this challenge has instead been passed onto the corner-sharing triangular network found on the kagome lattice.

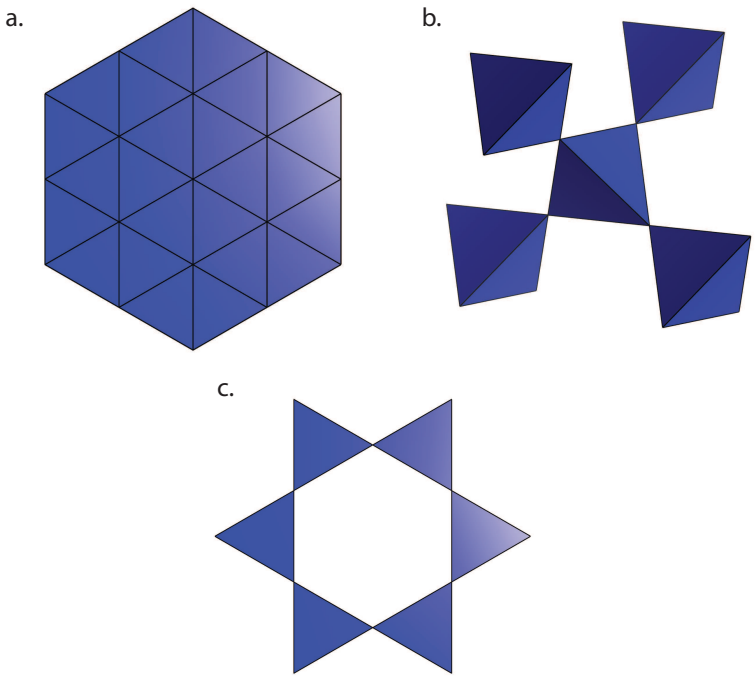

Figure 3.2: **a.** An edge-sharing triangular lattice. **b.** A vertex-sharing tetrahedral lattice, commonly known as the pyrochlore lattice. **c.** The vertex-sharing triangular lattice, commonly known as the kagome lattice.

3.1.2 The kagome lattice

The low-coordination of the corner-sharing triangular kagome lattice of magnetic ions, shown in Figure 3.2c, is predicted not to order even at $T = 0$ due to a macroscopic ground state degeneracy and zero energy excitations [13, 1]. The majority of current interest in KHMs is focussed on $S = \frac{1}{2}$ materials, however until recently no experimental examples existed and beforehand research was limited

to classical KHMs with $S > \frac{1}{2}$. The materials within this family provide the archetypal examples of geometrically frustrated magnets and it is necessary to review them.

The jarosite family of materials are the most studied kagome antiferromagnets [1]. They have the generalised formula $AB_3(SO_4)_2(OH)_6$ where $A = Na^+$, K^+, Rb^+, NH_4^+, Ag^+ and H_3O^+ and $B = Fe^{3+}$, Cr^{3+} and V^{3+}, therefore providing classical models with $S = \frac{5}{2}$ to more quantum with $S = 1$ [14]. The crystal structure is described in the $R\bar{3}m$ space group and the kagome triangles retain 3-fold rotational symmetry to give an isotropic nearest-neighbour interaction. However, the materials are prone to off-stoichiometry with hydronium incorporation at the A site and loss of the B site [15] and whilst the defect formation is hard to model and quantify, it inevitably effects the magnetic properties of the material.

The magnetic properties of the jarosite family depends heavily on the occupation of the A- and B-sites. Jarosite itself ($A = K^+$, $B = Fe^{3+}$) enters long-range magnetic order between $50 < T < 65\,\mathrm{K}$ to a 120° '$q = 0$' structure followed by a spin-canting transition [16]. The complex magnetic ordering is a result of a significant Dzyaloshinskii-Moriya interaction [17], in addition to both strong nearest-neighbour antiferromagnetism ($|\theta_\mathrm{W}| > 600\,\mathrm{K}$) and intraplanar coupling ($\mathbf{k} = (00\frac{3}{2})$), with this frustration also causing short-range fluctuations in the ordered regime. In the Cr^{3+} analogue, a partial antiferromagnetic transition occurs at $T_\mathrm{N} \sim 2\,\mathrm{K}$ with a $\mathbf{k} = (000)$ propagation vector, showing the B-site cation significantly changes the intraplanar coupling, with the remaining spins in a gapless spin liquid state [18]. Frustration is completely absent from the vanadium jarosites, which enters long-range collinear antiferromagnetic order at $T_\mathrm{N} \sim 20\,\mathrm{K}$ [19].

Hydronium jarosite ($A = H_3O^+$, $B = Fe^{3+}$) has attracted the majority of research in the family as it does not enter long-range magnetic order and instead displays spin-glass behaviour, in stark contrast to the remaining $B = Fe^{3+}$ members [1]. The glassy behaviour is closely related to spin anisotropy created by distortion around the Fe^{3+} site [20], however the behaviour below the glassy transition is distinct from other site- or bond-disordered spin glasses, for instance it is highly temperature insensitive [21]. Overall, the jarosite family have considerably progressed theories and understanding of magnetic frustration through their unconventional ground states and complex magneto-structural couplings.

$SrCr_{9p}Ga_{12-9p}O_{19}$ (SCGO) and $Ba_2Sn_2ZnCr_{7p}Ga_{10-7p}O_{22}$ (BSZCGO) are another family of excellent model magnets with corner-sharing triangular lattices. Rather than kagome compounds they are instead pyrochlore slabs (Figure 3.3) separated by either Cr–Cr pairs in SCGO or diamagnetic ions in BSZCGO. Both compounds suffer from Cr/Ga site disorder causing spin vacancies in the magnetic layers, although this does not destroy the frustration and the spins remain dynamic down to $T = 20\,\mathrm{mK}$, well below the spin-glass transition, $T_\mathrm{g} \sim 5\,\mathrm{K}$ [22]. The role of defects remains an open question in these materials and, in fact, the dependence of T_g on defect concentration is not similar to any conventional spin-glass [23], again suggesting an unconventional mechanism behind the glassy behaviour, as in the jarosites.

Research into the kagome materials discussed in this section swiftly advanced the field of frustrated magnetism and instigated a hunt for further synthetic examples of kagome-based magnets. In particular,

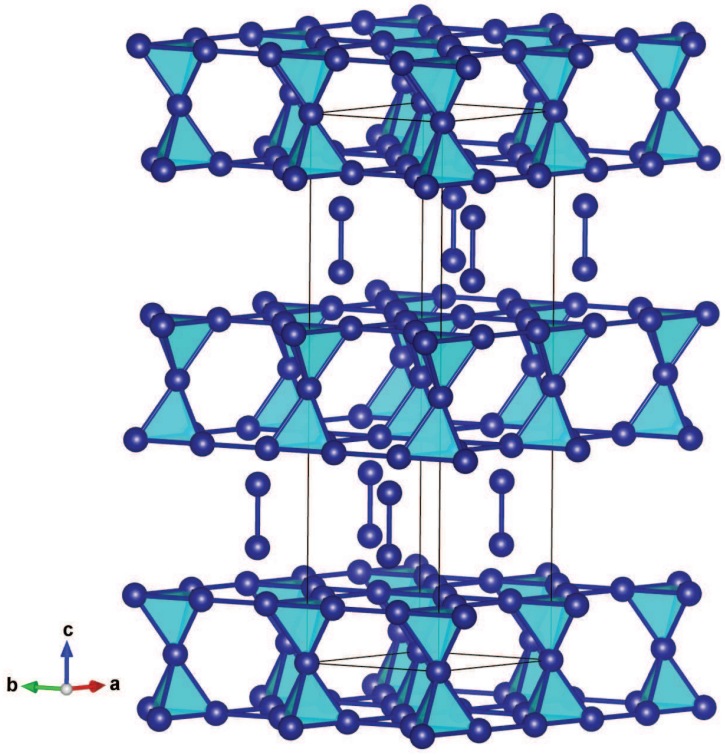

Figure 3.3: Crystal structure of SCGO showing the pyrochlore slabs separated by Cr–Cr pairs along the c-axis. In BSZCGO the pyrochlore slabs take the same shape, however there are no Cr–Cr pairs between the slabs making it a structurally improved model kagome system.

the jarosites, SCGO and BSZCGO do not offer insights into quantum fluctuations, which must be tackled by $S = \frac{1}{2}$ materials, as will now be discussed.

3.2 Quantum frustration

Geometrically frustrated magnets with low spin, *i.e.* $S < 1$, can be prevented from magnetically ordering at $T = 0$ due to strong quantum fluctuations. In some respects this state could be seen as a 'quantum paramagnet', however classical fluctuations are quite different from their quantum counterparts. In the presence of strong quantum fluctuations, the ground state may consist of a large superposition of configurations in which each spin points simultaneously in many different directions with no symmetries broken and therefore no associated order parameter [24]. Such a state remains elusive experimentally but is predicted to have numerous exotic properties such as long-range spin entanglement and fractional $S = \frac{1}{2}$ excitations.

In the quantum limit of frustration the spins can be represented as paired singlets, or valence bonds (VBs), and these non-magnetic ($S = 0$) entities define the physics of these systems. However, depending on whether the VB arrangement breaks translational symmetry, the resultant ground states can be split into two categories: (i) valence bond crystals (VBCs) when this symmetry is broken and (ii) quantum spin liquids (QSLs) when it is not. Both states have attracted much attention from both theoreticians

and experimentalists, however it is QSLs that are the most alluring. Their failure to be described by any symmetry breaking has brought about suggestions of a new kind of order, 'quantum order', with new fluctuations and excitations [25]. First, in order to fully understand QSLs, it is first necessary to discuss further valence bonds and VBCs.

3.2.1 Valence bond crystals

A valence bond contains two $S = \frac{1}{2}$ spins oppositely aligned in order to minimise the Heisenberg antiferromagnetic coupling between them. When a VB configuration is the favoured magnetic ground state, as is predicted for several Heisenberg models [1], for instance on the kagome lattice, no Néel order occurs at $T = 0\,\mathrm{K}$. A simple nearest-neighbour VB configuration on the kagome lattice is shown in Figure 3.4a where spins are paired with exchange J and singlets are coupled by J'. It is important to note here that whilst the dimers are long-range ordered, the same cannot be said for the spins which remain disordered. When $J' = 0$ the ground state is a trivial product of the singlets, however with $J' > 0$ fluctuations are induced that couple VBs over longer distances (Figure 3.4b). Despite this latter point, a single parent VB configuration (or a small number of degenerate ones) is usually energetically preferable and the fluctuations create new configurations that differ slightly from this.

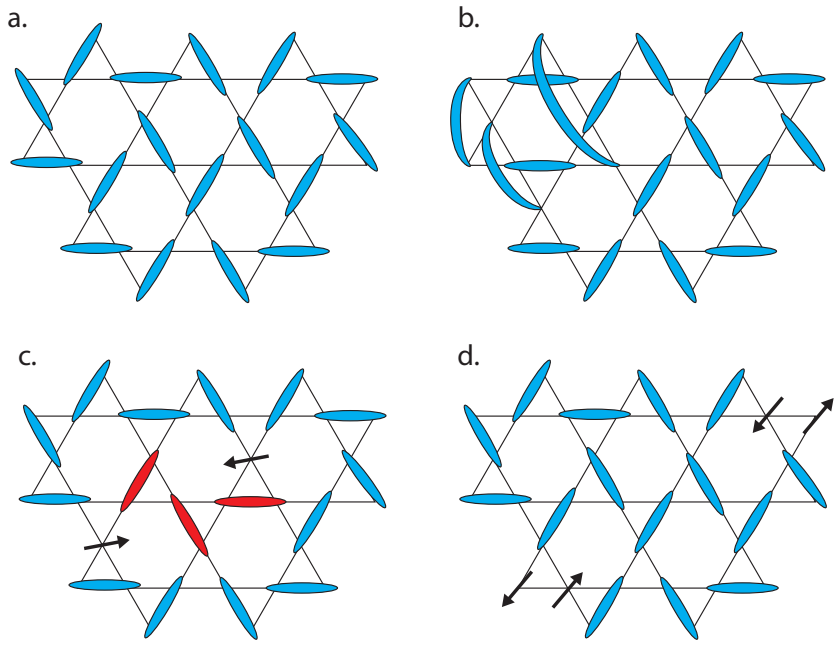

Figure 3.4: **a.** A simple nearest neighbour VB configuration on the kagome lattice with exchange J within dimers and $J' = 0$ between dimers. **b.** When $J' > 0$, fluctuations dress the configuration from **a.** with a different VB pattern, some of which are longer-range. **c.** A broken singlet in a VBC causes a rearrangement of local VBs which has an energy cost that scales with the distance between the spinons. **d.** At large spinon separations it is energetically favourable for an additional singlet to break, confining them so they cannot propagate. Therefore, $S = \frac{1}{2}$ excitations cannot occur in a VBC.

VBC excitations involve $\Delta S = 1$ transitions that are gapped. Spinon, $S = \frac{1}{2}$, excitations cannot exist in a VBC due to the favourable parent VBC configuration. Breaking a singlet necessarily creates

misaligned dimers with a configuration of higher energy than the parent structure, shown in Figure 3.4c. This energy cost scales with the distance between the spinons and creates a force to restore the parent VBC configuration. If the distance is significantly large, it is energetically favourable to break an additional singlet and the parent VBC confines both of these to their creation point (Figure 3.4d). As we will see, the lack of a favoured parent VB configuration in a QSL means there is no mechanism to confine spinons.

3.2.2 Resonating valence bonds and quantum spin liquids

Having introduced VBCs the discussion can smoothly transition to QSLs. In VBCs energetically favourable dimer configurations break translational symmetry and cause long-range dimer order. However, if no preferred VB configuration exists the ground state is a superposition of a large number of VB configurations with equal weighting and all very different from one another. From our discussion on VBCs, it is evident that QSLs do not break any regular symmetries and have no long-range order even in the dimer correlations. Perhaps the defining characteristic is their excitations which are $S = \frac{1}{2}$ spinons and can occur as there is no mechanism in a QSL to confine them allowing them to propagate freely. The signature of this in a neutron scattering experiment is a continuum of excitations in energy and momentum and provides a key experimental hallmark of a QSL. With a large enough VB ground state manifold, QSLs are often termed Resonating Valence Bond (RVB) states, although the distinction between them is not clear [2, 1]. This extensive degeneracy allows $S = 0$ excitations, termed visons, in addition to spinons and this fact lies behind Anderson's prediction of superconductivity arising from doped RVBs [26].

The intriguing properties of QSLs do not stop there. According to classical theory, they do not break any symmetries and are instead disordered. They, therefore, cannot be described by Landau theory. However, they are thought to possess 'quantum order' that characterises their excitations and phase transitions, as Landau theory does for classical states, and are therefore highly entangled rather than being disordered [25]. The properties that arise from quantum order are thought to lay the foundation for the multitude of exotic transport properties that are predicted from QSLs and RVBs, such as high-T_{C} superconductivity and fractionalised quantum Hall effects [26, 27].

The most likely model system for observing QSL physics are $S = \frac{1}{2}$ KHMs [28, 29, 30]. State-of-the-art theoretical calculations of these systems are inconclusive, with evidence pointing to either a VBC or QSL ground states, either gapped or gapless [31, 32]. As we will see, finding experimental evidence for such states in real systems is far from trivial.

3.3 $S = \frac{1}{2}$ kagome magnets

There are only a few magnets that approximate to the idealised $S = \frac{1}{2}$ KHM model. The majority of research has focussed around three materials: volborthite, herbertsmithite and vesignieite. Volborthite, $Cu_3V_2O_7(OH)_2.2H_2O$, was the first to be discovered and successfully synthesised [33]. Despite the slight distortion of its kagome lattice, which causes inequalities in the nearest-neighbour exchange interactions, it has attracted extensive research using a wide variety of characterisation techniques [34].

Herbertsmithite, γ-$ZnCu_3(OH)_6Cl_2$, hailed as the first structurally perfect model as it retains 3-fold symmetry in the kagome planes [35], has since been shown to suffer from significant antisite disorder which acts to dilute the magnetic lattice [36]. Vesignieite, $BaCu_3V_2O_8(OH)_2$, also suffers from a distortion of the kagome network but it is an order of magnitude less than volborthite, is the most recent of the three materials to be studied [37]. All of these materials possess a high degree of magnetic frustration and present excellent opportunities to explore QSL physics.

3.3.1 Herbertsmithite, $\gamma-ZnCu_3(OH)_6Cl_2$, and paratacamite related minerals

Paratacamite, $(Cu,Zn)Cu_3(OH)_6Cl_2$, is a secondary copper mineral found in many mines around the world [38]. Several derivatives and closely related minerals provide excellent model $S = \frac{1}{2}$ KHMs as they often crystallise with trigonal symmetry and have an undistorted kagome network of Cu^{2+} ions (Figure 3.5a). However, these minerals all have additional M^{2+} sites (M = Cu, Zn, Cd, Mg, Ni) that occupy either the centre of the kagome hexagons to build a triangular lattice or between the kagome layers forming a 3-dimensional pyrochlore lattice. The ionic sizes of all these ions are similar leading to significant site mixing between kagome and non-kagome sites that either introduces 3-dimensional magnetic exchange, dilutes the kagome lattice or forms an edge-sharing triangular magnetic network. The most studied $S = \frac{1}{2}$ KHM materials in this family include herbertsmithite, $\gamma-ZnCu_3(OH)_6Cl_2$ [35], kapellasite, $\alpha-ZnCu_3(OH)_6Cl_2$ [39], 'Mg-herbertsmithite', $\gamma-MgCu_3(OH)_6Cl_2$ [40], haydeeite, $\alpha-MgCu_3(OH)_6Cl_2$ [41], and further examples exist with SO_4 substituted for Cl [42], Cd for (Cu,Zn) [43] or both [44, 45].

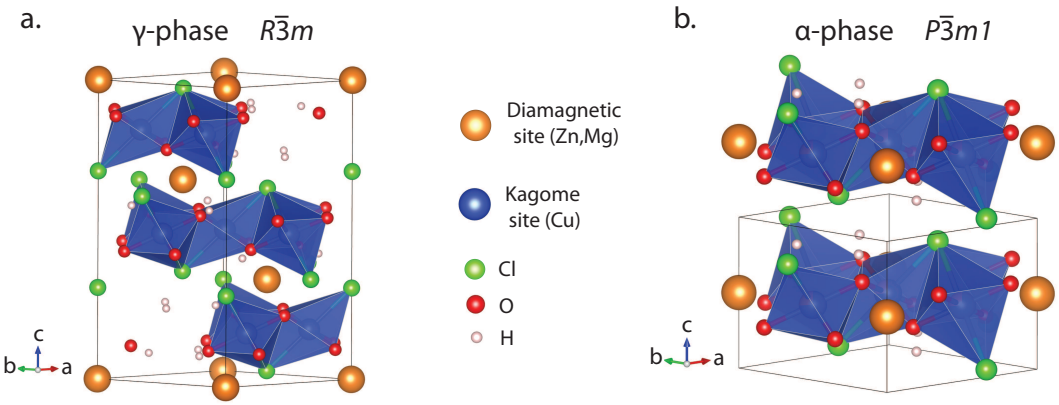

Figure 3.5: Crystal structures of the γ- **(a.)** and α-phases **(b.)** of $ACu_3(OH)_6Cl_2$ where $A = Zn^{2+}$ or Mg^{2+}. In the γ-phase the Cu^{2+} kagome planes are separated by AO_4Cl_2 octahedra raising the possibility of coupling between planes. The AO_4Cl_2 octahedra lie within the kagome plane in the α-phase and so the magnetic network is highly 2-dimensional. In both phases the similar size and valency of the kagome and A^{2+} sites causes significant site mixing and perturbs the ideal $S = \frac{1}{2}$ KHM model with further-neighbour interactions or dilution of the kagome lattice.

Herbertsmithite has attracted the most attention out of all the paratacamite-based minerals as a model $S = \frac{1}{2}$ KHM. With its successful synthesis around a decade ago it was hailed as the first structurally perfect $S = \frac{1}{2}$ KHM, with a trigonal $R\bar{3}m$ structure consisting of Cu^{2+} kagome planes with Zn^{2+}

sites linking these, and its lack of magnetic order down to $T = 2\,\mathrm{K}$ despite strong antiferromagnetic interactions ($\theta_\mathrm{W} = -314\,\mathrm{K}$) reinvigorated the search for QSL physics in these materials [35]. However, it has significant Cu^{2+}/Zn^{2+} site disorder that, as mentioned previously, introduces coupling between the kagome lattice as well as diluting the planes themselves and masks the intrinsic physics, particularly at very low temperatures [36, 46, 34]. Improved synthetic methods allowed growth of single crystals with fully occupied Cu^{2+} kagome planes and values as low as 15 % substitution of Cu^{2+} on the Zn^{2+} site [47]. Measurements on these crystals using a variety of techniques reveal a non-trivial, highly frustrated magnetic ground-state dominated by nearest-neighbour antiferromagnetic exchange although with perturbations from both a DM interaction and an easy-axis anisotropic exchange [48, 49, 50]. Despite defects and magnetic perturbations the material shows a continuum of low-energy spinon excitations, a clear signature of a quantum spin liquid state found through Raman and inelastic neutron scattering, adding significant weight behind the argument that the $S = \frac{1}{2}$ KHM is the best model system to observe such physics in 2-dimensions [51, 52].

Other members of the paratacamite family also show magnetically frustrated ground states. 'Mg-herbertsmithite' shares the same $R\bar{3}m$ crystal structure as its well known Zn-analogue with only $\sim 4\,\%$ Mg on the Cu kagome site and $\sim 17\,\%$ Cu on the Mg site [40]. It also has no sign of magnetic order down to $T = 0.02\,\mathrm{K}$ despite strong antiferromagnetic interactions ($\theta_\mathrm{W} = -284\,\mathrm{K}$) and the μSR signal does not even suggest spin freezing, making a spin liquid state likely [53]. Substitutions of the herbertsmithite structure with Cd^{2+}, SO_4^{2-} or both lead to symmetry lowering distortions that cause inequivalence of the Cu–Cu distances [42, 43, 44, 45]. All these materials again show strong antiferromagnetic interactions and either no long-range order, such as in $ZnCu_3(OH)_6SO_4$ and $CdCu_3(OH)_6Cl_2$ [42, 43], or a heavily suppressed transition as in $Cd_2Cu_3(OH)_6(SO_4)_2 \cdot 4H_2O$ ($\frac{\theta_\mathrm{W}}{T_\mathrm{N}} \sim 13$) [44]. In the latter, the magnetic order appears to coexist with spin singlets, quite a different scenario to the related minerals already discussed and argued to be a result of lattice distortions [45]. However, this is unlikely as the other Cl and Cd-analogues remain frustrated as $T \to 0\,\mathrm{K}$ despite distortions.

Kapellasite, $\alpha{-}ZnCu_3(OH)_6Cl_2$, and haydeeite, $\alpha{-}MgCu_3(OH)_6Cl_2$, crystallise with the slightly different $P\bar{3}m1$ space group compared to Mg- and Zn- herbertsmithite, causing the non-kagome Zn/Mg site to lie within the kagome plane in the centre of the hexagons, and both materials again have significant cation site mixing (Figure 3.5b)[41, 39]. Interestingly, both materials have very different magnetic responses defined by competing interactions, rather than the nearest-neighbour dominated ground state in herbertsmithite [54]. Kapellasite has a QSL-like inelastic neutron scattering response down to $T = 0.02\,\mathrm{K}$ which arises from dynamic short-range correlations based on a unique non-coplanar cuboc2 structure [55] yet haydeeite, on the other hand, goes through a ferromagnetic-like transition at $T_\mathrm{C} = 4.2\,\mathrm{K}$. The cuboc2 structure of kapellasite was correctly predicted from a classical kagome model with various further-neighbour exchange couplings [56]. Figure 3.6 shows the phase diagram from these calculations, along with the exchange paths, and suggests that even minor changes in J_i results in very different magnetic ground states. The J_i values for haydeeite are experimentally determined in Chapter 8 and prove that it does in fact lie in the ferromagnetic region of the phase diagram largely due to a

decrease in the energy of J_{d}.

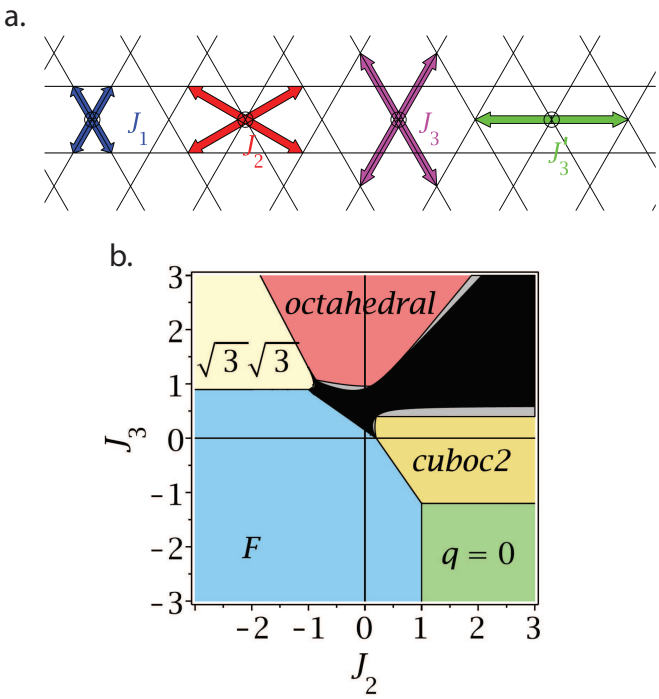

Figure 3.6: a. The magnetic superexchange paths on the kagome lattice that are used to calculate the classical magnetic ground states in the phase diagram of **b.**, where $J_1 = -0.1$ (ferromagnetic) and $J_3' = 0.2$. Evidently from the phase diagram, small changes of the various exchange terms can lead to very different magnetic structures. Both taken from [56].

Unfortunately, the role of defects and further neighbour-exchange in all these materials is difficult to quantify. Even for herbertsmithite, which shows minimal cation disorder and a geometrically perfect kagome network, recent calculations show small exchange terms between kagome layers (*without* defects) that may become important in defining the low-T magnetic ground state and perturb it from a true $S = \frac{1}{2}$ KHM model [57]. Therefore, the variety of exotic physics only further invigorates the search for better model systems.

3.3.2 Volborthite, vesignieite and similar model materials

Another group of materials that provide several excellent model $S = \frac{1}{2}$ KHMs are those based on Cu^{2+} kagome planes linked by $M^{5+}O_4$ tetrahedra (M = V or As), or related units such as M_2O_7, with various space filling ions between the planes, such as Ba^{2+}, K^+, H_2O, Pb^{2+} and Cl^-. In contrast to the paratacamite related materials, as all these ions are either aliovalent or have a large difference in ionic radius (*e.g.* $Ba^{2+} = 1.35$ Å, $Cu^{2+} = 0.73$ Å and $Pb^{2+} = 1.19$ Å [58]) there is little opportunity for cationic site disorder that perturbs the magnetism. However, as we will see, these materials often crystallise with monoclinic symmetry with a slightly distorted kagome lattice.

Volborthite, $Cu_3V_2O_7(OH)_2{\cdot}H_2O$, was the first synthetic $S = \frac{1}{2}$ KHM studied with respect to its magnetic properties [33], although had been synthesised some time before [59]. Built from Cu^{2+} kagome layers separated by V_2O_7 units and weakly bonded, space filling H_2O molecules, the structure is highly

2-dimensional with little opportunity for interlayer exchange or cationic disorder, as in herbertsmithite and the related paratacamite materials. However, two crystallographically inequivalent Cu sites form the kagome triangles and, consequently, there are two inequivalent Cu–Cu bond lengths that differ by $\sim 3\,\%$ [59], which is predicted to lift the degeneracy of the $S = \frac{1}{2}$ KAFM ground state [60].

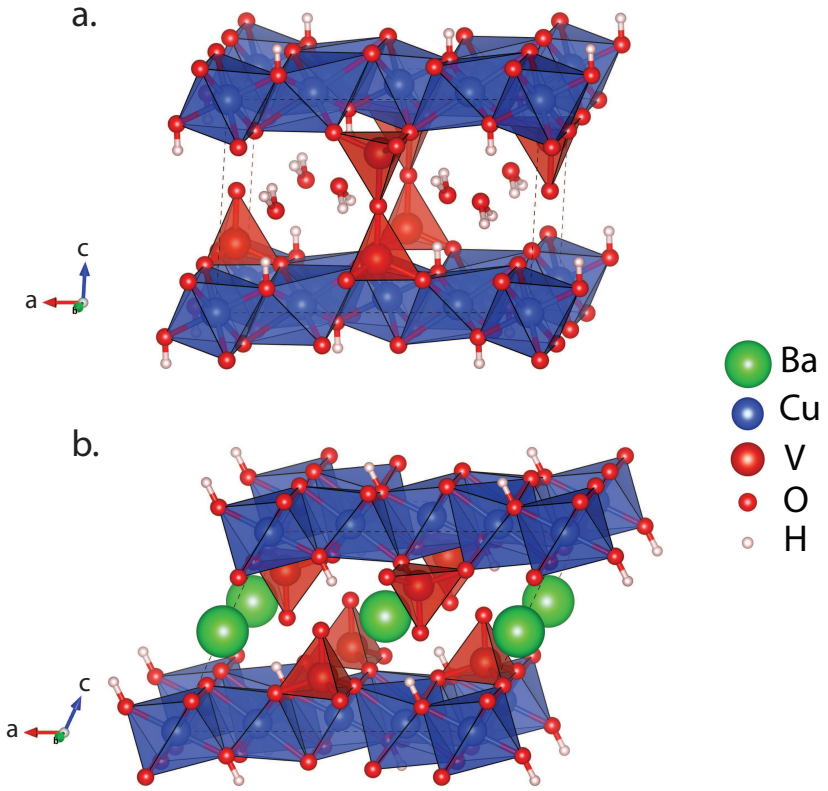

Figure 3.7: Crystal structures of **a.** volborthite, $Cu_3V_2O_7(OH)_2 \cdot 2H_2O$ [59] and **b.** vesignieite, $BaCu_3V_2O_8(OH)_2$ [61]. Both structures have monoclinic symmetry with slightly distorted kagome CuO_6 layers separated by VO_4 tetrahedra and either Ba^{2+} ions or H_2O molecules.

The magnetic properties of volborthite are defined by strong antiferromagnetic interactions, $\theta_W \sim -100\,K$, yet no magnetic transition occurs until $T < 2\,K$, the nature of which has been characterised with a variety of techniques and shown to be complex [62, 63, 64, 65]. Local probes, such as ^{51}NMR and μSR, show slowing down of spins below $T \sim 1\,K$ but remain slowly fluctuating at temperatures as low as $T = 0.02\,K$ with incommensurate or short-range order and a large density of low-energy excitations [63, 62, 65]. The short-range order below $T \sim 1\,K$ is confirmed by inelastic neutron scattering data, whilst this data also suggest strong exchange along Cu chains and weaker interchain interactions [64], previously predicted by DFT calculations [66]. Thus, the magnetic ground state appears to be a complex mix of short-range order and strong spin fluctuations.

Further intrigue to the physics of volborthite was added by the synthesis of single crystals [67]. These samples undergo a structural phase transition at $T \sim 310\,K$ that causes a significant change in the local coordination of one of the Cu^{2+} sites. CuO_6 octahedra are commonly Jahn-Teller distorted due to lone occupation of one of the d-orbitals with e_g symmetry and this transition is argued to be an ‘orbital

switching' of the lone electron between the d_{z^2} and d_{x^2-y2} orbitals. Concomitant with this structural transition is a large change in Weiss constant from $\theta_{\mathrm{W}} = -35\,\mathrm{K}$ at high-T to $\theta_{\mathrm{W}} = -140\,\mathrm{K}$ below. This highlights how the magnetic interactions are strongly defined by the orbital occupation and arrangement and, therefore, how orbital physics play an important role in $S = \frac{1}{2}$ KHMs. We will see in Chapter 5 that this transition in volborthite is better understood as a static Jahn-Teller ordering, rather than an 'orbital switching'.

Vesignieite, $BaCu_3V_2O_8(OH)_2$, has a crystal structure closely related to volborthite with Cu^{2+} kagome layers joined by VO_4 tetrahedra hydrogen bonded to hydroxide groups in the neighbouring plane, however some debate surrounds the crystal symmetry. A single crystal X-ray diffraction study of a natural sample refined the structure with monoclinic, $C12/m1$, symmetry and, therefore, slightly distorted kagome triangles [61]. Studies in the literature of powdered synthetic samples appear to agree with this conclusion, although with a Cu–Cu bond difference of only $\sim 0.07\,\%$, an order of magnitude less than volborthite [37, 68, 69]. On the other hand, recent studies on a synthetic single crystal refined the structure with rhombohedral, $R\overline{3}m$, symmetry and a geometrically perfect kagome lattice. Although they thought this was a new phase, β-vesignieite, its structure is almost identical to that found in the natural single crystal [61]. Certain sites have abnormally large displacement parameters that suggest significant disorder, casting doubt over the legitimacy of this structure [70]. This uncertainty is addressed in Chapter 6 of this thesis with an in depth crystallographic study of a number of vesignieite samples prepared using different methods.

The magnetic properties of vesignieite are quite distinct from the $S = \frac{1}{2}$ KHMs discussed thus far. The material goes through a magnetic transition at $T \approx 9\,\mathrm{K}$, although the behaviour is strongly sample dependent with ground states ranging from coexisting dynamic and frozen spins [71] to long-range order [69] depending on the synthetic method used. Considering the strong antiferromagnetic interactions and the negligible distortion of the kagome lattice, the transition at $T \sim 9\,\mathrm{K}$ is surprisingly high especially when compared to the materials previously discussed. The reason for this transition is found to be a significant *in-plane* DM interaction, determined from ESR data, that stabilises classical Néel order over any QSL ground state [72]. Chapter 7 discusses inelastic neutron scattering data collected on a high quality sample of vesignieite that evidence a unique non-coplanar magnetic structure not previously observed experimentally.

As explained in the first paragraph of this subsection, the underlying structure of volborthite and vesignieite is relatively flexible and can accommodate several different ions or molecules between the kagome planes. $KCu_3As_2O_7(OH)_3$ is one example that shares a similar structure to vesignieite yet has a ferromagnetic Weiss temperature, $\theta_{\mathrm{W}} \sim 13\,\mathrm{K}$, and undergoes an *antiferromagnetic* transition at a similar temperature, $T_{\mathrm{N}} \sim 7.2\,\mathrm{K}$ [73, 74]. This behaviour is argued to be a result of multiple nearest-neighbour and further-neighbour interactions that are allowed from occupation of the $d_{x^2-y^2}$ orbitals. Moreover, the magnetic structure below T_{N} is a complex helix and a spin-drive ferroelectricity appears at the transition. This highlights the exotic electronic transport properties that can occur in the magnetically frustrated regimes of $S = \frac{1}{2}$ KHMs, an aspect of these materials not often studied.

Other related minerals exist in nature, such as bayldonite, $PbCu_3As_2O_8(OH)_2$ [75], and engelhauptite, $KCu_3V_2O_7(OH)_2Cl$ [76], that further evidence the flexibility of these structures and open the possibility of massively expanding our database of model $S = \frac{1}{2}$ KHMs with determined synthetic efforts. As well as attempting to synthesise natural minerals, it is also useful and productive to alter know materials through substitutions at the non-magnetic sites. The success of this approach is shown in Chapter 5, which describes the synthesis of the Sr^{2+}-analogue of vesignieite, $SrCu_3V_2O_8(OH)_2$, a new $S = \frac{1}{2}$ KHM not previously found in nature.

3.3.3 Pseudo $S = \frac{1}{2}$ KHM model materials

From the previous section it is clear that the two most important structural criteria for model $S = \frac{1}{2}$ KHMs are: (i) a geometrically perfect kagome lattice and (ii) an undiluted kagome lattice that can be considered magnetically 2-dimensional. By loosening these restrictions we can discuss several additional materials that can nevertheless aid our understanding of $S = \frac{1}{2}$ KHM physics.

Perhaps the most studied of these is the vanadium oxyflouride $[NH_4]_2[C_7H_{14}N][V_7O_6F_{18}]$, which consists of a kagome lattice of $S = \frac{1}{2}$ V^{4+} separated by $S = 1$ V^{3+} ions [77]. Recent results show these magnetic sublattices are only weakly coupled making the material an excellent model $S = \frac{1}{2}$ KAFM [78]. Moreover, μSR experiments in the same study find no evidence of spin freezing down to $T = 0.04$ K and the persistent spin dynamics down to these temperatures hint at QSL behaviour. Cu(1,3-benzenedicarboxylate) is another example of an organometallic $S = \frac{1}{2}$ KHM, although in this material the large nearest-neighbour Cu–Cu distance (4.5541(2) Å) is not significantly shorter than the kagome interplanar distance (7.9716(3) Å) [79]. This leads to anisotropic ferromagnetic interactions between the planes despite a Weiss temperature, $\theta_W \sim -33$ K, suggestive of antiferromagnetism [79, 80]. μSR experiments are consistent with persistent spin dynamics well below the values of the exchange constants and a spin liquid ground state, however this cannot be reconciled with the ferromagnetic interactions and it is argued that this result is a false positive [80].

Another promising group of materials is the $A_2BCu_3F_{12}$ family. These offer a range of experimental models, however all current examples undergo structural transitions that significantly deform the kagome lattice [81]. Despite this, exotic magnetically frustrated behaviour is observed in some of these materials, such as the unique 'pinwheel' valence bond solid observed in $Rb_2Cu_3SnF_{12}$ [82]. The flexibility at the A- and B-sites in this family offer plenty of opportunities to chemically tailor a composition that retains 'perfect' kagome symmetry.

The experimental work detailed in this thesis deals with three different model $S = \frac{1}{2}$ KHMs. Chapter 5 introduces a new system, the Sr-analogue of the well studied mineral vesignieite, not previously reported in the literature. This chapter is placed first because the synthetic route used for this material was adapted for regular vesignieite and found to produce better quality powder samples than had previously been achieved. Therefore, Chapter 6 deals with these improved quality vesignieite samples and characterises their structure and Chapter 7 discusses experiments that determine their magnetic properties. The final chapter describes elastic and inelastic neutron scattering experiments on the mineral haydeeite, the Mg^{2+} analogue of kapellasite and a close relative of herbertsmithite.

Bibliography

[1] C. Lacroix, P. Mendels and F. Mila, *Introduction to Frustrated Magnetism: Materials, Experiment, Theory*, Springer, New York, 2011.

[2] P. W. Anderson, *Mater. Res. Bull.*, 1973, **8**, 153–160.

[3] M. Hemmida, H.-A. Krug von Nidda, N. Büttgen, A. Loidl, L. Alexander, R. Nath, A. Mahajan, R. Berger, R. Cava, Y. Singh and D. Johnston, *Phys. Rev. B*, 2009, **80**, 054406.

[4] P. Mendels, A. Olariu, F. Bert, D. Bono, L. Limot, G. Collin, B. Ueland, P. Schiffer, R. J. Cava, N. Blanchard, F. Duc and J. C. Trombe, *J. Phys. Condens. Matter*, 2007, **19**, 145224.

[5] F. Reynaud, D. Mertz, F. Celestini, J.-M. Debierre, A. Ghorayeb, P. Simon, A. Stepanov, J. Voiron and C. Delmas, *Phys. Rev. Lett.*, 2001, **86**, 3638–3641.

[6] S. Nakatsuji, Y. Nambu, H. Tonomura, O. Sakai, S. Jonas, C. Broholm, H. Tsunetsugu, Y. Qiu and Y. Maeno, *Science*, 2005, **309**, 1697–700.

[7] M. J. Harris, S. T. Bramwell, D. F. Mcmorrow, T. Zeiske and K. W. Godfrey, *Phys. Rev. Lett.*, 1997, **79**, 2554–2557.

[8] S. T. Bramwell and M. J. Gingras, *Science*, 2001, **294**, 1495–501.

[9] J. S. Gardner, S. R. Dunsiger, B. D. Gaulin, M. J. P. Gingras, J. E. Greedan, R. F. Kiefl, M. D. Lumsden, W. A. MacFarlane, N. P. Raju, J. E. Sonier, I. Swainson and Z. Tun, *Phys. Rev. Lett.*, 1999, **82**, 1012–1015.

[10] J. Ruff, B. Gaulin, J. Castellan, K. Rule, J. Clancy, J. Rodriguez and H. Dabkowska, *Phys. Rev. Lett.*, 2007, **99**, 237202.

[11] I. Mirebeau, P. Bonville and M. Hennion, *Phys. Rev. B*, 2007, **76**, 184436.

[12] B. Bernu, P. Lecheminant, C. Lhuillier and L. Pierre, *Phys. Rev. B*, 1994, **50**, 10048–10062.

[13] P. Lecheminant, B. Bernu, C. Lhuillier, L. Pierre and P. Sindzingre, *Phys. Rev. B*, 1997, **56**, 2521–2529.

[14] R. E. Stoffregen, C. N. Alpers and J. L. Jambor, *Rev. Mineral. Geochemistry*, 2000, **40**, 453–479.

[15] U. G. Nielsen, J. Majzlan and C. P. Grey, *Chem. Mater.*, 2008, **20**, 2234–2241.

[16] A. S. Wills, *Phys. Rev. B*, 2001, **63**, 064430.

[17] T. Yildirim and A. B. Harris, *Phys. Rev. B*, 2006, **73**, 214446.

[18] S.-H. Lee, C. Broholm, M. F. Collins, L. Heller, A. P. Ramirez, C. Kloc, E. Bucher, R. W. Erwin and N. Lacevic, *Phys. Rev. B*, 1997, **56**, 8091–8097.

[19] D. Grohol, Q. Huang, B. Toby, J. Lynn, Y. Lee and D. Nocera, *Phys. Rev. B*, 2003, **68**, 094404.

[20] W. G. Bisson and A. S. Wills, *J. Phys. Condens. Matter*, 2008, **20**, 452204.

[21] A. S. Wills, V. Dupuis, E. Vincent, J. Hammann and R. Calemczuk, *Phys. Rev. B*, 2000, **62**, R9264–R9267.

[22] Y. J. Uemura, A. Keren, K. Kojima, L. P. Le, G. M. Luke, W. D. Wu, Y. Ajiro, T. Asano, Y. Kuriyama, M. Mekata, H. Kikuchi and K. Kakurai, *Phys. Rev. Lett.*, 1994, **73**, 3306–3309.

[23] L. Limot, P. Mendels, G. Collin, C. Mondelli, B. Ouladdiaf, H. Mutka, N. Blanchard and M. Mekata, *Phys. Rev. B*, 2002, **65**, 144447.

[24] L. Balents, *Nature*, 2010, **464**, 199–208.

[25] X.-G. Wen, *Phys. Lett. A*, 2002, **300**, 175–181.

[26] P. W. Anderson, *Science*, 1987, **235**, 1196–1198.

[27] S.-S. Gong, W. Zhu and D. N. Sheng, *Sci. Rep.*, 2014, **4**, 6317.

[28] L. Balents, M. P. A. Fisher and S. M. Girvin, *Phys. Rev. B*, 2002, **65**, 224412.

[29] S. Ryu, O. Motrunich, J. Alicea and M. Fisher, *Phys. Rev. B*, 2007, **75**, 184406.

[30] S. Yan, D. A. Huse and S. R. White, *Science*, 2011, **332**, 1173–6.

[31] R. R. P. Singh, *Phys. Rev. B*, 2007, **76**, 180407.

[32] Y. Ran, M. Hermele, P. A. Lee and X.-G. Wen, *Phys. Rev. Lett.*, 2007, **98**, 117205.

[33] Z. Hiroi, M. Hanawa, N. Kobayashi, M. Nohara, H. Takagi, Y. Kato and M. Takigawa, *J. Phys. Soc. Japan*, 2001, **70**, 3377–3384.

[34] Z. Hiroi, H. Yoshida, Y. Okamoto and M. Takigawa, *J. Phys. Conf. Ser.*, 2009, **145**, 012002.

[35] M. P. Shores, E. A. Nytko, B. M. Bartlett and D. G. Nocera, *J. Am. Chem. Soc.*, 2005, **127**, 13462–3.

[36] A. Olariu, P. Mendels, F. Bert, F. Duc, J. Trombe, M. de Vries and A. Harrison, *Phys. Rev. Lett.*, 2008, **100**, 087202.

[37] Y. Okamoto, H. Yoshida and Z. Hiroi, *J. Phys. Soc. Japan*, 2009, **78**, 033701.

[38] M. E. Fleet, *Acta Crystallogr.*, 1975, **31**, 183–187.

[39] R. H. Colman, C. Ritter and A. S. Wills, *Chem. Mater.*, 2008, **20**, 6897–6899.

[40] R. H. Colman, A. Sinclair and A. S. Wills, *Chem. Mater.*, 2011, **23**, 1811–1817.

[41] R. H. Colman, A. Sinclair and A. S. Wills, *Chem. Mater.*, 2010, **22**, 5774–5779.

[42] Y. Li, B. Pan, S. Li, W. Tong, L. Ling, Z. Yang, J. Wang, Z. Chen, Z. Wu and Q. Zhang, *New J. Phys.*, 2014, **16**, 093011.

[43] T. McQueen, T. Han, D. Freedman, P. Stephens, Y. Lee and D. Nocera, *J. Solid State Chem.*, 2011, **184**, 3319–3323.

[44] H. Ishikawa, Y. Okamoto and Z. Hiroi, *J. Phys. Soc. Japan*, 2013, **82**, 063710.

[45] M. Fujihala, X.-G. Zheng, H. Morodomi, T. Kawae, A. Matsuo, K. Kindo and I. Watanabe, *Phys. Rev. B*, 2014, **89**, 100401.

[46] M. de Vries, J. Stewart, P. Deen, J. Piatek, G. Nilsen, H. Rönnow and A. Harrison, *Phys. Rev. Lett.*, 2009, **103**, 237201.

[47] D. E. Freedman, T. H. Han, A. Prodi, P. Müller, Q.-Z. Huang, Y.-S. Chen, S. M. Webb, Y. S. Lee, T. M. McQueen and D. G. Nocera, *J. Am. Chem. Soc.*, 2010, **132**, 16185–90.

[48] T. Han, S. Chu and Y. Lee, *Phys. Rev. Lett.*, 2012, **108**, 157202.

[49] O. Ofer, A. Keren, J. H. Brewer, T. H. Han and Y. S. Lee, *J. Phys. Condens. Matter*, 2011, **23**, 164207.

[50] T. Imai, M. Fu, T. H. Han and Y. S. Lee, *Phys. Rev. B*, 2011, **84**, 020411.

[51] D. Wulferding, P. Lemmens, P. Scheib, J. Röder, P. Mendels, S. Chu, T. Han and Y. Lee, *Phys. Rev. B*, 2010, **82**, 144412.

[52] T.-H. Han, J. S. Helton, S. Chu, D. G. Nocera, J. A. Rodriguez-Rivera, C. Broholm and Y. S. Lee, *Nature*, 2012, **492**, 406–410.

[53] E. Kermarrec, P. Mendels, F. Bert, R. H. Colman, A. S. Wills, P. Strobel, P. Bonville, A. Hillier and A. Amato, *Phys. Rev. B*, 2011, **84**, 100401.

[54] O. Janson, J. Richter and H. Rosner, *Phys. Rev. Lett.*, 2008, **101**, 106403.

[55] B. Fåk, E. Kermarrec, L. Messio, B. Bernu, C. Lhuillier, F. Bert, P. Mendels, B. Koteswararao, F. Bouquet, J. Ollivier, A. D. Hillier, A. Amato, R. H. Colman and A. S. Wills, *Phys. Rev. Lett.*, 2012, **109**, 037208.

[56] L. Messio, C. Lhuillier and G. Misguich, *Phys. Rev. B*, 2011, **83**, 184401.

[57] H. O. Jeschke, F. Salvat-Pujol and R. Valentí, *Phys. Rev. B*, 2013, **88**, 075106.

[58] R. D. Shannon, *Acta Crystallogr.*, 1976, **A32**, 751–767.

[59] M. A. Lafontaine, A. Le Bail and G. Férey, *J. Solid State Chem.*, 1990, **85**, 220–227.

[60] A. Schnyder, O. Starykh and L. Balents, *Phys. Rev. B*, 2008, **78**, 174420.

[61] M. Zhesheng, H. Ruilin and Z. Xiaoling, *Acta Geol. Sin.*, 1991, **4**, 145–151.

[62] A. Fukaya, Y. Fudamoto, I. Gat, T. Ito, M. Larkin, A. Savici, Y. Uemura, P. Kyriakou, G. Luke, M. Rovers, K. Kojima, A. Keren, M. Hanawa and Z. Hiroi, *Phys. Rev. Lett.*, 2003, **91**, 207603.

[63] F. Bert, D. Bono, P. Mendels, F. Ladieu, F. Duc, J.-C. Trombe and P. Millet, *Phys. Rev. Lett.*, 2005, **95**, 087203.

[64] G. J. Nilsen, F. C. Coomer, M. A. de Vries, J. R. Stewart, P. P. Deen, A. Harrison and H. M. Rø nnow, *Phys. Rev. B*, 2011, **84**, 172401.

[65] M. Yoshida, M. Takigawa, H. Yoshida, Y. Okamoto and Z. Hiroi, *Phys. Rev. Lett.*, 2009, **103**, 077207.

[66] O. Janson, J. Richter, P. Sindzingre and H. Rosner, *Phys. Rev. B*, 2010, **82**, 104434.

[67] H. Yoshida, J.-I. Yamaura, M. Isobe, Y. Okamoto, G. J. Nilsen and Z. Hiroi, *Nat. Commun.*, 2012, **3**, 860.

[68] R. H. Colman, F. Bert, D. Boldrin, A. Hillier, P. Manuel, P. Mendels and A. S. Wills, *Phys. Rev. B*, 2011, **83**, 180416.

[69] M. Yoshida, Y. Okamoto and H. Yoshida, *J. Phys. Soc. Japan*, 2013, **82**, 013702.

[70] H. Yoshida, Y. Michiue, E. Takayama-Muromachi and M. Isobe, *J. Mater. Chem.*, 2012, **22**, 18793.

[71] J. Quilliam, F. Bert, R. H. Colman, D. Boldrin, A. S. Wills and P. Mendels, *Phys. Rev. B*, 2011, **84**, 180401.

[72] A. Zorko, F. Bert, A. Ozarowski, J. van Tol, D. Boldrin, A. S. Wills and P. Mendels, *Phys. Rev. B*, 2013, **88**, 144419.

[73] Y. Okamoto, H. Ishikawa, G. J. Nilsen and Z. Hiroi, *J. Phys. Soc. Japan*, 2012, **81**, 033707.

[74] G. J. Nilsen, Y. Okamoto, H. Ishikawa, V. Simonet, C. V. Colin, A. Cano, L. C. Chapon, T. Hansen, H. Mutka and Z. Hiroi, *Phys. Rev. B*, 2014, **89**, 140412.

[75] V. Sumin de Portilla, M. P. Quevedo and V. I. Stepanov, *Am. Mineral.*, 1981, **66**, 148–153.

[76] I. V. Perkov, O. I. Sildra, N. V. Chukanov, V. O. Yapaskurt, S. N. Britvin, S. V. Krivovichev, W. Schuller and B. Ternes, *Mineral. Mag.*, 2013, **77**, 2695–2709.

[77] F. H. Aidoudi, D. W. Aldous, R. J. Goff, A. M. Z. Slawin, J. P. Attfield, R. E. Morris and P. Lightfoot, *Nat. Chem.*, 2011, **3**, 801–6.

[78] L. Clark, J. C. Orain, F. Bert, M. A. De Vries, F. H. Aidoudi, R. E. Morris, P. Lightfoot, J. S. Lord, M. T. F. Telling, P. Bonville, J. P. Attfield, P. Mendels and A. Harrison, *Phys. Rev. Lett.*, 2013, **110**, 207208.

[79] E. A. Nytko, J. S. Helton, P. Müller and D. G. Nocera, *J. Am. Chem. Soc.*, 2008, **130**, 2922–2923.

[80] O. Ofer, L. Marcipar, V. Ravi Chandra, S. Gazit, D. Podolsky, D. P. Arovas and A. Keren, *Phys. Rev. B*, 2014, **89**, 205116.

[81] S. A. Reisinger, C. C. Tang, S. P. Thompson, F. D. Morrison and P. Lightfoot, *Chem. Mater.*, 2011, **23**, 4234–4240.

[82] K. Matan, T. Ono, Y. Fukumoto, T. J. Sato, J. Yamaura, M. Yano, K. Morita and H. Tanaka, *Nat. Phys.*, 2010, **6**, 865–869.

Chapter 4

Experimental Techniques

This chapter describes the techniques used during the experimental work in this thesis. Initially it covers hydrothermal synthesis methods before moving onto analytical techniques, discussing both the theoretical and practical elements of them.

4.1 Synthetic techniques

Synthesis of new materials, or improving qualities of known samples, is one of the important aims of this thesis. The majority of samples discussed were prepared *via.* hydrothermal synthesis, aside from Section 6.3 of Chapter 6 and Chapter 8 where wet chemistry techniques were used and will not be discussed here. The autoclave bombs used for hydrothermal synthesis were teflon-lined acid digestion vessels from Parr Instruments, which consist of a 15 ml teflon vessel and lid placed inside a steel protective autoclave with a spring-loaded screw closure that maintains constant pressure in the reaction vessel. Reactions were performed at a maximum temperature of 220 °C, above which the teflon can deform, in both neutral or acidic conditions. After reactions are complete, the bombs are taken out of the oven and left to cool naturally to room temperature before opening. Specifics of individual reactions are detailed in the relevant chapters where necessary.

4.2 Diffraction

Powder diffraction is an indispensable technique for many scientists and has been the staple analytical tool for materials chemists for decades. It is based on the premise that crystalline materials may act as a diffraction grating for radiation with a wavelength comparable to the samples lattice spacing. The condition for diffraction is given by the now famous Braggs's law:

$$n\lambda = 2d\sin\theta \tag{4.1}$$

where n indicates which layers are diffracting, d is the lattice spacing, θ is the angle of incidence and λ is the radiation wavelength, where the latter is commonly X-rays, neutrons or electrons (Figure 4.1a). A more generalised version of this is reached by considering the change in momentum transfer, $\mathbf{Q}$, of a scattered particle with initial and final wavevectors, $\mathbf{k}_i$ and $\mathbf{k}_f$, respectively. The vector diagram of this scattering process through an incident angle θ is shown in Figure 4.1b and leads to the equation:

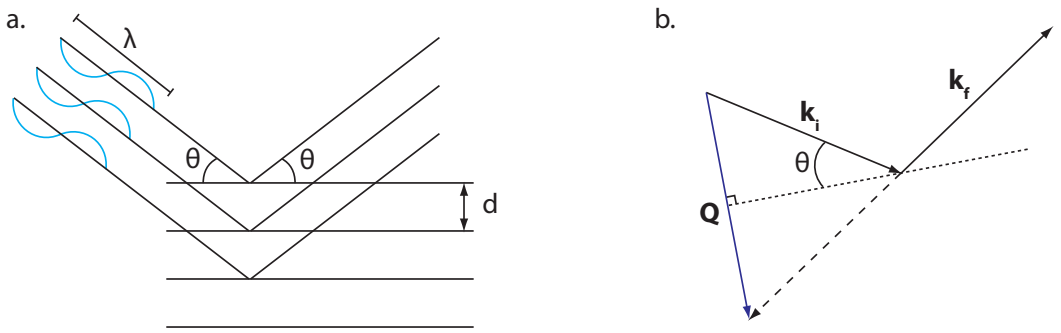

Figure 4.1: a. A schematic of Braggs's law for radiation with wavelength λ diffracting from lattice spacing d at incident angle θ. **b.** Vector diagram for a scattering event in terms of momentum transfer, $\mathbf{Q}$, of a particle with incident and final wavevectors $\mathbf{k}_\mathrm{i}$ and $\mathbf{k}_\mathrm{f}$.

$$\mathbf{Q} = \frac{4\pi \sin\theta}{\lambda} \tag{4.2}$$

In addition to being able to determine d from Braggs's law, the fact that the incident radiation is scattered by atoms in the crystal allows us to also measure the positions of those atoms within the unit cell. This is done using the structure factor which sums up the amplitude of all the scattered waves from each atom, j, in the unit cell:

$$F_{hkl} = \sum_{j=1}^{N} f_j \, \mathrm{e}^{\mathrm{i}2\pi(hx+ky+lz)} \tag{4.3}$$

where f_j is the scattering form factor of atom j, N is the number of atoms in the unit cell, h, k and l are the miller indices of the plane and x, y and z are the coordinates of the atom j within the plane. Equation 4.3 assumes stationary atoms, however thermal energy oscillates atoms around their equilibrium position and weakens F_{hkl}. To account for atomic displacements one must add a multiplicative term known as the Debye-Waller factor, so that:

$$F_{hkl} = \sum_{j=1}^{N} f_j \exp[\mathrm{i}2\pi(hx+ky+lz)] \exp\left(-\frac{\beta_j Q^2}{4\pi}\right) \tag{4.4}$$

where β_j determines the spherical displacement of atom j, commonly in units of Å^2. This can be further expanded to model anisotropic displacements in the form of an ellipsoid defined by six terms: β_{11}, β_{22}, β_{33}, β_{12}, β_{13} and β_{23}. Once the structure factor is determined, one can calculate the intensity, I_{hkl}, of diffracted X-rays that satisfies Braggs's law as $I_{hkl} \propto |F_{hkl}|^2$, or more precisely the complex conjugate of the structure factor.

The nature of the scattering from different radiations allows access to different atomic information. X-rays are scattered from the electron cloud and thus the form factor increases smoothly with the square of the number of electrons. Moreover, the diffuse nature of the electron cloud means the scattering cross-section has an inversely proportional dependence on Q. Contrastingly, neutrons scatter from the nucleus and the form factor varies drastically between elements and even isotopes within elements. Also, as the

nucleus is several orders of magnitude smaller than the electron cloud, neutron scattering is effectively a point scattering process and there is no Q dependence of the scattering cross-section.

From what has been discussed so far, neutrons appear superior to X-rays as a radiation source for structural information. However, X-rays have two major advantages. Firstly, X-ray production is far easier than neutrons, allowing the former to be produced in a lab environment or even in portable devices. Neutron production is limited to reactor or spallation sources requiring large facilities and expensive, highly specialised equipment. Secondly, mastery of X-ray instrumentation exceeds that of neutrons such that flux and resolution of the former are often several orders of magnitude greater. In ideal scenarios, the two techniques are used in parallel to provide complimentary structural information.

In addition to scattering of incoming neutrons from the nucleus, as the neutron is spin-$\frac{1}{2}$ it also interacts with the electronic moment. This characteristic revolutionised the study of magnetic materials as it allows the determination of magnetic structures from neutron diffraction, in addition to nuclear structures. The neutron-electron interaction shares similarities with those discussed for X-rays: the form factor is Q dependent, even more so than X-rays as only unpaired electrons contribute to the scattering. Therefore, data collected at low Q is often required to observe magnetic Bragg peaks.

4.2.1 Lab-based X-ray powder diffraction

Small scale production of X-rays in a laboratory is achieved using hot cathode ray tubes. The majority of these devices consist of a tungsten wire cathode that releases electrons upon application of an electrical current towards a metallic target anode. The interaction of the electrons with the metallic target produces X-rays *via.* two main processes: (i) Brehmstrahlung radiation is released due to deceleration of the electrons and produces a large range of X-ray energies (ii) characteristic X-rays are produced due to electronic excitations in the target metal and upon relaxing release X-rays with specific energies that depend on the metallic element. This second process delivers the most useful X-ray source for diffraction experiments and the two most common metal targets and their characteristic X-ray wavelengths are copper ($\lambda_{k_\alpha} = 1.54184\,\text{Å}$) and molybdenum ($\lambda_{k_\alpha} = 0.71073\,\text{Å}$).

Typical modern laboratory powder diffractometer setups involve an X-ray source, an electronic X-ray detector and a goniometer which allows movement of at least one out of the sample, the source and the detector. Two common diffraction geometries are termed Bragg-Brentano and Debye-Scherrer. The former consists of a planar sample with two goniometer combinations: (i) θ-θ where the detector and source are rotated and (ii) θ-2θ where the sample and detector are rotated. This method is well suited for highly absorbing samples and can result in fast data acquisition times, although the latter is often outweighed by only allowing the installation of a small detector. Debye-Scherrer geometry employs a parallel beam by using a collimator on the incoming radiation and therefore only the detector is rotated. Commonly a capillary is used to hold the sample and this is advantageous for samples where crystallites preferentially pack along certain crystallographic directions. However, for heavier atoms the transmission geometry used for capillary samples can cause absorption problems, whereby the reduction in the X-ray intensity is given by:

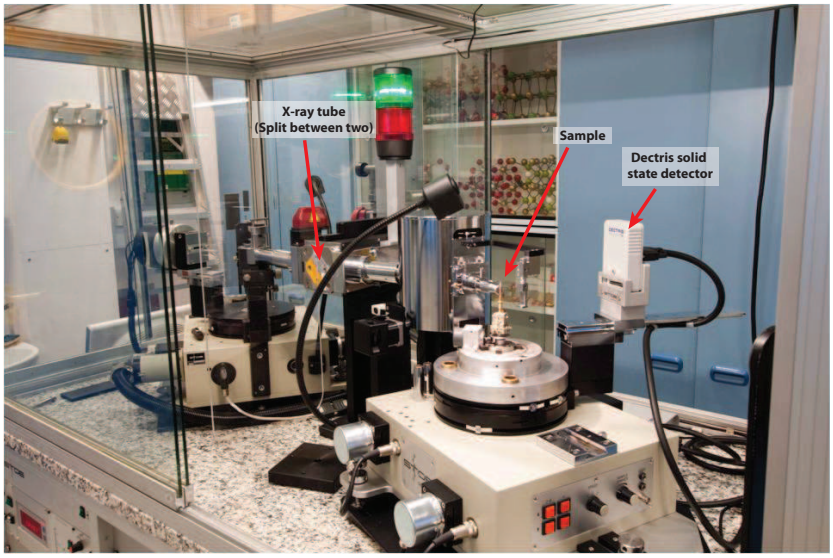

Figure 4.2: The STOE STADI-P powder diffractometer in transmission geometry used throughout this thesis. The instrument is equipped with a Cu X-ray tube split between two diffractometers and a primary Ge (111) monochromator that selects $k_{\alpha 1}$ radiation. The Dectris MYTHEN 1k solid state detector is commonly used at synchrotron sources and allows exceptionally short collection times without compromising on resolution. Picture courtesy of Martin Vickers, UCL.

$$I = I_0 \, \mathrm{e}^{-\mu l} \tag{4.5}$$

where μ is the total linear absorption coefficient and l is the distance travelled through the sample.

Throughout this thesis, data from only one laboratory powder diffractometer is presented. The diffractometer is a modern STOE STADI-P in Debye-Scherrer geometry utilising Cu K_α X-rays. An incoming beam Ge monochromator is equipped to remove Cu $K_{\alpha 2}$ radiation, followed by a single slit collimator designed for capillary samples of < 0.5 mm diameter and a micro strip solid state Dectris MYTHEN 1k detector, commonly used at synchrotron sources. For temperature dependent studies, the diffractometer is equipped with an Oxford Instruments CryoJet which allows measurements at temperatures between 100 and 500 K. A picture of the instrument is shown in Figure 4.2.

4.2.2 Synchrotron powder diffraction

Synchrotron radiation is emitted when a charged particle, such as an electron, follows a curved path at relativistic speeds. The typical setup to produce synchrotron radiation begins with the production of electrons from a cathode, similarly to the cathode ray tube. The electrons are accelerated to close to the speed of light in what is known as a linac, before being inserted into a booster ring and further accelerated to energies > 1 GeV. At this point the electrons are inserted into a larger diameter storage ring where they constantly emit electromagnetic radiation tangential to their direction of travel. This radiation is controlled by maneuvering the electrons through magnetic devices, known as bending magnets, wigglers and undulators, and directed down beamlines. The beamlines contain all the optics and experimental equipment that deliver the X-rays as required to the sample. The X-ray brilliance at the sample is several

orders of magnitude larger than can possibly be achieved in a laboratory based X-ray diffractometer.

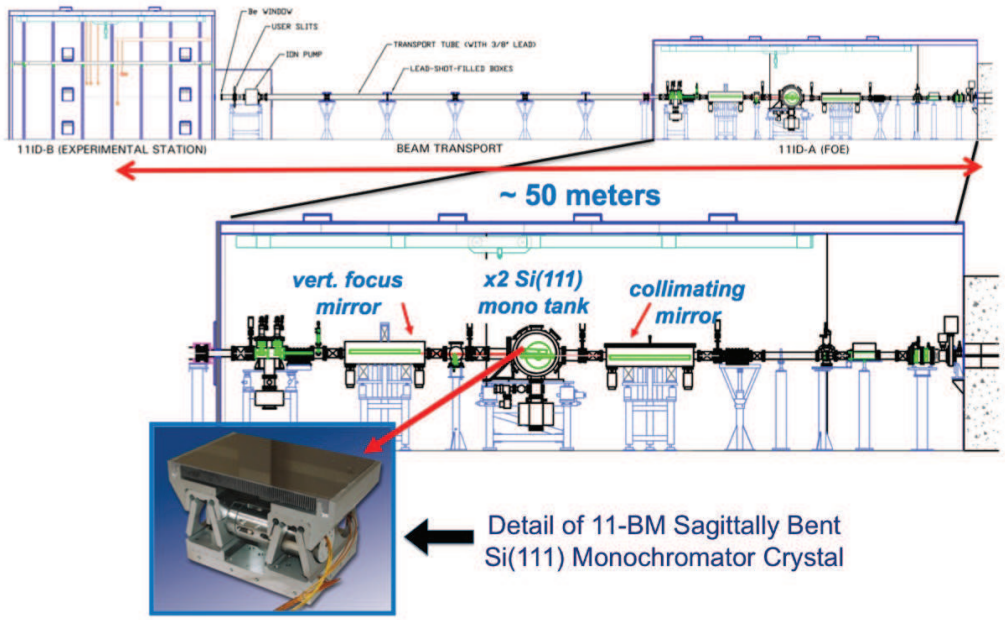

Figure 4.3: Layout of the high-resolution powder synchrotron diffraction beamline 11-BM at the Advanced Photon Source, Argonne National Laboratory, USA. Experiments in this thesis were performed at this beamline using a mail-in service. The beamline commonly uses ~ 30 keV X-rays ($\lambda \sim 0.41$ Å) and samples are loaded in 0.8 mm Kapton capillaries which have a negligible contribution to the diffraction pattern. Taken from [1]

X-rays with a vast range of energies can be utilised at synchrotrons and individual beamlines can even tune their energies to the experimental requirements. In this thesis, experiments were performed at the high-resolution 11-BM beamline at the Advanced Photon Source, Argonne National Laboratory, USA. A schematic of the instrument is shown in Figure 4.3. 11-BM is located on a bending magnet source and operates over an energy range $15 - 35$ keV. The initial hutch houses the beamline optics, including a collimating mirror, a 20 mm offset fixed-exit double-crystal Si (111) monochromator (27.6 m from the source), and a 1 m vertical focusing mirror. The second monochromator crystal is sagittally bent for horizontal focusing. The main experimental hutch is located $\sim$50 m from the source, at the center of which is a Huber two-circle diffractometer mounted on a large optical table. The diffractometer has a unique multi-analyzer detection assembly, consisting of 12 independent Si (111) crystal analyzers and $LaCl_3$ scintillation detectors. This enables simultaneous high-speed ($\sim$ 1 hour) and high-resolution ($\Delta Q/Q \approx 2 \times 10^{-4}$) data collection.

4.2.3 Neutron powder diffraction

Diffraction experiments where neutrons are used as a probe must be performed at large scale facilities due to the difficulties in producing them. The majority of neutron sources used for such experiments fall under two categories: reactor and spallation sources. Reactor sources are based around a fission reaction which delivers a constant source of neutrons, whereas spallation sources involve bombardment

of a target with a proton beam which can be used to produce them constantly or in short pulses (ms). For both sources, the neutrons produced must be thermalised in a moderator to the required energy before being delivered to the beamlines. Within each facility several moderators exist providing cold ($\sim 20\,\mathrm{K}$, $3 \rightarrow 20\,\mathrm{\AA}$), thermal ($\sim 300\,\mathrm{K}$, $1 \rightarrow 3\,\mathrm{\AA}$) and hot ($\sim 2000\,\mathrm{K}$, $0.3 \rightarrow 1\,\mathrm{\AA}$) neutrons.

With regards to diffraction experiments, pulsed and reactor sources provide different advantages and disadvantages. Reactor sources generally use a constant wavelength (CW) neutron source, analogous to X-ray diffraction experiments previously discussed. With the aid of single crystal mosaics, such as single crystal of Ge or Si, high flux monochromatic neutron beams can be delivered to the sample and diffracted neutrons are measured as a function of scattering angle. Pulsed sources use time-of-flight (TOF) methods, where the structure of the polychromatic pulsed neutron beam and the time it takes for each neutron to reach the detector is used to calculate the neutron energy/wavelength using:

$$\lambda = \frac{ht}{m_{\mathrm{n}} L} \tag{4.6}$$

where t is the flight time, L is the flight distance and m_{n} is the neutron mass. Combined with Braggs's law (Equation 4.2) gives us a direct conversion between time-of-flight and Q:

$$t = \frac{4\pi m_{\mathrm{n}} L \sin\theta}{hQ} \tag{4.7}$$

Consequently, each detector measures a full diffraction pattern and large numbers of detectors are arranged in banks at various scattering angles. Low-angle banks have a high flux and measure to high-Q values, whilst high-angle banks measure with higher resolution to lower Q but have limited flux.

This thesis presents experiments performed at the medium-resolution, high-flux powder diffraction WISH beamline at the pulsed neutron source at ISIS, Harwell, UK [2]. WISH receives neutrons from a solid methane moderator at incident wavelengths between $1.5 \rightarrow 15\,\mathrm{\AA}$ ($Q \sim 0.06 \rightarrow 4.5\,\mathrm{\AA}^{-1}$). This neutron energy range combined with the large Q-range covered by each detector bank gives WISH a high flux of detected neutrons whilst maintaining the intrinsically low background of a pulsed neutron source, making it ideal for observing magnetic Bragg peaks for simultaneous magnetic and nuclear structural refinement.

4.2.4 Diffraction data analysis

Powder diffraction data holds a vast amount of information on a sample, from relatively basic phase identification to complex atomic disorder or structural strain. As we have seen, all this information is held in the structure factor, F_{hkl}, and this is determined from the integrated intensities of the Bragg peaks. However, a large number of parameters contribute to the peak position, intensity and shape and a comprehensive model that takes account of all of it is extremely difficult to create. In the vast majority of cases several approximations or constraints must be enforced in order to successfully extract the required information, however this must always be done whilst taking into account physical relevance. All-in-all analysis of powder diffraction data is a double edged sword: the reasons that make it such a powerful tool also allow it to produce meaningless results.

The initial problem is to index the diffraction pattern, that is to assign each of the Bragg peaks to a hkl index, and in crystals with low symmetry this can be one of the most challenging analytical tasks in powder diffraction. Several different mathematical approaches exist but all are likely to fail when poor quality data is used, for instance with several overlapping or unknown impurity peaks. If successful, the indexing stage gives the correct Bravais lattice, but it cannot distinguish between space groups within this class that give the same 2θ positions due to geometrical ambiguities. In order to distinguish between these it is necessary to either: (i) use prior knowledge of the crystal structure obtained from previous experiments or (ii) perform a full structural refinement for each probable space group and determine the most reliable.

Once the Bravais lattice and rough lattice constants are known, the latter can be further refined using a whole powder fitting procedure. Ignoring the atomic content of the unit cell, this can be performed by treating each peak intensity as an individual refinement parameter, methods known as Le Bail or Pawley extraction depending on the specifics. If no knowledge of the atomic positions are known, the extracted intensities from these fits can be used for a full structure solution, however these refinement methods are often purely used for accurate lattice constant and peak profile parameters if a good atomic model exists. The rest of this section focusses on the latter case, as the former is not used in this thesis.

With knowledge of the unit cell dimensions, space group (or several indistinguishable suggestions), peak profile parameters and a good atomic model from prior knowledge of the material, a full crystal structure refinement can be performed. In single crystal structure refinement, this is a relatively simple problem as $|F_{hkl}|$ can be determined from the sheer number of integrated peak intensities. However, in powder diffraction this proves impossible due to the condensation of structural information into a 1-dimensional diffraction spectrum. The most common structural refinement routine is called the Rietveld method, which treats each data point as a least-squares quantity and minimises the difference between the observed and calculated values for each, using the equation:

$$\sum_i w_i (y_{o,i} - y_{c,i})^2 \tag{4.8}$$

where $y_{o,i}$ and $y_{c,i}$ and the observed and calculated intensities, respectively, at the i^{th} data point and w_i is a weighting factor [3]. Calculating $y_{c,i}$ involves convolution of many effects from structural parameters, such as lattice parameters, symmetry, atomic fractional coordinates, site occupations and magnetic moments, and global parameters, *i.e.* background, radiation intensity, Lorentz-Polarisation factor, profile shape, sample roughness, absorption and many more. Many of these are highly correlated and so we come back to the point that without an accurate model for each of these, built from a good knowledge of the structure and diffraction physics, the results obtained can be completely meaningless.

Several software packages exist for performing the data analysis procedures discussed so far and each has advantages and disadvantages. The majority of structural analysis in this thesis uses TOPAS [4], whose particular advantage lies in the ability to manually define functions, for instance to model abnormal peak shapes or refine structures using symmetry adapted distortion modes. Fullprof is another software package particularly powerful in magnetic crystallography and modelling time-of-flight neu-

tron diffraction data [5]. Other specific crystallographic analysis software are used in combination with these packages. SARAh uses representational analysis (Chapter 2.4.3, Page 27) to build magnetic structures that can then be refined in Fullprof [6]. The Bilbao crystallographic server contains many useful programs, with PSEUDO and TRANSTRU often used during this research [7, 8].

4.3 Inelastic neutron scattering

Inelastic neutron scattering is an extremely powerful tool well known to physicists but also becoming an indispensable technique for biologists and chemists. The technique distinguishes between elastic and inelastic neutron scattering processes, in contrast to neutron diffraction where no discrimination is made, allowing any mechanism where a change in energy occurs to be directly probed. Examples include phonons, magnons and crystal-field excitations as well as time-dependent processes such as diffusion within samples.

In elastic collisions, the wavevectors $|\mathbf{k}_i|$ and $|\mathbf{k}_f|$ are equal and our definition of Q in that scenario is given by equation 4.2. When $|\mathbf{k}_i| \neq |\mathbf{k}_f|$, *i.e.* an inelastic process, the general relationship between Q and the scattering angle, θ, is given by:

$$Q^2 = k_i^2 + k_f^2 - 2k_i k_f \, cos\, 2\theta \tag{4.9}$$

The associated change in energy of a neutron in a scattering process is commonly quoted in frequency, ω ($E = \hbar\omega$), given by:

$$\omega = \frac{\pi h}{m_{\mathrm{n}}} \left(\frac{1}{\lambda_i^2} - \frac{1}{\lambda_f^2} \right) \tag{4.10}$$

In an experiment, the actual quantity measured is the total scattering cross section:

$$\frac{d^2\sigma}{d\Omega dE_f} = \frac{\sigma_{\mathrm{scat}} k_f}{4\pi k_i} N S(\mathbf{Q}, \omega) \tag{4.11}$$

with σ_{scat} the scattering cross-section and $S(\mathbf{Q}, \omega)$ is the scattering function. The latter is the quantity plotted in inelastic neutron scattering experiments and is given by:

$$S(\mathbf{Q}, \omega) = \frac{1}{2\pi h} \int I(\mathbf{Q}, t) e^{-i\omega t} dt \tag{4.12}$$

From this equation, the time dependence of the scattering function is evident as $I(\mathbf{Q}, t)$ is a function of time, t, although in a solid the approximation $I(\mathbf{Q}, t) = I(\mathbf{Q})$ can be made. A common manipulation of $S(\mathbf{Q}, \omega)$ is to extract the dynamic susceptibility, $\chi''(\mathbf{Q}, \omega)$, which is directly related to the processes that absorb energy. The relationship between the scattering function and the dynamic susceptibility is given by:

$$S(\mathbf{Q}, \omega) = \frac{1}{1 - \exp(\frac{-E_i}{k_{\mathrm{B}} T})} \chi''(\mathbf{Q}, \omega) \tag{4.13}$$

where T is the temperature and k_{B} is the Boltzmann constant.

Two common instruments are used for performing inelastic neutron scattering experiments: triple axis spectrometers and time-of-flight (TOF) instruments. The former are extended elastic setup, or double axis, with an additional analyser stage that allows energy discrimination of the scattered beam. This is usually performed with a monochromator crystal that selects particles that satisfy the Bragg condition and therefore the required E_f. TOF techniques have already been discussed earlier, but further distinctions are made in inelastic TOF instruments: those with a fixed E_i are termed direct geometry and must employ choppers to select specific neutron velocities, whilst those with polychromatic incident radiation are termed indirect geometry and utilise energy analysers. In this thesis, only direct geometry TOF instruments are used.

4.4 Magnetic susceptibility

Magnetic susceptibility measurements are the first port of call when characterising the magnetic properties of a material. In Chapter 2 (Page 15), we derived the temperature and field dependence of the magnetic susceptibility, χ, of a paramagnet and how to determine mean-field interactions in the paramagnetic regime of an ordered magnet. Therefore, a lot of information can be extracted from measurements of χ and given the ease with which data can be collected, particularly compared to neutron diffraction or scattering experiments, make it an invaluable tool.

Several methods exist for measuring χ of a material. The simplest of these is the Gouy balance, whereby the mass of a sample is measured with and without the application of a magnetic field from an electromagnet. Susceptibility values from the Gouy balance often have a large error associated with them and are limited to a small temperature range. Modern techniques utilise a superconducting magnet and the most common instrument used is called a Superconducting QUantum Interference Device (SQUID). The sensitivity of a SQUID is several orders of magnitude better than the majority of instruments, with the ability to measure fields as small as $\sim 10^{-18}\,\mathrm{T}$, making them ideal for characterising frustrated magnets with small ordered moments and subtle changes in χ. Furthermore, they are able to measure from liquid helium, $T < 4\,\mathrm{K}$, to room temperatures and in a variety of applied fields.

The basic concept behind the workings of a SQUID lies in the Josephson effect, specifically the DC Josephson effect for the majority of SQUIDs. The DC Josephson effect is the indefinite tunneling of a DC current through an insulating link in a superconducting wire. To utilise this, a DC-SQUID involves a superconducting circuit with a circular region where the two branches of the circle contain a Josephson junction (Figure 4.4a). The superconducting current applied to the circuit splits equally between the two branches and when an applied field is passed through the ring, *i.e.* from a sample, the phase at the two junctions shifts discontinuously in quantised units of flux. The voltage change across the ring is directly related to the number of flux quanta, $\Phi = 2\pi\hbar/e2 \sim 2.07 \times 10^{-15}\,\mathrm{T\,m^2}$, giving rise to the extraordinary sensitivity of the SQUID. To decrease background noise and non-linear relaxation of the superconducting magnet the superconducting wire has two central coils with single coils wound in the opposite direction above and below this (Figure 4.4b). The flux quanta in the single coils should exactly cancel the central double coil, allowing errors to be accounted for.

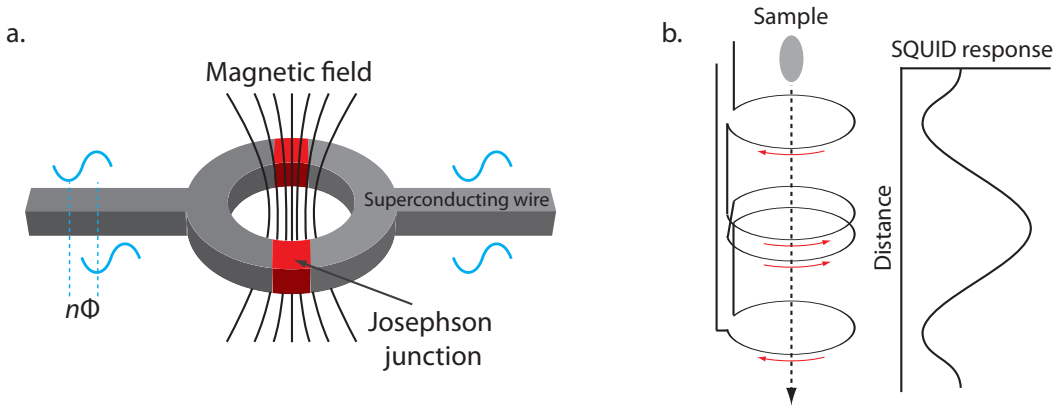

Figure 4.4: **a.** A schematic of a SQUID used for measuring magnetic susceptibility, χ. The phase of a superconducting current passing through the Josephson junctions shifts by a certain number of flux quanta when a magnetic field is applied in the middle of the ring. The flux quanta, $n\Phi$, is directly related to the voltage measured across the ring. **b.** The arrangement of the superconducting SQUID coils. Single coils are placed above and below a central double coil wound in the opposite direction, giving the response shown on the right as the sample is moved through the SQUID. The flux quanta from the two single coils should exactly cancel the central coils and any discrepancies allows errors to be accounted for.

4.5 Raman spectroscopy

Raman scattering is a powerful technique for measuring vibrational, rotational and other low-energy excitations within a sample. It utilises the Raman effect, which is caused by inelastic scattering of visible light from the excited energy states of the sample. Whilst similar to infrared spectroscopy where the incident photon is absorbed by some vibration that causes a change in dipole moment, Raman scattering can only occur where a change in electric dipole polarisation occurs. Often an intense Raman band is weakly IR active and vice-versa, therefore the two techniques are complimentary. Both are local techniques and can give important information on local symmetry that, for instance, may be unobservable using X-ray diffraction. Specifically for crystalline materials useful information can be gained on phonons, as well as other excitations such as magnons.

Each peak in a Raman spectra corresponds to some excitation of the sample, however correlating the two is often non-trivial particularly if the material in question has several atoms in the unit cell. In this thesis, Raman active modes are calculated using a site symmetry approach whereby the symmetry of every site in the unit cell is treated individually, as employed by the SAM program of the Bilbao crystallographic server [9].

The spectrometer used for data collection in this thesis was a Renishaw micro-Raman spectrometer. It consists of a Renishaw spectrograph using Kayser notch filters and a CCD detector coupled to a microscopy for point-by-point analysis and accurate focussing. Incident laser energies are variable but here only 514.5 nm was used. Temeprature dependent measurements were made using a Linkam THMS600 which can measure between $-196 < T < 600\,^{\circ}\mathrm{C}$ in an inert nitrogen atmosphere.

Bibliography

[1] *http://11bm.xray.aps.anl.gov/description.html*.

[2] L. C. Chapon, P. Manuel, P. G. Radaelli, C. Benson, L. Perrott, S. Ansell, N. J. Rhodes, D. Raspino, D. Duxbury, E. Spill and J. Norris, *Neutron News*, 2011, **22**, 22–25.

[3] R. A. Young, *The Rietveld Method*, Oxford University Press, Oxford, 1993.

[4] Bruker AXS, *TOPAS V4: General profile and structure analysis software for powder diffraction data*, 2008.

[5] J. Rodriguez-Carvajal, *Phys. B*, 1993, **192**, 55–69.

[6] A. S. Wills, *Phys. B*, 2000, **278**, 680–681.

[7] E. Kroumova, M. I. Aroyo, J. M. Perez-Mato, S. Ivantchev, J. M. Igartua and H. Wondratschek, *J. Appl. Crystallogr.*, 2001, **34**, 783–784.

[8] M. I. Aroyo, J. M. Perez-Mato, C. Capillas, E. Kroumova, S. Ivantchev, G. Madariaga, A. Kirov and H. Wondratschek, *Zeitschrift für Krist.*, 2006, **221**, 15–27.

[9] E. Kroumova, M. I. Aroyo, J. M. Perez-Mato, A. Kirov, C. Capillas, S. Ivantchev and H. Wondratschek, *Phase Transit. A Multinatl. J.*, 2003, **76**, 155–170.

Chapter 5

Sr-vesignieite, $SrCu_3V_2O_8(OH)_2$, a $S = \frac{1}{2}$ kagome antiferromagnet with spin and orbital frustration

5.1 Introduction

Since the prediction by Anderson of the quantum spin liquid (QSL) state and its potential involvement in the high-T_C superconductor La_2CuO_4 [1, 2], the search for such a state has been a 'holy grail' of frustrated magnetism and condensed matter physics in general. These exotic states are purely quantum mechanical in origin and their properties include highly entangled macroscopic ground states and fractional particle excitations [3]. Experimentally, conclusive evidence of a QSL remains elusive, but the $S = \frac{1}{2}$ kagome antiferromagnet (KAFM) is the most promising model system to make such a discovery. Characterised by quantum spins on a geometrically frustrated lattice of corner-sharing triangles, only a handful of model materials exist and they all suffer from imperfections that mask the intrinsic physics or perturb the delicate QSL ground states. Consequently, an essential aim of current research is to expand our library of experimental systems and further populate the phase diagram of the $S = \frac{1}{2}$ KAFM ground state. Only with this additional information can we hope to unravel the intrinsic physics and definitively find a QSL. To this end, the following chapter introduces a new model material; the Sr^{2+} analogue of the well studied $S = \frac{1}{2}$ KAFM vesignieite, from now on termed 'Sr-vesignieite'.

5.2 Expanding the library of model $S = \frac{1}{2}$ kagome antiferromagnets

A review of the literature on $S = \frac{1}{2}$ KAFMs is given in Chapter 3 (Page 38). From this, it is evident that not many synthetic systems exist and all suffer from some type of perturbation that makes them a less than ideal model. A common method of discovering new materials that have potential as model $S = \frac{1}{2}$ KAFMs is by searching mineralogical databases for naturally occurring minerals with perfect or near-perfect Cu^{2+} kagome networks, particularly those recently discovered. This has so far proved successful in discovering the majority of our current models, such as herbertsmithite, volborthite and

vesignieite [4, 5, 6].

Subtle changes to known materials, preferably without disrupting the $S = \frac{1}{2}$ magnetic lattice, offers an alternative and effective method of expanding our experimental library, while also furthering our understanding of the parent structure. This has proved particularly successful in the herbertsmithite family through the synthesis of 'Mg-herbertsmithite' [7] and (Zn,Mg,Cd)$Cu_3(OH)_6(SO_4)_2$ [8, 9, 10]. Whilst derivatives of the herbertsmithite structure are well studied and new ones regularly discovered, very few exist in the vesignieite family. The only synthetic isomorph is $KCu_3As_2O_7(OH)_3$ [10], although the natural mineral bayldonite, $PbCu_3As_2O_8(OH)_2$, offers another potential example if it can be synthesised [11]. Whilst both of these minerals are arsenates, it implies the crystal structure is flexible and similar substitutions could be made in vesignieite, $BaCu_3V_2O_8(OH)_2$.

An obvious choice for substitution at the Ba^{2+} site of vesignieite is Pb^{2+} considering that the mineral bayldonite exists in nature. However, due to the inert pair effect the local coordination of Pb^{2+} in minerals is often heavily distorted, which is the case for bayldonite, affecting the magnetism of the Cu^{2+} kagome network [12]. Another option for substitution is Sr^{2+}, whose crystal radius is only 0.01 Å smaller than Pb^{2+} and is not affected by the inert pair effect. The remainder of this chapter details the successful synthesis and both structural and magnetic characterisation of 'Sr-vesignieite', $SrCu_3V_2O_8(OH)_2$.

5.3 Synthesis of 'Sr-vesignieite', $SrCu_3V_2O_8(OH)_2$

Vesignieite is commonly synthesised by reflux in a NH_4OH aqueous solution [13]. The formation of Schweizer's reagent, $Cu[(NH_3)_4(H_2O)_2](OH)_2$, from the $Cu(OH)_2$ starting reagent brings the Cu^{2+} into solution and aids the production of vesignieite. However, using $Sr(CH_3COO)_2$ in place of $Ba(CH_3COO)_2$ as a first attempt to synthesise 'Sr-vesignieite' proved unsuccessful. The initial blue solution of Schweizer's reagent gradually turns black either with or without heating the reaction. The black powder was found to be CuO from X-ray diffraction.

Inspiration for a different approach to the synthesis was taken from the material volborthite. Structurally, vesignieite and volborthite have very much in common (Figure 5.1). Both have slightly distorted Cu_2O_6 kagome planes which are linked by VO_4 tetrahedral groups, although the latter adopt slightly different geometries. In addition, the interplanar regions are 'filled' with Ba^{2+} and H_2O in vesignieite and volborthite respectively. In volborthite, the H_2O molecules are hydrogen bonded between hydroxide and VO_4 groups bound to adjacent kagome layers. This weak interplanar bonding creates the possibility of substituting the H_2O molecules without drastically disturbing the remaining structure. However, given that the initial attempts at synthesising 'Sr-vesignieite' were unsuccessful, it is likely not to be a particularly stable structure when compared to vesignieite. This is unsurprising given the 0.17 Å smaller ionic radius of 6-coordinated Sr^{2+} (1.18 Å) compared to Ba^{2+} (1.35 Å) [14].

Similar approaches to that described above for layered copper materials could not be found in the literature. Instead, two synthetic methods were attempted with inspiration taken from the literature on other copper hydroxide based inorganic minerals: (i) refluxing volborthite powder in an Sr^{2+} solution [13] and (ii) a hydrothermal reaction of volborthite powder in Sr^{2+} solution [16]. Method (i) did not al-

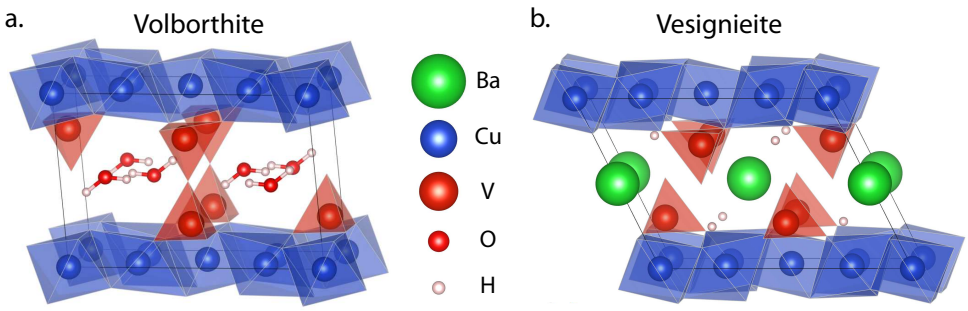

Figure 5.1: a. The crystal structure of volborthite, $Cu_3V_2O_7(OH)_2 \cdot 2H_2O$. The water molecules sit between the planes of CuO_6 kagome layers. This structure provides a useful starting reagent for synthesis of 'Sr-vesignieite', as the water molecules are easily displaced by Sr^{2+} in a hydrothermal reaction. **b.** Crystal structure of vesignieite, $BaCu_3V_2O_7(OH)_2$ [15]. Ba^{2+} ions fill the voids between the kagome planes, where the latter are further joined by hydrogen bonding between hydroxide and VO_4 groups.

low for any reaction of the volborthite, even after extended reaction times on the order of days. However, initial attempts using method (ii) did provide suitable conditions to encourage the reaction of the volborthite powder, as evidenced from X-ray diffraction data, and provided an opportunity for experimentation with the conditions.

Initial attempts at the hydrothermal synthetic method were performed in 15 ml PTFE-lined steel autoclaves, described in Chapter 4, heated in fan-assisted ovens. Volborthite was synthesised from a simple room temperature reaction. $Cu(OH)_2$ was first made from a reaction of $Cu(NO_3)_2{\cdot}H_2O$ (Alfa Aesar, 12.6432 mmol, 2599.1 mg) and NaOH (Sigma-Aldrich, 25.2865 mmol, 1011.3 mg) in distilled water and collected using centrifugation. In a 100 ml conical flask, the $Cu(OH)_2$ and V_2O_5 (Sigma-Aldrich, 4.2144 mmol, 766.4 mg) are stirred in 100 ml distilled water for 2 days and the resulting volborthite is washed with acetone and dried on a rotary evaporator. For the 'Sr-vesignieite' reaction, the Sr^{2+} source used was strontium acetate, mirroring the same salt as used for the Ba^{2+} source in the vesignieite reaction [16]. The pre-prepared volborthite (0.4214 mmol, 200 mg) and $Sr(CH_3COO)_2{\cdot}0.5H_2O$ (Sigma-Aldrich, 0.4214 mmol, 90.5 mg) was placed in the PTFE-liner with 10 ml H_2O. The reaction equation for this method is assumed to be:

$$\begin{aligned} Cu_3V_2O_7(OH)_2 \cdot 2H_2O + Sr(CH_3COO)_2 \cdot 0.5H_2O + 0.5H_2O \\ \rightarrow SrCu_3V_2O_8(OH)_2 + 2CH_3COOH + 2H_2O \end{aligned} \tag{5.1}$$

A reaction at 220 °C for 1 day resulted in a mix of green and black powder at the bottom of the PTFE reaction vessel. A powder X-ray diffraction pattern of this powder can be seen in Figure 5.2. In order to determine the presence of any vesignieite-like phase a Pawley extraction was performed on the XRD data using the lattice parameters from vesignieite as a starting point. It is clear that a phase with similar lattice parameters exists, however not all the peaks are modelled suggesting the presence of additional phases or an incorrect structure. The additional peaks did not match with any materials found in a literature search for oxide or hydroxide materials containing Sr, Cu and V. Extending the search to

Sr-analogues of Cu- and V-bearing materials revealed the major additional phase to be the Sr-analogue of the mineral mottramite ($PbCu_4VO_4OH$) [17], from now on termed 'Sr-mottramite'. With both 'Sr-mottramite' and 'Sr-vesignieite' phases included in the refinement some peaks remain unaccounted for (Figure 5.2). As will be discussed in Section 5.4, these are in fact related to the 'Sr-vesignieite' structure. Whilst no magnetic data could be found for mottramite or 'Sr-mottramite', the presence of $S = \frac{1}{2}$ d^9 Cu^{2+} ions will lead to magnetic contributions and therefore minimising the impurity concentration in the synthesised samples is important for determining the intrinsic magnetic response of 'Sr-vesignieite'.

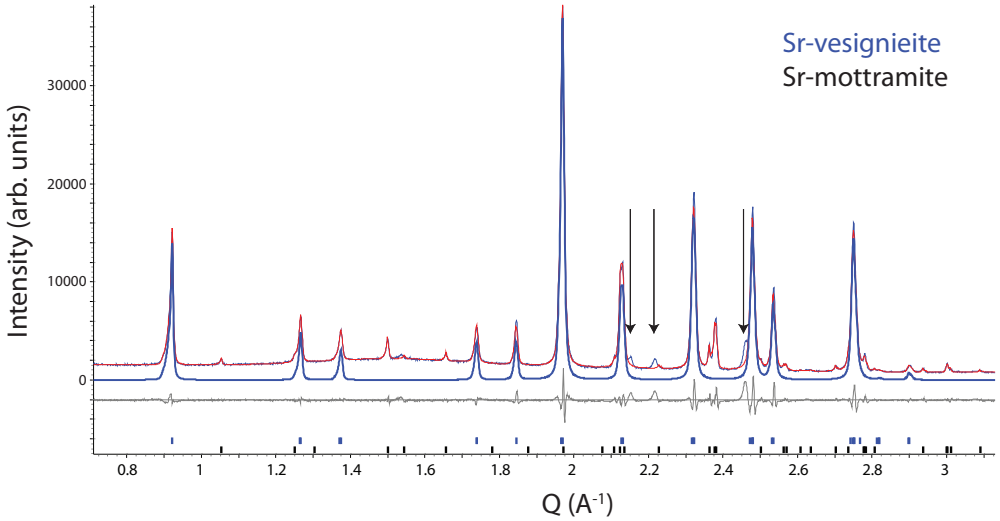

Figure 5.2: Pawley refinement of data collected on a sample with mixed 'Sr-vesignieite' and 'Sr-mottramite' phases performed using the TOPAS software package (Cu k_α STOE STADI-P, described in Chapter 4) [18]. The blue line is the calculated contribution from the 'Sr-vesignieite' phase and the red line is the calculated pattern with contributions from both phases. The black arrows indicate peaks unaccounted for by either phase.

In addition to the 'Sr-mottramite' impurity phase, a black powder was often produced in the reaction vessels, particularly at higher temperatures. Centrifugation of the samples in 15 ml water at 4400 rpm for 2 mins caused two layers to form: the bottom layer containing the black powder and the top, green layer containing the 'Sr-vesignieite' and 'Sr-mottramite' phases. The desired top layer could be collected by carefully using a spatula. Analysis of the black powder using x-ray diffraction showed it to be poorly crystalline and thus phase identification proved difficult. The top layer contained a mix of 'Sr-vesignieite' and 'Sr-mottramite', however further centrifugation of this mixture under the same conditions did not allow separation of the phases.

Instead of using post-synthetic separation methods, attempts were made to eliminate the 'Sr-mottramite' impurity phase through varying the reaction conditions. The solution pH in hydrothermal reactions is a condition that is commonly and easily varied. As strontium acetate is used as the Sr^{2+} containing reagent, it was logical to use acetic acid (CH_3COOH) to acidify the reaction solution. Three reactions were performed with 0, 0.05 and 0.1 ml of acetic acid (Sigma Aldrich, $\geq 99\,\%$) added to the PTFE-liner along with the H_2O, which equated to a solution pH ~ 3 and ~ 2.5 for the latter two, respectively. Figure 5.3a shows a comparison of the XRD spectra of the products from these reactions. A

reduction in peak intensity of the 'Sr-mottramite' impurity phase is observed upon addition of 0.05 ml of acetic acid, however further additions do not significantly reduce the impurity further.

The reaction duration is another variable that is easily changed in hydrothermal syntheses. Figure 5.3b shows the effect of reaction time with conditions of 220 °C and 0.05 ml acetic acid on the 'Sr-mottramite' impurity level. Whilst increasing reaction time reduces the impurity amount, it also increases the amount of the black, amorphous product resulting in very low yields of 'Sr-vesignieite'. Whilst this makes it simple to synthesise small amounts of pure 'Sr-vesignieite', it becomes difficult to produce large amounts.

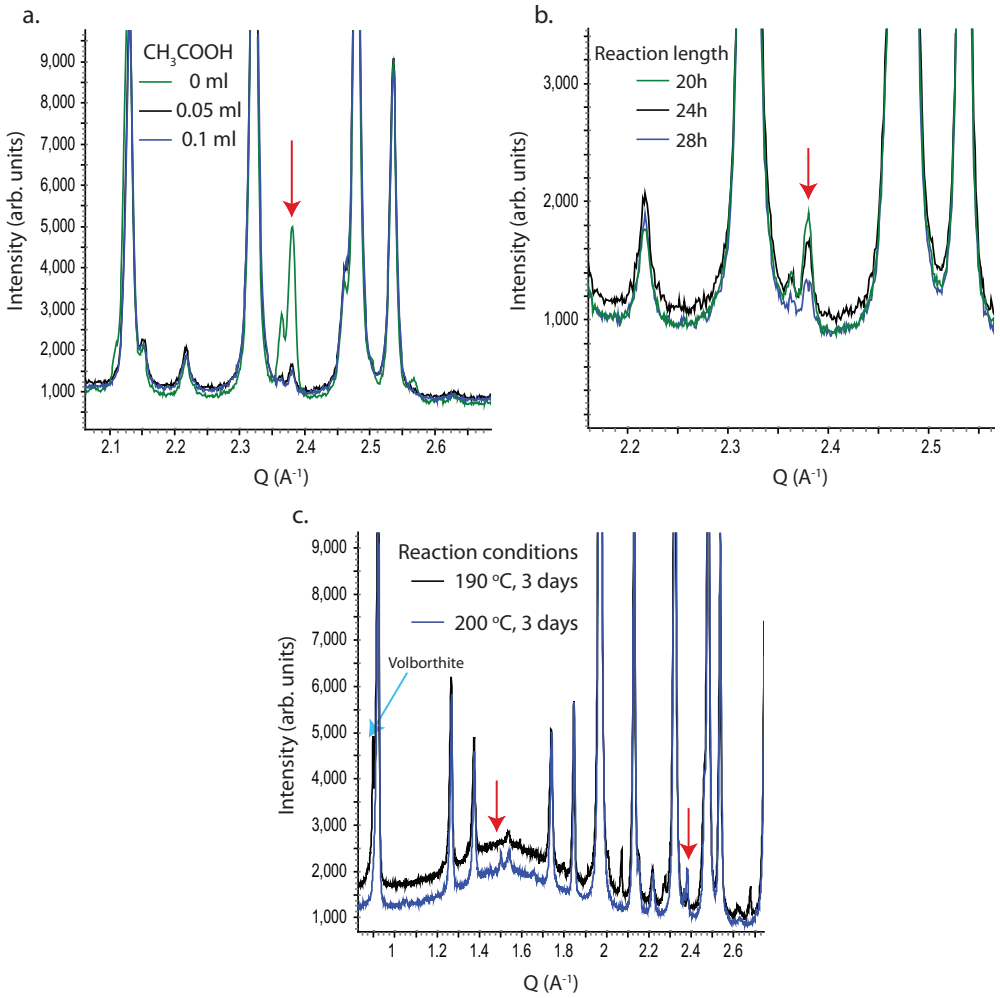

Figure 5.3: **a.** X-ray diffraction data collected on samples prepared with various quantities of acetic acid, CH_3COOH. With no acetic acid addition a large impurity peak is observed at $Q \sim 2.35\,\text{Å}^{-1}$ associated with the 'Sr-mottramite' structure. Adding 0.05 ml acetic acid significantly reduces the size of the impurity peak, however further additions of acetic acid does not reduce it further. **b.** Comparison of samples prepared with 0.05 ml acetic acid and reacted at 220 °C for various times. Increasing reaction time causes a small reduction in the size of the 'Sr-mottramite' impurity peak but also significantly reduces the yield of 'Sr-vesignieite'. **c.** The 'Sr-mottramite' peaks (red arrows) appear after all the volborthite has reacted, as shown by these two reactions performed at different temperatures.

At 220 °C the reaction proceeds quickly, with all volborthite having reacted within 20 hours. Lowering the temperature will generally slow all reactions and as each competing reaction will have a different temperature dependence such changes should give insight into the reaction mechanism. Figure 5.3c shows XRD data comparing reactions at 200 and 190 °C for 3 days. It is notable here that at 200 °C all volborthite has reacted, whilst at 190 °C there is still a significant volborthite peak at $\sim 0.9\,\text{Å}^{-1}$. However, no 'Sr-mottramite' peak is present at the lower temperature, compared to at 200 °C where the impurity has again started to form. This suggests 'Sr-mottramite' is only produced once the majority of the volborthite has reacted. Subsequently, the impurity percentage decreases, as shown in Figure 5.3b, however the yield of the poorly crystalline, black powder increases at the expense of both crystalline products, limiting the yield of desired 'Sr-vesignieite'.

Evidently, a compromise must be made between the purity and yield of the final product depending on requirements of sample size and quality. In order to perform characterisation measurements on samples that were prepared under the same conditions, a large sample was produced by performing several reactions side-by-side and combining the resulting products. Therefore, the following final synthesis procedure was performed five times and the resulting sample was used for characterisation throughout the rest of this chapter.

The final preparation conditions are as follows. Powdered volborthite (200 mg, 0.4214 mmol) was lightly ground in an agate mortar and pestle for ∼1 minute and added to a 15 ml PTFE reaction vessel along with $Sr(CH_3COO)_2$ (90.5 mg, 0.4214 mmol), H_2O (10 ml) and CH_3COOH (0.05 ml). The solution was stirred for 2 mins before being sealed in a steel autoclave and placed in an oven at 220 °C for 1 day. The autoclave was removed from the oven and left to cool to room temperature before opening. The reaction solution was removed using a pipette and the green powder collected in a 15 ml centrifuge tube with distilled water and centrifuged for 2 minutes. The water was disposed of and the top, green coloured layer collected using a spatula and centrifuged in 15 ml of water again. The tube was refilled with acetone and the powder stirred to disperse it before centrifuging again. This process was repeated twice more with acetone before being placed in a 100 ml round-bottomed flask and the acetone removed *via.* rotary evaporation. The final yield of 'Sr-vesignieite' was 80 mg (35 %) and 400 mg when combined with the other four reactions.

5.4 Structural characterisation – a $S = \frac{1}{2}$ KAFM with a $P3_121$ structure

Initial characterisation of the 'Sr-vesignieite' structure was performed using local laboratory powder X-ray diffractometers. As with vesignieite, this method is limited by the high X-ray absorption common to all materials containing heavy elements measured in transmission geometry. Nevertheless, the data collected allowed accurate Pawley refinements, whereby intensities are refined independently, which revealed the crystal symmetry class. To overcome this problem for Rietveld analysis powder diffraction data was collected using high energy synchrotron radiation. Before discussing the results, it is useful to discuss the crystal structure of vesignieite.

5.4.1 Crystal structure of vesignieite, $BaCu_3V_2O_8(OH)_2$

The only detailed crystallographic study of vesignieite was an X-ray diffraction experiment performed on a natural single crystal [15]. The study concluded that vesignieite crystallises in the monoclinic $C12/m1$ space group with lattice parameters $a = 10.270(2)$, $b = 5.911(1)$ and $c = 7.711(2)$ Å and $\alpha = 90$, $\beta = 116.42(3)$ and $\gamma = 90\,°$ (Figure 5.4a). The Cu^{2+} kagome layers are built from two crystallographically inequivalent Cu sites which results in isosceles triangles with two distinct Cu–Cu bond lengths (Figure 5.4b). The Cu sites are octahedrally coordinated by oxygens with an axially compressed Jahn-Teller distorted geometry. The kagome layers are separated by VO_4 tetrahedra, whose basal oxygens are shared with the CuO_6. The apical oxygen of the VO_4 is hydrogen bonded to a hydroxide group on the adjacent kagome layer and also coordinates with the Ba^{2+} ion: the weak coordination of the former is indicated by its large anisotropic displacement parameter.

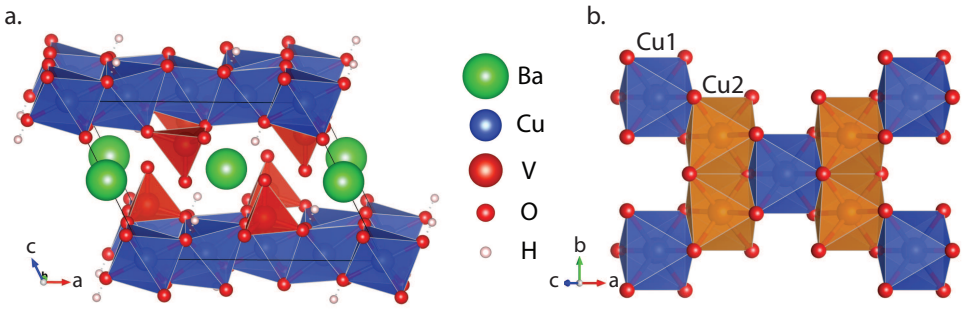

Figure 5.4: **a.** Crystal structure of vesignieite determined from single crystal X-ray diffraction performed on a natural sample [15]. The structure is described with $C12/m1$ symmetry and has lattice parameters $a = 10.270(2)$, $b = 5.911(1)$ and $c = 7.711(2)$ Å and $\alpha = 90$, $\beta = 116.42(3)$ and $\gamma = 90\,°$. **b.** The same structure as **a.** showing that the kagome planes are made from two crystallographically inequivalent Cu sites, causing isosceles Cu_3 triangles rather than equilateral.

The crystal structure lies very close to a higher symmetry rhombohedral description in $R\bar{3}m$. The three-fold axis in $R\bar{3}m$ make the Cu triangles equilateral and build a structurally 'perfect' kagome lattice, *i.e.* all Cu–Cu bond lengths and nearest-neighbour Cu-O–Cu superexchange paths are identical. Recent analysis of X-ray diffraction data from synthetic single crystal samples have suggested the structure has overall $R\bar{3}m$ symmetry, however the VO_4 tetrahedra is significantly disordered and is best modelled by splitting the site occupation [19]. This highlights the significant disorder within the vesignieite structure and the uncertainty surrounding its true description.

5.4.2 Lab X-ray diffraction

As previously described in Section 5.3, powder X-ray diffraction data collected on 'Sr-vesignieite' throughout the synthetic optimisation process shared similar peak positions and relative intensities to those of vesignieite [16]. Therefore, the monoclinic vesignieite structure was a good starting point for analysing the diffraction patterns. Data for 'Sr-vesignieite' collected on a Cu K_α STOE STADI-P diffractometer, described in Chapter 4, is shown in Figure 5.5. Figure 5.5a shows a Pawley refinement of the data with the vesignieite unit cell as a starting model ($C12/m1$, $a = 10.210$, $b = 5.903$, $c = 7.739$ Å

and $\beta = 116.15°$) [15]. Whilst the fit looks reasonable, the black arrows highlight small peaks that do not match with any reflections from the original structure. These peaks did not index with the known 'Sr-mottramite' impurity phase identified during the synthesis nor any published structure. Therefore, to fully characterise the structure the diffraction pattern in Figure 5.5 was indexed using the TOPAS software suite [18]. The Bravais lattices included in the indexing routine were: trigonal, tetragonal, orthorhombic and monoclinic. The solutions with independent space groups and best goodness-of-fit factors are shown in Table 5.1.

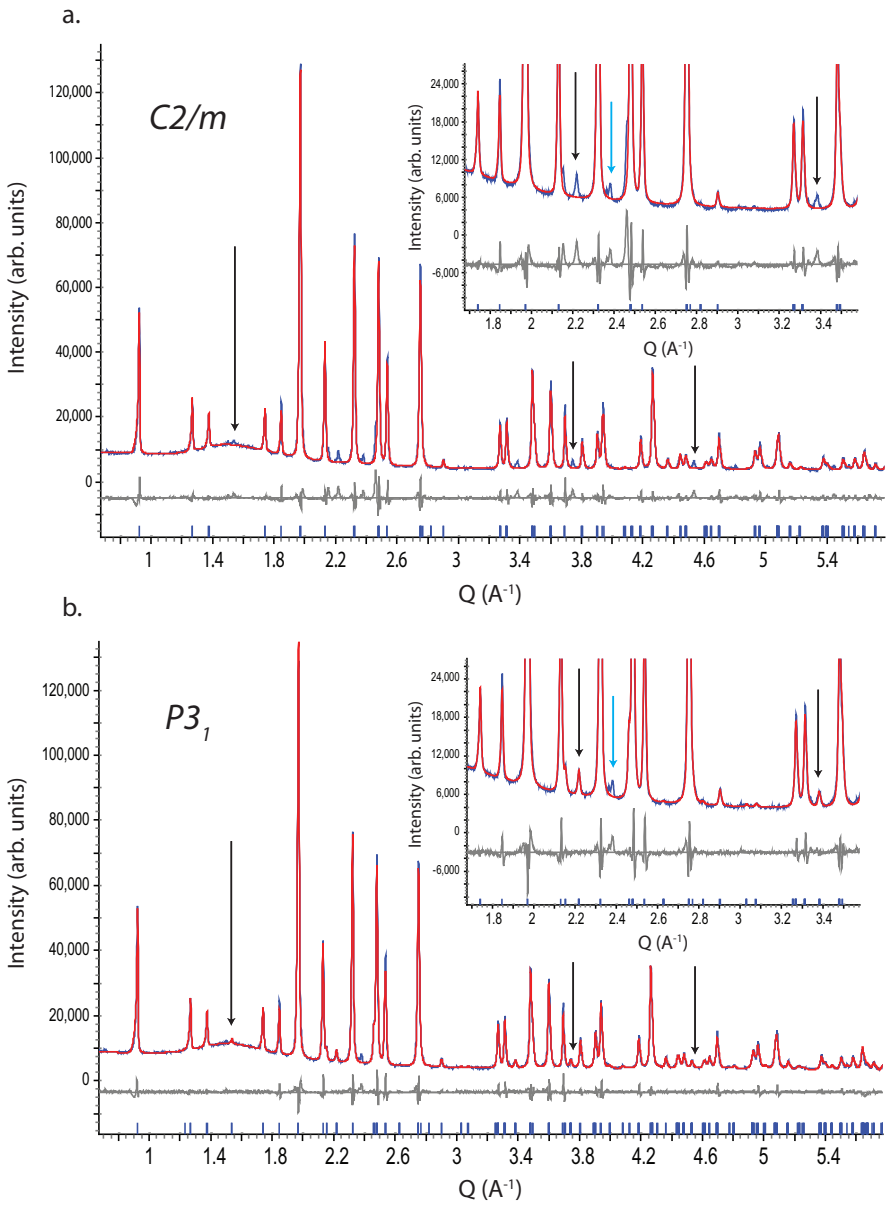

Figure 5.5: A comparison of Pawley refinements on data collected on a 'Sr-vesignieite' sample using a **a.** $C12/m1$ space group and **b.** $P3_1$ space group (Cu K_α STOE STADI-P). The black arrows indicate peaks unaccounted for by the $C12/m1$ structure, but well fitted with the $P3_1$ structure. The blue arrows indicate the reflections from the 'Sr-mottramite' impurity phase.

Figure 5.5b shows a Pawley refinement using the space group and lattice parameters with the best

		Lattice parameters					
Space Group	GOF	a (Å)	b (Å)	c (Å)	α (°)	β (°)	γ (°)
$P3_1$	13.33	5.8992	5.8992	20.4044	90	90	120
$P3$	12.89	5.8981	5.8981	20.4052	90	90	120
$C222$	12.77	10.1761	3.8613	20.3939	90	90	90
$P4/n$	10.56	5.1003	5.1003	20.4427	90	90	90

Table 5.1: The best solutions from indexing the powder X-ray diffraction pattern shown in Figure 5.5. The $P3_1$ structure gives the highest goodness-of-fit whilst not over predicting peaks, as $P3$ predicts a peak at low $Q \sim 0.6\,\text{Å}^{-1}$ which is not present in the data. Therefore, the $P3_1$ structure is the best solution to the data.

goodness-of-fit from Table 5.1: the $P3_1$ solution with $a = b = 5.8992$ and $c = 20.4044\,$Å. This space group accounts for the peaks that could not be fitted using the monoclinic $C12/m1$ structure, which are highlighted with black arrows. The blue arrow shows an impurity peak originating from the Sr-mottramite impurity phase. The insets of Figures 5.5a and b show zoomed regions of the Pawley refinements which highlight the 'Sr-mottramite' impurity peak and the additional peaks at $Q \sim 2.15, 2.2, 2.46$ and 3.4 Å^{-1} which are only fitted with the $P3_1$ structure. A $P3$ structure also has a high goodness-of-fit, but predicts the (002) peak at very low $Q \sim 0.6\,\text{Å}^{-1}$ that is not present in the data. Therefore, the $P3_1$ structure gives the best fit without over prediction of peaks, making it the best solution.

It is important to note that in powder diffraction several space groups within the same crystal class may be indistinguishable solely from their observed hkl indices. For instance, Pawley refinements using the space groups $P3_2$, $P3_112$, $P3_121$, $P3_212$, $P3_221$, $P6_2$, $P6_4$, $P6_222$ and $P6_422$ will give identical results to that shown in 5.5b for $P3_1$. In order to distinguish between these solutions structural refinement is required. Unfortunately, this is problematic in the case of this material due to high X-ray absorption in transmission geometry: with $\lambda = 1.54\,$Å and a capillary diameter of 0.3 mm the value of μR is 3.30 for this material. Ideally, μR should be less than 1 so that no absorption correction is needed. This can easily be achieved at a synchrotron with high energy X-rays, whilst also benefiting from the excellent resolution and flux at such facilities.

5.4.3 Synchrotron study - 11-BM

To perform Rietveld refinements and therefore extract information such as atomic positions for 'Sr-vesignieite', data were collected at the high-resolution powder diffraction beamline 11-BM at the Advanced Photon Source in the Argonne National Laboratory, United States. Measurements were made with X-rays of $E = 30\,$keV ($\lambda = 0.413827\,$Å) in a 0.3 mm capillary giving a $\mu R = 0.34$. The beamline uses 12 independent Si (111) single crystal analysers allowing exceptionally high-speed ($< 1\,$hr) and high-resolution ($\Delta Q/Q \approx 2 \times 10^{-4}$) data collection. A full description of the beamline is given in Chapter 4 (Page 53).

Rietveld refinements were performed using the TOPAS software suite [18]. Instrumental profile parameters were obtained by refining an LaB_6 standard sample with well defined lattice parameters and minimal sample broadening. The 'Sr-vesignieite' data evidenced a significant hkl-dependent sample

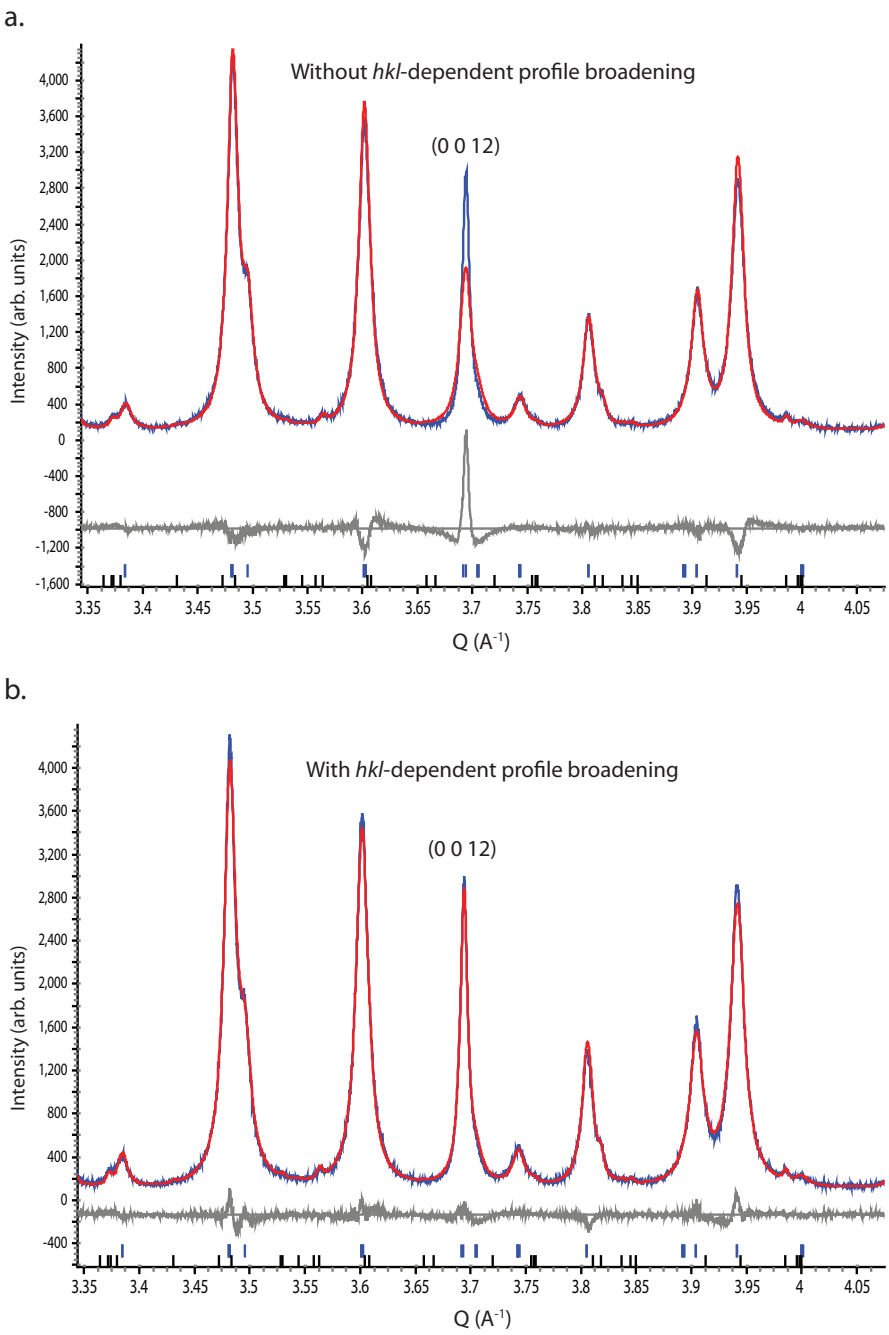

Figure 5.6: **a.** Rietveld refinement of the synchrotron diffraction data collected on 'Sr-vesignieite' without using Stephens's *hkl*-dependent profile broadening function. **b.** Including Stephens's anisotropic model, circles convolution and 2θ-offset for the $00l$ reflections significantly improves the quality of the fit.

broadening, particularly of the $00l$ reflections (Figure 5.6). As such, the sample related broadening across the whole pattern was modelled solely using Stephens's hkl-dependent model for the trigonal crystal system [20]. Additionally for the $00l$ reflections, a circles convolution ($1 - |\frac{\epsilon_m}{\epsilon}|^2$ for $0 \leq \epsilon \leq \epsilon_m$) and 2θ-offset was required for these, often used for extreme size or strain effects [21]. This anomaly is also observed in vesignieite (Chapter 6) and is likely related to stacking faults and/or strain.

A trial Rietveld refinement was performed using a structural model adapted from vesignieite: in

Supergroup	$u_{\max}$ (Å)	Max $u_{Cu^{2+}}$ (Å)	Max $u_{Sr^{2+}}$ (Å)	Max $u_{O^{2-}}$ (Å)
$P3_112$	1.075	0.959	1.075	0.811
$P3_121$	0.399	0.190	0.201	0.399
$P6_4$	1.189	1.001	1.148	0.546

Table 5.2: The three possible higher symmetry structures of 'Sr-vesignieite' that correctly index the observed data. The maximum atomic displacement induced in the transformation from the $P3_1$ to the $P3_121$ structure is significantly less than the other two, particularly for the Sr^{2+} and Cu^{2+} positions which are well determined from X-ray diffraction.

the $P3_1$ space group there are 18 inequivalent crystallographic atoms, compared to 9 in $C12/m1$. To determine the legitimacy of the $P3_1$ structure, the refinement was initially performed with all atomic coordinates free, except for hydrogen which was fixed to the three-fold axis in the rhombohedral structure of β-vesignieite to give a hydroxide bond of ~ 1 Å [19]. Isotropic displacement parameters for the Ba, Cu and V sites refined stably however the O sites were fixed to the values from the β-vesignieite structure. The resulting atomic information is shown in Appendix A. A good fit is afforded with these positions ($\chi^2 = 1.433$ for 62 parameters) and they importantly account for the extra reflections not observed in the monoclinic structure.

As discussed earlier, space groups with the same reflection conditions can be difficult to distinguish using powder diffraction due to symmetry equivalent reflections with the same d-spacing. The indexing results for 'Sr-vesignieite' represent the lowest symmetry solution out of the space groups which give identical results. Therefore, it is necessary to test for pseudosymmetry of the refined structure by investigating the minimal supergroups of $P3_1$ to determine if any represent a suitable higher-symmetry solution.

The program PSEUDO provides an easy way to check the minimal supergroups of a given structure for any pseudosymmetry [22]. Inputting the refined structure gives four higher symmetry structures that do not cause invalid Wyckoff splittings after transformation: $R3$, $P3_121$, $P3_112$ and $P6_4$. $R3$ can immediately be eliminated as a potential solution as it does not correctly index the diffraction data. To distinguish between the remaining solutions, PSEUDO calculates the maximum atomic displacements, $\mu_{\max}$, caused by the transformations to the respective space groups. These results can be seen in Table 5.2. The transformation to $P3_121$ causes the smallest maximum displacement, $u_{\max} = 0.399$ Å. Looking at the individual atoms, the transformations to $P3_112$ and $P6_4$ cause significant displacement of Sr^{2+} and Cu^{2+} which should be quite well defined in the $P3_1$ structure from the Rietveld refinement. Contrastingly, these ions remain relatively close to their original values in the transformation to $P3_121$. Furthermore, the largest $u_{\max}$ is for an O^{2-} ion whose position will not be as accurately defined in the $P3_1$ structure by Rietveld refinement. Searching this $P3_121$ structure for further hidden symmetry produced results that did not index the data correctly.

Rietveld refinement of the $P3_121$ structure obtained from PSEUDO was performed using a similar process to that discussed for $P3_1$. Instrumental broadening was modelled using values taken from a

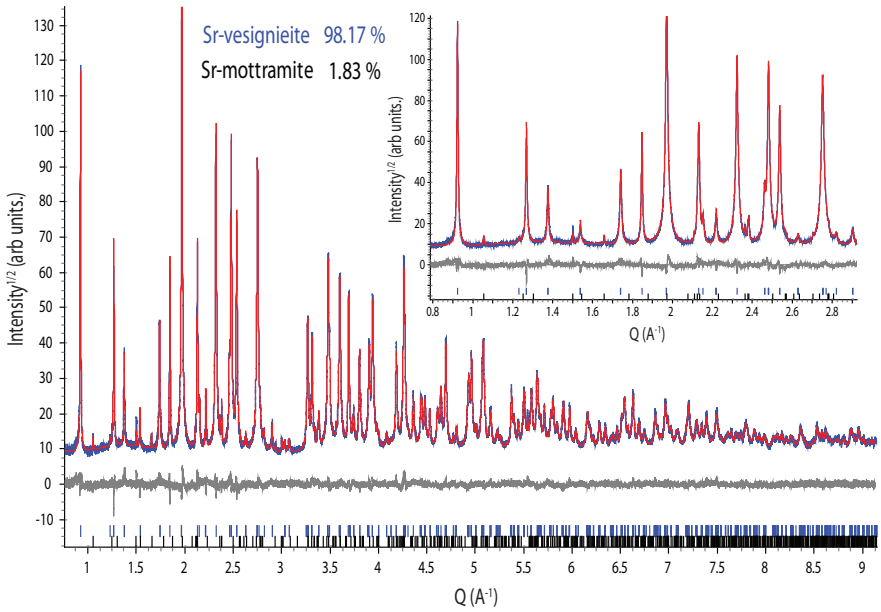

Figure 5.7: Final Rietveld refinement of powder synchrotron diffraction data collected on 11-BM at the APS for 'Sr-vesignieite' ($\lambda = 0.413827$ Å), plotted with $\sqrt{\text{Intensity}}$ for clarity. The inset shows a zoomed region of the low-Q fit. The final goodness-of-fit parameters were $\chi^2 = 1.413$ and $R_{\text{wp}} = 6.878$ for 71 variables in the $P3_121$ space group.

refinement of a standard LaB_6 standard and sample broadening the same as the Rietveld refinement discussed for the $P3_1$ structure. All atomic coordinates were freely refined and the hydrogen fixed to the position described in the $P3_1$ structure. Anisotropic displacement parameters (ADPs) were stably refined for the Sr^{2+}, V^{5+} and two Cu^{2+} sites, with the latter fixed to be equal. Remaining ADPs for the oxygen positions were taken from a single crystal study of vesignieite performed at room temperature [19]. A Rietveld model of a 'Sr-mottramite' phase was also included and refined to ~ 2 % of the sample.

The atomic positions and displacement parameters from the Rietveld refinement using the $P3_121$ structure are shown in Table 5.3. The goodness-of-fit parameters were $\chi^2 = 1.413$ and $R_{\text{wp}} = 6.878$. Further refinement of the structure in $P3_1$, with all appropriate transformations, did not improve the fit: the R_{wp} value lowers to 6.793 however the χ^2 value, which takes account of the additional parameters, increases to 1.462. Furthermore, refinement of the atomic displacement parameters resulted in unphysical values. These support the finding that $P3_121$ is the correct structure for 'Sr-vesignieite' and no further symmetry lowering is required.

5.4.4 Discussion

Vesignieite was originally suggested to crystallise in the monoclinic space group $C12/m1$ with the Cu^{2+} kagome lattice built from isosceles triangles due to the lack of a 3-fold rotation axis [15]. Synthetic single crystal samples were argued to crystallise in the higher symmetry $R\bar{3}m$ space group, and thus contain a structurally 'perfect' kagome lattice, although significant disorder within the material may lower the overall symmetry [19]. Thus the $P3_121$ space group which describes 'Sr-vesignieite' is a unique structure for these closely related materials. This section will describe the repercussions these

Lattice parameters							
a (Å)	b (Å)	c (Å)	α (°)	β (°)	γ (°)		
5.89577(2)	5.89577(2)	20.41260(10)	90	90	120		
Atomic information							
Site	Ox. state	Wyckoff	x	y	z	Occ	B_{iso} (Å^2)
Sr1	2+	$3a$	0.66621(14)	0	$\frac{1}{3}$	1	0.8508
Cu1	2+	$6c$	0.69046(19)	0.50041(56)	0.83476(8)	1	0.9064
Cu2	2+	$3a$	0	0.19513(64)	$\frac{1}{6}$	1	0.9064
O11	2-	$6c$	0.16898(179)	0.98345(76)	0.56090(32)	1	2.8907
O12	2-	$6c$	0.54277(182)	0.73147(70)	0.91304(24)	1	2.8907
O13	2-	$6c$	0.82149(186)	0.35377(90)	0.23147(37)	1	2.8907
O21	2-	$6c$	0.66685(94)	0.02187(91)	0.12491(11)	1	0.9927
O31	2-	$6c$	0.78198(70)	0.11098(68)	0.00360(14)	1	3.1811
V1	5+	$6c$	0.71568(21)	0.04730(19)	0.92689(3)	1	0.0404
H1	1+	$6c$	0.66667	0.00000	0.07193	1	0.7896
Anisotropic displacement parameters (Å^2)							
Site	u_{11}	u_{22}	u_{33}	u_{12}	u_{13}	u_{23}	
Sr1	0.00681(58)	0.01358(48)	0.00514(30)	0	0.00012	0	
Cu1	0.00586(25)	0.01164(42)	0.01900(29)	0.00592(38)	0.00402(28)	0.00598(33)	
Cu2	0.00586(25)	0.01164(42)	0.01900(29)	0.00592(38)	0.00402(28)	0.00598(33)	
O11	0.03310	0.03310	0.03310	0.01240	-0.01370	0.01370	
O12	0.03310	0.03310	0.03310	0.01240	-0.01370	0.01370	
O13	0.03310	0.03310	0.03310	0.01240	-0.01370	0.01370	
O21	0.01600	0.01600	0.00570	0.00800	0	0	
O31	0.06800	0.06800	0.00620	0.05000	-0.00040	0.00040	
V	0.00051(48)	0.00025(46)	0.00052(33)	0	0	0	

Table 5.3: Lattice parameters, atomic positions and displacement parameters of 'Sr-vesignieite' obtained from Rietveld refinement of the synchrotron data at 300 K using the space group $P3_121$. The fixing of the hydrogen position is described in the text. The anisotropic displacements of the oxygens and isotropic displacement of the hydrogen were taken from the β-vesignietie structure [19].

symmetry elements have on the salient crystallographic features.

Figure 5.8a shows the refined crystal structure of 'Sr-vesignieite'. As in vesignieite no 3-fold axis is present but there is a 3_1 screw axis which relates all kagome planes by rotating each adjacent one by 120 °. The distance between planes is $\frac{c}{3} = 6.8042(1)$ Å, indicating that the system remains highly 2-dimensional. Linking the planes are VO_4 tetrahedra which share 3 basal oxygens with the CuO_6 of the kagome planes, whilst the apical oxygen is hydrogen bonded to the hydroxide group attached to the adjacent kagome plane. Sr^{2+} ions fill the remaining space between the planes.

A star unit of the kagome network is shown in Figure 5.8b. These are built from two crystallographically inequivalent Cu^{2+} ions and these form a pattern of Cu1 chains whilst the Cu2 sites complete the edge-sharing triangles by joining these chains. The symmetry of the kagome star is quite different from both the $R\bar{3}m$ and $C12/m1$ descriptions of vesignieite. The lack of a 3-fold axis and a $2/m$ element means the sides of each triangle are unrelated and, thus, the triangles are built from 3 inequivalent Cu–Cu bond lengths. These values (Cu–Cu = 2.933(3), 2.949(3) and 2.964(3) Å) give a difference in Cu–Cu bond lengths of 1.06 %, which lies in between the similar distortions of vesignieite (0.07 %) and volborthite (3.06 %) [13, 23].

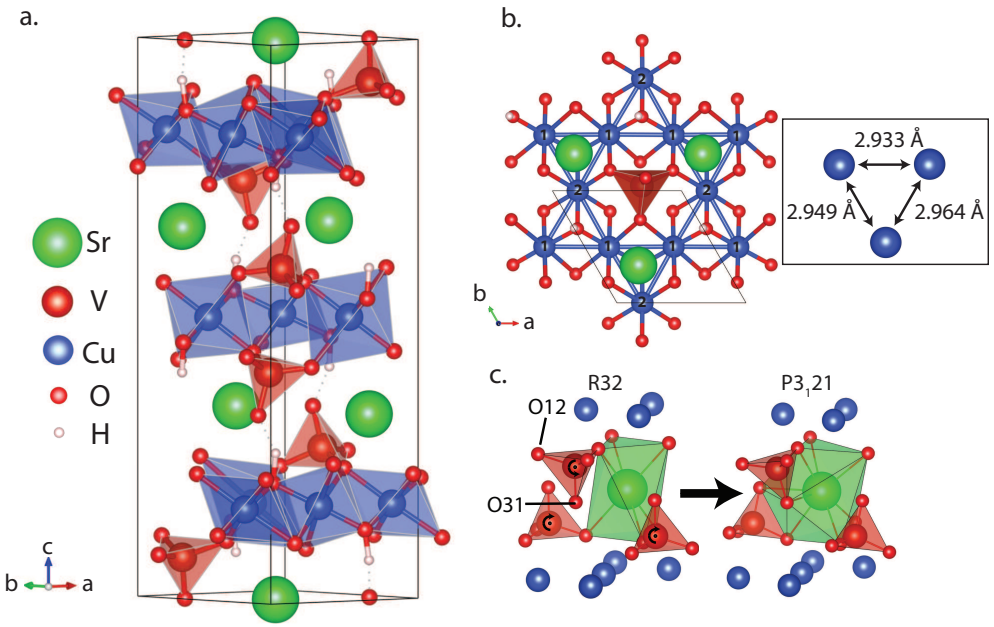

Figure 5.8: a. The refined crystal structure of 'Sr-vesignieite' with lattice parameters $a = b = 5.89577(2)$ Å and $c = 20.41260(10)$ Å and $\alpha = \beta = 90\,°$, $\gamma = 120\,°$. The kagome planes of CuO_6 are separated by VO_4 tetrahedra and Sr^{2+} ions. **b.** A star unit of the kagome plane. The symmetry of the $P3_121$ space group means the kagome structure is made from chains of Cu1 sites linked by Cu2 sites, whilst three unequal Cu–Cu bond distances build the triangles of the kagome lattice. **c.** Compared to a higher symmetry rhombohedral description, the VO_4 tetrahedra have rotated towards the Sr^{2+} ion bringing into an 8-coordination geometry. This raises the bond valency of the Sr^{2+} site towards the idealised value of 2.

Between the kagome planes, the 'Sr-vesignieite' structure contains some further interesting features. A useful comparison here is a higher symmetry, rhombohedral description. Taking the $R\bar{3}m$ structure of vesignieite and finding the chain of maximal subgroups to 'Sr-vesignieite' gives the space group $R32$ as the closest rhombohedral space group to $P3_121$. Figure 5.8c shows that, relative to the $R32$ structure, the VO_4 tetrahedra undergo a concerted tilt which brings the Sr^{2+} ion into an 8-coordinate geometry. In 8-coordinate geometry the Sr^{2+} site has a bond valence of 1.43 (28 % deviation from 2), an 11 % increase from the rhombohedral structure (bond valence = 1.21). Such a geometry is not possible in $R32$ or $C12/m1$ as the symmetry of the Sr^{2+} site is 32 and $.2/m.$ respectively, rather than $.2.$ in $P3_121$ (Using the notation from the International Tables of Crystallography [24]).

As in many Cu^{2+} containing materials, the CuO_6 octahedra in 'Sr-vesignieite' are distorted from O_h geometry due to the Jahn-Teller effect. This occurs due to unequal occupation of the Cu^{2+} d-orbitals with e_g symmetry and, in the majority of experimental cases, causes an elongation of the octahedral bonds along a single axis [25]. Interestingly, the two crystallographically unique CuO_6 octahedra in 'Sr-vesignieite' adopt axially compressed and rhombically distorted geometries, the latter meaning an octahedron with 2 short, 2 intermediate and 2 long bonds. Such Cu^{2+} octahedral geometries are often misinterpreted as due to static Jahn-Teller distortions, but as we will see this is not always the case.

In the literature, axially compressed and rhombically distorted Cu^{2+} octahedral geometries often indicate a dynamic Jahn-Teller effect and a degeneracy of the d-orbitals [25]. As these orbitals host the lone electrons and mediate the superexchange, degeneracy and fluctuations has important consequences on the magnetic properties. Kugel' and Khomskii discussed this in depth and introduced a spin-orbital superexchange (KK) model to describe the combination of the Jahn-Teller effect and magnetism [26]. Materials with exotic properties arising from the interplay of orbital and spin degrees of freedom have recently garnered much interest, such as proposed quantum spin-orbital liquid states in $FeSc_2S_4$ and $Ba_3CuSb_2O_9$ [27, 28]. Including orbital frustration, and the inherent spatial dependence associated with the orbital component, in a QSL ground state is predicted to have significant consequences on their properties, therefore these materials are of great interest theoretically [29, 30]. Unfortunately, no experimental examples currently exist. The next chapter discusses the dynamic Jahn-Teller effects in 'Sr-vesignieite' and how this material provides a unique example through which to study simultaneous spin and orbital frustration.

5.5 Investigation of the dynamic Jahn-Teller effect

To determine the presence of dynamic Jahn-Teller effects in 'Sr-vesignieite' further measurements were taken and are discussed in this section. Although diffraction techniques are not ideal for observing dynamic crystallographic features, by collecting data at a range of temperatures dynamic processes can be revealed through abnormal temperature dependencies. Before discussing the results it is useful to discuss the origins of the dynamic Jahn-Teller effect and its manifestation in materials.

5.5.1 The dynamic Jahn-Teller effect and its manifestation in materials

The Jahn-Teller (JT) effect can occur in any non-linear molecule or complex with a spatially degenerate electronic ground state. The effect is common amongst the transition metals and is most pronounced in octahedral complexes when an uneven number of electrons occupy the d-orbitals with e_g symmetry, such as Cu^{2+} d^9 complexes, as these orbitals point directly at the ligands. The degeneracy of electronic ground states is relieved by a geometric distortion of the local coordination, which couples to the energy of the system and lowers it. In crystalline materials, this often causes a structural phase transition and a long-range orbital ordering.

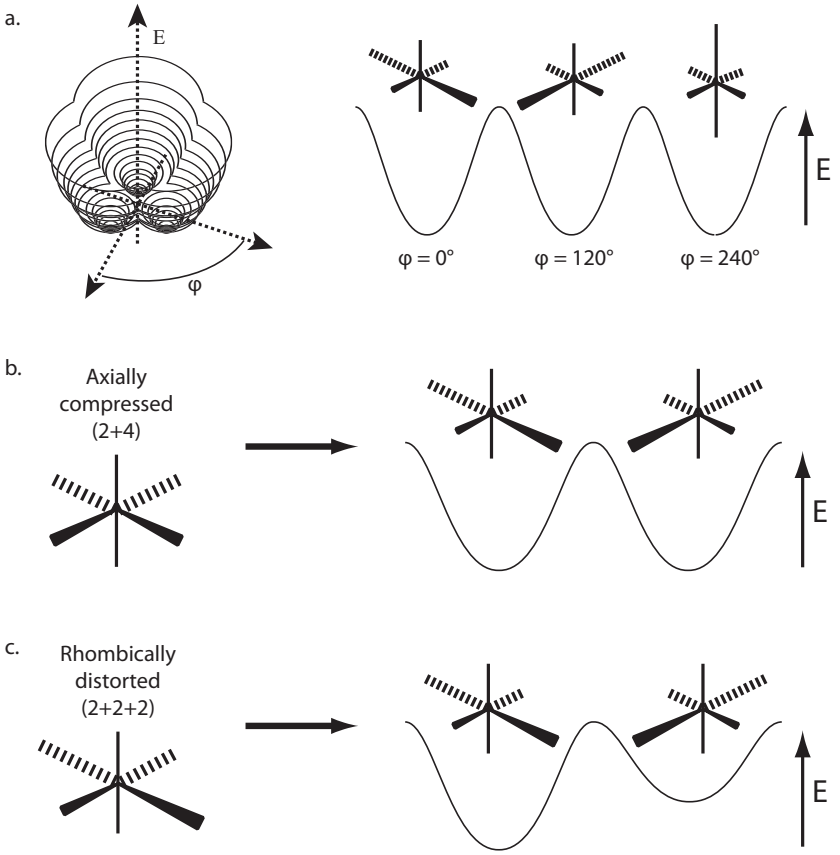

Figure 5.9: **a.** The Mexican hat potential energy surface for a Jahn-Teller distorted octahedron. The three energy minima correspond to Jahn-Teller distortions along the three crystallographic directions. If the energy barrier between them is lower than the thermal energy all three will be simultaneously occupied and the Jahn-Teller effect is *dynamic*. **b. - c.** In the majority of Cu^{2+} complexes the Jahn-Teller effect causes axial elongation due to preferential filling of the d_{z^2} orbital. Therefore, an axially compressed octahedron observed *via.* diffraction often indicates a dynamic fluctuation between two axially elongated geometries due to long-range averaging (**b.**). When the two geometries lie at different energies (**c.**) the average structure is a rhombically distorted octahedron with 2 long, 2 medium and 2 short bonds.

In cubic symmetry, three energetically equivalent Jahn-Teller distorted octahedral geometries exist and these sit in the minima of the so-called Mexican Hat potential energy surface (Figure 5.9a) [26]. If thermal energy is sufficiently high to pass the energetic barriers between these minima, all three

distorted geometries will be populated and the material is said to possess a *dynamic* Jahn-Teller effect. Importantly, using long-range diffraction techniques, such a scenario is observed as a perfect octahedral coordination due to structural averaging.

In the majority of materials, the electronic states of the Jahn-Teller ion couple with the crystal structure and cause the potential energy surface to warp. This can, for instance, lead to scenarios where (i) two lower energy wells lie at the same energy or (ii) two lower energy wells lie at similar energies. In the case of (i) and where an axially elongated distortion occurs at each minima, the structure observed *via.* diffraction at sufficiently high thermal energy would be of an axially *compressed* octahedron (Figure 5.9b). Whereas in (ii), a diffraction experiment would see a rhombically distorted (2-2-2) octahedron (Figure 5.9c).

In order to understand the Jahn-Teller effect in 'Sr-vesignieite' it is important to briefly look at how it manifests in other materials. In the vast majority of experimental cases it has been shown that for the Cu^{2+} d^9 ion the JT effect causes the lone electron to preferentially occupy the d_{z^2} orbital [31]. As the d_{z^2} orbital forms a σ^* antibonding MO with the ligands, partial occupation of it lengthens the bond between them resulting in an axially *elongated* octahedron. Therefore, an axially *compressed* octahedron observed *via.* diffraction techniques is commonly a time average between two *elongated* octahedra and this has proven to be true for the the majority of cases [25, 31].

The Cu–O bond lengths of the 'Sr-vesignieite' structure refined from the synchrotron data at 300 K are shown in Figure 5.10. It is clear that the $Cu1O_6$ octahedra adopts a rhombically distorted geometry, whilst $Cu2O_6$ is axially compressed. Both of these octahedral shapes indicate that they are dynamically fluctuating between two axially elongated geometries. A dynamic Jahn-Teller effect has two important consequences on the magnetic properties of the material. Firstly, whether each CuO_6 octahedra is elongated or compressed defines whether the lone electron that mediates the superexchange occupies the $d_{x^2-y^2}$ or d_{z^2} orbital. Secondly, concomitant spin and orbital frustration is predicted to have significant ramifications on the quantum ground state of QSLs. To determine the legitimacy of this model, T-dependent X-ray diffraction experiments were performed.

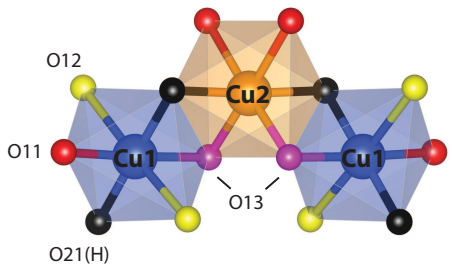

	Bond lengths (Å)	
	Cu1	Cu2
O11	2.049(8)	2.236(7)
O12	2.468(7) 2.521(7)	—
O13	2.091(8)	2.172(9)
O21(H)	1.882(5) 1.926(7)	1.928(5)

Figure 5.10: The local coordination of the two Cu^{2+} sites in 'Sr-vesignieite' and the associated Cu–O bond lengths at 300 K. The Cu2 site forms a $Cu2O_6$ octahedra that is axially compressed. The Cu1 site also forms a $Cu1O_6$ octahedra but is rhombically distorted. Both of these octahedral geometries suggest that the Cu sites are undergoing dynamical Jahn-Teller fluctuations.

5.5.2 Temperature dependent X-ray diffraction

As Bragg diffraction is not a local technique, the structure observed is averaged over large length scales and, therefore, dynamical, local features are hard to detect. One common method of confirming a dynamic Jahn-Teller effect with crystallographic techniques is to measure site anisotropic displacements. For instance, in $KCu_3As_2O_7(OH)_3$ the displacement parameters of the Cu ligands are large and aligned consistent with a stretching of the Cu–ligand bond [32]. However, X-ray powder diffraction does not often give accurate displacement parameters, particularly for oxygen sites as the O^{2-} form factor is small.

Temperature dependent X-ray diffraction is an alternative technique used to determine dynamic Jahn-Teller effects. The Cu–O bond lengths in a CuO_6 octahedra would normally be expected to decrease with temperature and all have a similar temperature dependence. However, in the presence of a dynamic Jahn-Teller effect certain bonds would be expected to lengthen with decreasing temperature due to increased population of the axially elongated structure. This section details temperature dependent lab based X-ray diffraction used to determine the temperature dependence of the Cu–O bond lengths in 'Sr-vesignieite'.

Measurements were performed on a STOE Stadi-P diffractometer. This diffractometer is aligned in Debye-Scherrer geometry and is equipped with a Cu k_α radiation source and a primary Ge(111) monochromator to filter out Cu $k_{\alpha 2}$ radiation. The detector is a solid state Dectris Mythen 1K as used on the high-resolution synchrotron beamline I11 at the Diamond Light Source, UK. The temperature stage used was an Oxford Instruments CryoJetHT. In order to minimise absorption so that no corrections were required, measurements were performed in a 0.2 mm diameter borosilicate capillary ($\mu R \sim 0.79$ for $SrCu_3V_2O_8(OH)_2$ with 1 g cc^{-1} packing density). At several temperatures between 100 and 400 K, spectra were collected between 10 and 100 ° 2θ ($8.7 > d > 0.97$ Å) for between 6 and 12 hours. All fitting procedures were performed using the TOPAS software package [18].

Upon cooling, a change in behaviour in the c/a lattice parameter ratio occurs below $T_{\mathrm{JT}} \approx 230$ K (Figure 5.11a). The temperature dependence of the lattice parameters is a good indication of a Jahn-Teller transition and is often accompanied by a structural symmetry change [33]. No extra peaks or peak splittings appear in the spectra below T_{JT} and refinements using the $P3_1$ space group, which has the same powder averaged *hkl* conditions, did not improve the fit but destabilised the oxygen positions. However, not all Jahn-Teller transitions induce a global symmetry change, for instance in $LaMnO_3$ a similar Jahn-Teller transition occurs with no change in average crystallographic symmetry [34].

Further evidence of a Jahn-Teller transition on the Cu1 site is seen in the temperature dependence of the Cu1–O12 bond length: a sudden increase in this bond length accompanies the change in behaviour of the c/a ratio. This increases the rhombic distortion of the $Cu1O_6$ octahedra and is accommodated within the structure by a simultaneous rotation of the VO_4 rotation. The VO_4 rotation can be parameterised by the position of the apical O31 oxygen within the plane of the Sr^{2+} ions, as shown in Figure 5.11b. At T_{JT}, the percentage bond length change of Sr–O31, shown in Figure 5.11c, indicates an abrupt shift of the O31 consistent with a rotation of the VO_4. The cause of this transition is compatible with a static,

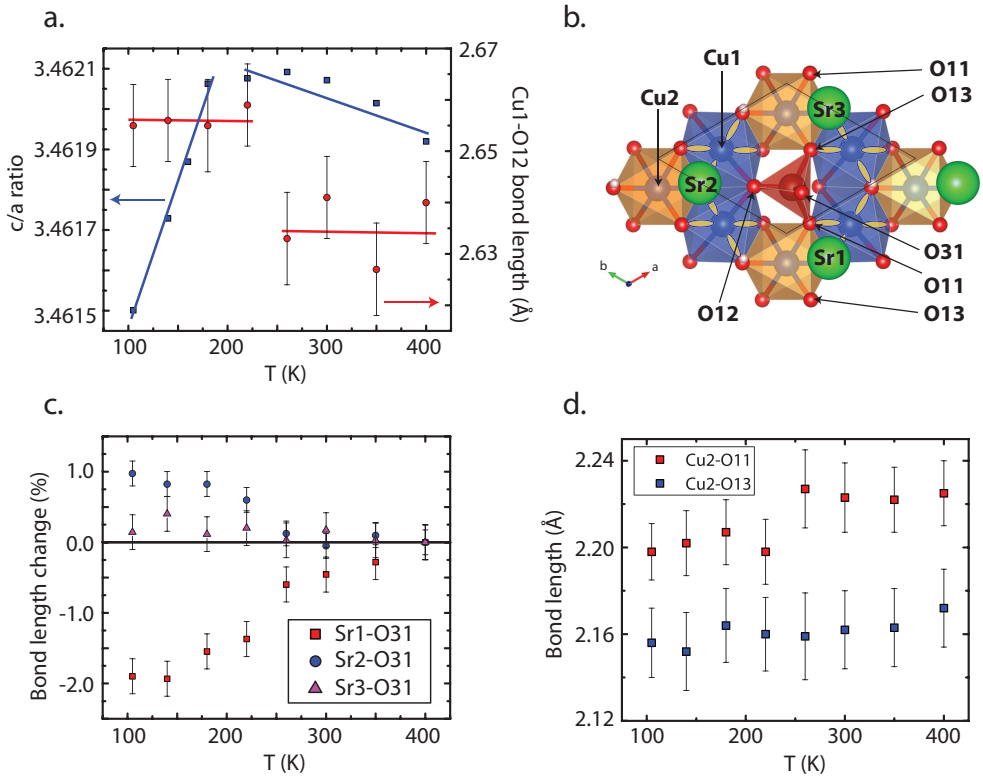

Figure 5.11: **a.** The temperature dependence of the c/a lattice parameter ratio and Cu1–O12 bond length obtained from Rietveld refinement of X-ray diffraction data. A change in behaviour of c/a at $T_{\mathrm{JT}} \approx 230\,\mathrm{K}$ coincides with an abrupt elongation of the Cu1–O12 bond, signalling a cooperative JT distortion on the Cu1 sites. **b.** A view of a kagome plane along the [001] direction. At T_{JT} the O31 atom shifts towards Sr1, as shown in **c**, due to rotation of the VO_4 caused by the cooperative JT. The JT distortion aligns the Cu1 $d_{x^2-y^2}$ as shown. **d.** Temperature dependence of the Cu2–O11 and –O13 bonds. A transition to an axially elongated or rhombically distorted $Cu2O_6$ can not be inferred from this.

co-operative JT distortion of the $Cu1O_6$ chains along the [110] direction. Such a transition aligns the Cu1 $d_{x^2-y^2}$ orbitals in an antiferro-orbital arrangement as indicated in Figure 5.11b.

The Cu2 site does not show any similar transition to a static JT state in this temperature range. The four longer Cu2–O11 and Cu2–O13 bonds instead shorten with decreasing temperature (Figure 5.11d), which is characteristic of the VO_4 tilting. A static Jahn-Teller distortion requires elongation of one of these bonds concomitant with a lowering of the global $P3_121$ symmetry, *i.e.* to $P3_1$, and local Cu2 site symmetry. As stated earlier, refinements in the lower $P3_1$ symmetry destabilised the oxygen positions, however by duplicating the O11 and O13 sites, setting each to half occupancy and allowing their positions to refine freely effectively mimics this symmetry lowering of the $Cu2O_6$ octahedra. This does not improve the quality of the fit nor show any bond elongation, indicating that the Jahn-Teller effect remains dynamic on the Cu2 site down to $T = 100\,\mathrm{K}$.

5.6 Magnetic characterisation

The $P3_121$ structure of 'Sr-vesignieite' does not retain the 3-fold symmetry of the kagome triangles, however the distortion of $\sim 1\,\%$ is metrically tiny and the material is expected to host competing interactions as in volborthite and vesignieite. This section details the magnetic properties of 'Sr-vesignieite' using a SQUID magnetometer and compares these with vesignieite. It is useful to first briefly overview the magnetic properties of vesignieite.

5.6.1 A review of the magnetic properties of vesignieite

The magnetic properties of vesignieite are heavily dependent on sample quality and preparation techniques. Initial samples made *via.* hydrothermal synthesis by Hiroi *et al.* are characterised by Curie-Weiss behaviour down to $T \sim 50\,\mathrm{K}$ and no long-range order down to $T = 2\,\mathrm{K}$ [16]. In the same study, they fitted the high-T region of χ^{-1} to get a Weiss temperature $\Theta_\mathrm{W} = -77\,\mathrm{K}$ that indicates strong antiferromagnetic interactions, but long-range order is heavily suppressed well below this temperature. At $T = 20\,\mathrm{K}$ a small hump occurs in χ followed by a sharp increase below $T = 10\,\mathrm{K}$, supposedly due to paramagnetic-like impurity spins (Figure 5.12a). From the similarities between the superexchange paths of vesignieite ($\angle \mathrm{Cu-O-Cu} = 101.4\,^\circ$ [19]) and 'Sr-vesignieite' ($100.1 < \angle \mathrm{Cu-O-Cu} = 102.9\,^\circ$), one would expect Θ_W of the latter to be roughly the same magnitude.

Higher quality samples of vesignieite prepared *via.* a reflux reaction by Colman *et al.* reveal a magnetic transition at $T = 9\,\mathrm{K}$ that coincides with a ZFC-FC splitting in χ, as shown in Figure 5.12b [13]. Local probe techniques used on these samples, such as μSR and NMR, reveal a heterogeneous ground state of static and dynamic spins that develops below this transition [13, 35]. Two separate studies further improved sample quality by using high-temperature hydrothermal annealing and extended hydrothermal synthesis, and in both the magnetic transition at $T = 9\,\mathrm{K}$ develops into a sharp peak that resembles a transition to a long-range antiferromagnetic state (Figure 5.12c) [19, 36]. This transition is surprisingly high given the negligible distortion of the kagome lattice, $\sim 0.07\,\%$, however ESR measurements show a significant in-plane Dzyaloshinskii-Moriya (DM) interaction, D_p, that is argued to suppress quantum fluctuations and induce Neél order (Figure 5.12d) [37]. Given that the magnitude and direction of the DM vector is sensitive to the local symmetry of the superexchange path, D_p could be expected to be different in 'Sr-vesignieite' due to the change in symmetry compared to its Ba-analogue.

5.6.2 Magnetic susceptibility of 'Sr-vesignieite'

Measuring the magnetic susceptibility of 'Sr-vesignieite' is the first step to understanding its magnetic properties. The subtle structural changes due to the different symmetry, compared to vesignieite, makes 'Sr-vesignieite' an interesting $S = \frac{1}{2}$ KAFM in its own right but also provides useful comparisons with its Ba-analogue.

Measurements were taken on a Quantum Design MPMS-7 DC-SQUID magnetometer with 58.20 mg of the same sample used for the structural analysis described above. Zero-field cooled (ZFC) and field-cooled (FC) susceptibility measurements were taken in a 100 Oe field between $2 < T(\mathrm{K}) < 300$ starting at base temperature and are shown in Figure 5.13a. The data reveals a relatively sharp tran-

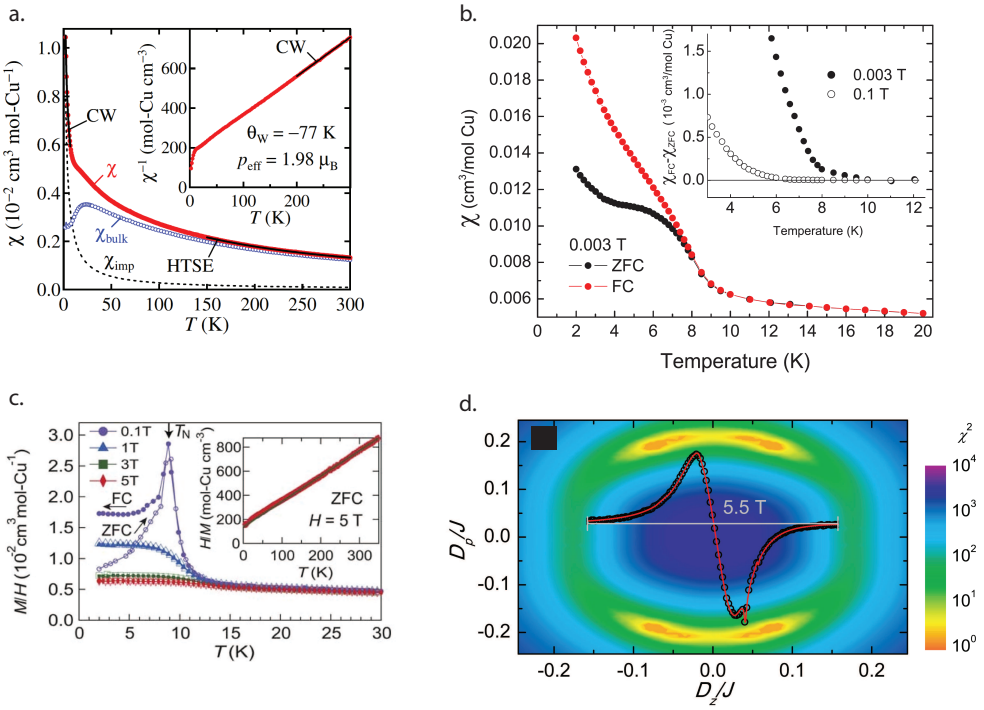

Figure 5.12: **a. - c.** Magnetic susceptibility measurements collected on vesignieite samples of varying quality. **a.** Data collected from a sample of poor quality prepared under hydrothermal conditions. No clear, long-range transition is observed at low temperature but a broad hump occurs at $T \sim 20\,\mathrm{K}$ [16]. **b.** Data collected from a sample with improved quality prepared *via.* a reflux reaction. A transition at $T = 9\,\mathrm{K}$ is much clearer and is accompanied by a ZFC-FC splitting [13]. **c.** High-quality samples prepared using an extended hydrothermal synthesis. A clear transition is seen that indicates the onset of long-range order [19]. **d.** Fits to EPR data collected on a poor quality vesignieite sample reveal a significant in-plane DM interaction that was proposed to induce classical Néel order [37].

sition $T_\mathrm{N} = 11\,\mathrm{K}$ with an associated separation of ZFC and FC data. This data is remarkably similar to high-quality samples of vesignieite (5.12c). Re-plotting the data as χ^{-1} *vs.* T and fitting the the temeprature range $150 < T < 300\,\mathrm{K}$ to a Curie-Weiss law gives a Weiss temperature, $\Theta_\mathrm{W} = -100 \pm 5\,\mathrm{K}$, demonstrating strong antiferromagnetic interactions and showing the magnetic transition is heavily suppressed with respect to this mean field (Figure 5.13b). As expected, Θ_W of 'Sr-vesignieite' is of a similar magnitude to that of vesignieite, although 20 K more negative, because of the similar superexchange bond angles: 100.1 °, 101.5 ° and 102.9 ° in 'Sr-vesignieite' and between 101.4 and 101.8 ° in vesignieite, depending on the study [15, 19].

A plot of χT *vs.* T is shown in Figure 5.13c along with the same data collected on a poor quality sample of vesignieite prepared *via.* a reflux reaction. The behaviour between the two samples is remarkably similar down to $T = 11\,\mathrm{K}$ at which point χT of 'Sr-vesignieite' suddenly increases whilst that of vesignieite is quite featureless. Below the transition in 'Sr-vesignieite' χT peaks at $T \sim 9\,\mathrm{K}$ and then decreases rapidly indicating both ferromagnetic and antiferromagnetic interactions are present. Whilst χT behaves very differently between the two materials at low T, the derivative of χT with respect to T,

as shown in the inset of Figure 5.13c, reveals the similarities at the transition although evidently this is much stronger in 'Sr-vesignieite'.

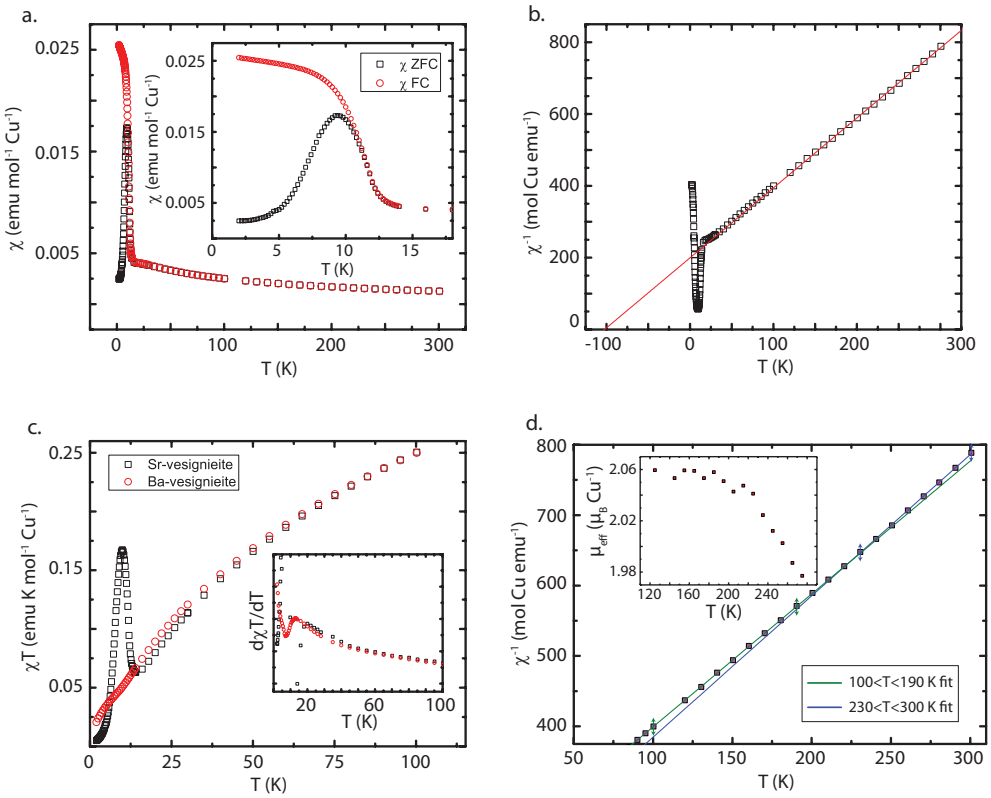

Figure 5.13: **a.** A plot of ZFC and FC χ *vs.* T in a measuring field of 100 Oe. The inset highlights the transition at $T_N = 11$ K and concomitant ZFC-FC splitting. **b.** A plot of χ^{-1} *vs.* T and linear fit to the $150 \leq T \leq 300$ K region giving $\Theta_W = -100 \pm 5$ K demonstrates strong antiferromagnetic interactions. **c.** A comparison of χT *vs.* T between 'Sr-vesignieite' and vesignieite. The temperature dependence of χT for the two materials appears to behave quite differently at low T, however the derivative of χT shows that they actually have very similar behaviour although the transition is offset by ~ 5 K. **d.** The high T region of χ^{-1} *vs.* T changes gradient slightly at $T \sim 210$ K, and fits either side of the transition give different Θ_W and C values as explained in the text. **inset.** Fits of 50 K regions between 100 and 300 K show μ_{eff} to increase with decreasing temperature and plateau at $T \sim 210$ K, coinciding with the static Jahn-Teller transition on the Cu1 site.

A closer look at χ^{-1} *vs.* T at high temperature reveals an unusual temperature dependence, shown in Figure 5.13d. At $T \sim 210$ K a slight change in gradient occurs and fits to the linear regions $100 < T < 190$ K and $230 < T < 300$ K yield different Weiss temperatures and Curie constants: $\Theta_W = -92$ K and $C = 0.498$ emu K mol^{-1} at high temperature and $\Theta_W = -112$ K and $C = 0.530$ emu K mol^{-1} in the low temperature region. Using the same fitting procedure for several 50 K regions between $T = 100$ and 300 K, the calculated effective moment, μ_{eff}, increases upon cooling before plateauing at $\sim 2.05\,\mu_B$ Cu^{-1} below $T \sim 210$ K (Figure 5.13d inset). For a $S = \frac{1}{2}$ ion the expected spin-only moment is $\mu_{eff} = 2g\sqrt{S(S+1)}\mu_B = 1.73\,\mu_B$, but values larger than this are seen in other Cu^{2+} containing minerals due to orbital contributions. Furthermore, the increase in μ_{eff} evidences an increased anisotropy

of the Cu^{2+} geometry and the temperature at which it plateaus coincides with the cooperative Jahn-Teller transition of the Cu1 site revealed from the X-ray diffraction data.

5.7 Discussion

Degeneracy of the e_{g} orbital doublet in octahedral Cu^{2+} ions is always lifted in any real system due to the Jahn-Teller effect, which causes either an axial elongation or compression of the local geometry. This local lattice distortion affects the orbital-orbital interactions and often leads to long-range orbital order. It is possible, however, that degeneracies still exist globally so that no long-range orbital ordering occurs. In such a case the orbitals are frustrated and possess a degree of freedom that can couple with the spins, which has important consequences on the superexchange. Kugel and Khomskii [26] developed a spin-orbital superexchange (KK) model to describe such effects in magnetic Jahn-Teller systems. Moreover, the frustration can be enhanced on geometrically frustrated lattices, such as triangular and kagome, and when both spin and orbital components are frustrated theory has predicted exotic ground states such as quantum spin-orbital liquids [30].

Experimentally, very few examples exist that display coexisting spin and orbital frustration on a geometrically frustrated lattice. The most studied example is $LiNiO_2$ where the triangular Ni^{3+} lattice enters neither magnetic nor Jahn-Teller long-range order down to the lowest temperatures measured [38]. However, recent research suggests the spin and orbital components are effectively decoupled in this material due to the 90° Ni–O–Ni bond angle and a spin-orbital liquid state does not exist [39].

There are no examples in the literature of spin and orbital frustration hosted on the kagome lattice. In the following section, I propose that 'Sr-vesignieite' provides the first example of such a material and this section discusses how the orbital frustration materialises. Furthermore, the findings in this chapter provide strong evidence that orbital frustration should be included in discussions of several other $S = \frac{1}{2}$ KAFMs.

5.7.1 Orbital and spin frustration in 'Sr-vesignieite'

As shown and discussed earlier in this chapter in Section 5.4, the two Cu sites in 'Sr-vesignieite' have different local geometries that reveal vital information about their electronic ground state. At room temperature, X-ray powder diffraction shows the Cu1 site to adopt a rhombically distorted CuO_6 octahedron, whilst the $Cu2O_6$ is axially compressed. These geometries suggest that both are dynamically fluctuating between two Jahn-Teller distorted configurations, and that the lone e_{g} electron occupies the $d_{x^2-y^2}$ orbital. As the temperature is lowered, the Cu1 site appears to enter a static Jahn-Teller state, however even at 100 K the Cu2 site remains dynamically distorted.

The orbital diagram of the Cu^{2+} sites in 'Sr-vesignieite' below $T_{\mathrm{JT}} \sim 210\,\mathrm{K}$ is shown in Figure 5.14a. The Cu1 sites form chains along the [110] direction and their $d_{x^2-y^2}$ orbitals are antiferro-orbitally arranged along these chains. The Cu2 sites link these chains and form a triangular superlattice with their $d_{x^2-y^2}$ orbitals fluctuating between two configurations. This situation is reminiscent of the spin and orbital frustration on the triangular Ni^{3+} lattice in the material $LiNiO_2$ discussed earlier. In this material, the 90 ° Ni–O–Ni superexchange path causes the spin coupling, J_{S}, and spin-orbital coupling,

J_{ST}, to be far weaker than the orbital coupling, J_T [39]. Consequently, in 90 °exchange systems spins and orbitals cannot strongly influence eachother and a spin-orbital liquid cannot exist. Conversely, in materials with 180 °exchange paths, such as perovskites, J_S, J_T and J_{ST} are all of similar magnitude and able to strongly couple with each other.

a.

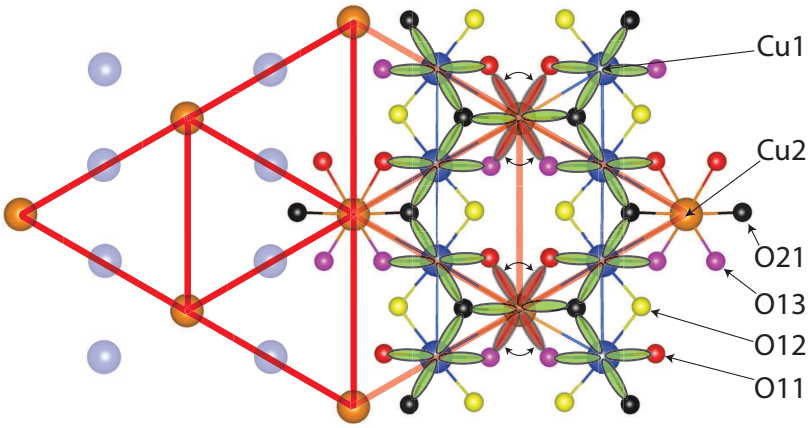

b.

Cu1-Cu1	Angle	Cu1-Cu2	Angle
∠Cu1-O12-Cu1	72.1(1)˚	∠Cu1-O11-Cu2	85.6(2)˚
∠Cu1-O21-Cu1	104.4(2)˚	∠Cu1-O13-Cu2	87.8(2)˚
		∠Cu1-O21-Cu2	103.6(2)˚ 100.3(2)˚

Figure 5.14: **a.** Diagram of the Cu^{2+} $d_{x^2-y^2}$ orbitals below the Jahn-Teller transition $T_{JT} \sim 210\,K$. The Cu1 sites form an antiferro-orbitally ordered state in chains along the [110] direction. The Cu2 sites remain dynamically distorted and decorate the kagome lattice with a triangular superlattice. **b.** The ∠Cu–O–Cu superexchange bond angles. The paths involving the O21(H) hydroxide group is expected to favour antiferromagnetic exchange but also involve spin-orbital exchange coupling.

The ∠Cu–O–Cu bond angles of 'Sr-vesignieite', *i.e.* the possible superexchange paths, are shown in Figure 5.14b. These can be classified in two groups: (i) paths involving the μ_3-hydroxide group, O21(H), which coordinates the three Cu^{2+} of each kagome triangle with bond angles $100 < \angle$Cu–O21(H)–Cu$< 105\,°$(ii) paths involving the μ_4-O11, -O12 and -O13 oxygens, which coordinate with two Cu^{2+} in addition to the V^{5+} and Sr^{2+} ions with bond angles ∠Cu–O–Cu $< 90\,°$. These arrangements have two important consequences. Firstly, multiple superexchange paths between each Cu site with various bond angles between 72 and 105 ° are possible, which could favour either ferromagnetic or antiferromagnetic exchange according to the Goodenough-Kanamori rules and *via.* comparison with other Cu^{2+} compounds [40, 41]. It also opens the possibility of further-neighbour exchange across

the kagome hexagon *via.* the VO_4 tetrahedra, which share the O11, O12, O13 sites with the CuO_6. Secondly, the Cu–O21(H)–Cu path aligns with the partially filled $d_{x^2-y^2}$ in all cases and has a bond angle of between 100 and 105 °, therefore coupling between spin and orbital superexchange is expected to be strong along this path.

5.7.2 Evidence for dynamic Jahn-Teller effects in related kagome magnets

As 'Sr-vesignieite' has several crystallographic similarities with other $S = \frac{1}{2}$ KAFMs, it is natural to explore whether orbital frustration should be discussed in relation to these other materials. A thorough review of Jahn-Teller distortions in several Cu^{2+} containing minerals predicted dynamic Jahn-Teller effects in the closely related kagome-based minerals volborthite ($Cu_3V_2O_7(OH)_2.2H_2O$), bayldonite ($PbCu_3As_2O_8(OH)_2$) and $KCu_3As_2O_7(OH)_3$ [25]. All three contain rhombically distorted CuO_6 octahedra and have anisotropic displacements of the oxygens consistent with dynamic fluctuations. Furthermore, volborthite and $KCu_3As_2O_7(OH)_3$ also contain axially compressed octahedra and again the anisotropic displacements are consistent with dynamic fluctuations. Conversely, one Cu site in bayldonite adopts an axially elongated octahedra and the anisotropic displacements of these oxygens are small and roughly spherical, suggesting they are static.

Reexamination of recent results on synthetic samples of both volborthite, vesignieite and $KCu_3As_2O_7(OH)_3$ provides further evidence of dynamic Jahn-Teller fluctuations in this group of $S = \frac{1}{2}$ KAFMs. In single crystals of volborthite, a first-order structural transition occurs at $T \sim 310\,\mathrm{K}$ that causes a sudden elongation of a Cu–O bond that transforms the CuO_6 octahedra from an axially compressed to elongated geometry, shown in Figure 5.15a [42]. This is argued as a unique 'orbital switching' transition, however it is more easily understood as a transition to a static Jahn-Teller state.

In synthetic single crystals of vesignieite the single Cu site forms an axially compressed CuO_6 octahedron (Figure 5.15b) [19]. The large anisotropic parameters on the four equatorial oxygens of the CuO_6 indicate that they are unstable, whilst the two axial oxygens have small and roughly spherical displacements. As in volborthite and bayldonite [25], this indicates a dynamic Jahn-Teller effect between two axially elongated configurations aligned along either pair of opposite equatorial oxygens. In $KCu_3As_2O_7(OH)_3$, the situation is remarkably similar to 'Sr-vesignieite' whereby chains of Cu^{2+} are statically Jahn-Teller distorted whilst another Cu^{2+} site joins the chains and is dynamically distorted (Figure 5.15c) [43].

5.8 Future work

The synthesis of pure, protonated 'Sr-vesignieite', $SrCu_3V_2O_8(OH)_2$, is established in this chapter as well as structural and bulk magnetic characterisation. Expanding on this work, it would be extremely useful to perform heat capacity measurements to characterise both the high-temperature Jahn-Teller and the magnetic transition. Both should produce anomalies in C_p that would give information on the nature of the transition, *i.e.* whether it is first- or second-order, as well as reveal the entropy change at each.

Due to the strong spin-lattice coupling of the Jahn-Teller effect, magnetic transitions often induce JT order. Therefore, high-resolution X-ray or synchrotron diffraction below T_N is required to determine

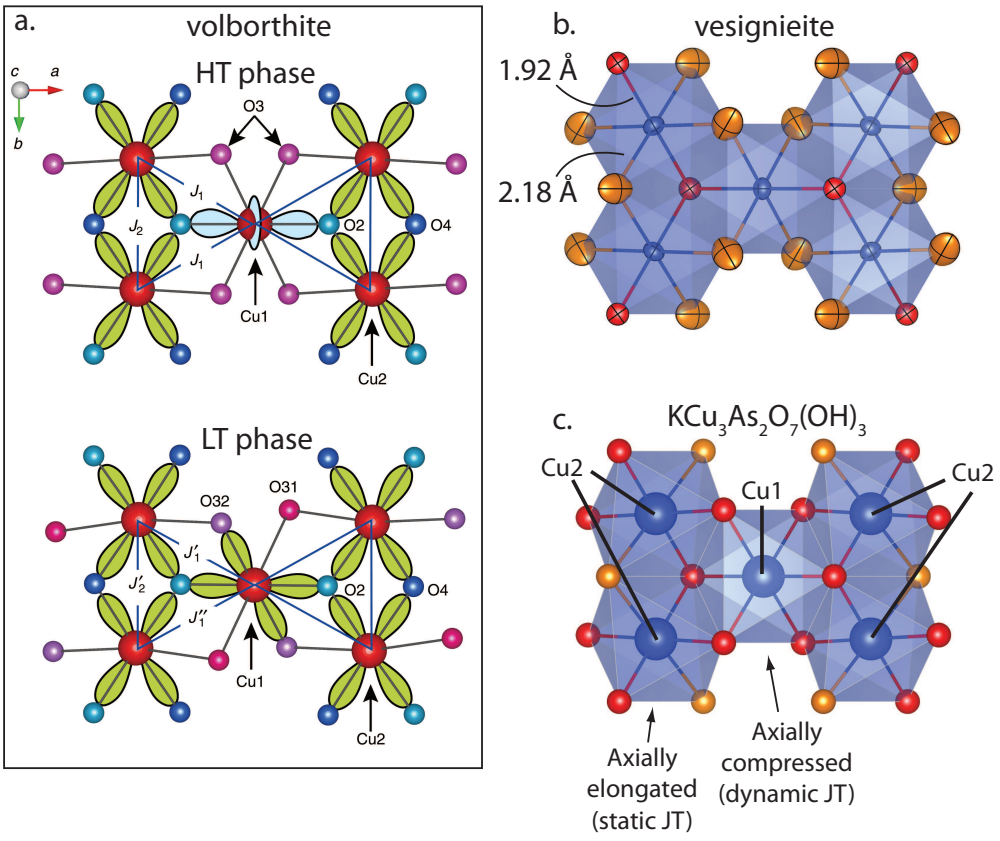

Figure 5.15: a. High temperature and low temperature structural phases of volborthite single crystals proposed by Yoshida *et al.* [42]. The transition between the states is argued to be a unique 'orbital switching' transition, however it is easily understood as an orbital ordering on the Cu1 site. **b.** Crystal structure of a single crystal vesignieite sample [19]. The large anisotropic displacements of the equatorial oxygens on the compressed CuO_6 suggest they are dynamic on the time scale of the data, whereas the axial oxygens have small, roughly spherical displacements and are relatively static. These anisotropic displacements are consistent with dynamic Jahn-Teller fluctuations on all Cu sites. **c.** $KCu_3As_2O_7(OH)_3$ has a similar distribution of distorted CuO_6 as in 'Sr-vesignieite': chains of cooperatively JT distorted Cu2 sites are joined by a triangular superlattice of dynamic JT Cu1 sites [43].

if the JT effect on the Cu2 site orders at low-T. A combined neutron diffraction study would complement this experiment by (i) improving the quality of the refined oxygen positions, which are crucial in characterising the JT effect and (ii) revealing any magnetic Bragg peaks below, thus allowing refinement of the magnetic structure. The latter experiment is challenging due to the difficulties in synthesising a scaled-up deuterated sample: preliminary attempts at doing this resulted in large impurity phases that were difficult to minimise or remove.

Knowledge of the magnetic structure makes inelastic neutron scattering a particularly important tool for determining the magnetic exchange interactions and helping us understand the physics of $S = \frac{1}{2}$ magnets and perturbations, such as further-neighbour and DM interactions [44, 45, 46, 47].

Finally, the synthesis of 'Sr-vesignieite' opens up possibilities of further modifications in the vesignieite family. Limited success has been achieved with the synthesis of 'Pb-vesignieite', but producing

pure samples of this material is very challenging considering the stability of mottramite, $PbCuVO_4(OH)$. There is also opportunity for substituting on the V^{5+} site, which seems particularly feasible given the natural occurrence of bayldonite, $PbCu_3As_2O_8(OH)_2$, and the recent synthesis of $KCu_3As_2O_7(OH)_3$ [43].

5.9 Conclusions

This chapter presents the synthesis and characterisation of a new $S = \frac{1}{2}$ KAFM 'Sr-vesignieite', the Sr^{2+} analogue of the well studied frustrated magnet vesignieite. Synchrotron and X-ray diffraction experiments show this new material crystallises with a $P3_121$ which is quite different to any other models in this family. Structural refinements and comparisons with other materials reveal that the nuclear structure consists of a kagome lattice built from two inequivalent Cu^{2+} sites, one of which enters a static Jahn-Teller state at $T_{\mathrm{JT}} \sim 230\,\mathrm{K}$ whilst the other remains dynamically distorted to 100 K and decorates the kagome network with a triangular sublattice. The resulting ordering of the superexchange mediating orbitals is very different to those proposed for other $S = \frac{1}{2}$ KAFMs and forces a revaluation of that previously proposed for vesignieite, as is discussed in the next chapter.

Measurements of the magnetic susceptibility, χ, show 'Sr-vesignieite' is magnetically frustrated with an ordering transition suppressed to $T_{\mathrm{N}} \sim 11\,\mathrm{K}$ despite strong antiferromagnetic interactions, $\theta_{\mathrm{W}} \sim -100\,\mathrm{K}$. To corroborate the structural data, evidence of the Jahn-Teller transition is seen in the magnetic data through an enhancement of the effective moment, μ_{eff}, as the temperature is lowered towards T_{JT}. However, as the other Cu site remains dynamic down to at least $T = 100\,\mathrm{K}$, 'Sr-vesignieite' provides a rare example to study the interplay of spin and orbital frustration and, to the best of my knowledge, the only such one on the kagome lattice. These findings encourage further experiments, particularly at low temperature, to determine the nuclear and magnetic properties of this material, whilst also raising the possibility of orbital frustration in several other $S = \frac{1}{2}$ KAFMs.

Bibliography

[1] P. W. Anderson, *Mater. Res. Bull.*, 1973, **8**, 153–160.

[2] P. W. Anderson, *Science*, 1987, **235**, 1196–1198.

[3] L. Balents, *Nature*, 2010, **464**, 199–208.

[4] R. S. W. Braithwaite, K. Mereiter, W. H. Paar and A. M. Clark, *Mineral. Mag.*, 2004, **68**, 527–539.

[5] M. A. Lafontaine, A. Le Bail and G. Férey, *J. Solid State Chem.*, 1990, **85**, 220–227.

[6] G. I. C. Schneider and H. J. Lauenstein, *Mineral. Mag.*, 1992, **56**, 67–69.

[7] R. H. Colman, A. Sinclair and A. S. Wills, *Chem. Mater.*, 2011, **23**, 1811–1817.

[8] M. Fujihala, X.-G. Zheng, H. Morodomi, T. Kawae, A. Matsuo, K. Kindo and I. Watanabe, *Phys. Rev. B*, 2014, **89**, 100401.

[9] Y. Li, B. Pan, S. Li, W. Tong, L. Ling, Z. Yang, J. Wang, Z. Chen, Z. Wu and Q. Zhang, *New J. Phys.*, 2014, **16**, 093011.

[10] H. Ishikawa, Y. Okamoto and Z. Hiroi, *J. Phys. Soc. Japan*, 2013, **82**, 063710.

[11] R. L. Frost, A. López, G. de Oliveira Gonçalves, R. Scholz and Y. Xi, *J. Mol. Struct.*, 2014, **1056-1057**, 267–272.

[12] V. Sumin de Portilla, M. P. Quevedo and V. I. Stepanov, *Am. Mineral.*, 1981, **66**, 148–153.

[13] R. H. Colman, F. Bert, D. Boldrin, A. Hillier, P. Manuel, P. Mendels and A. S. Wills, *Phys. Rev. B*, 2011, **83**, 180416.

[14] R. D. Shannon, *Acta Crystallogr.*, 1976, **A32**, 751–767.

[15] M. Zhesheng, H. Ruilin and Z. Xiaoling, *Acta Geol. Sin.*, 1991, **4**, 145–151.

[16] Y. Okamoto, H. Yoshida and Z. Hiroi, *J. Phys. Soc. Japan*, 2009, **78**, 033701.

[17] M. A. Cooper and F. C. Hawthorne, *Can. Mineral.*, 1995, **33**, 1119–1124.

[18] Bruker AXS, *TOPAS V4: General profile and structure analysis software for powder diffraction data*, 2008.

[19] H. Yoshida, Y. Michiue, E. Takayama-Muromachi and M. Isobe, *J. Mater. Chem.*, 2012, **22**, 18793.

[20] P. W. Stephens, *J. Appl. Crystallogr.*, 1999, **32**, 281–289.

[21] R. E. Dinnebier and S. J. L. Billinge, *Powder diffraction: theory and practice*, Royal Society of Chemistry, 2008.

[22] J. M. Igartua, M. I. Aroyo and J. M. Pérez-Mato, *Phys. Rev. B*, 1996, **B54**, 12744–12752.

[23] Z. Hiroi, M. Hanawa, N. Kobayashi, M. Nohara, H. Takagi, Y. Kato and M. Takigawa, *J. Phys. Soc. Japan*, 2001, **70**, 3377–3384.

[24] *The International Tables of Crystallography, Volume C*, Volume C edn., 1999.

[25] P. C. Burns and F. C. Hawthorne, *Can. Mineral.*, 1996, **34**, 1089–1105.

[26] K. I. Kugel' and D. I. Khomskii, *Sov. Phys. Usp.*, 1982, **25**, 231–254.

[27] A. Krimmel, M. Mücksch, V. Tsurkan, M. Koza, H. Mutka and A. Loidl, *Phys. Rev. Lett.*, 2005, **94**, 237402.

[28] Y. Ishiguro, K. Kimura, S. Nakatsuji, S. Tsutsui, A. Q. R. Baron, T. Kimura and Y. Wakabayashi, *Nat. Commun.*, 2013, **4**, 2022.

[29] P. Corboz, M. Lajkó, A. M. Läuchli, K. Penc and F. Mila, *Phys. Rev. X*, 2012, **2**, 041013.

[30] C. Lacroix, P. Mendels and F. Mila, *Introduction to Frustrated Magnetism: Materials, Experiment, Theory*, Springer, New York, 2011.

[31] M. A. Halcrow, *Dalt. Trans.*, 2003, **23**, 4375–4384.

[32] H. Effenberger, *Zeitschrift für Krist.*, 1989, **188**, 43–56.

[33] A. Yamada and M. Tanaka, *Mater. Res. Bull.*, 1995, **30**, 715–721.

[34] J. Rodríguez-Carvajal, M. Hennion, F. Moussa, A. H. Moudden, L. Pinsard and A. Revcolevschi, *Phys. Rev. B*, 1998, **57**, 3189–3192.

[35] J. Quilliam, F. Bert, R. H. Colman, D. Boldrin, A. S. Wills and P. Mendels, *Phys. Rev. B*, 2011, **84**, 180401.

[36] M. Yoshida, Y. Okamoto and H. Yoshida, *J. Phys. Soc. Japan*, 2013, **82**, 013702.

[37] A. Zorko, F. Bert, A. Ozarowski, J. van Tol, D. Boldrin, A. S. Wills and P. Mendels, *Phys. Rev. B*, 2013, **88**, 144419.

[38] F. Reynaud, D. Mertz, F. Celestini, J.-M. Debierre, A. Ghorayeb, P. Simon, A. Stepanov, J. Voiron and C. Delmas, *Phys. Rev. Lett.*, 2001, **86**, 3638–3641.

[39] M. Mostovoy and D. Khomskii, *Phys. Rev. Lett.*, 2002, **89**, 227203.

[40] X. Rocquefelte, K. Schwarz and P. Blaha, *Sci. Rep.*, 2012, **2**, 759.

[41] Y. Mizuno, T. Tohyama and S. Maekawa, *Phys. Rev. B*, 1998, **57**, 5326–5335.

[42] H. Yoshida, J.-I. Yamaura, M. Isobe, Y. Okamoto, G. J. Nilsen and Z. Hiroi, *Nat. Commun.*, 2012, **3**, 860.

[43] Y. Okamoto, H. Ishikawa, G. J. Nilsen and Z. Hiroi, *J. Phys. Soc. Japan*, 2012, **81**, 033707.

[44] T.-H. Han, J. S. Helton, S. Chu, D. G. Nocera, J. A. Rodriguez-Rivera, C. Broholm and Y. S. Lee, *Nature*, 2012, **492**, 406–410.

[45] B. Fåk, E. Kermarrec, L. Messio, B. Bernu, C. Lhuillier, F. Bert, P. Mendels, B. Koteswararao, F. Bouquet, J. Ollivier, A. D. Hillier, A. Amato, R. H. Colman and A. S. Wills, *Phys. Rev. Lett.*, 2012, **109**, 037208.

[46] G. J. Nilsen, F. C. Coomer, M. A. de Vries, J. R. Stewart, P. P. Deen, A. Harrison and H. M. Rönnow, *Phys. Rev. B*, 2011, **84**, 172401.

[47] G. J. Nilsen, Y. Okamoto, H. Ishikawa, V. Simonet, C. V. Colin, A. Cano, L. C. Chapon, T. Hansen, H. Mutka and Z. Hiroi, *Phys. Rev. B*, 2014, **89**, 140412.

Chapter 6

Crystallographic studies of the near-perfect model $S = \frac{1}{2}$ KAFM vesignieite, $BaCu_3V_2O_8(OH)_2$

6.1 Introduction

Following the analysis of 'Sr-vesignieite' presented in the previous chapter it was necessary to perform new experimental investigations of vesignieite, $BaCu_3V_2O_8(OH)_2$ itself. The reasons for this are two-fold, firstly it was important to determine if the new hydrothermal synthetic method used for 'Sr-vesignieite' could be adapted for its Ba-analogue. Moreover, the trigonal $P3_121$ structure found for 'Sr-vesignieite' adds further confusion to the debate surrounding the crystal structure of vesignieite: both monoclinic $C12/m1$ and rhombohedral $R\bar{3}m$ structures have been suggested for the latter and the space group symmetry has important consequences on the kagome lattice and nature of the magnetic interactions [1, 2]. Therefore, it was decided to reinvestigate the crystal structure of vesignieite with these new findings in mind.

First synthesised in 2009, the mineral vesignieite, $BaCu_3V_2O_8(OH)_2$, is a relatively new experimental $S = \frac{1}{2}$ kagome magnet [3]. It is highly magnetically frustrated with a magnetic transition suppressed to well below the strength of the magnetic exchange field. The onset of the magnetic transition at $T_N \sim 9\,K$ is consistent between samples, however the behaviour at T_N is dependent on sample preparation techniques. Behaviour ranges from complex heterogeneous ground states with partial spin freezing to complete long-range $q = 0$ magnetic order.

This chapter details high resolution synchrotron and lab-based X-ray diffraction experiments which aimed to clarify the true structure of vesignieite. I show that the material crystallises with trigonal $P3_121$ symmetry as in 'Sr-vesignieite', although in poorly crystalline samples certain features of the structure are disordered. The local coordination of the Cu^{2+} octahedra reveals dynamic Jahn-Teller (JT) fluctuations, which suggests orbital as well as spin frustration. A new synthetic route to highly crystalline samples is also presented.

6.2 Background

6.2.1 Crystallography of vesignieite

Vesignieite has been discovered in several mines situated worldwide. The first thorough crystallographic analysis was performed on a natural single crystal sample obtained from a mine in Cambrian Chigou black shale system, China [1] and the majority of subsequent crystallographic analysis on synthetic samples is based on this study. This sample crystallised in monoclinic symmetry with space group $C12/m1$ and lattice parameters $a = 10.270(2)$, $b = 5.911(1)$ Å and $c = 7.711(2)$ Å and $\beta = 116.421(3)°$. Interestingly, this lattice is extremely close to a higher symmetry $R\bar{3}m$ space group (angular tolerance of 0.16 °) [4].

The monoclinic structure of vesignieite is shown in 6.1 and whilst described in Chapter 5 it is useful to again discuss it. The materials defining feature is the Cu^{2+} kagome planes, formed from layers of CuO_6 octahedra, stacked along the [001] direction and spaced by 6.91 Å [1]. The kagome planes are separated by BaO_6 trigonal antiprisms and VO_4 tetrahedra. Adjacent kagome planes are connected by the BaO_6 and VO_4 units. The BaO_6 shares all its oxygens with the CuO_6 of the kagome planes, whilst the three basal oxygens of the VO_4 tetrahedra are shared with the CuO_6 of one kagome plane and the apical oxygen is hydrogen bonded to a hydroxide group bonded to an adjacent kagome plane. An important consequence of this combination of cations for magnetism is that there is no opportunity for site-mixing. In several model $S = \frac{1}{2}$ KAFM materials, such as herbertsmithite, the Cu^{2+} site mixes with similar sized diamagnetic cations, diluting the magnetic lattice.

The geometry of the CuO_6 octahedra in vesignieite is also noteworthy. From X-ray diffraction, on both crystallographic Cu sites the CuO_6 octahedra is axially compressed, with four longer (2.1 - 2.2 Å) and two shorter (~ 1.9 Å) Cu–O bonds. As discussed for 'Sr-vesignieite', this is strong evidence that the CuO_6 are fluctuating between two JT distorted configurations. Moreover, both single crystal diffraction studies on vesignieite samples reveal anisotropic displacements on the oxygens consistent with this theory [1, 2]. The resulting partial $d_{x^2-y^2}$ occupation is in contrast to the previously described d_{z^2} orbital order [3]. The consequences of this will be discussed later in the chapter.

We can now discuss the specific structural features present depending on whether we describe the structure with monoclinic or rhombohedral symmetry. From a magnetism perspective, the most important consequence of reducing the symmetry from rhombohedral to monoclinic is on the kagome planes. In rhombohedral symmetry, the kagome structure is built from a single crystallographic Cu site, however the reduction to monoclinic symmetry splits this into two inequivalent Cu sites and, consequently, two different Cu–Cu bond lengths and superexchange interactions. Therefore, in monoclinic symmetry, the material is not a structurally *perfect* $S = \frac{1}{2}$ KAFM, as defined by having a 3-fold rotation axis. As both Cu sites sit on special positions, the inequivalence of the Cu–Cu bonds is metrically defined by the a and b lattice parameters. In synthesised samples, the bond inequivalence is found to be < 0.1 % [5], an order of magnitude less than the similar $S = \frac{1}{2}$ KAFM volborthite [6].

Recently, Yoshida *et al.* successfully synthesised single crystal samples of vesignieite (termed β-vesignieite) *via.* a hydrothermal method [2]. Single crystal X-ray diffraction indicate that these samples

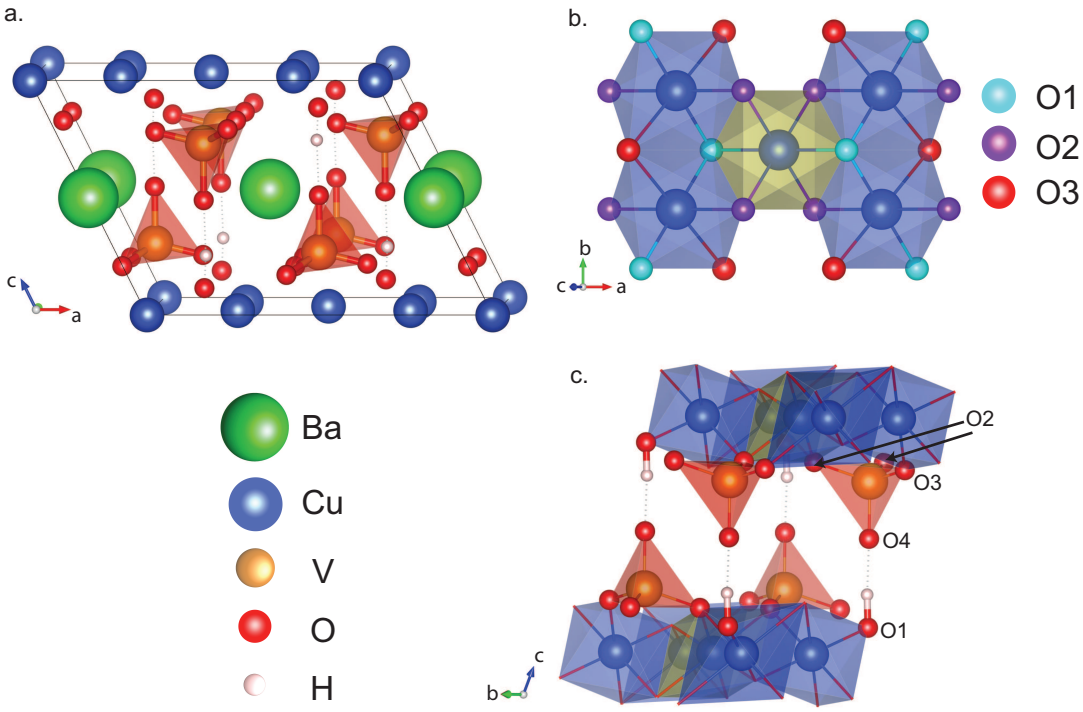

Figure 6.1: a. Unit cell of monoclinic vesignieite structure in space group $C12/m1$ with lattice parameters $a = 10.270(2)$, $b = 5.911(1)$, $c = 7.711(2)$ Å and $\beta = 116.421(3)^\circ$. **b.** A view of the kagome planes in vesignieite showing the CuO_6 octahedra and their sharing of oxygens. **c.** A view of the connectivity of the kagome planes in vesignieite. The basal oxygens of the VO_4 are coordinated to the CuO_6 of the kagome planes and the apical oxygen is hydrogen bonded to the hydroxide group attached to the adjacent kagome plane.

crystallise with $R\bar{3}m$ symmetry and lattice parameters $a = 5.9295(10)$ Å and $c = 20.790(4)$ Å. The structural refinement was significantly improved by allowing the V and apical O of the VO_4 to refine off the special position they occupy and adjusting their occupancies accordingly. This group claimed this disorder can be modelled locally, *i.e* does not cause a global symmetry reduction, and leaves the kagome planes undistorted. Thus, β-vesignieite is considered a structurally *perfect* KAFM due to the kagome planes retaining the 3-fold rotation axis of $R\bar{3}m$.

It is noteworthy that the local coordination of the sole crystallographic Cu site in β-vesignieite is similar to monoclinic vesignieite: the CuO_6 octahedron is axially compressed with bond lengths of 2.183 Å and 1.916 Å [2]. Anisotropic displacement of the oxygen on the shorter Cu–O bonds is small and roughly symmetrical, whilst the oxygen of the longer bonds is large and aligned consistent with a fluctuating bond. Therefore, dynamic JT fluctuations of the CuO_6 may also be a feature of β-vesignieite and a symmetry lowering to monoclinic is not required to accomodate them.

The discovery of the rhombohedral structure of β-vesignieite brings into question the true structure of synthetic vesignieite samples. In powder X-ray diffraction, a symmetry reduction from $R\bar{3}m$ to $C12/m1$ would result in existing peaks being split rather than the appearance of new peaks, making it very difficult to discern between the two scenarios. Given the structural consequences of the lower

symmetry, and its relation to the magnetic properties of the material, determining the true structure of vesignieite is an important investigation.

6.2.2 Synthetic routes to vesignieite

Vesignieite can be synthesised using either hydrothermal or wet chemistry methods, such as reflux reactions. The methods that exist in the literature can be divided into three categories:

- **Method 1**: Hydrothermal reaction of $Cu(OH)_2$, V_2O_5 and $Ba(CH_3COO)_2$ in a PTFE-lined steel autoclave at 180°C for 24 h [3]. The X-ray diffraction peaks from these samples are broad evidencing poor crystallinity. However, the crystallinity can be significantly improved by hydrothermal annealing in water at 580°C for 24 h [7]. Unless otherwise stated in the text, samples prepared *via.* Method 1 will refer to the latter with better crystallinity.

- **Method 2**: Reflux reaction adopted from synthesis of the layered Cu^{2+} kagome material $NH_4Cu_2Mo_2O_{10}H_3$ [8]. The reaction is performed with $Cu(OH)_2$, V_2O_5 and $Ba(CH_3COO)_2$ in a 28 % 100 ml NH_4OH/H_2O solution and refluxed for $\sim$ 4 h in an oil bath [5]. The $Cu(OH)_2$ is brought into solution *via.* reaction with the NH_4 to form Schweizer's reagent, $[Cu(NH_4)_4(H_2O)_2]^{2+}$, which improves the crystallinity of the final product as evidenced from X-ray diffraction. From work in my M.Sci. project, the sample crystallinity was shown to improve further with hydrothermal annealing at ~ 200°C in a PTFE-lined autoclave [5, 9].

- **Method 3**: Hydrothermal reaction of $Cu(OH)_2$, V_2O_5 and $BaCl_2 \cdot 2H_2O$ in a 1 % HNO_3 aqueous solution [2]. The PTFE-lined reaction vessel was heated to 180°C before being cooled over $\sim$ 11 days at $0.6°C\,h^{-1}$ to produce $\sim$ 0.25 mm hexagonal-plate-like crystallites large enough for single crystal X-ray diffraction.

The magnetic properties of vesignieite are highly dependent on the synthetic method used. For samples prepared *via.* Method 2, the magnetic susceptibility as a function of temperature for various hydrothermal annealing times is shown in Figure 6.2a. All samples evidently go through a transition at $T_N \sim 9$ K, however the transition is not well defined and appears to be dominated by a paramagnetic-like contribution. With hydrothermal annealing the transition begins to resemble more closely that expected for long-range antiferromagnetic order. Similar behaviour is observed for samples prepared *via.* Method 1 (Figure 6.2): before hydrothermal annealing the transition is poorly defined but after annealing at 580 °C a clear antiferromagnetic transition is seen at T_N. Samples prepared using Method 3 also show a sharp antiferromagnetic-like transition at T_N, shown in Figure 6.2c, that closely resembles the behaviour of samples from Method 2.

The cause of the sample dependent magnetic properties remains unclear. X-ray diffraction shows no sign of crystalline or amorphous impurity phases, in any of the samples, that may contribute a magnetic signal. In fact, the sample prepared from Method 2 *does* show impurity peaks in the X-ray diffraction spectrum, but no anomalous low-T magnetic behaviour is observed and instead there is a clear transition at T_N that closely resembles that from the single crystals of Method 3 [7]. Thus, it appears that the sample dependent magnetic properties are likely intrinsic and related to crystallographic disorder, such

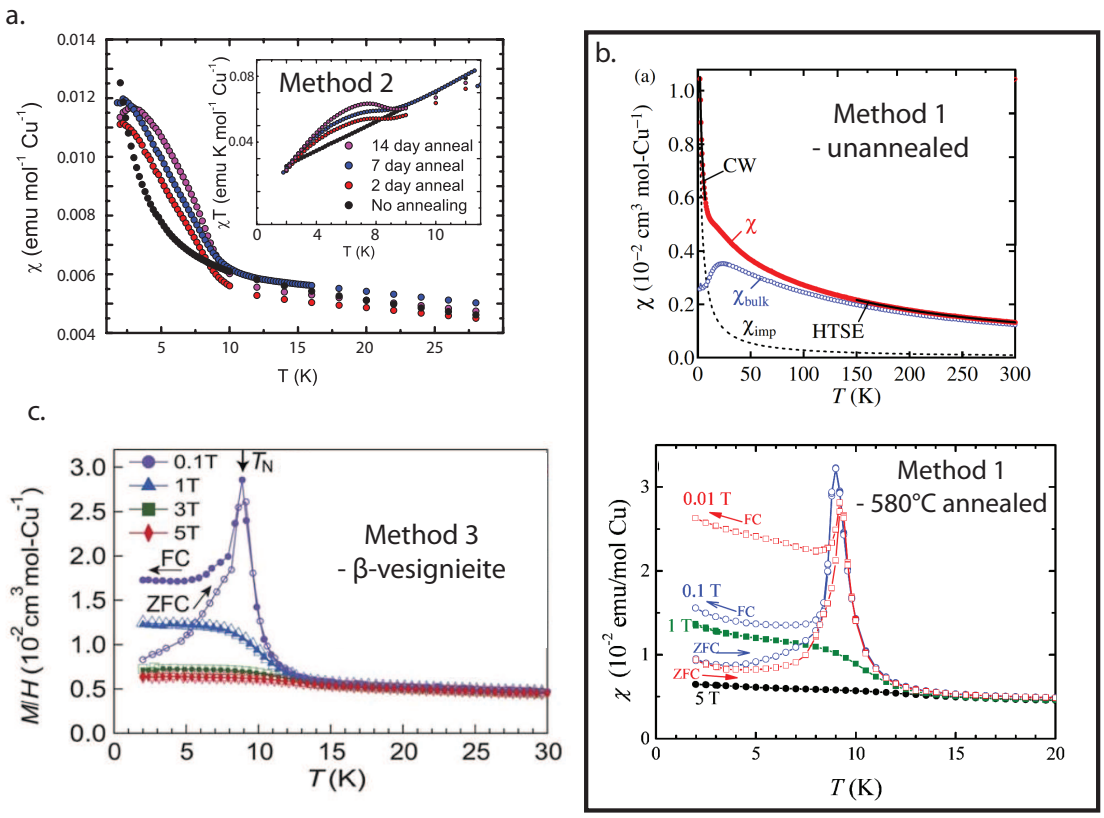

Figure 6.2: **a.** Magnetic susceptibility of vesignieite samples prepared using a reflux reaction described in Method 2 in the text and subsequently hydrothermally annealed. Upon annealing the transition at $T \approx 9\,\mathrm{K}$ becomes clearer and more closely resembles a long-range ordering transition. These measurements were made during my M.Sci. project [9]. **inset** χT for the same samples showing the clearer transition with annealing and the introduction of an antiferromagnetic component. **b.** Magnetic susceptibility of vesignieite samples prepared hydrothermally (**top**) and subsequently annealed at 580 °C (**bottom**) as described in Method 1 in the text [7]. Compared to other vesignieite samples the transition temperature has not changed, but the transition is much sharper indicating an entry into long-range magnetic order rather than spin disorder. **c.** Magnetic susceptibility of single crystalline β-vesignieite, purported to crystallise with an undistorted kagome lattice, prepared *via.* a slow cool hydrothermal annealing process as described in Method 3 in the text [2].

as lattice defects or strain. Hence the sharpening of the transition associated with hydrothermal annealing in samples from Method 1, which may be expected to remove defects or relieve strain. The next section of this chapter studies the effects of annealing on the crystal structure through synchrotron diffraction and Raman spectroscopy, which clarifies the crystallographic disorder.

6.3 Study into the effects of hydrothermal annealing on vesignieite

For this study, vesignieite samples were prepared using a reflux method. The reaction equations are:

$$3\mathrm{Cu(NO_3)_2 \cdot H_2O} + 2\mathrm{NaOH} \rightarrow 3\mathrm{Cu(OH)_2} + 2\mathrm{NaNO_3} + \mathrm{H_2O} \tag{6.1}$$

$$3\mathrm{Cu(OH)_2} + \mathrm{Ba(CH_3COO)_2} + \mathrm{V_2O_5} \rightarrow \mathrm{BaCu_3V_2O_8(OH)_2} + 2\mathrm{CH_3COOH} + \mathrm{H_2O} \tag{6.2}$$

First, the $Cu(OH)_2$ is synthesised by reacting $Cu(NO_3)_2{\cdot}H_2O$ (2610.8 g) and NaOH (1015.9 g), in a 1:2 molar ratio, in distilled water (50 ml). After 5 mins stirring, the gelatinous blue $Cu(OH)_2$ is collected using centrifugation at 4400 rpm for 2 mins in two 50 ml centrifuge tubes. In a 1000 ml round-bottomed flask the $Cu(OH)_2$, $Ba(CH_3COO)_2$ (1083.5 mg) and V_2O_5 (769.9 mg) are mixed in a 3:1:1 molar ratio with NH_4OH (250 ml) and H_2O (50 ml). The flask is placed in an oil bath preheated to 130 °C and an air condenser is attached. The reaction solution is stirred for 3 hours, after which the flask is taken off the heat and the green powder allowed to settle for 5 mins. After decanting off the clear solution, the powder is washed with 3×50 ml H_2O and 3×50 ml acetone. The collected yield is ~ 90 %.

Hydrothermal annealing is performed in 20 ml PTFE-lined acid digestion bombs. 300 mg of vesignieite is placed in the PTFE-liner along with 10 ml distilled water, which is subsequently magnetically stirred for 2 mins to disperse any clumps of material. The reaction vessel is sealed and placed in an oven preheated to 220°C. After the desired annealing time the bombs are removed from the oven and left to cool to room temperature. The annealed powder is washed with 3×50 ml distilled water and 3×50 ml acetone before being dried on a rotary evaporator. Six samples were prepared in total, with annealing times of 2 h, 6 h, 1 day, 3 days and 7 days in addition to an unannealed sample. X-ray diffraction data collected on a STOE STADI-P powder diffractometer confirm that each sample has the peak positions and intensities expected for vesignieite and is phase pure within the limits of impurity detection (~ 1 %) [1].

6.3.1 Powder synchrotron diffraction

High-resolution powder diffraction using synchrotron radiation is an excellent tool for accurately determining the crystallographic properties of materials. The ability to achieve very high resolution is particularly useful for structures with overlapping peaks, such as would be the case for a monoclinic vesignieite structure. Furthermore, the heavy elements in vesignieite cause it to be highly absorbing of X-rays, rendering patterns collected using low energy radiation, such as that from Cu, useless for Rietveld refinement. High energy X-rays can easily be used at a synchrotron facility, minimising problems from absorption.

The synchrotron data were collected at the 11-BM high resolution powder diffraction beamline at the Advanced Photon Source, Argonne, USA. X-rays with wavelength $\lambda = 0.413827$ Å ($E = 30$ keV) were used and each sample was measured for 1 h in the range $0.5 < 2\theta < 50°$. Samples were mounted in Kapton capillaries with 0.8 mm inner diameter, giving a $\mu R < 0.5$. Due to the excellent signal-to-noise of the data, all spectra in this chapter are plotted with the square root of the intensity in order to highlight small features.

Figure 6.3a shows a plot of the spectra collected on the unannealed and 7 day annealed samples. On first inspection, both spectra show similar positions and intensities of the Bragg peaks, with the most obvious difference being a reduced background in the 7 day annealed sample. On closer inspection, several additional peaks with very weak intensity are apparent in the 7 day annealed but not the unannealed sample. Figures 6.3a shows the appearance of a peak at $Q \approx 2.20$ after 1 day annealing which grows in intensity after 7 days. In figure 6.3b a similar trend is seen for a peak at $Q \approx 4.50$ Å^{-1} and a weak peak

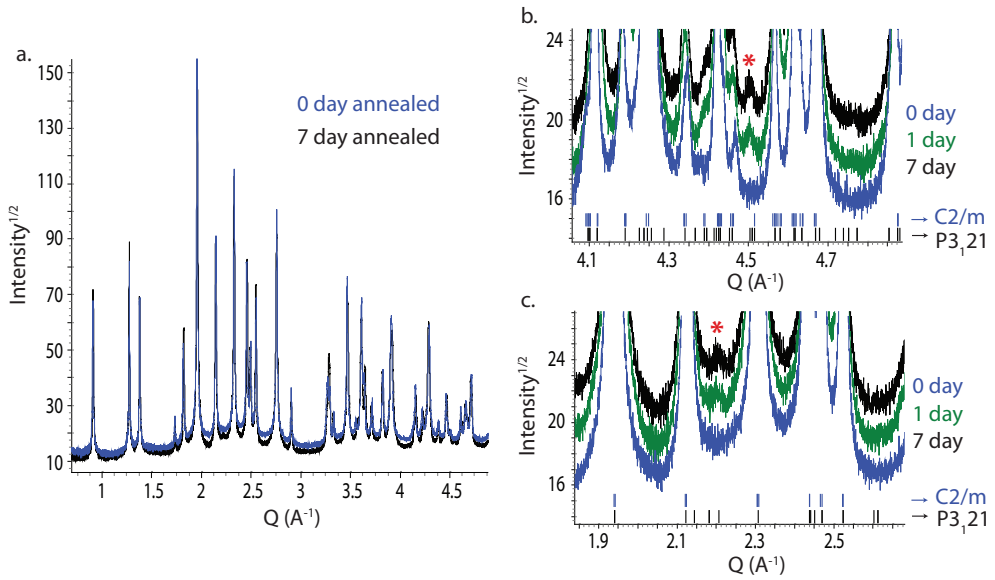

Figure 6.3: **a.** Synchrotron data collected at the 11-BM beamline ($\lambda = 0.41$ Å) at the APS, USA on unannealed and annealed vesignieite samples prepared *via.* a reflux method and subsequent hydrothermal annealing. **b. and c.** Zoomed regions of the synchrotron data showing the appearance of peaks at $Q \sim 2.2$, 4.55 and 4.75 Å^{-1} with hydrothermal annealing. These additional peaks cannot be indexed with the monoclinic $C12/m1$ structure of vesignieite described in the literature [1]. Instead, these peaks index with $P3_1$ symmetry, as shown by the blue tick marks.

at $Q \approx 4.75$ Å^{-1} . More peaks of similar weakness apparent in the 7 day sample are found at $Q \approx 3.72$ and 4.51 Å^{-1} (Appendix B, Figure B.1).

In previous powder diffraction studies of vesignieite, the data has been well modelled by a monoclinic structure with $C12/m1$ symmetry [1, 10, 5]. The calculated hkl reflections from a Pawley refinement for a $C12/m1$ structure are shown as black tick marks in Figures 6.3a and b. This structure clearly does not predict reflections at $Q \approx 2.20$ or 4.75 Å^{-1} and whilst it does place a reflection in the vicinity of the peak at $Q \approx 4.50$ Å^{-1} , it is slightly misaligned. These peaks are found to align with the $P3_121$ structure proposed for 'Sr-vesignieite' (Chapter 5). The locations of the predicted hkl indices from a Pawley refinement using a $P3_121$ structure are shown as blue tick marks in Figures 6.3a and b and all peaks in these regions are accounted for.

Interestingly, the peak at $Q \approx 2.2$ Å^{-1} associated with the $P3_121$ structure is also seen in the diffraction pattern published by Yoshida *et al.* of a sample prepared using Method 1 discussed earlier, which involves post-synthesis annealing at 580 °C [7]. Figure 6.4 shows the diffraction pattern of this sample from [7]. At 31.4° 2θ ($Q = 2.21$ Å^{-1} with $\lambda = 1.5405$ Å) a low intensity peak can be seen which matches well with the peak in the data from our 7 day annealed sample shown in Figure 6.3b. Yoshida *et al.* assumed the monoclinic structure was correct for their sample and attributed all unexpected peaks to impurities, indicated by the black arrows in Figure 6.4.

Turning back to the synchrotron data, a Pawley refinement was performed on the data collected on the 7 day annealed sample using the $P3_121$ structure with the program TOPAS and a fundamental

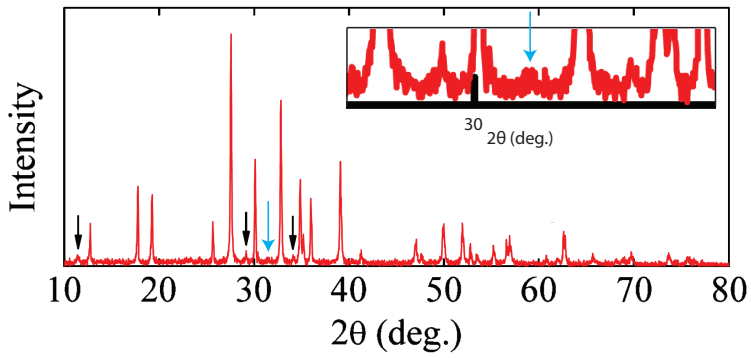

Figure 6.4: X-ray diffraction pattern of a vesignieite sample prepared using Method 1 described in the text, which involves annealing at high temperature (580 °C), published by Yoshida *et al.* [7]. The annealing process introduced impurities, indicated by the black arrows. The sample was assumed to have monoclinic symmetry and all unexpected peaks were attributed to an impurity phase. It is noteworthy that the peak at 34.2 ° ($Q = 2.2\,\text{Å}^{-1}$ with $\lambda = 1.54\,\text{Å}$) aligns with predictions for the $P3_121$ structure (inset).

parameters approach of modelling the instrumental broadening [11]. For the sample related profile, Stephen's model of anisotropic peak broadening was required to fit the hkl-dependent peak shapes [12]. This model fits the majority of peaks well apart from the peak at $Q \approx 2.2\,\text{Å}^{-1}$ associated with the trigonal structure (Figure 6.5a). The fit is poor because the peak is very broad compared to the rest of the pattern. Anisotropic peak broadening is often associated with lattice size or strain effects, however as the specific broadened reflections are related to the trigonal structure it suggests that the crystallographic features of this structure are disordered.

To model the broad peaks associated with the trigonal structure, Pawley refinements were performed with two phases: one $C12/m1$ phase with a profile modelled with Stephens's approach and another $P3_121$ phase with a separate profile of a simple convolution of Gaussian and Lorentzian components. To stabilise the refinement, the majority monoclinic phase was fitted first and the peak intensities and profile parameters subsequently fixed. The second $P3_121$ phase was then added and allowed to refine freely. The final refinement for the 7 day annealed sample is shown in Figure 6.5b. Notably, the fit around the $Q = 2.2\,\text{Å}^{-1}$ region is significantly improved with the two phase refinement as the broadness of this peak is correctly modelled.

Refinements were performed for data from all samples using the method described above. Changes in certain profile parameters as a function of annealing time reveals useful information related to the ordering of the trigonal phase. The ξ parameter of the $C12/m1$ phase describes the mixing of Gaussian and Lorentzian contributions, where $\xi = 0$ is a fully Gaussian and $\xi = 1$ a fully Lorentzian contribution. A plot of ξ as a function of annealing time is shown in Figure 6.5c and reveals an increase in Gaussian contribution with longer annealing times. As the Gaussian peak shape, compared to Lorentzian, is narrower at the base of the peak, a more Gaussian-like peak indicates less diffuse scattering at its base. Therefore, the increased Gaussian contribution may result from the ordering of the trigonal phase.

The $P3_1$ phase profile is described by hkl-independent Gaussian and Lorentzian convolutions

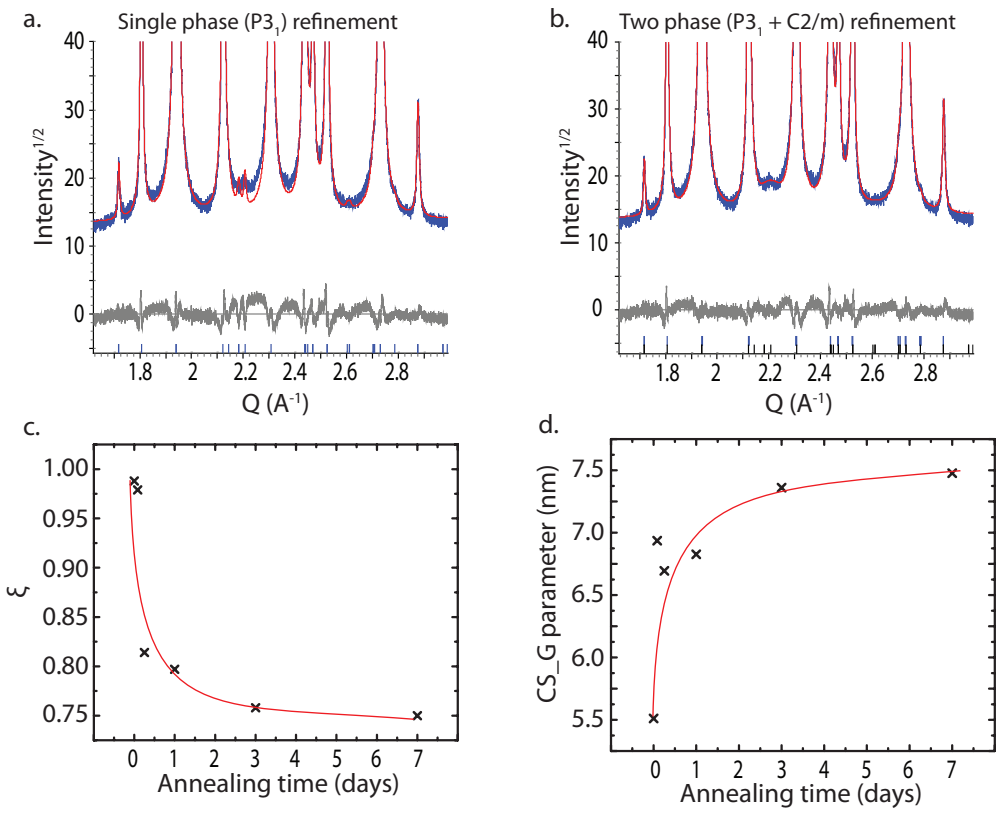

Figure 6.5: **a.** Refinement of synchrotron data collected on the 7 day annealed sample using a single $P3_121$ phase. The profile of the new peaks are much broader than those associated with the monoclinic structure. **b.** A two phase refinement of data collected on the 7 day annealed sample. The profile function for the two phases was allowed to refine freely giving a much better fit to the data. **c.** The refined Gaussian-Lorentzian mixing parameter for the $C12/m1$ phase ($\xi = 1 \rightarrow$ Lorentzian) showing a more Gaussian-like peak shape with hydrothermal annealing and, thus, a narrower peak shape at the base of the peak. **d.** The refined CS_G parameter for the $P3_1$ phase, which describes the Gaussian contribution and crystallite size, therefore showing improved crystallinity of this phase with hydrothermal annealing.

termed CS_G and CS_L in TOPAS, respectively. A plot of the CS_G parameter as a function of annealing time is shown in Figure 6.5d. The parameter value also reflects the sample crystallite size, which can be generalised as the ordered length scale of the phase. Therefore the increase of CS_G as a function of annealing time indicates greater order of the trigonal phase.

Williamson-Hall plots provide a useful way of determining structural disorder, such as lattice strain and size effects, from X-ray diffraction data [13]. The method is based on the fact that both strain- and size-broadening are non-linear in θ and can approximately be expressed by:

$$\beta_{\text{tot}} \cos\theta = \beta_{\text{strain}} \sin\theta + \beta_{\text{size}} \tag{6.3}$$

where β_{tot} is the total broadening, β_{size} is the size broadening component and β_{strain} is the strain broadening component. Thus, a plot of $\beta_{\text{tot}} \cos\theta$ *vs.* $\sin\theta$ gives β_{strain} as the gradient and β_{size} as the y-intercept. For the spectra from each sample, the first twelve peaks were fitted individually to determine

$\beta_{\rm tot}$ (integral breadth), from which the Williamson-Hall plots could be made.

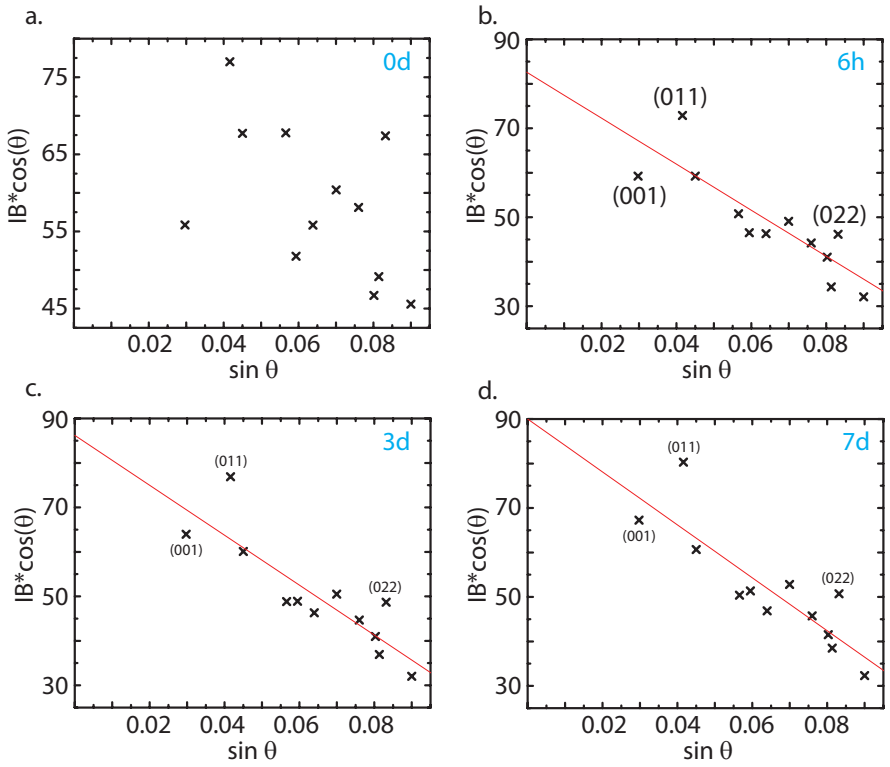

Figure 6.6: Williamson-Hall plots showing $\beta_{\rm tot}\cos\theta$ (integral breadth) as a function of $\sin\theta$ for the **a.** unannealed, **b.** 6 h annealed, **c.** 3 d annealed and **d.** 7 d annealed vesignieite samples. The more linear distribution of the points with increased annealing indicates less crystallite strain and the increase in y-intercept a larger crystallite size.

Williamson-Hall plots for the un-annealed, 6h, 3d and 7d samples are shown in Figure 6.6. There is no clear θ dependence for the un-annealed sample, thus there is no attempt at fitting the data with a straight line. This indicates severe strain effects within the sample, as an ideal sample should display a linear $\beta_{\rm tot}$ dependence with $\sin\theta$. For the other plots, the data were fitted with a straight line (shown in red). With longer annealing time $\beta_{\rm size}$ increases which indicates larger crystallite sizes in the annealed samples. $\beta_{\rm strain}$ is large and negative in all samples, but decreases with longer annealing times. This latter phenomena can be a result of lattice shrinkage [14], seen in the refined cell volume (Appendix B, Figure B.2). The $(0kk)$ reflections are indicated in Figure 6.6 as they are particular outliers and the significance of this will be discussed later in the chapter.

The substantial strain issues, combined with the large scattering from Ba^{2+}, Cu^{2+} and V^{5+}, made refinement of the oxygen positions from the synchrotron data unstable. Therefore, Rietveld analysis did not reveal any further useful information. Instead, investigation of the crystallographic disorder was performed with Raman spectroscopy.

6.3.2 Raman spectroscopy

Raman spectra were collected using a Renishaw spectograph with a CCD detector and microscope for point-by-point analysis, described fully in Chapter 4 (Page 59). The measuring wavelength was

514.5 nm. All vesignieite samples discussed in the previous section were measured between 100 and 4000 cm^{-1}. In order to collect high quality data a good focus was required on small powdered clusters or, ideally, individual crystallites. To make this easier, samples (~ 10 mg) were ultrasonicated for 5 mins in 10 ml acetone and a small amount pipetted onto a glass slide to dry, leaving an even dispersion of crystallites.

Figure 6.7 shows the $< 1000\,cm^{-1}$ region of the Raman spectra where the majority of bands lie. The bands at higher wavenumbers ($> 2000\,cm^{-1}$) associated with OH^- vibrations are broad and relatively featureless (Appendix B, Figure B.2). Between $700 - 1000\,cm^{-1}$ are several sharp peaks that have previously been associated from Raman data collected on a natural sample with the VO_4 group, whilst those below 700 cm^{-1} arise from Cu–O and Ba–O as well as lattice vibrations [15]. The spectra shown here match very well with those in the literature [15, 16], with good agreement of both peak positions and widths.

Table 6.1 shows the calculated Raman active modes using site symmetry analysis [17] for various space group symmetries that have been suggested for vesignieite in this chapter and in the literature. It is clear that any structural transitions between these would result in a noticeable change in the number of visible Raman modes. Therefore, from the spectra in Figure 6.7, it is clear that no such transition occurs upon hydrothermal annealing. The most significant change is a decrease in the linewidth of all the peaks with longer hydrothermal annealing, which is often related to sample crystallinity or local order/disorder [18, 19]. This agrees well with our conclusions from the synchrotron powder diffraction data: no structural transition occurs upon hydrothermal annealing but the trigonal structure becomes more ordered. However, the nature of this ordering remains unclear.

The absolute number of peaks in the Raman spectrum is hard to determine and relate to those expected from the various symmetries listed in Table 6.1. From Figure 6.7, there are at least 15 observable bands between 150 and 1200 cm^{-1}, whilst above this there are at least 7 bands [15]. There may also be some weak, broad bands below 150 cm^{-1} [16]. This gives at least 22 Raman bands, which is close to that expected for $C12/m1$ although this structure is ruled out from the synchrotron powder diffraction data. In particular, the number of observable bands is far less than that expected for $P3_1$ or $P3_121$. However, as these calculations are from site symmetry analysis, the discrepancies may arise from some sites having higher symmetry than the global description.

Space group	Active modes	Total modes	Reference
$R\bar{3}m$	$6A_{1g} + 7E_g$	13	[2]
$P3_121$	$26A_1 + 53E$	79	Chapter 5
$P3_1$	$53E + 53^1E + 53^2E$	159	Chapter 5
$C12/m1$	$13A_g + 8B_g$	21	[1]
$C2$	$25A + 26B$	51	

Table 6.1: Raman active modes for the vesignieite structure described in various space group symmetries, calculated using site symmetry analysis.

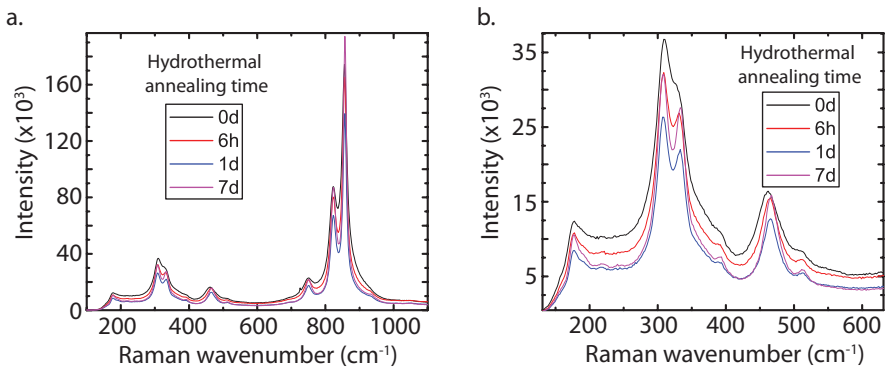

Figure 6.7: Raman spectra collected for unannealed and annealed vesignieite samples prepared *via* a reflux method. With annealing no new Raman peaks appear indicating no change in symmetry. The only noticeable change is a narrowing of the peaks which can be related to increased crystallinity. These observations agree with the conclusion that all vesignieite samples adopt $P3_1$ symmetry, however some aspects of the structure involve disorder which is reduced by annealing.

6.4 Synthesis and crystallographic study of high quality vesignieite samples

The quest for higher quality samples in the study of magnetic properties of geometrically frustrated materials is of great importance. In the previous sections, crystallographic disorder is shown to be a significant issue in vesignieite samples. Here a new synthetic route is described to high quality vesignieite samples that adopt a fully ordered trigonal structure. Crystallographic analysis of these samples reveals a dynamic JT effect, similar to 'Sr-vesignieite', that persists to low temperatures.

6.4.1 Synthesis

The synthesis of 'Sr-vesignieite' (Chapter 5, Page 62) involves reaction of the layered copper vanadate volborthite, $Cu_3V_2O_7(OH)_2{\cdot}2H_2O$, with $Sr(CH_3COO)_2$ under hydrothermal conditions. The desired product from this reaction is impure and requires manual separation, but is highly crystalline. With the discovery of this synthetic route to 'Sr-vesignieite', it was logical to attempt the same for vesignieite. Unlike the 'Sr-vesignieite' synthesis, no mottramite-like impurity phase occurs and so acidification of the reaction solution is not required.

The final synthetic method is as follows. Unannealed volborthite, $Cu_3V_2O_7(OH)_2$, (0.8466 mmol, 474.6 mg) is gently ground for 2 mins in an agate mortar and pestle to make a uniform powder with no large clumps and placed in a 15 ml PTFE-liner along with $Ba(CH_3COO)_2$ (0.8466 mmol, 246.7 mg). 10 ml distilled water is added to the liner and the solution is magnetically stirred for 2 mins. The liner is placed inside a Parr Instruments steel autoclave, sealed and put in an oven preheated to 190 °C. The reaction is left for 2 days before taking out the autoclave and allowing it to cool to room temperature. The solvent is removed using a pipette and the green powder is collected in a 15 ml centrifuge tube with distilled water, centrifuged for 2 mins and the water discarded again. This is repeated twice more with distilled water then three times with acetone before finally removing the acetone on a rotary evaporator.

The resulting yield from these reactions is $\sim 90\,\%$. For deuterated samples, the experimental conditions are the same except D_2O is used in place of H_2O. Deuterated volborthite is not required as it contributes a negligible amount of H/D to the reaction ($\sim 9 \times 10^{-5}\,\%$). A small amount of an unidentified, black impurity phase is produced, however this is only faintly visible when the sample is centrifuged and is not revealed in any analytical techniques.

6.4.2 X-ray diffraction

An X-ray diffraction pattern of the new synthetic vesignieite samples, prepared using the method described above, is shown in Figure 6.8. The pattern was measured on a STOE STADI-P diffractometer described in Chapter 4 (Page 52). The peak positions closely match other vesignieite samples [5, 10], but as is the case for 'Sr-vesignieite' several peaks cannot be indexed with the published monoclinic or rhombohedral structures, indicated by the black arrows in the figure. To determine the structure from the X-ray diffraction data a similar method to that employed for 'Sr-vesignieite' in Chapter 5 was used. Indexing the powder pattern using the TOPAS software package yields the best solution as $P3_1$, whilst other potential solutions are listed in Table 6.2. Although all the best solutions index all the observed peaks, the lattice parameters for $P2$, $P2_1$ and $Pnc2$ have unreasonable values for the vesignieite structure due to the large elongation of the unit cell. Therefore, $P3_1$ gives the best fit and lattice parameters consistent with the vesignieite structure.

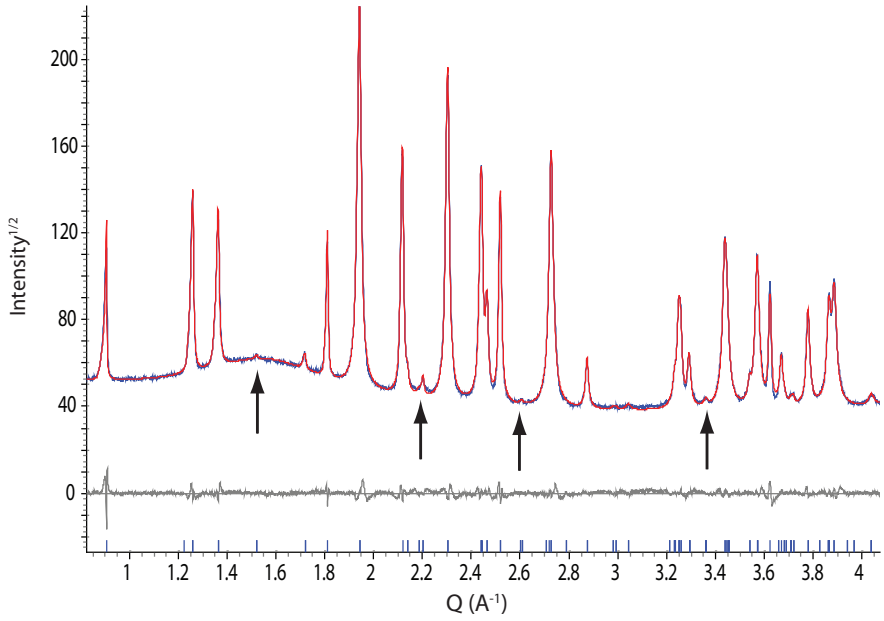

Figure 6.8: Pawley refinement of X-ray diffraction data collected on vesignieite prepared by the new hydrothermal synthetic method described in Section 6.4.1. The data are well fitted with a $P3_1$ structure with lattice parameters $a = 5.92931(8)$ and $c = 20.8008(4)$ Å. The black arrows indicate peaks that are unindexed by the published monoclinic and rhombohedral structures of vesignieite.

A Pawley fit to the X-ray diffraction data using the $P3_1$ structure in Table 6.2 is shown in Figure 6.8. The $P3_1$ structure gives an excellent fit to the data with lattice parameters $a = 5.92931(8)$ and $c = 20.8008(4)$ Å. To correctly model the peak profile, Stephens's anisotropic peak broadening model

			Lattice parameters					
Space group	Goodness-of-fit	Unindexed peaks	a (Å)	b (Å)	c (Å)	α (°)	β (°)	γ (°)
$P3_1$	32.76	0	5.922	5.922	20.822	90	90	120
$P2$	29.85	0	21.077	5.1288	2.962	90	81.8	90
$P2_1$	27.47	0	21.039	5.131	2.962	90	98.0	90
$Pnc2$	27.08	0	20.826	5.128	3.627	90	90	90

Table 6.2: A table showing the best results from indexing powder X-ray diffraction data of vesignieite prepared via the new hydrothermal synthetic method described in Section 6.4.1. The lattice parameters of $P3_1$ are consistent with the vesignieite structure, however those of the other space groups are greatly distorted and do not agree well.

is required, however this broadening is much smaller and less complex than for samples prepared *via.* a reflux method.

In order to refine atomic positions and displacement parameters using the Rietveld method, excellent quality data is required to large Q values. Collecting this data for vesignieite using lab X-ray diffractometers is problematic due to the large absorption of the heavy Ba, Cu and V atoms. Even with high energy Mo X-rays ($\lambda = 0.7093$ Å), the absorption of vesignieite in a 0.2 mm capillary with a 0.6 packing fraction is $\mu R \sim 1.1$ and thus corrections are required. To minimise the problems with absorption, synchrotron and neutron powder diffraction experiments were performed on these new samples of vesignieite. The flux and resolution from a synchrotron source are both vastly better than from a lab X-ray diffractometer, whilst the ability to use high energy X-rays removes the need for absorption corrections. This allows data to be collected to high-Q and access to a large number of reflections. Neutron diffraction gives valuable structural information on smaller elements, such as O and H/D, which are difficult to obtain using X-rays due to their small structure factor. In vesignieite this is particularly important as it contains several O and H/D atoms. The next section describes these experiments.

6.4.3 Powder neutron diffraction

Powder neutron diffraction data were collected at the high resolution HRPD beamline at ISIS, UK. A 1.8 g deuterated sample was loaded in a slab holder with 10 mm thickness. Measurements were taken at 4.2 and 20 K for 300 μA (7.5 h) and at 100 K for 150 μA (6.25 h). All structural refinements of the data were performed using the TOPAS software package [11].

For Rietveld refinement of the 4.2 K HRPD data spectra from both 90 ° and back-scattering banks were used and a CeO_2 standard was refined to obtain accurate instrumental parameters. Initial attempts using the monoclinic structure of vesignieite did not predict all the observed peaks, again disproving this structure. Given the confirmation of trigonal symmetry from lab X-ray diffraction, the starting model for Rietveld refinement was taken from the $P3_121$ 'Sr-vesignieite' structure described in the previous chapter (Page 66), with Ba^{2+} substituted for Sr^{2+}. Refinement of the lattice parameters and all atomic positions and isotropic displacements (bar V and with the O11, O12 and O13 site displacements fixed to be equal) gave a good fit to the data, although with anomalously large errors on the displacement

parameters (Appendix B, Table B.1). The deuterium position was placed ~ 1 Å from the hydroxide oxygen and it refined to an O–D bond length of 1.046 Å and to full occupancy. The final goodness-of-fit parameters were $R_{\rm wp} = 3.73$ and $\chi^2 = 1.062$ for 76 parameters.

The geometry of the refined CuO_6 octahedra closely resembles that described for 'Sr-vesignieite'. Using the advantages of neutron over X-ray diffraction in refining O positions, further attempts were made to search for subtle features of a dynamic JT effect. Various methods were used in this refinement to look for signatures of such an effect in the oxygen positions and displacement parameters. The data were not good enough to refine anisotropic displacement parameters, however splitting the oxygen positions of the CuO_6 octahedra is a useful alternative to this as it gives the directional information of the displacement.

For all oxygens of the CuO_6 octahedra, except the hydroxide oxygens, splitting the O11, O12 and O13 sites significantly improved the quality of the fit, lowering $R_{\rm wp}$ from 3.732 to 3.615 and χ^2 from 0.062 to 0.060 *i.e.* a ~ 3 % drop in each and also resolved the anomalously large errors on the displacement parameters seen previously. Splitting the O21(H) site further lowers the goodness-of-fit but the displacement parameter refined to a large negative number. To stabilise the refinement the O11, O12 and O13 must share the same displacement parameter which refines to a very small number (0.08 Å^2) and could not be refined simultaneously with the positions. This is unsurprising, since splitting the sites is effectively modelling the atomic displacement so the two are highly correlated and therefore unstable. The refined atomic information with the split oxygen sites is given in Appendix B, Table B.2.

Figure 6.9 shows the coordination of the two Cu sites in vesignieite from refinement with the split oxygen positions, along with the refined Cu–O bond lengths, at 4.2 K. Initially, discussion will focus on the Cu2 site. The alignment of the O11 and O13 oxygens around the Cu2 site is roughly parallel to the Cu2–O11 and Cu2–O13 bonds, respectively. Each of these oxygens is also bonded with Cu1, however their alignment is roughly perpendicular to this site. This is evident in the Cu–O bond lengths, for instance the difference between the Cu2–O11 bond lengths is 0.285 Å whereas this is only 0.075 Å for Cu1–O11. This is consistent with a dynamic JT effect on the Cu2 site, where the bonds with O11 and O13 are fluctuating between short and long configurations.

It is important to note that due to the C2 symmetry of the Cu2 site, the O11 atoms neighbour each other in the octahedron, *i.e.* $\angle$O11–Cu2–O11 $\sim 90\,^\circ$ (the same occurs for O13), and the O21(H) atoms are aligned on opposite sides of the central copper. Therefore, the $Cu2O_6$ cannot be statically JT distorted along either O11 or O13 bonds in this space group. Refinements in the lower symmetry space group $P3_1$, which lower the Cu2 site symmetry and allow it to be axially distorted, do not improve the quality of the fit. Furthermore, the refined structure in $P3_1$ is not consistent with a static JT distortion on the Cu2 site: the four equatorial Cu2–O bonds all refine to large values (< 2.2 Å). Thus, the neutron diffraction data provides strong evidence that the Cu2 site remains dynamically distorted at $T = 4.2$ K, well below $T_{\rm N}$.

The Cu1 has a quite different local coordination to the Cu2 site. Cu1 is bonded to O11, O13, 2 $\times$ O21(H) and 2 $\times$ O12 and the site has no symmetry restriction which means it cannot host an axial

a.

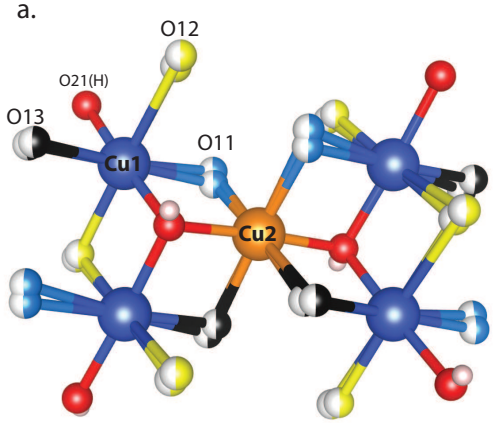

b.

		Cu1		Cu2	
		Bond length (Å)	Bond difference	Bond length (Å)	Bond difference
O11	long short	2.148 2.073	0.075	2.286 2.001	0.285
O12	long short	2.512 2.190	0.322		
	long short	2.576 2.221	0.355		
O13	long short	2.119 1.994	0.125	2.416 2.032	0.384
O21(H)		1.911 1.925		1.862	

Figure 6.9: Details of the vesignieite structure obtained form Rietveld refinement of neutron diffraction data collected at 4.2 K. **(Left)** Local coordination of the Cu1 and Cu2 sites that build the kagome planes and **(right)** the Cu–O bond lengths for both sites. The refinement was improved by splitting the oxygen sites to model the atomic displacement. The alignment of the split sites indicates the Cu2 is dynamically fluctuating between two JT distorted configurations. The Cu1 site appears to be statically distorted due to the displacement of the O11 and O13 sites as well as the long Cu1–O12 bond.

JT distortion. Figure 6.9 again shows the local coordination of the Cu1 site as well as the Cu1–O bond lengths. There are three distinct groups of Cu1–O bond lengths, long Cu1–O12, medium Cu1–O11 and –O13 and short Cu1–O21(H), giving the CuO_6 a rhombically distorted geometry which suggests dynamic JT fluctuations between two states of unequal energy. However, the alignments of the split O11 and O13 sites are not consistent with dynamic fluctuations but a static distortion, as they are aligned perpendicular to the Cu1 site. This is most clear in the bond length difference of the Cu1–O11 and –O13 bonds shown in the table: these bond differences are much smaller than for all other Cu–O bonds (~ 0.1 *vs.* > 0.28).

The split O12 site causes a large difference in Cu1–O12 bond lengths, which could be interpreted as a result of dynamic JT fluctuations. However, upon closer inspection, the O12 atom that links the Cu1 chains and the split O12 atoms align perpendicular to the Cu1–Cu1 bond. The large difference in the Cu1–O12 bond lengths may be a result of vibrations along the chains due to fluctuations of the neighbouring $Cu2O_6$. The length of the Cu1–O12 bond is further evidence that the $Cu1O_6$ is statically distorted, as it is significantly longer than the other four Cu1–O bonds. Therefore, at $T = 4.2\,\mathrm{K}$ it appears that the Cu1 site is statically distorted.

Data collected at 20 K, which lies above the magnetic transition in vesignieite of $T \approx 9\,\mathrm{K}$, are very similar to that collected at 4.2 K. Figure 6.10 shows both data sets as well as a difference plot (4 - 20 K). The most noticeable feature of the difference plot is the peak at $Q \approx 2.75\,\mathrm{Å}^{-1}$, which aligns with the most intense peak in the diffraction pattern. This may be a minor nuclear structural change or a magnetic Bragg peak, but this is hard to determine from this data. However, the overall similarities between the data collected at both temperatures indicates that there is no structural phase transition. Furthermore, the refined structure at 20 K is qualitatively the same as that at 4.2 K. The Cu1 and Cu2 sites adopt a 2+2+2 and axially compressed geometry, respectively, and the displacement of the oxygens modelled by site

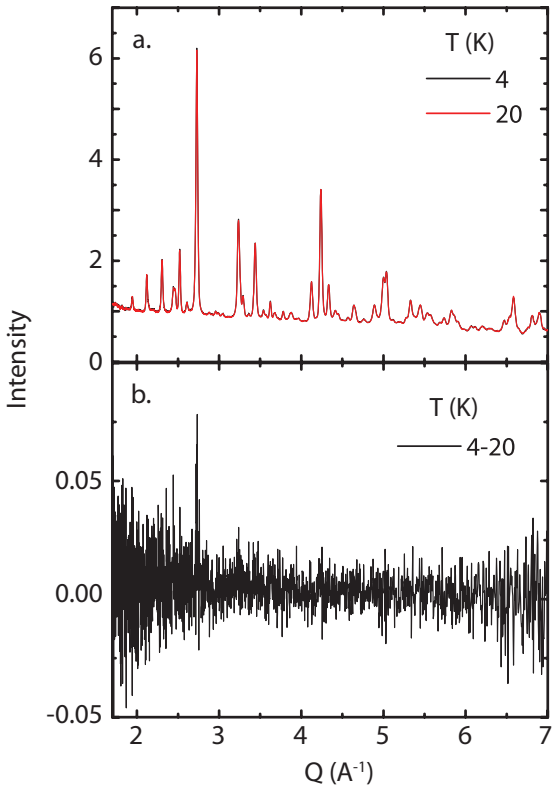

Figure 6.10: **a.** Neutron diffraction data collected at 4.2 and 20 K on bank 2 at the high-resolution HRPD beamline at ISIS, UK. **b.** Difference plot of 4.2-20 K. The peak at $Q \approx 2.75\,\text{Å}^{-1}$ may be a minor nuclear structure change but could also be a magnetic Bragg peak. The lack of features in the rest of the plot indicates no nuclear phase transition occurs between the temperatures.

splitting are similar and lead to the same conclusions as at low temperature.

The refinement of the 100 K data did not allow splitting of the oxygen sites. It caused the displacement parameters of the split sites to become large and negative, but using one site for each oxygen resolved this issue. The refined structure, however, has similar characteristics to that at low temperatures as the Cu1 and Cu2 sites retain the same distorted geometries. The cause of the refinement instabilities may originate from (i) the larger thermal parameters at high temperature correlating strongly with the split oxygen positions and/or (ii) the 100 K data was only collected for half the time as the other two temperatures.

The refined mean lengths for each Cu–O bond at 4, 20 and 100 K are shown in Table 6.3. Whilst there is no obvious temperature dependence for each bond, it is noteworthy that the proposed dynamic Cu–O bonds vary by ≥ 0.06 Å between the refinements whilst the static Cu–O21(H) bonds vary by only 0.01 or 0.02 Å. This indicates a greater certainty in the refined Cu–O21(H) bonds, which would be expected of static rather than dynamic bonds. Higher quality neutron diffraction data at more temperature steps, perhaps combined with synchrotron diffraction, may give an accurate temperature dependence of these Cu–O bonds and help prove their static and dynamic nature, as was done in the Cu^{2+} Tutton salts [20].

The high-resolution powder neutron diffraction data indicates that vesignieite, like the isoelectronic

	Mean bond length (Å)			Cu–O_{max} - Cu–O_{min} (Å)
Cu–O bond	4 K	20 K	100 K	
Cu1–O11	2.11	2.04	2.02	0.09
Cu1–O12	2.38	2.45	2.38	0.07
Cu1–O13	2.06	2.12	2.07	0.06
Cu1–O21(H)	1.92	1.93	1.91	0.02
Cu2–O11	2.14	2.15	2.24	0.10
Cu2–O13	2.22	2.18	2.14	0.08
Cu2–O21(H)	1.86	1.85	1.86	0.01

Table 6.3: The refined mean Cu–O bond lengths between $4.2 < T < 100$ K for vesignieite obtained from high-resolution powder neutron diffraction data. The 2+2+2 rhombically distorted $Cu1O_6$ and 2+4 axially compressed $Cu2_6$ occurs at all temperatures, indicating the Cu2 site remains dynamically JT distorted at 4.2 K. The large range in bond lengths with temperature for the Cu–O11, Cu–O12 and Cu–O13 bonds is expected of dynamic bonds. Contrastingly, the static Cu–O21(H) bonds do not have a large T-dependence due to a greater certainty of refined values.

material 'Sr-vesignieite', possesses a dynamic JT effect. The Cu2 site remains dynamic at 4.2 K, well below the magnetic transition at $T \approx 9$ K, whilst the refinement at 100 K suggests that the Cu1 site is statically distorted at this temperature. In 'Sr-vesignieite', the Cu1 site transitions to a static JT state at $T_{\rm JT} \approx 230$ K (Chapter 5), therefore it is useful to determine if a similar JT transition occurs in these samples of vesignieite. The next section discusses variable temperature synchrotron diffraction in the temperature region $100 < T < 300$ K, performed in an attempt to further characterise the JT state of the two copper sites.

6.4.4 Powder synchrotron diffraction

Data was collected on the same vesignieite sample used in the previous section at the high-resolution synchrotron powder diffraction 11-BM beamline at the Advanced Photon Source (APS), Argonne National Lab, Illinois, USA using a rapid access service. The sample was loaded in a 0.8 mm kapton capillary with a packing density of $\rho = 0.90\,\mathrm{g\,cm^{-3}}$ and measured with a wavelength $\lambda = 0.413827$ Å to give an absorption $\mu R = 0.2$. Data were collected at 100, 140, 180, 220, 260 and 295 K up to $Q \approx 8\,\mathrm{Å^{-1}}$ ($d \approx 0.79$ Å). A full description of the beamline is given in Chapter 4 (Page 53).

Rietveld refinements were initially attempted with the 100 K data starting from the refined model from the neutron diffraction data collected at the same temperature. Unfortunately, the presence of the heavy Ba^{2+}, Cu^{2+} and V^{5+} ions made the refinement insensitive to the oxygen positions and the errors are too large to accurately obtain their temperature dependence. Therefore, analysis in this section is restricted to Pawley refinements which give the temperature dependence of the lattice parameters.

The refined lattice parameters for vesignieite as a function of temperature are plotted in Figure 6.11a and b. c decreases linearly as a function of temperature, whereas a levels off as the temperature is lowered to 100 K. The temperature dependence of a is evident in the c/a ratio, which appears to peak maximally at ~ 275 K before decreasing rapidly. This behaviour is similar to 'Sr-vesignieite', also

plotted in Figure 6.11b, and in that material indicates the static JT transition of the Cu1 site.

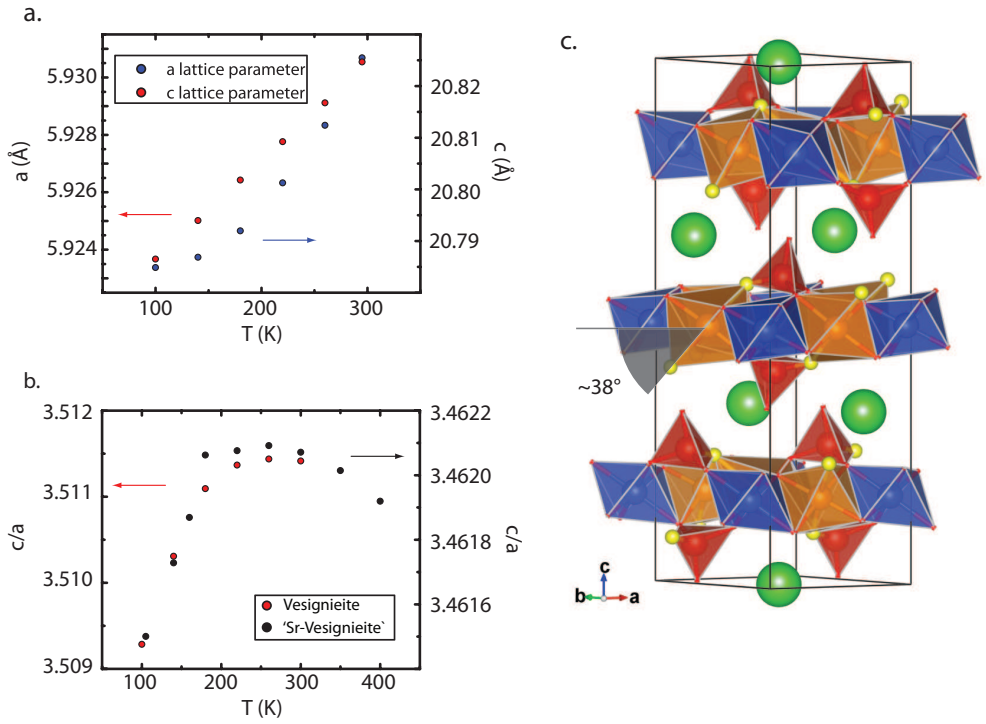

Figure 6.11: Temperature dependence of the a and c lattice parameters for vesignieite from powder synchrotron diffraction in **a.** and of the c/a ratio for both vesignieite and 'Sr-vesignieite' in **b**. The change in behaviour of c/a in 'Sr-vesignieite' is due to a JT transition and the similar behaviour in vesignieite indicates a similar process. **c.** The JT transition involves elongation of the Cu1–O12 bond (O12 atom highlighted in yellow), which makes an angle of $\sim 38^\circ$ with the ab plane. Combined with the relatively weak interplanar connections, this means the JT transition has the biggest effect on the a lattice parameter, explaining the observed lattice parameter temperature dependence.

JT transitions are well parameterised by the temperature dependence of the c/a ratio [21, 22]. In the case of vesignieite, the kagome layers lie in the ab plane and the long Cu1–O12 bond of the 2+2+2 rhombically distorted CuO_6 octahedra also lies mostly within this plane, making a $\sim 38^\circ$ angle with it (Figure 6.11c). Therefore, a lengthening of the Cu1–O12 bond due to a transition to a static JT state would be expected to increase the a lattice parameter. The relatively weak bonding between the kagome planes, rather than the close packing of CuO_6 in the ab plane, may dampen any effect on c due to the JT transition. The temperature dependence of the c/a ratio can be understood within this model of the JT transition.

First- and second-order JT transitions have been documented in the literature [22]. The spinel $LiMn_2O_4$ undergoes a first-order JT phase transition with a structural symmetry lowering from cubic $Fd\bar{3}m$ to orthorhombic $I4_1amd$ [21]. The behaviour of the crystallographic parameters discussed for vesignieite suggest the transition may also be first-order, however any structural symmetry lowering is much harder to define. Evidently the lower symmetry structure must index with the same hkl, as no new peaks or peak splittings are observed in this temperature range. There is also a possibility that the JT

transition does not result in a lowering of the structural symmetry, as occurs in $LaMnO_3$ [23].

6.4.5 Raman spectroscopy

In Section 6.3, the effect of hydrothermal annealing on poor quality vesignieite samples is discussed with respect to Raman data, whereby the Raman linewidth parameterises the sample disorder. A comparison of the Raman spectra collected for vesignieite samples prepared using old and new synthetic methods is shown in Figure 6.12a. The sample prepared *via.* the old technique was annealed for 7 days and therefore the peak width is narrower than an unannealed sample and yet the sample prepared *via.* the new method has significantly narrower peaks. Furthermore, the spectra of the new sample shows no extra Raman peaks and therefore there is no change in local symmetry between the samples. This corroborates the previous theory that vesignieite crystallises with $P3_121$ symmetry and crystallographic changes between samples are related to an ordering of the $P3_121$ structure.

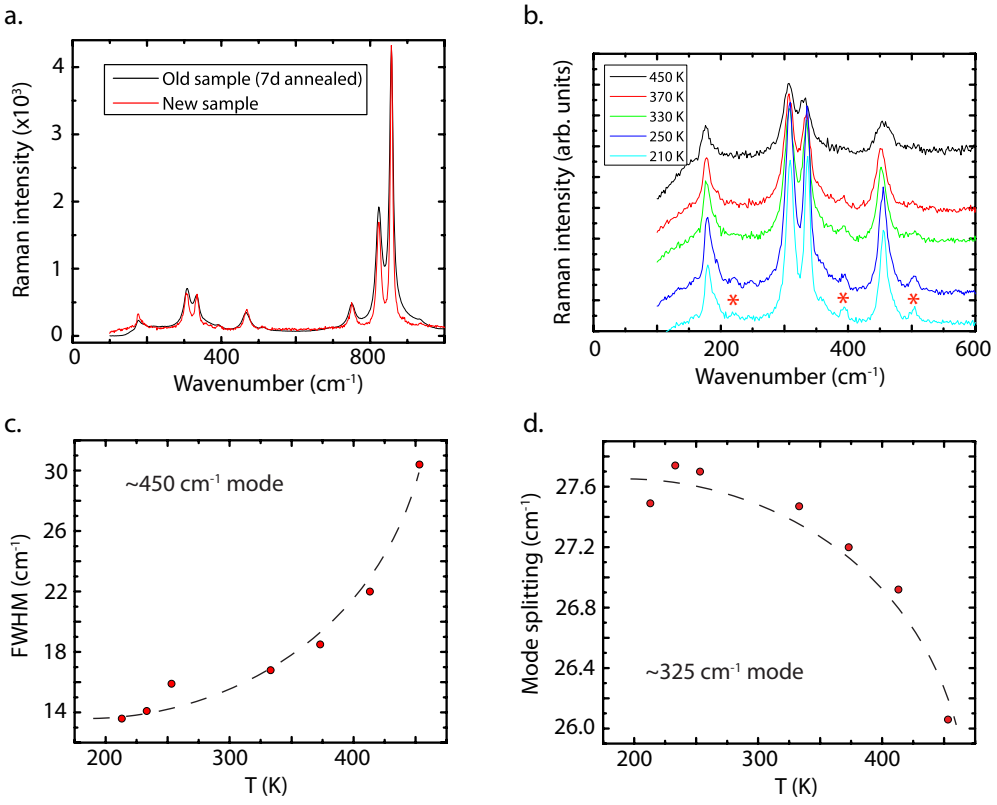

Figure 6.12: a. Comparison of Raman spectra of vesignieite samples prepared using old and new synthetic methods. The new sample shows no extra peaks but a decrease in peak FWHM, indicating that the samples feature the same local symmetry and the new samples are significantly more crystalline. **b.** Temperature dependence of the Raman spectra for the new vesignieite samples. A general broadening of the modes occurs as the temperature is increased, whilst the modes indicated have disappeared by 450 K. **c.** The temperature dependence of the FWHM of the mode at 450 cm^{-1} showing it broadens significantly with increasing temperature **d.** The splitting of the $\sim$ 325 cm^{-1} mode as a function of temperature. The splitting remains constant above $\sim$ 300 K in agreement with the transition to a static JT state.

Raman spectroscopy is a useful technique for investigating JT transitions as it is sensitive to the local

symmetry changes that occur, often indistinguishable *via.* diffraction techniques. In the related $S = \frac{1}{2}$ kagome mineral volborthite, temperature dependent Raman spectroscopy revealed a symmetry lowering transition at low temperature, previously unobserved in polycrystalline samples [16]. The nature of this transition is not well understood, but is likely related to a structural transition observed at much higher temperature in a single crystal and may be suppressed in poorly crystalline samples [24].

Temperature dependent Raman spectra were collected on the same deuterated vesignieite sample used for neutron and synchrotron diffraction. The temperature stage used was a Linkam THMS600 with spectra collected between 210 and 450 K in the wavenumber region $100 < \nu < 1500\,\mathrm{cm}^{-1}$. Achieving a good focus with the Raman microscope was difficult due to the temperature stage, therefore the signal-to-noise is much poorer than previous measurements and regions above $1500\,\mathrm{cm}^{-1}$ are very noisy. Low energy regions of spectra at selected temperatures are shown in Figure 6.12b.

As expected, a general broadening of modes occurs with increasing temperature, of the type previously documented in the literature for powdered vesignieite samples [16]. To quantify this the $\sim 450\,\mathrm{cm}^{-1}$ mode, which appears to consist of a single excitation, was fitted with a Lorentzian and the refined FWHM plotted as a function of temperature, shown in Figure 6.12c. The FWHM is relatively constant below 300 K, however above this temperature the linewidth increases rapidly. This temperature dependence is also evident in the modes indicated in the figure: above 300 K their intensity rapidly decreases until they are difficult to distinguish by 450 K.

The Raman shift of the double peak at $\sim 350\,\mathrm{cm}^{-1}$ has a remarkably similar temperature dependence to the linewidth. Fitting this with two Lorentzians, the difference between the centres of the two peaks is plotted as a function of temperature in Figure 6.12d. The splitting is relatively constant at $\sim 27.6\,\mathrm{cm}^{-1}$ below 300 K, but then decreases rapidly above this temperature. Extrapolating this graph to higher temperatures, the two peaks quickly merge likely indicating a structural transition. Site symmetry analysis [4] of the $P3_121$ structure of vesignieite predicts $26\mathrm{A}_1 + 53\mathrm{E}_1$ Raman active modes but only $6\mathrm{A}_{1\mathrm{g}} + 7\mathrm{E}_{\mathrm{g}}$ for the $R\bar{3}m$ structure. Therefore a transition to a higher symmetry rhombohedral structure, such as that suggested for β-vesignieite [2], would result in a dramatic decrease in the number of Raman peaks. The merging of the modes at $\sim 325\,\mathrm{cm}^{-1}$ hints at this eventuality.

The plateauing of these features in the Raman spectra below 300 K coincides with the distinct change in the temperature dependence of the $\frac{c}{a}$ ratio and both can be understood within the theory of a JT transition. In $LaMnO_3$, a similar Raman phonon mode broadening occurs at the cooperative JT transition to that shown in Figure 6.12c [25]. In this material, the mode FWHM has a relatively shallow increase at temperatures well below the JT transition, but approaching the transition it rapidly increases and persists well above it due to dynamic JT fluctuations. The merging of the $325\,\mathrm{cm}^{-1}$ modes also suggests an eventual transition, which would be expected in the fully dynamic JT state of vesignieite.

6.5 Diamagnetic doping of vesignieite, $\mathbf{BaCu_{3-x}Zn_xV_2O_8(OH)_2}$

Diamagnetic doping of frustrated magnets has proven to be a useful tool for investigating their intrinsic properties. In the related mineral volborthite, doping revealed its frustrated ground state to be less robust than other known kagome-based magnets [26]. In the kagome bilayer SCGO, the dynamic spin proper-

ties do not drastically change above the site percolation threshold, p_c, showing they do not arise from a collective phenomenon and are localised [27].

Studies of doped vesignieite samples are not present in the literature. As well as providing a useful magnetic study, doped vesignieite samples should also help in characterising the nuclear structure, particularly as diamagnetic ions will necessarily be non-JT active. This chapter details some crystallographic studies of Zn^{2+} doped vesignieite, $BaCu_{3-x}Zn_xV_2O_8(OH)_2$, using diffraction techniques and Raman spectroscopy.

6.5.1 Synthesis

The synthetic route described in Section 6.4.1 provides the basis for producing Zn^{2+} doped vesignieite samples. To successfully dope vesignieite, it is first necessary to synthesise doped volborthite samples, $Cu_{3-x}Zn_xV_2O_7(OH)_2 \cdot 2H_2O$. Methods of doing this in the literature involve hydrothermal synthesis [26], however here it was achieved *via.* a simple reaction: a mixture of $Cu(OH)_2$, $Zn(OH)_2$ and V_2O_5 are stirred in 100 ml distilled water for 2 days at room temperature, with the required starting reagents for a 2 g theoretical yield calculated from the following reaction equations:

$$Cu(NO_3)_2 \cdot H_2O + 2NaOH \rightarrow Cu(OH)_2 + 2NaNO_3 + H_2O \tag{6.4}$$

$$Zn(CH_3COO)_2 \cdot 2H_2O + 2NaOH \rightarrow Zn(OH)_2 + 2Na(CH_3COO) + H_2O \tag{6.5}$$

$$(3-x)Cu(OH)_2 + (x)Zn(OH)_2 + V_2O_5 + 2H_2O \rightarrow Cu_{3-x}Zn_xV_2O_7(OH)_2 \cdot 2H_2O + 3H_2O \tag{6.6}$$

The final synthetic method for $BaCu_{3-x}Zn_xV_2O_8(OH)_2$ is as follows, with exact reagent amounts for the different x values given in Appendix B, Table B.3. $Cu(NO_3)_2 \cdot H_2O$ or $Zn(CH_3COO)_2 \cdot H_2O$ and NaOH are separately dissolved in 30 ml distilled water in 100 ml conical flasks. Once dissolved the two solutions are combined and stirred for 5 mins using a magnetic stirrer. The resulting $Cu(OH)_2$ or $Zn(OH)_2$ is collected in a 50 ml centrifuge tube with ~ 50 ml distilled water, centrifuged for 2 mins at 4400 rpm and the water then discarded. This process is repeated once more before the two reagents are poured into a 100 ml conical flask with distilled water to ensure all powder is collected. V_2O_5 is then added to the conical flask, along with a magnetic stirrer, and the solution made up to 100 ml with distilled water. The flask is covered and stirred for 2 days at 200 rpm at room temperature. The green/yellow powder is collected in a 50 ml centrifuge tube and washed three times with ~ 50 ml distilled water and then three times with 50 ml acetone before being dried on a rotary evaporator.

The Zn-doped volborthite is then used to produce Zn-doped vesignieite with the exact same hydrothermal method described in the previous section, where starting reagents are calculated from the reaction equation:

$$Cu_{3-x}Zn_xV_2O_7(OH)_2 \cdot 2H_2O + Ba(CH_3COO)_2 \rightarrow BaCu_{3-x}Zn_xV_2O_8(OH)_2 + 2CH_3COOH + H_2O \tag{6.7}$$

For $x = 0, 0.15, 0.2, 0.3, 0.6, 1$ and 2, these reactions were performed by an undergraduate M.Sci. student in our group (Zoe Chambers) and are detailed in full in [28]. For $x = 3$, *i.e.* 'Zn-vesignieite' $BaZn_3V_2O_8(OH)_2$, I performed the reaction using exactly the same method. Refined lattice parameters from lab X-ray diffraction data show an increase in the c lattice parameter as a function of x that indicates successful Zn^{2+} doping [28], as Zn^{2+} has a slightly larger ionic radius than Cu^{2+}.

6.5.2 Lab X-ray diffraction study

Lab based X-ray diffraction spectra were collected at room temperature for samples of Zn-doped vesignieite with $x = 0.15, 0.6, 1, 2$ and 3. A STOE STADI-P spectrometer was used where each sample was loaded in a borosilicate capillary with 0.3 mm diameter. A full description of the diffractometer is found in Chapter 4 (Page 52).

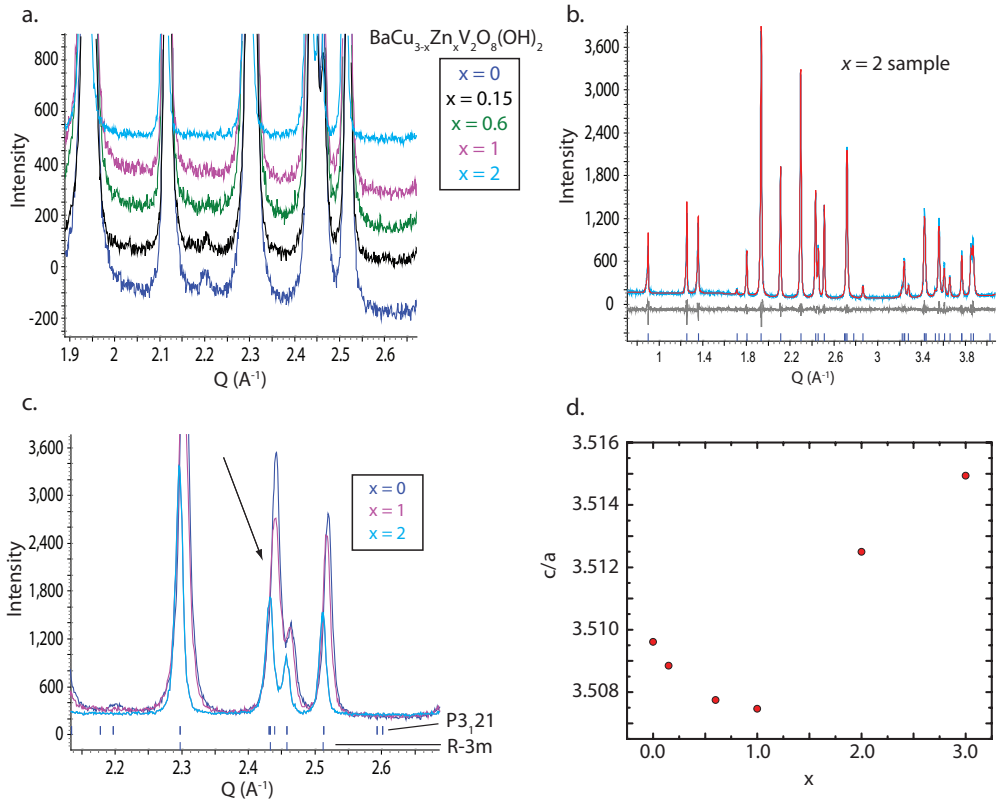

Figure 6.13: **a.** X-ray diffraction data of $BaCu_{3-x}Zn_xV_2O_8(OH)_2$ with a range of x values. The peak at $Q \sim 2.2\,\text{Å}^{-1}$ is associated with a $P3_121$ structure and reduces in intensity with increased x. **b.** Pawley refinement of a sample with $x = 2$ based on a powder X-ray diffraction study with $R3$ symmetry. **c.** A distinct change in peak position and narrowing of the profile between $1 < x < 2$ signifies a phase transition. **d.** The c/a lattice parameter ratio shows a significant change in behaviour above $x = 1$ that coincides with the peak shift.

Figure 6.13a shows X-ray diffraction spectra for Zn-doped vesignieite samples with various x values. With increasing x, the most intense peak associated with the $P3_121$ structure at $Q = 2.2\,\text{Å}^{-1}$ gradually reduces in intensity. At $x = 1$ it is hard to determine if the peak is present, however by $x = 2$ it has disappeared and this Q-region has a very flat background. Other smaller peaks that index with the

$P3_121$ structure are also not present in the spectrum of the $x = 2$ sample and it instead indexes with $R\overline{3}$ symmetry. The data is excellently fitted with $R\overline{3}$ symmetry suggesting the sample has gone through a structural phase transition by $x = 2$ (Figure 6.13b).

Further evidence of a structural phase transition is found in a significant peak shift and lattice parameter change in the $1 < x < 2$ region. Figure 6.13c highlights the peak at $Q = 2.44\,\text{Å}^{-1}$ that is defined by three reflections in $P3_121$, but only one in $R\overline{3}$. Between $1 < x < 2$ this peak appears to sharpen, as would be expected in the higher symmetry rhombohedral structure. This shift is quantified in the c/a lattice parameter ratio plotted in Figure 6.13d, which shows a clear change of behaviour above $x = 1$.

6.5.3 Raman spectroscopy

Raman spectra were collected using the same equipment previously described in this chapter and fully detailed in Chapter 4 (Page 59). Samples with $x = 0, 0.15, 0.3, 0.6, 1, 2$ and 3 were measured between $100 < \nu < 4000\,\text{cm}^{-1}$ using a green laser with wavelength of $\lambda = 514.5\,\text{nm}$. To achieve an accurate focus on the Raman microscope samples were dispersed in acetone, briefly ultrasonicated and placed onto a glass slide using a pipette. Once dry, small crystallite clumps could be focussed on to obtain the best signal-to-noise.

A comparison of the low wavenumber region of the Raman spectra for samples with $x = 0, 1, 2$ and 3 is shown in Figure 6.14a. No significant changes occur between $x = 0$ and 1 aside from slight shifts in the Raman peaks, as would be expected upon cation substitution. However, above $x = 1$ the spectra changes dramatically with large peak shifts and intensity changes. The splitting of the mode at $\sim 300\,\text{cm}^{-1}$ is plotted in Figure 6.14d and shows a sudden change between $1 < x < 2$ in excellent agreement with the structural transition predicted from the X-ray diffraction data.

The high wavenumber region is shown in Figure 6.14b, although the $x = 3$ sample is plotted in Figure 6.14c as its high background makes it hard to compare with all samples. Above $2000\,\text{cm}^{-1}$, the spectra remain similar and as this region is mostly defined by vibrations involving H this is unsurprising, however between $1000 < \text{cm}^{-1} < 2500$ several peaks broaden or disappear between $1 < x < 2$ and in the $x = 3$ sample this region is relatively featureless aside from the fluorescence.

The significant changes in Raman bands between $1 < x < 2$ coincides with the structural transition observed in the X-ray diffraction data. The X-ray diffraction data of the $x = 2$ sample revealed that the sample crystallised with $R\overline{3}$ symmetry, however several space groups have the same pattern of observed diffraction peaks in powder averaged diffraction data and Pawley refinements are unable to determine between them. $R\overline{3}m$ offers a likely high symmetry description of vesignieite, as shown in the analysis of β-vesignieite [2], however $R32$ is also a possibility as it is a minimal supergroup of $P3_121$. The Raman active modes of the vesignieite structure in each of these descriptions, obtained from group theory analysis, is shown in Table 6.4.

To compare the low- and high-symmetry structures of doped vesignieite samples, the Raman spectra for the $x = 0$ and $x = 3$ samples were fitted to obtain the number of modes. The background was defined by a spline interpolation of manually defined points and the Raman modes were each modelled

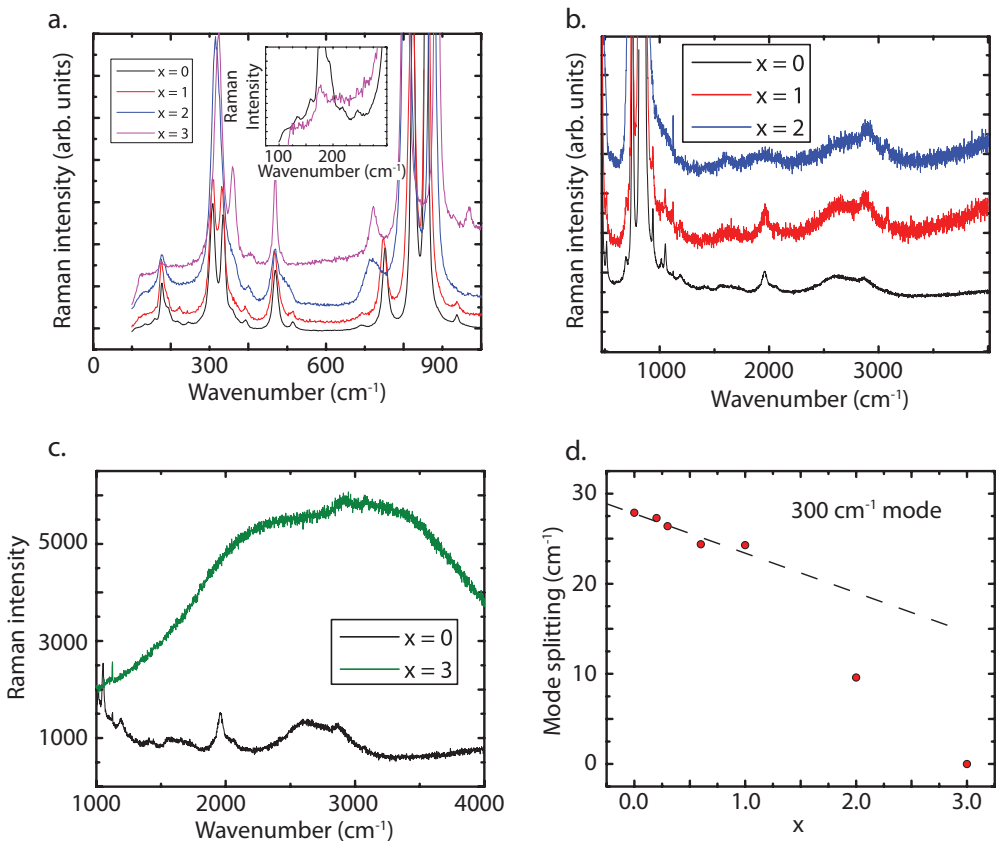

Figure 6.14: **a.** Comparison of the low wavenumber region of the Raman spectra collected for doped vesignieite samples with $0 < x < 3$. The two peaks at $\sim 325\,\mathrm{cm}^{-1}$ merge above $x = 2$, which is a good indication of a structural transition. The inset shows the $< 300\,\mathrm{cm}^{-1}$ region where significantly fewer peaks are present in the $x = 3$ sample. **b.** High wavenumber region for the $x = 0, 1$ and 2 samples. The modes between $1000 < x\mathrm{cm}^{-1}2500$ significantly broaden between $1 < x < 2$ and some disappear completely. **c.** A comparison of the high wavenumber region for the $x = 0$ and 3 samples. The large fluorescence for the $x = 3$ sample limits the analysis, but it is clear that there are very few peaks in this region. **d.** Splitting of the $\sim 300\,\mathrm{cm}^{-1}$ mode as a function of x. The sudden change at $x = 2$ indicates a structural phase transition in agreement with the X-ray diffraction data. The dashed line is a guide to the eye.

by a Lorentzian peak shape. The final fit for the low wavenumber regions are shown in Figure 6.15a and b. The $x = 0$ and $x = 3$ samples are excellently modelled by 19 and 10 peaks respectively and for both samples the FWHM of any peak does not exceed $25\,\mathrm{cm}^{-1}$ suggesting there are no unobserved splittings.

The 10 modes in low wavenumber region of the data on the $x = 3$ sample is significantly less than the 19 fitted to the $x = 0$ data. The large difference in the number of modes is strong evidence that the two samples adopt different structures. This is corroborated by the high wavenumber region which does not appear to contain many peaks, particularly when compared to the $x = 0$ sample (Figure 6.14c). The number of observable peaks for the $x = 3$ sample then matches well with the 13 peaks predicted for a $R\bar{3}m$ structure and is significantly less than for $R32$. Therefore, the structural phase transition with increasing x in doped vesignieite is from $P3_121$ to $R\bar{3}m$.

Space group	Raman active modes	Total modes
$P3_121$	$26A_1 + 53E$	79
$R32$	$8A_1 + 17E$	25
$R\bar{3}m$	$6A_{1g} + 7E_g$	13

Table 6.4: Raman active modes for the vesignieite structure in each of the descriptions, predicted from site symmetry analysis [4].

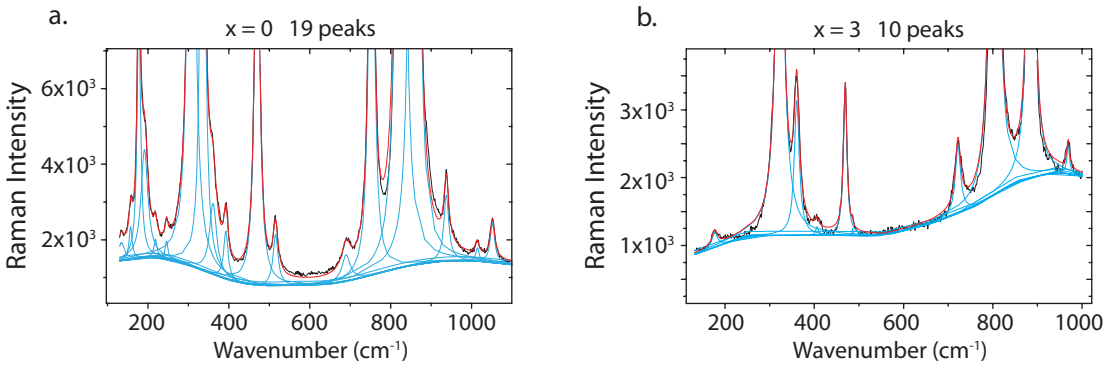

Figure 6.15: a. A fit to the Raman data of the $x = 0$ sample with multiple Lorentzian peaks. This region of the spectrum is excellently modelled with 19 peaks. **b.** A similar fit to the Raman data of the $x = 3$ sample. The same region for this sample can be modelled with only 10 peaks, providing strong evidence that the structural transition in doped vesignieite is between $P3_121$ and $R\bar{3}m$.

6.6 Discussion

The results in this chapter show that vesignieite crystallises with trigonal $P3_121$ symmetry, rather than the monoclinic or rhombohedral structures previously suggested in the literature [1, 2]. Analysis of the local Cu^{2+} coordination reveals a dynamic JT effect, similar to that shown in 'Sr-vesignieite'. It is important to now discuss how both this revised structure and the inclusion of orbital frustration impacts our understanding of the magnetic properties in this $S = \frac{1}{2}$ KAFM.

6.6.1 Revised $P3_121$ structure of vesignieite

The X-ray diffraction data show how the revised $P3_121$ structure of vesignieite is masked in poor quality samples due to crystallographic disorder. Evidently, in highly crystalline samples the $P3_121$ structure is fully ordered and the Cu1 sites enter a cooperative JT state. It logically follows that the crystallographic disorder is related to the JT transition. From the Williamson-Hall plots in Section 6.3 the structure shows particular strain along the $[0kk]$ directions, likely due to stacking faults created in the crystallisation process. Figure 6.16 shows the $(0kk)$ planes in the $P3_121$ structure, which contain the O12 atoms of the elongated $Cu1O_6$ bonds on the JT distorted Cu1 site. A possible scenario for these faults is between domains of dynamic and static JT ordered regions along chains of Cu1 sites. This partial order fits in with the broad diffraction and Raman features in poorly crystalline samples, whilst in annealed or high-quality samples with fewer stacking faults the structure has entered a fully ordered JT state with $P3_121$ symmetry. Such a model resembles an order-disorder transition as a function of annealing, similar to

that observed in $LaMnO_3$ as a function of temperature [29].

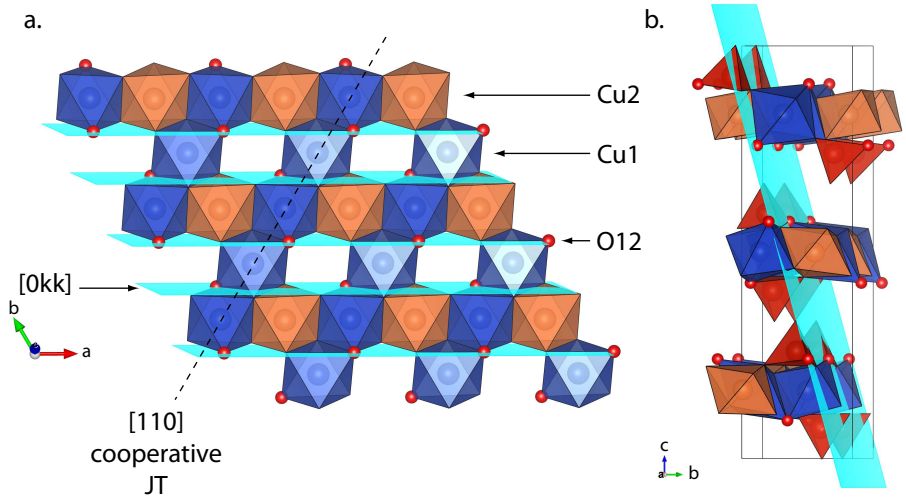

Figure 6.16: **a.** A view of the vesignieite structure along the [001] direction. The $(0kk)$ planes show significant disorder such as strain or stacking faults in poorly crystalline samples of vesignieite with broad diffraction and Raman features (highlighted in blue). These planes contain the O12 atoms of the elongated cooperative JT distortion on the $Cu1O_6$. Therefore, the stacking faults may result from domains of static and dynamic JT distortions along the Cu1 chains. **b.** A view of the crystal structure showing all three kagome planes within the unit cell. The 3_1 screw axis rotates each kagome plane by 120° along [00l] but powder averaging makes all planes equivalent with respect to the [0kk] disorder.

Doping with the diamagnetic and non-JT active Zn^{2+} ion ($BaCu_{3-x}Zn_xV_2O_8(OH)_2$) gives further insight into the JT structure of vesignieite. Above $x = 2$ there is no evidence of short-range or long-range JT distortions in the diffraction data and the material adopts a rhombohedral $R\bar{3}m$ structure. Thus, the percolation limit for a cooperative JT effect must lie between $1 < x < 2$, which is close to that observed in $Ba_2Cu_{1-x}Zn_xWO_6$ (0.77) [30]. Zn^{2+} doping does not broaden the Raman spectra but instead peaks disappear or merge suggesting a transition to a higher symmetry structure but not of order-disorder type. Furthermore, no soft phonon mode with $\nu \to 0\,\mathrm{cm}^{-1}$ near the transition is easily observed in the Raman spectra indicative of a displacive transition. Therefore, the transition with Zn^{2+} doping is a different process to that induced by annealing or temperature, but these results strongly suggests that the Jahn-Teller active Cu sites drive a symmetry lowering transition to $P3_121$ in pure vesignieite.

6.6.2 A magnetic model with coupled orbitals and spins

Improving the quality of vesignieite samples evidently strengthens the magnetic transition at $T_\mathrm{N} \sim 9\,\mathrm{K}$. As the sample improvements induce a cooperative JT transition, the latter must therefore aid stabilisation of long-range magnetic order. This observation could be understood as general relieving of frustration with reduced orbital degeneracy: it is often the case that orbital order coincides with spin order [31]. The increased frustration in poor quality samples is evidenced by the absence of a clear transition in χ and heterogeneous ground states of frozen and dynamic spins [32]. These observations agree with the picture of JT domains: spins freeze when in JT ordered regions, but remain dynamic in fully orbitally

frustrated regions.

A further consequence of the $P3_121$ structure in vesignieite is a change in the orbital occupation compared to previous analysis. The nearest neighbour superexchange path was previously thought to be mediated by the oxygen of the OH^{-1} group *via.* the d_{z^2} orbitals of two Cu^{2+} sites [3]. This distinguished it from both herbertsmithite, where the Cu^{2+} $d_{x^2-y^2}$ orbitals mediate the superexchange, and volborthite, where both Cu^{2+} $d_{x^2-y^2}$ d_{z^2} are singly occupied on different sites. Instead, the Cu^{2+} $d_{x^2-y^2}$ orbitals mediate all the superexchange paths in vesignieite, which leaves open multiple exchange paths *via.* both the μ_3-hydroxide group and the oxygens of the VO_4 tetrahedron. The latter may allow further nearest-neighbour superexchange *via.* the VO_4, for instance across the kagome hexagon as occurs in kapellasite [33].

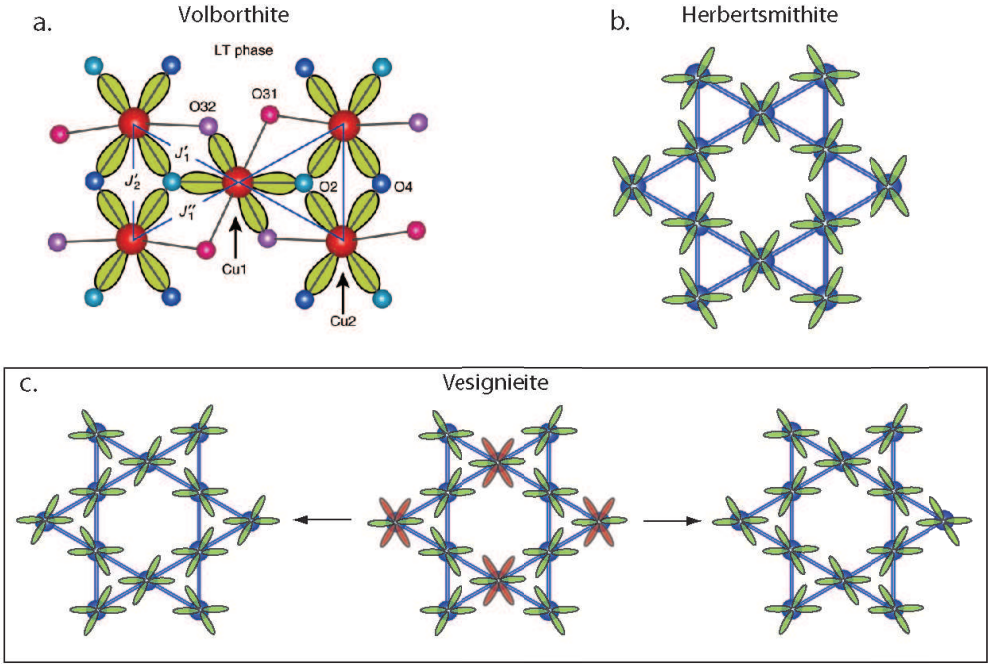

Figure 6.17: **a.** Orbital ordering diagram of high-quality volborthite single crystals at $T < 310\,\mathrm{K}$ [24]. The ordering does not have 3-fold rotational symmetry resulting in an inequivalence of exchange interactions. **b.** In herbertsmithite, the orbital ordering retains 3-fold symmetry on each kagome triangle and therefore there is no such inequivalence in the exchange interactions. **c.** The revised orbital ordering of vesignieite resembles that of volborthite. Ordering of the dynamic JT Cu^{2+} site necessarily destroys the 3-fold rotation axis and results in a mixture of ferro- and antiferro-orbital order.

A comparison between the orbital arrangement of the $S = \frac{1}{2}$ KAFMs volborthite, vesignieite and herbertsmithite is shown in Figure 6.17. In volborthite, recent experiments on single crystals confirmed that at low temperatures the orbital ordering diagram is as shown in Figure 6.17a, whereby the central Cu^{2+} site has entered a static JT distortion that destroys the 3-fold rotational symmetry of the exchange interactions. Consequently both ferro- and antiferro-orbital order occurs within the kagome plane that causes an inequivalence of the exchange interactions. In herbertsmithite, Figure 6.17b, the orbitals are ordered in a 120 °structure that retains the 3-fold rotation axis that relates them. The orbital ordering dia-

gram of vesignieite has more resemblance with volborthite than herbertsmithite, Figure 6.16c. Ordering of the dynamic Cu^{2+} site necessarily destroys the 3-fold rotational symmetry and produces a mixture of ferro- and antiferro-orbital order. Interestingly, the neutron diffraction data indicates that the Cu^{2+} site remains dynamic down to at least $T = 4.5\,\mathrm{K}$, well below the $T = 310\,\mathrm{K}$ orbital ordering transition of high-quality volborthite samples.

6.7 Future work

The powder neutron diffraction data discussed in this chapter provides strong evidence of the orbitally disordered state below T_N. To complement this data, a Raman scattering study at and below T_N using these new high quality samples would give information on any local symmetry changes that are not resolved with diffraction techniques. A previous Raman experiment on a poor quality sample revealed changes below $T \sim 30\,\mathrm{K}$ that they attributed to a magnetic scattering process, but they did not elaborate any further on its origins [16]. Analysis of such data with this new model of vesignieite may help to clarify the changes observed.

6.8 Conclusions

Vesignieite is one of the best model $S = \frac{1}{2}$ KAFM systems with no site-disorder such as in herbertsmithite or kapellasite and only a negligible distortion of the kagome lattice. However, the sample dependent magnetic behaviour found in the literature has hindered a true understanding of this material, such as the the cause of the magnetic transition despite the nearly ideal structure. Section 6.3 in this chapter describes diffraction and Raman experiments that reveal significant crystallographic disorder in vesignieite, the degree of which appears to define the magnetic properties. Through hydrothermal annealing the disorder can be reduced to reveal a $P3_121$ structure not previously reported. Evidence for the latter is also found in diffraction data from the literature, suggesting that this trigonal structure is universal to vesignieite samples.

In Section 6.4, a new synthetic method is detailed, adapted from that used for 'Sr-vesignieite' in Chapter 5, that produces high quality samples of powdered vesignieite. From analysis of diffraction and Raman data, these samples have significantly reduced crystallographic disorder and a trigonal $P3_121$ structure with distorted CuO_6 octahedra consistent with dynamic Jahn-Teller effects, as also found in 'Sr-vesignieite'. Diamagnetically Zn^{2+} doped samples reveal that the Jahn-Teller distortion on one of the Cu sites causes a symmetry lowering transition from rhombohedral to the refined trigonal structure in pure vesignieite. However, one of the Cu sites remains dynamic down to $T = 4.2\,\mathrm{K}$, as shown from the neutron diffraction data, well below the magnetic ordering transition. The persistence of orbital frustration down to very low temperatures means we must reevaluate our understanding of the magnetic properties in vesignieite by including the effects of orbital physics, particularly when compared to other $S = \frac{1}{2}$ KAFMs.

Bibliography

[1] M. Zhesheng, H. Ruilin and Z. Xiaoling, *Acta Geol. Sin.*, 1991, **4**, 145–151.

[2] H. Yoshida, Y. Michiue, E. Takayama-Muromachi and M. Isobe, *J. Mater. Chem.*, 2012, **22**, 18793.

[3] Y. Okamoto, H. Yoshida and Z. Hiroi, *J. Phys. Soc. Japan*, 2009, **78**, 033701.

[4] M. I. Aroyo, J. M. Perez-Mato, C. Capillas, E. Kroumova, S. Ivantchev, G. Madariaga, A. Kirov and H. Wondratschek, *Zeitschrift für Krist.*, 2006, **221**, 15–27.

[5] R. H. Colman, F. Bert, D. Boldrin, A. Hillier, P. Manuel, P. Mendels and A. S. Wills, *Phys. Rev. B*, 2011, **83**, 180416.

[6] Z. Hiroi, M. Hanawa, N. Kobayashi, M. Nohara, H. Takagi, Y. Kato and M. Takigawa, *J. Phys. Soc. Japan*, 2001, **70**, 3377–3384.

[7] M. Yoshida, Y. Okamoto and H. Yoshida, *J. Phys. Soc. Japan*, 2013, **82**, 013702.

[8] C.-D. Wu, C.-Z. Lu, X. Lin, S.-F. Lu, H.-H. Zhuang and J.-S. Huang, *J. Alloys Compd.*, 2004, **368**, 342–348.

[9] D. Boldrin, *M. Sci.*, University College London, 2010.

[10] Z. Hiroi, H. Yoshida, Y. Okamoto and M. Takigawa, *J. Phys. Conf. Ser.*, 2009, **145**, 012002.

[11] Bruker AXS, *TOPAS V4: General profile and structure analysis software for powder diffraction data*, 2008.

[12] P. W. Stephens, *J. Appl. Crystallogr.*, 1999, **32**, 281–289.

[13] R. E. Dinnebier and S. J. L. Billinge, *Powder diffraction: theory and practice*, Royal Society of Chemistry, 2008.

[14] A. Khorsand Zak, W. H. Abd. Majid, M. E. Abrishami and R. Yousefi, *Solid State Sci.*, 2011, **13**, 251–256.

[15] R. L. Frost, S. J. Palmer, J. Čejka, J. Sejkora, J. Plášil, S. Bahfenne and E. C. Keeffe, *J. Raman Spectrosc.*, 2011, **42**, 1701–1710.

[16] D. Wulferding, P. Lemmens, H. Yoshida, Y. Okamoto and Z. Hiroi, *J. Phys. Condens. Matter*, 2012, **24**, 185602.

[17] E. Kroumova, M. I. Aroyo, J. M. Perez-Mato, A. Kirov, C. Capillas, S. Ivantchev and H. Wondratschek, *Phase Transit. A Multinatl. J.*, 2003, **76**, 155–170.

[18] V. Srikanth, H. Idink, W. B. White, E. C. Subbarao, H. Rajagopal and a. Sequeira, *Acta Crystallogr. Sect. B Struct. Sci.*, 1996, **52**, 432–439.

[19] R. J. Nemanich, S. A. Solin and R. M. Martin, *Phys. Rev. B*, 1981, **23**, 6348–6356.

[20] M. A. Hitchman, W. Maaskant, J. V. D. Plas, C. J. Simmons and H. Stratemeier, *J. Am. Chem. Soc.*, 1999, **121**, 1488–1501.

[21] A. Yamada and M. Tanaka, *Mater. Res. Bull.*, 1995, **30**, 715–721.

[22] G. A. Gehring and K. A. Gehring, *Rep. Prog. Phys.*, 1975, **38**, 1–89.

[23] J. Rodríguez-Carvajal, M. Hennion, F. Moussa, A. H. Moudden, L. Pinsard and A. Revcolevschi, *Phys. Rev. B*, 1998, **57**, 3189–3192.

[24] H. Yoshida, J.-I. Yamaura, M. Isobe, Y. Okamoto, G. J. Nilsen and Z. Hiroi, *Nat. Commun.*, 2012, **3**, 860.

[25] L. Martin-Carron and A. de Andres, *Eur. Phys. J. B*, 2001, **22**, 11–16.

[26] F. Bert, D. Bono, P. Mendels, J.-C. Trombe, P. Millet, A. Amato, C. Baines and A. Hillier, *J. Phys. Condens. Matter*, 2004, **16**, S829–S834.

[27] A. Keren, Y. J. Uemura, G. Luke, P. Mendels, M. Mekata and T. Asano, *Phys. Rev. Lett.*, 2000, **84**, 3450–3.

[28] Z. Chambers, *M. Sci.*, University College London, 2014.

[29] E. Granado, J. A. Sanjurjo, C. Rettori, J. J. Neumeier and S. B. Oseroff, *Phys. Rev. B*, 2000, **62**, 304–307.

[30] D. Reinen, *J. Solid State Chem.*, 1979, **27**, 71–85.

[31] K. I. Kugel' and D. I. Khomskii, *Sov. Phys. Usp.*, 1982, **25**, 231–254.

[32] J. Quilliam, F. Bert, R. H. Colman, D. Boldrin, A. S. Wills and P. Mendels, *Phys. Rev. B*, 2011, **84**, 180401.

[33] B. Bernu, C. Lhuillier, E. Kermarrec, F. Bert, P. Mendels, R. H. Colman and A. S. Wills, *Phys. Rev. B*, 2013, **87**, 155107.

Chapter 7

Magnetic characterisation of vesignieite - a non-coplanar antiferromagnet

In the previous chapter, a crystallographic study of high-quality samples of vesignieite revised the crystal structure of this $S = \frac{1}{2}$ KAFM. The newly assigned crystal structure of vesignieite, and 'Sr-vesignieite', has $P3_121$ symmetry that corresponds to a symmetry reduction from a higher symmetry rhombohedral structure driven by a cooperative Jahn-Teller (JT) distortion on a sublattice of the Cu kagome network, with the remaining Cu sites dynamically JT distorted even at $T = 4.5\,\mathrm{K}$. Consequently, the previous orbital-ordering diagram predicted in vesignieite is incorrect and our understanding of the material's magnetic properties must be revised in light of this new model.

This chapter details magnetometry and inelastic neutron scattering measurements collected on high-quality vesignieite samples discussed in the previous chapter. Initially, a brief overview of the magnetic properties of vesignieite will be given followed by details of a scaled-up, deuterated synthesis method. The following two sections deal with SQUID measurements and powder inelastic neutron scattering experiments performed at the MERLIN and IN5 beamlines at ISIS and ILL, respectively. Finally, the results from these experiments will be discussed with relation to the newly defined crystal structure and compared with other frustrated magnets.

7.1 A review of magnetism in vesignieite

Detailed discussions of the magnetic properties of vesignieite are already given in Chapters 5 and 6, therefore this is intentionally brief and concentrates on features relevant to the rest of the chapter. An important point when discussing the properties of vesignieite is that they are highly dependent on the synthetic method used for sample preparation. As discussed in Chapter 6, this sample dependency is related to crystallographic disorder. This section discusses the sample dependent magnetic properties and what information this has given us on the intrinsic magnetism of vesignieite.

First, it is useful to briefly review the methods used for synthesis of vesignieite, as previously discussed in Chapter 6.2.2:

- **Method 1**: Hydrothermal reaction at $180^{\circ}\mathrm{C}$ followed by annealing at $580^{\circ}\mathrm{C}$ for 24 h to improve crystallinity [1, 2].

- **Method 2**: Reflux reaction followed by hydrothermal annealing at $\sim 200°\mathrm{C}$ to improve crystallinity [3, 4]. Chapter 6.3 presents a crystallographic study of these samples.

- **Method 3**: Slow-cooled hydrothermal reaction in acidified conditions to produce $\sim 0.25\,\mathrm{mm}$ single crystals [5].

The magnetic susceptibility of vesignieite displays highly frustrated properties. This is most easily characterised by the frustration ratio $f = \frac{|\Theta_\mathrm{w}|}{T_\mathrm{N}} \approx 77/9 = 8.6$, *i.e.* the antiferromagnetic transition is suppressed to well below the strength of the antiferromagnetic mean field interactions [6]. In samples prepared *via.* Method 2, which contain significant crystallographic disorder, the transition at $T_\mathrm{N} \sim 9\,\mathrm{K}$ features only a broad hump followed by a subsequent increase in χ as $T \to 0\,\mathrm{K}$ [3]. With improved sample quality, such as through longer annealing times in Method 2, the transition becomes clearer and a concomitant ZFC-FC splitting occurs [3, 4]. Samples prepared using Methods 1 and 3 display a sharp transition that peaks at $T = 9\,\mathrm{K}$ and then decreases as $T \to 0\,\mathrm{K}$, resembling a long-range antiferromagnetic transition [2, 5].

Local probe magnetic techniques also reveal the sample dependent magnetic properties. μSR measurements taken on a sample prepared using Method 2 revealed a heterogeneous ground state of dynamic and frozen spins below T_N [3]. ^{51}V-NMR measurements on the same sample confirmed the heterogeneous ground state and determined that the intrinsic susceptibility closely resembles the quantum spin liquid state of herbertsmithite [7]. However, measurements on samples prepared using Methods 1 and 3 are not consistent with a QSL ground state. ^{63,65}Cu-NMR measurements performed on these samples indicate the onset of long-range magnetic order involving all magnetic sites [2]. Yoshida *et al.* suggest the magnetic order has a $k = 0$ propagation vector, although such a deduction is difficult to gain from local probe NMR techniques. Further evidence against a QSL state comes from Raman scattering, which did not reveal a continuum of spinon excitations, as expected for a QSL and seen in herbertsmithite [8, 9].

Interestingly, it is not the distorted kagome lattice that drives the system away from a QSL state, as this is negligibly small in vesignieite [10], but instead a significant in-plane Dzyaloshinskii-Moriya (DM) interaction, D_p [11]. The DM interaction is predicted to be key in stabilising long-range ordered magnetic states on the $S = \frac{1}{2}$ KAFM [12] and may explain the quite different ground states observed, for instance, in herbertsmithite where the out-of-plane DM interaction is not large enough to destabilise the spin liquid ground state [13].

No further magnetic characterisation of high-quality samples exist in the literature and previous analysis of magnetic data have been performed without inclusion of orbital degeneracy originating from the dynamic JT effect. Therefore, determining the magnetic structure in vesignieite is of importance to (i) determine whether orbital physics impacts the magnetic ground state and (ii) to aid progress of theory, such as building a magnetic ground state phase diagram with respect to the DM interaction. The former raises interesting possibilities, such as spin-orbital liquid ground states, whilst the latter will build a better understanding of intrinsic $S = \frac{1}{2}$ KAFM physics and its stability to external perturbations.

7.2 Deuterated synthesis

In order to perform neutron scattering experiments on vesignieite, $BaCu_3V_2O_8(OH)_2$, it is necessary to synthesise a large deuterated sample. The synthesis described in Chapter 6 which involves the use of volborthite as a starting reagent is easy to adapt for deuterated samples largely because it is not necessary to first deuterate volborthite itself. This is evident when the amounts of deuterium present in the two sources of D in the starting reagents is calculated: 8.66×10^{-6} mol in 200 mg volborthite, $Cu_3V_2O_7(OH)_2{\cdot}2H_2O$, and 0.1 mol in 10 ml D_2O. Therefore, the only adaptation required for a deuterated synthesis is to use D_2O instead of H_2O as the reaction solvent and the full synthetic method is given in Chapter 6 (Page 102). Further attempts to scale-up the yield to $\sim$ 1 g of product resulted in long reaction times and problems with impurities. Therefore, a large sample was made from combination of several hydrothermal reactions.

Specifically for the sample synthesised and characterised in this chapter, a $\sim$ 9g sample was made from 20 reactions. This is slightly lower than the expected yield ($\sim$ 10 g) due to sample losses in washing and drying procedures. The final product was confirmed to be phase pure by X-ray diffraction (Appendix C, Figure C.1) and the refined lattice parameters are in good agreement with protonated samples ($a = b = 5.9283(4)$ and $c = 20.8163(13)$ Å compared with Chapter 6, Page 102).

7.3 Magnetic susceptibility – SQUID magnetometry

A 71.06 mg sample of deuterated vesignieite prepared under the conditions described in the previous section was measured in a Quantum Design DC-7 MPMS SQUID magnetometer, described fully in Chapter 4. Zero-field cooled (ZFC) and field-cooled (FC) data were collected between 2 and 300 K in a measuring field of 100 Oe, as well as a high-field cooled (HFC) dataset whereby the sample was cooled from 300 K in a 70,000 Oe field before changing to a 100 Oe field and measuring the same as the ZFC and FC runs. Data was also collected on two samples prepared using Method 2: a reflux method with samples then left unannealed or annealed for 3 days (Section 6.3) for comparison with the new samples. Comparisons in this section are also made with data collected on 'Sr-vesignieite' described in Chapter 5.

The ZFC-FC-HFC data for the new vesignieite samples are shown in Figure 7.1a. The temperature dependence of the ZFC and FC data is very similar to 'Sr-vesignieite', but the transition is shifted in vesignieite to slightly lower temperatures, $T_N \sim 9$ K, in agreement with the literature [1]. A further transition at $T_2 \sim 4.5$ K occurs in the ZFC data but not in the FC, whilst the HFC data has an anomalous bump at T_2 followed by a roughly constant χ as $T \to 0$ K and this hysteresis suggests the transition is ferromagnetic. The inverse susceptibility is plotted in Figure 7.1b and a fit to the linear $150 < T < 300$ K region gives a Weiss constant, $\theta_W = -80$ K, and Curie constant, $C = 0.4497$ emu K mol^{-1} Cu^{-1}, with the latter giving an effective moment, $\mu_{eff} = 1.90\,\mu_B$ mol^{-1} Cu^{-1}. These values agree well with many values quoted in the literature for a range of vesignieite samples [3, 1, 5].

A plot of χT for various vesignieite samples is shown in Figure 7.1c. The transition in the new samples clearly shows an initial ferromagnetic increase before an antiferromagnetic component causes a significant decrease in χT as $T \to 0$ K. Above $T = 20$ K the behaviour of both samples is remarkably

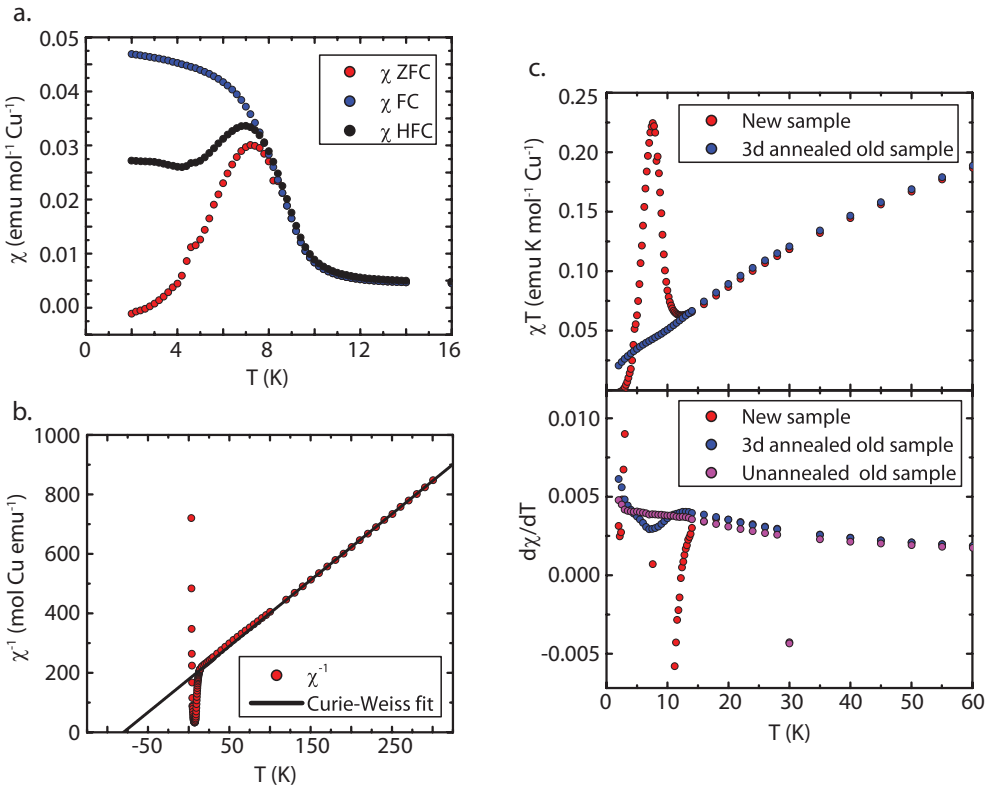

Figure 7.1: a. Zero-field cooled (ZFC) and field-cooled (FC) magnetic susceptibility data for the new vesignieite sample measured in a 100 Oe field. For the high-field-cooled (HFC) data, the sample was cooled from 300 K to 2 K in a 70,000 Oe field, before measured on warming in a 100 Oe field. **b.** A plot of χ^{-1} *vs.* T with a linear Curie-Weiss fit to the $150 < T < 300$ K region giving $\theta_{\rm W} = -80$ K, $C = 0.4497$ emu K mol^{-1} Cu^{-1} and $\mu_{\rm eff} = 1.90$. **c. Top** A comparison of χT for a new sample and one prepared using Method 2. **Bottom** $d\chi T/dT$ for three vesignieite samples of varying quality. The transition at $T_{\rm N} = 9$ K strengthens with improved crystallinity.

similar and by instead looking at $d\chi T/dT$, lower panel of Figure 7.1c, it becomes clear that a transition occurs in all samples of vesignieite, but improving the quality strengthens this significantly.

For 'Sr-vesignieite', the high temperature fits to the inverse susceptibility are strongly dependent upon the temperature region used. A similar analysis for vesignieite, by performing fits to 50 K regions of χ^{-1} between $100 < T < 300$ K and calculating $\mu_{\rm eff}$, is shown in Figure 7.2a. Both low- and high-quality vesignieite samples show a similar temperature dependence of $\mu_{\rm eff}$, with the flat line indicating the value obtained from fitting the whole $100 < T < 300$ K region. Considering vesignieite and 'Sr-vesignieite' are isoelectronic, the difference in fitted $\mu_{\rm eff}$ values is remarkable and suggests that the increase below $T = 140$ K in vesignieite is the same JT transition occurring in 'Sr-vesignieite' below $T = 280$ K. Calculating $\mu_{\rm eff} = \sqrt{8\chi T}$, instead of using linear Curie-Weiss law fits, shows a similar T-dependence for all samples, Figure 7.2b, and the difference between the two procedures is due to the unsuitability of the Curie law. A similar enhancement of $\mu_{\rm eff}$ occurs in the JT transition in Ag_2NiO_2 due to an increased Landé g-factor from spin-orbit coupling [14]. Unfortunately, further $\mu_{\rm eff}$ fits below $T \sim 100$ K are limited by deviations from Curie-Weiss behaviour associated with the build-up of short-

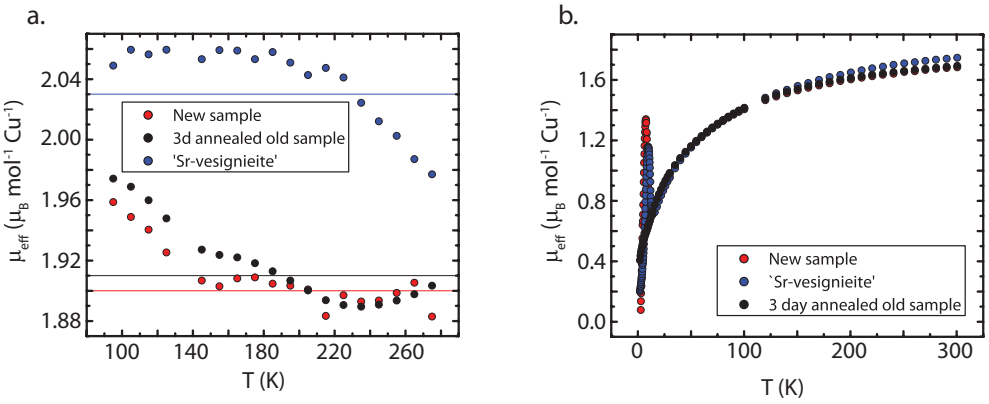

Figure 7.2: **a.** μ_{eff} calculated from linear fits to χ^{-1} *vs.* T in 50 K regions. The JT transition in 'Sr-vesignieite' coincides with the plateau of μ_{eff}. From the data of both vesignieite samples, this transition appears to occur at a much lower temperature. **b.** μ_{eff} calculated from $\mu_{\text{eff}} = \sqrt{8\chi T}$ for the same three samples. The saturated value at high temperature for all samples is close to that expected for a $S = \frac{1}{2}$ system, *i.e.* $\mu_{\text{eff}} = 1.73\,\mu_{\text{B}}$.

range correlations.

Magnetisation, M, data as a function of applied field, H, were measured for the new samples at $T = 2\,\text{K}$, well below both T_{N} and T_2 transitions. The full data is shown in Figure 7.2a, whilst a zoomed region of the plot is shown in Figure 7.2b. The data bears a close resemblance to the single crystal samples prepared with Method 3 [5], with a linear H-dependence above the coercive field, $H_{\text{C}} \sim 5,000\,\text{Oe}$, and hysteretic behaviour at low fields. The spontaneous ferromagnetic moment, $\mu_{\text{FM}} = 0.005\,\mu_{\text{B}}\,\text{mol}^{-1}\,\text{Cu}^{-1}$, is a very small percentage of the expected full ordered moment and suggests the presence of a weak ferromagnetic interaction [5], *i.e.* DM exchange.

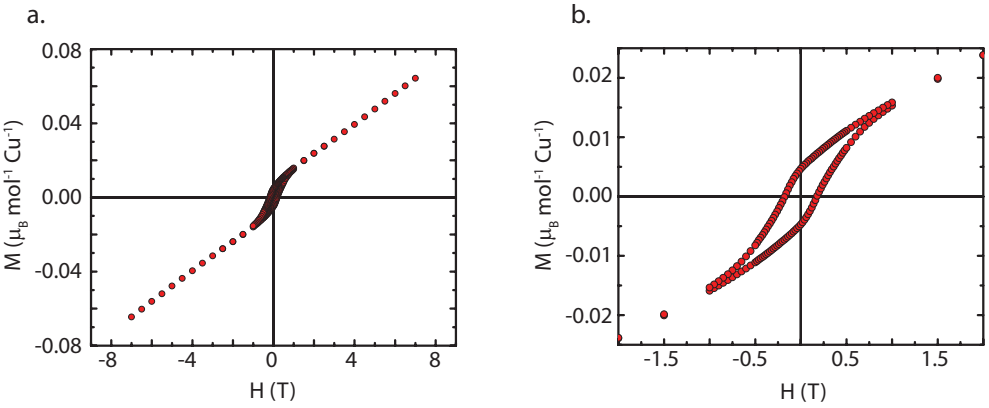

Figure 7.3: **a.** Magnetisation, M, as a function of field, H, measured at $T = 2\,\text{K}$ for the new vesignieite samples. **b.** Zoomed region of the data in **a** showing the low field hysteretic behaviour. The spontaneous moment of $0.005\,\mu_{\text{B}}$ is a very small percentage of the expected ordered moment, indicating the ferromagnetic component is weak and may originate from a DM interaction.

7.4 Powder inelastic neutron scattering

Inelastic neutron scattering is the primary technique for observing magnetic excitations, through which the exchange couplings can be determined. The technique has proved very powerful in revealing exotic physics in many other $S = \frac{1}{2}$ KAFMs, such as haydeeite (Chapter 8), kapellasite [15], volborthite [16] and herbertsmithite [9]. The long-range ordering transition in χ of vesignieite should reveal spin-waves associated with the magnetic structure, aiding the extraction of exchange parameters.

7.4.1 Preliminary experiment

A preliminary experiment was performed on a small deuterated sample of vesignieite on the MERLIN spectrometer at ISIS. The exchange interaction extracted from high temperature series expansion of bulk susceptibility is approximately $J \sim 50\,\mathrm{K}$ ($\sim 5\,\mathrm{meV}$) [1, 5], makes MERLIN a good instrument to investigate the excitations as it has high neutron flux down to $E_\mathrm{i} \sim 7\,\mathrm{meV}$. A 1.897 g sample was loaded in aluminium foil which was wrapped around the inside of an aluminium sample can resulting in a sample height of 4 cm. Initial measurements at $T = 6.5\,\mathrm{K}$ with incoming energies of $E_\mathrm{i} = 88, 40$ and $20\,\mathrm{meV}$ did not reveal any magnetic scattering. At $E_\mathrm{i} = 10\,\mathrm{meV}$ and $T = 2\,\mathrm{K}$ a flat mode at 4 meV appears with an abnormal Q-dependence whereby the intensity decreases between $1 < Q < 2\,\mathrm{Å}^{-1}$ before increasing again for $Q > 2\,\mathrm{Å}^{-1}$ (Figure 7.4a). This flat mode disappears above T_N, as shown in the $T = 2\,\mathrm{K}$ data of Figure 7.4b, confirming it is magnetic in origin. Unfortunately, the small sample size and lower flux at $E_\mathrm{i} = 10\,\mathrm{meV}$ on MERLIN, compared to higher energies, made any further observations difficult.

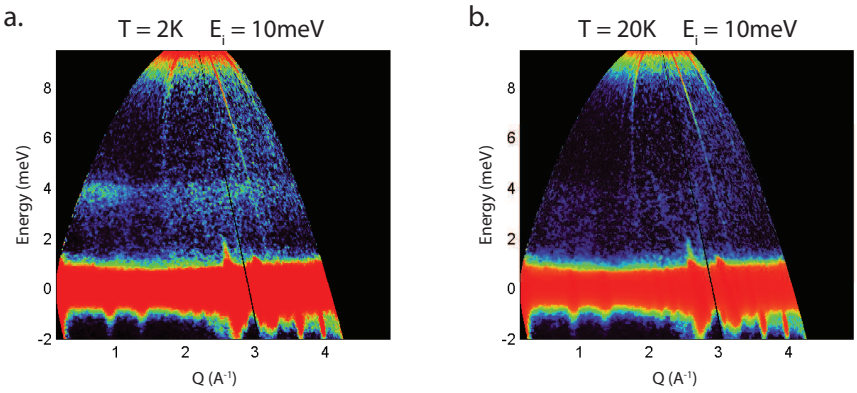

Figure 7.4: Powder inelastic neutron scattering data of vesignieite collected on the MERLIN spectrometer, ISIS, with $E_\mathrm{i} = 10\,\mathrm{meV}$ at **a.** $T = 2\,\mathrm{K}$ and **b.** $T = 20\,\mathrm{K}$. A flat 4 meV magnetic excitation appears below T_N.

7.4.2 Determination of the spin-wave excitations - IN5

Given that the energy range of interest in vesignieite is lower than expected, the IN5 cold neutron time-of-flight spectrometer at the ILL is a more appropriate instrument for observing the magnetic excitations. A 7.37 g deuterated sample was loaded into a 15 mm outside diameter aluminium can with no insert and measurements were performed in a standard ‘orange’ cryostat. Data reduction involved removing bad spectra, subtracting empty can runs and normalising to vanadium.

Measurements with neutrons of wavelength $\lambda = 3.2$ Å ($E_\mathrm{i} \sim 8$ meV) were made to analyse the flat mode at 4 meV observed on MERLIN. Data was collected at $T = 1.6, 6, 15$ and 25 K with a chopper speed of 12000 rpm and a 1:2 ratio between choppers. $S(Q,\omega)$ plots measured at the four temperatures are shown in Figure 7.5. At $T = 1.6$ K, well below the magnetic ordering transition $T_\mathrm{N} = 9$ K, the flat band is clearly visible and extends out to at least $Q = 3$ Å^{-1} . At lower energies, additional scattering at low-Q resembles two spin-wave branches emanating from the elastic line and a further, weaker branch appears at $Q \sim 1.75$ Å^{-1} . At $T = 6$ K, above the small magnetic anomaly in the SQUID data at $T_2 = 4.5$ K, the scattering is very similar to that at $T = 1.6$ K but appears more diffuse, particularly in the flat 4 meV band. Upon further heating through T_N, the flat mode disappears. However spin-wave-like scattering can still be seen at low-Q, although this appears to be superimposed on increased background scattering. These features remain up to $T > 2T_\mathrm{N} = 25$ K, where the scattering now resembles a spin-liquid-like response, such as that from kapellasite [15].

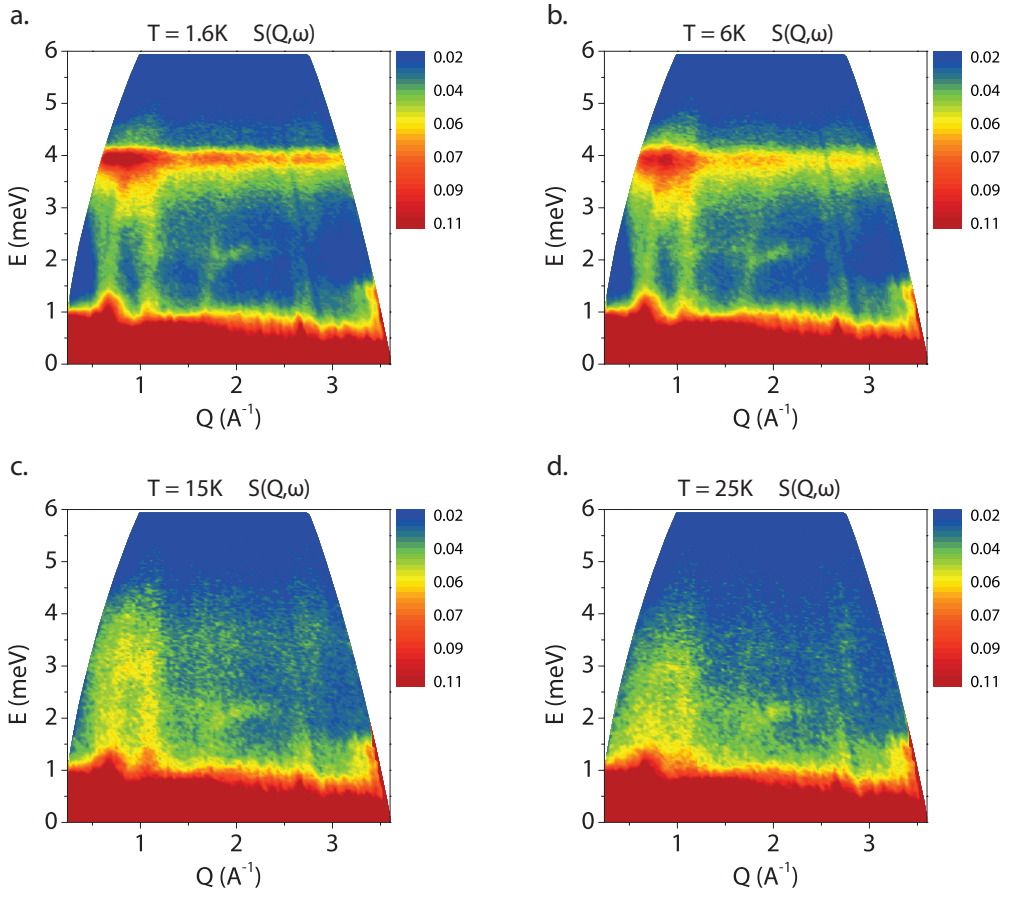

Figure 7.5: Powder inelastic neutron scattering data of vesignieite collected on the IN5 spectrometer, ILL, with $E_\mathrm{i} = 8$ meV neutrons at **a.** $T = 1.6$ K, **b.** $T = 6$ K, **c.** $T = 15$ K and **d.** $T = 25$ K. Below T_N well defined spin-wave excitations appear as well as the intense flat 4 meV mode seen on MERLIN. Above T_N the flat mode disappears but the spin-wave-like excitations remain up to at least $T = 25$ K, albeit more diffuse and less well defined.

The magnetic scattering still present at $T = 25$ K makes temperature subtractions of $S(Q,\omega)$ difficult. Figure 7.6a-c shows the imaginary part of the dynamic magnetic susceptibility, $\chi''(Q,\omega)$, obtained

by dividing $S(Q,\omega)$ with the temperature Bose factor, $1-\exp(-E/k_{\mathrm{B}}T)$. In $\chi''(Q,\omega)$ some diffuse magnetic scattering remains at low-Q and E at $T = 25\,\mathrm{K}$, however it provides a cleaner background for the temperature subtraction. The $T = 1.6 - 25\,\mathrm{K}$ $\chi''(Q,\omega)$ data is shown in Figure 7.6c and clearly shows the magnetic scattering. The subtraction also removes some spurion scattering, such as at $E \sim 2\,\mathrm{meV}$ and $Q \sim 2\,\mathrm{\AA}^{-1}$. At first glance, the flat mode with more conventional spin-wave like excitations in vesignieite resembles that seen in the $S = \frac{5}{2}$ Fe-jarosites, shown in Figure 7.6d [17]. In these materials the spectra can be well fitted to reveal significant in-plane and out-of-plane DM interactions and predicting effectively the low-E gap in the magnetic excitations. Therefore, as EPR data collected on vesignieite predicts a large in-plane DM interaction, it is important to determine if a gap exists in the neutron scattering data [11]. This will be discussed later with data measured at smaller E_{i}.

The low-Q spin-wave branches emanate from the elastic line at Q values that do not correspond to nuclear structure peaks. The first three nuclear peaks appear at $Q = 0.9, 1.25$ and $1.3\,\mathrm{\AA}^{-1}$ (Chapter 6, Page 103), however peaks are seen just above the elastic line from the spin-waves at $Q \sim 0.6$ and $1.1\,\mathrm{\AA}^{-1}$. This indicates that the spin-waves arise from antiferromagnetic correlations with $k \neq 0$ and not from a $k = 0$ structure, as predicted by Cu-NMR [2]. Indexing of the magnetic structure is discussed later with data collected at lower E_{i}.

A closer look at the temperature dependence of the magnetic scattering reveals some interesting features. The flat 4 meV and spin-wave excitations have quite different temperature dependencies evident from the $\chi''(Q,\omega)$ data: at $T = 6\,\mathrm{K}$ both excitations exist (Figure 7.7a), however when heated through T_{N} the spin-waves remain but there is no sign of the flat mode (Figure 7.7b). Constant $E = 2.0\,\mathrm{meV}$ cuts of $\chi''(\phi,\omega)$ for all temperatures, shown in Figure 7.7c, have peaks at $Q \sim 0.7, 1.1$ and $1.7\,\mathrm{\AA}^{-1}$ from the spin-wave branches and although these peaks broaden and become weaker upon heating, they are visible at all temperatures. A constant $Q = 1.0\,\mathrm{\AA}^{-1}$ cut of the same data at $T = 1.6\,\mathrm{K}$ has contributions from both the spin-wave, the broad peak at $E = 3\,\mathrm{meV}$, and the flat mode, the sharp peak at $E = 4\,\mathrm{meV}$ (Figure 7.7d). Above T_{N} the sharp 4 meV peak is absent and only the broad peak from the spin-wave is seen, even at $T = 25\,\mathrm{K}$.

The different temperature dependence of the flat-mode and lower energy spin-wave-like excitations is an interesting feature of the data. The 4 meV flat excitation may correspond to an optical spin-wave branch, the strong intensity caused by the high density of states characteristic of flat modes, which disappears above T_{N} as expected. However, the low energy acoustic spin-wave branches remain well above T_{N} which may indicate that the magnetic correlations are still well developed at higher temperatures, a characteristic often found in spin liquid regimes [18, 19].

An alternative explanation is related to the dynamic JT effect already discussed for vesignieite in Chapter 6. The dissimilar temperature dependence of the 4 meV excitation, compared to the lower energy excitations, suggests that there are two separate contributions to the magnetic scattering. Whilst the spin-wave-like excitations are characteristic of an ordered antiferromagnetic structure, one possibility for the origins of the flat 4 meV excitation is the dynamic JT effect and it is noteworthy that a similar inelastic response occurs in the orbital liquid state of $FeSc_2S_4$, whereby a flat excitation occurs due to vibronic

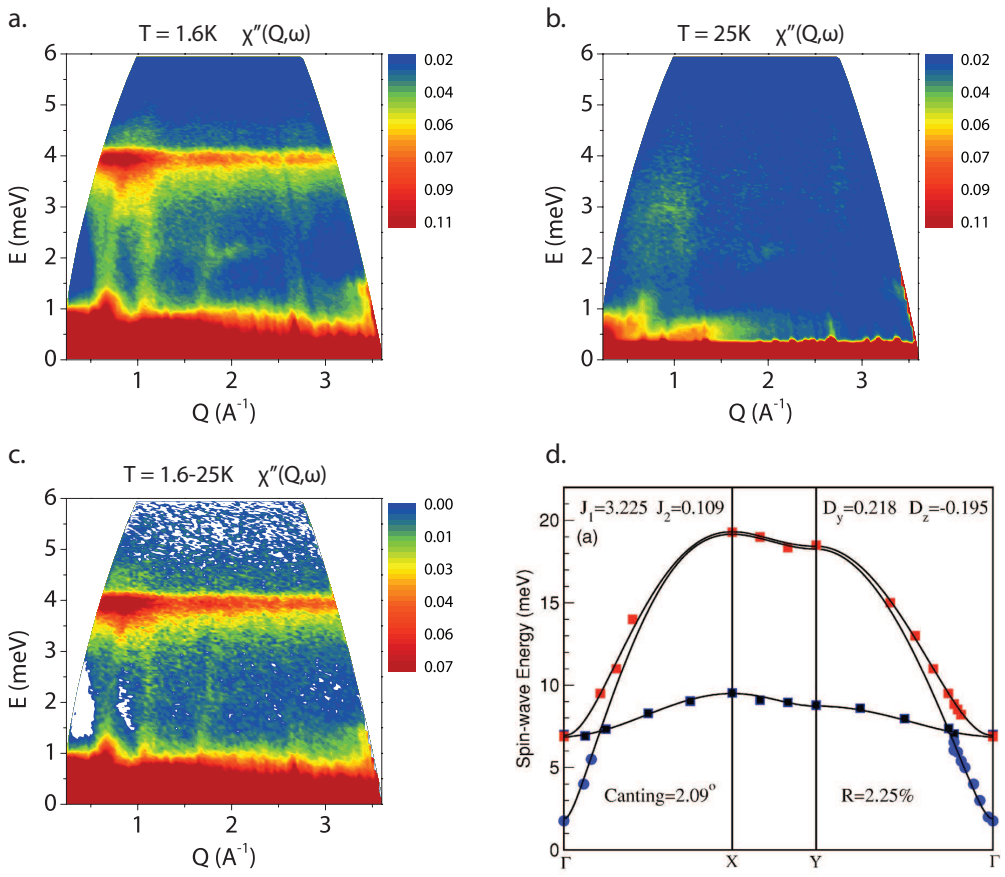

Figure 7.6: Imaginary part of the dynamic susceptibility, $\chi''(Q,\omega)$, of vesignieite measured with $E_\mathrm{i} = 8\,\mathrm{meV}$ neutrons at **a.** $T = 1.6\,\mathrm{K}$, **b.** $T = 25\,\mathrm{K}$ and **c.** a $T = 1.6 - 25\,\mathrm{K}$ temperature subtraction. **d.** The spin-wave excitation spectrum of the $S = \frac{5}{2}$ kagome antiferromagnet Fe-jarosite resembles the magnetic scattering of vesignieite [17].

coupling of the dynamic JT effect [20]. Inclusion of spin-orbit coupling makes the excited vibronic level magnetic dipole active and therefore visible by neutron scattering. In vesignieite, a possible scenario might be a splitting of the JT energies induced by the long-range magnetic order.

To determine the dispersion of the spin-wave branches at $E < 4\,\mathrm{meV}$ and to resolve a spin gap, measurements were taken using neutrons with an incoming energy $E_\mathrm{i} = 3.55\,\mathrm{meV}$. Data was collected at four temperatures: $T = 1.6, 6, 15$ and $30\,\mathrm{K}$ for $\sim 6\,\mathrm{h}$ with a chopper speed of 12000 rpm and a 2:3 chopper speed ratio. $\chi''(Q,\omega)$, for each temperature at this wavelength is shown in Figure 7.8. The spin waves are well defined below T_N but the steepness of the slope makes it difficult to determine the spin-wave stiffness with precision. As at $E_\mathrm{i} = 8\,\mathrm{meV}$, the spin-waves are clearly seen well above T_N although significantly broader in Q as shown by the constant $E = 1.5\,\mathrm{meV}$ cuts in Figure 7.8d. These 'sloppy' spin waves, or paramagnons, are commonly attributed to short-range correlations and are often observed in the paramagnetic regime of magnets [21]. With respect to the proposed low-E excitation gap, the $T = 1.6\,\mathrm{K}$ spectrum suggests it is present but its close proximity to the elastic line means it may be an artefact of the Bose correction. Measurements at yet lower E_i were required to confirm its presence or absence.

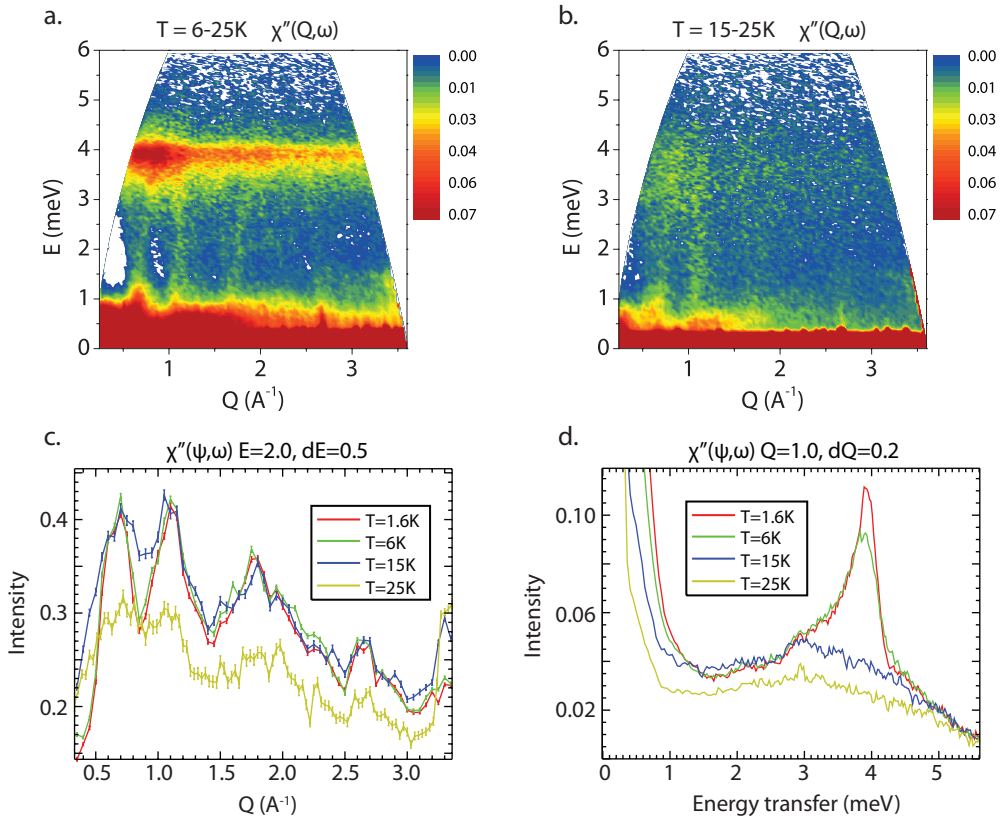

Figure 7.7: a. $T = 6 - 25\,\mathrm{K}$ and **b.** $T = 15 - 25\,\mathrm{K}$ temperature subtractions of the $\chi''(Q,\omega)$ data for vesignieite measured with $E_\mathrm{i} = 8\,\mathrm{meV}$ neutrons. The flat excitation disappears abruptly above T_N, whilst the spin-waves remain well above the transition. **c.** Constant $E = 2\,\mathrm{meV}$ strips of $\chi''(\phi,\omega)$ data showing peaks at $Q \sim 0.6, 0.9$ and $1.6\,\mathrm{meV}$ from the spin-wave branches that remain up to $T = 25\,\mathrm{K}$. **d.** Constant $Q = 1.0\,\mathrm{\AA}^{-1}$ strips of the same data. At low-T two contributions centred at 3 and 4 meV are superimposed, arising from the spin-waves and flat mode, respectively. No evidence of the 4 meV excitation remains at $T = 25\,\mathrm{K}$, but the broad scattering centred at 3 meV due to the spin waves remains.

To confirm the presence of an excitation gap, hinted at with the data at $E_\mathrm{i} = 3.55\,\mathrm{meV}$, measurements were performed with neutrons of $E_\mathrm{i} = 1.94\,\mathrm{meV}$ at $T = 1.6, 6$ and 30 K. $\chi''(Q,\omega)$ at $T = 1.6$ and 30 K are shown in Figures 7.9a and b, respectively. At base temperature a clear gap is seen in the spin-waves and a constant Q strip at $Q = 0.62\,\mathrm{\AA}^{-1}$, shown in Figure 7.9c, confirms the gap and puts the value at $E \sim 0.45\,\mathrm{meV}$. In the same plot, a comparable Q strip at $Q = 0.52\,\mathrm{\AA}^{-1}$ that does not integrate over the spin-wave branch shows no gap. The slightly increased background at $Q = 0.62\,\mathrm{\AA}^{-1}$ compared to at $Q = 0.52\,\mathrm{\AA}^{-1}$ is likely due to scattering from the magnetic Bragg peak in the elastic line. At $T = 6\,\mathrm{K}$, the gap is less well defined even though the spin-waves have similar intensity (Figure 7.9d). At $T = 30\,\mathrm{K}$ no gap is present however the scattering increases linearly before plateauing at $E \sim 0.6\,\mathrm{meV}$, indicating that even above T_N the excitations have a strong E-dependence. The development of a distinct gap between $1.6 < T < 6\,\mathrm{K}$ may indicate that the transition at $T_2 = 4.5\,\mathrm{K}$ is related to the DM component.

At $E_\mathrm{i} = 1.94\,\mathrm{meV}$ the Q-resolution is much improved over data collected at shorter wavelengths,

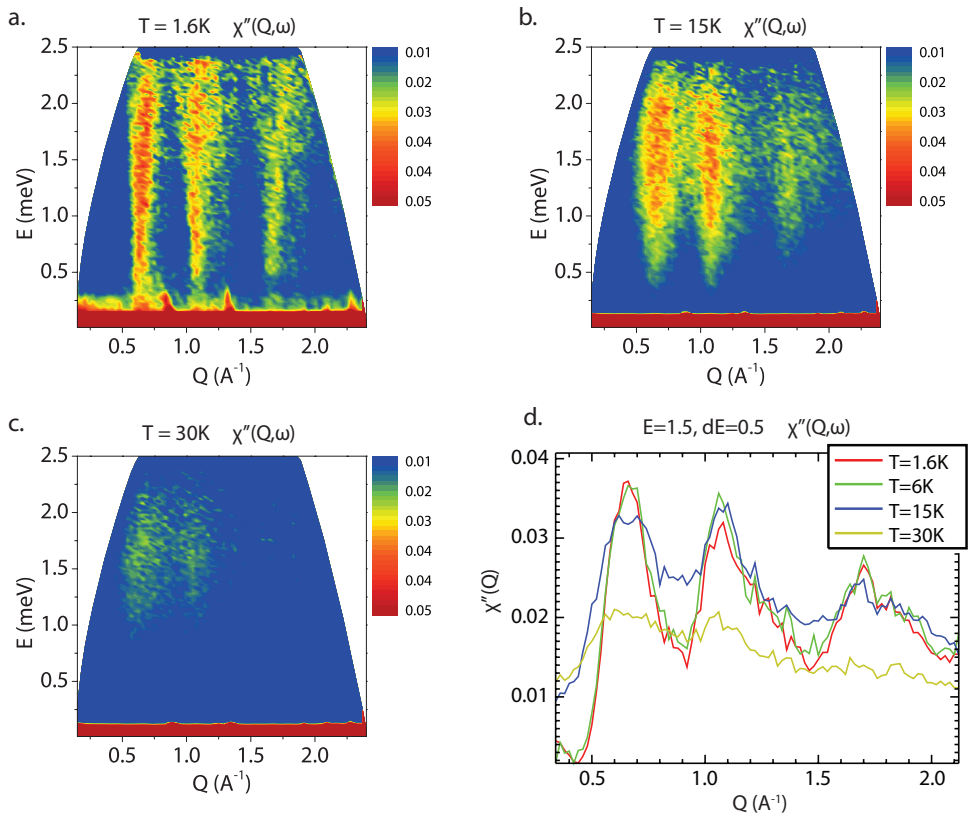

Figure 7.8: Imaginary part of the dynamic susceptibility for vesignieite measured with neutrons of $E_\mathrm{i} = 3.55\,\mathrm{meV}$ at **a.** $T = 1.6\,\mathrm{K}$, **b.** $T = 6\,\mathrm{K}$, **c.** $T = 15\,\mathrm{K}$ and **d.** $T = 30\,\mathrm{K}$. The steepness of the antiferromagnetic spin-waves in this E-range makes it difficult to determine the stiffness and therefore the exchange values. The spin-waves broaden significantly in Q above T_N but remain up to at least $T = 30\,\mathrm{K}$, indicating that antiferromagnetic fluctuations persist to high temperatures. The presence of a gap in the excitations remains inconclusive with this E_i.

making analysis of the elastic line much easier. Constant E strips of the elastic line with an energy width $dE = 0.05\,\mathrm{meV}$ for $T = 1.6$ and $30\,\mathrm{K}$ are shown in Figure 7.9e. Two peaks appear at $Q \sim 0.6$ and $1.1\,\mathrm{Å}^{-1}$ at $T = 1.6\,\mathrm{K}$ that are not present above T_N and align with the antiferromagnetic spin-waves. Searching the high-symmetry directions of the Brillouin zone for likely k-vectors that index with these positions, $k = \frac{1}{2}, 0, 0$ predicts peak positions that agree with the data, listed in Table 7.1. According to these, the magnetic Bragg peaks in the data consist of two or three reflections, which explains their large width in Q. The peak predicted at $Q \sim 0.86\,\mathrm{Å}^{-1}$ lies close to a nuclear Bragg peak and cannot be resolved from this experiment.

7.4.3 Magnetic ordering

Cuts along the elastic line of $T = 1.6 - 30\,\mathrm{K}$ $S(\phi, \omega)$ data show peaks that align with the nuclear peaks, as well as magnetic Bragg peaks that do not (Figure 7.10a). All of these peaks cannot be indexed with a unique k and, from a closer look at the raw data, the peaks that align with the nuclear may originate from a significant increase in the background below T_N (Figure 7.10b). As magnetic contributions to the background are expected to reduce below a magnetic ordering transition, due to a decrease in

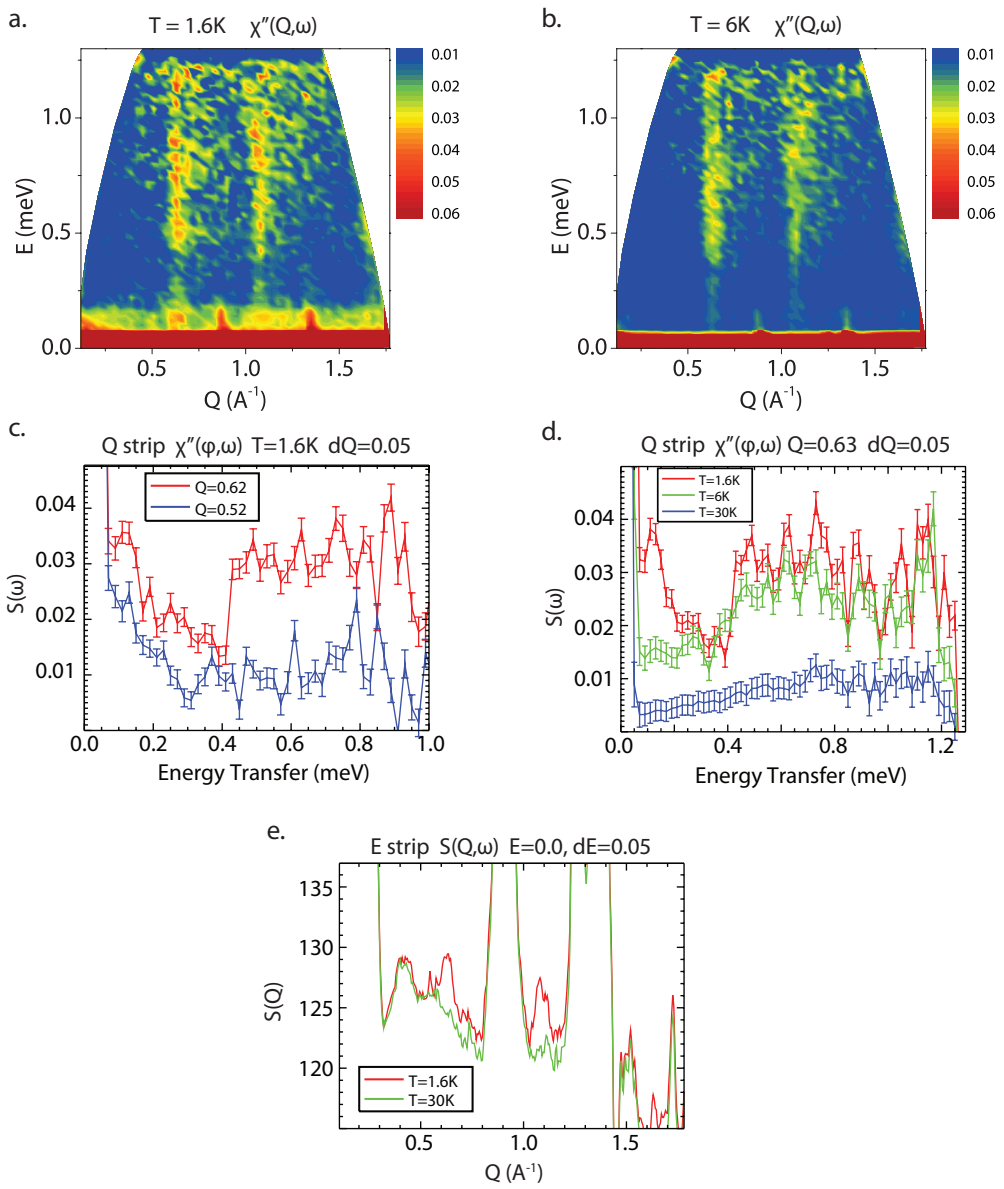

Figure 7.9: Imaginary part of the dynamic susceptibility of vesignieite collected with neutrons of $E_\mathrm{i} = 1.94\,\mathrm{meV}$ at **a.** $T = 1.6$ and **b.** 30 K. **c.** Constant $Q = 0.52$ and $0.62\,\mathrm{\AA}^{-1}$ cuts of $\chi''(\phi,\omega)$ at $T = 1.6\,\mathrm{K}$. The cut a $Q = 0.62\,\mathrm{\AA}^{-1}$ shows a gap in the spin-wave excitations at $E \sim 0.45\,\mathrm{meV}$, which is not present at $Q = 0.52\,\mathrm{\AA}^{-1}$. **d.** Temperature dependence of the spin gap. At $T = 6\,\mathrm{K}$, the gap is not as well defined than at $T = 1.6\,\mathrm{K}$, whilst at $T = 30\,\mathrm{K}$ the gap is absent. **e.** Constant E cuts of the elastic line at $T = 1.6$ and 30 K. Magnetic Bragg peaks appears below T_N at $Q = 0.6$ and $1.1\,\mathrm{\AA}^{-1}$ which index with the $k = \frac{1}{2}, 0, 0$ propagation vector.

paramagnetic scattering, the background increase could originate from the nuclear structure.

The magnetic structures of the $S = \frac{1}{2}$ kagome magnets kapellasite and haydeeite are well described by the classical magnetic structures described in the paper by Messio *et al.* [22]. Interestingly, the predicted stable magnetic structures encompass exotic non-coplanar octahedral, cuboc1 and cuboc2 states, with the latter present in kapellasite [15]. These non-coplanar magnetic structures have unit cells dou-

$(k = \frac{1}{2}, 0, 0)$ $a = b = 5.93\,\text{Å}^{-1}$, $c = 20.80\,\text{Å}^{-1}$, $\alpha = 90°$, $\beta = 90°$, $\gamma = 120°$

Reflection #	h	k	l	d (Å)	Q (Å^{-1})
1	$\frac{1}{2}$	0	0	10.28	0.61
2	$-\frac{1}{2}$	0	1	9.22	0.68
3	$-\frac{1}{2}$	0	2	7.31	0.86
4	$\frac{1}{2}$	-1	0	5.93	1.06
5	$-\frac{1}{2}$	0	3	5.75	1.09
6	$-\frac{1}{2}$	1	1	5.71	1.10

Table 7.1: The predicted reflection positions for a $k = \frac{1}{2}, 0, 0$ magnetic structure with lattice parameters $a = b = 5.934$ and $c = 20.804\,\text{Å}$ $\alpha = 90$, $\beta = 90$ and $\gamma = 120°$. The Q values here match well with the magnetic Bragg peaks observed on IN5. The reflection at $Q = 0.86\,\text{Å}^{-1}$ lies very close to a nuclear Bragg peak and so its presence cannot be confirmed.

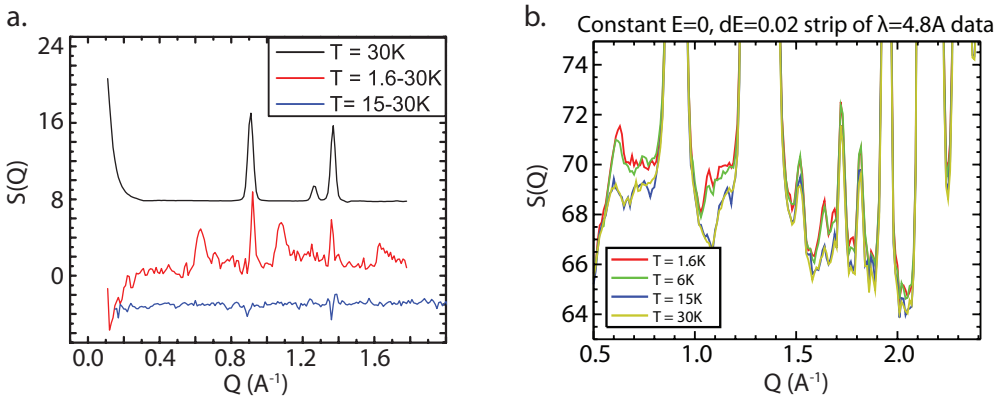

Figure 7.10: **a.** Comparison of cuts along the elastic line at $T = 30\,\text{K}$ and two temperature subtractions. **b.** Cuts along the elastic line of $E_\text{i} = 3.55\,\text{meV}$ data at four different temperatures. The change in background below $T = 15\,\text{K}$ explains the peaks in the $T = 1.6 - 30\,\text{K}$ temperature subtraction centred on the nuclear Bragg peaks in **a**.

bled along the a and b directions compared to the regular ferromagnetic or $q = 0$ states and are thus described with a $k = \frac{1}{2}, 0, 0$ propagation vector. It is therefore useful to compare whether the vesignieite $k = \frac{1}{2}, 0, 0$ magnetic structure corresponds to any of these non-coplanar structures.

The calculated powder-averaged $S(Q)$ for the octahedral, cuboc1 and cuboc2 magnetic states, based on a 2-dimensional kagome lattice such that the Q vectors are given by $Q = (h, k)$, are shown in Figures 7.11a-c [22]. A good fingerprint for distinguishing between the three states is by the presence of the first two peaks, which are indexed as $(\frac{1}{2}, 0, 0)$ and $(\frac{1}{2}, -1, 0)$, respectively. The $(\frac{1}{2}, 0, 0)$ and $(\frac{1}{2}, 0, 1)$ reflections are observed in the vesignieite spectra at $Q \approx 0.61\,\text{Å}^{-1}$, ruling out the cuboc1 structure which does not have any intensity for $(\frac{1}{2}, 0, l)$ reflections. Consequently, the $(\frac{1}{2}, 0, 2)$ reflection

at $Q = 0.86\,\text{Å}^{-1}$ should be present, however this lies very close to a nuclear Bragg peak and is therefore impossible to resolve in this data. To distinguish between the cuboc2 and octahedral structures, it is necessary to look for the presence, or not, of the $(\frac{1}{2}, -1, l)$ reflections. The $(\frac{1}{2}, -1, 0)$ and $(\frac{1}{2}, -1, 1)$ for vesignieite occur at $Q = 1.06$ and $1.10\,\text{Å}^{-1}$, respectively, and a magnetic Bragg peak is observed in the experimental data in this Q-region (Figure 7.10a). Care must be taken in assigning the hkl of this peak as the $(\frac{1}{2}, 0, 3)$ occurs at $Q = 1.09\,\text{Å}^{-1}$ and is present in both the cuboc2 and octahedral structures. However, the broadness of the peak in the experimental data, similar to the peak at $Q \approx 0.61\,\text{Å}^{-1}$, strongly suggests it consists of several reflections. Therefore, both $(\frac{1}{2}, 0, l)$ and $(\frac{1}{2}, -1, l)$ type reflections are observed experimentally and this is only consistent with the octahedral structure, as described in the table of Figure 7.11.

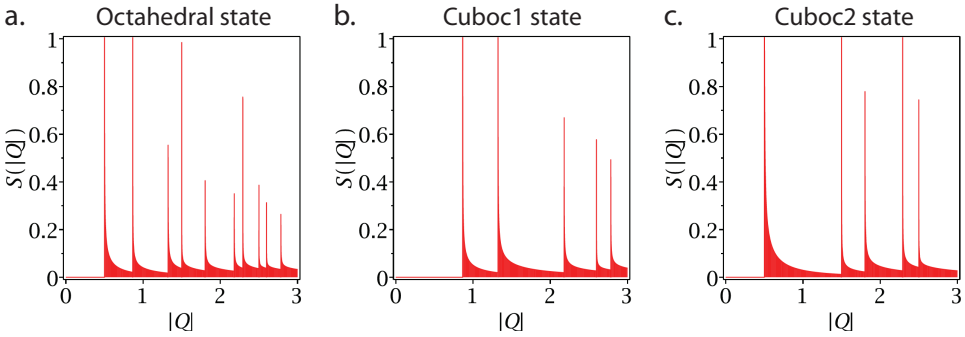

hkl	Vesignieite		$\|Q\|$ from [22]	Octahedral	Cuboc1	Cuboc2
	Q (Å^{-1})	Present				
$\frac{1}{2}, 0, 0$	0.61	×	0.5	×		×
$\frac{1}{2}, 0, 1$	0.68	×	1.12	×		×
$\frac{1}{2}, 0, 2$	0.86	?	1.12	×		×
$\frac{1}{2}, -1, 0$	1.06	×	0.87	×	×	
$\frac{1}{2}, 0, 3$	1.09	×	1.12	×		×
$\frac{1}{2}, -1, 1$	1.10	×	0.87	×	×	

Figure 7.11: Calculated powder-averaged $S(Q)$ for the non-coplanar **a.** octahedral, **b.** cuboc1 and **c.** cuboc2 RMOs [22]. The observed magnetic Bragg peaks in the vesignieite experimental data agree with those predicted for the octahedral structure (See table).

7.5 Discussion

The role of orbital physics in vesignieite is well established in Chapter 6 and the interplay between spin and orbital degrees of freedom has led to a myriad of fascinating properties and electronic ground states, from colossal magnetoresistance in the manganites [23] through liquid-like states in Tb_2TiO_7, $Ba_3CuSb_2O_9$ and $FeSc_2S_4$ [24, 25, 20] to multiferroicity and orbital-glassiness in $FeCr_2S_4$ [26]. Vesignieite is a very interesting addition to this list as it combines orbital and quantum $S = \frac{1}{2}$ spin frustration

on the highly geometrically frustrated kagome lattice. Such a combination has not previously been reported in the literature, however determining the underlying physics of this material is far from trivial.

As discussed and well documented in the literature, vesignieite shows a large degree of spin frustration with the magnetic transition suppressed to $\sim \theta_{\mathrm{W}}/9$. Furthermore, the material also possesses orbital degeneracy: at high temperature all Cu^{2+} sites are dynamically JT distorted, whilst at $T = 4.5\,\mathrm{K}$, in the magnetically ordered regime, the kagome lattice is decorated by both dynamic and cooperatively ordered JT Cu^{2+} sites. Further weight is added behind this theory by the temperature dependence of the fitted effective moment, μ_{eff} (Figure 7.2a). The increase of μ_{eff} with decreasing temperature indicates an increased anisotropy of the Cu^{2+} environment, *i.e* a JT effect, as a similar trend is observed in the triangular magnet Ag_2NiO_2 whereby the T-dependence of μ_{eff} is caused by changes in the Landé g-factor from spin-orbit coupling [14]. Whilst the crystal structure of vesignieite is strong evidence that the remaining Cu^{2+} remain dynamic below T_{N}, further evidence such as from EPR performed on these high-quality samples would be beneficial.

The magnetic susceptibility and neutron scattering results confirm that the transition at $T_{\mathrm{N}} = 9\,\mathrm{K}$ is to an antiferromagnetically ordered structure, although the former also reveals a weak ferromagnetic component. The combination of antiferro- and ferromagnetically ordered components is common in kagome magnets due to the Dzyaloshinskii-Moriya interaction, which tends to introduce a ferromagnetic canting of the antiferromagnetic structure [27]. The $\sim 0.4\,\mathrm{meV}$ gap in the spin-wave excitation spectrum is strong evidence of a DM interaction in vesignieite, previously observed in ESR experiments [11], and it is found to open a spin gap similar to that in the $S = \frac{5}{2}$ kagome antiferromagnet Fe-jarosite [17]. The temperature dependence of the spin gap suggests it occurs at the $T_2 = 4.5\,\mathrm{K}$ transition seen in the bulk susceptibility and thus the latter may be related to a DM component, *i.e.* weak ferromagnetism with a saturated moment of $\sim 0.005\,\mu_{\mathrm{B}}$. Interesting implications of the DM interaction are only recently coming to light, such as the topological magnon Hall effect [28]. The inclusion of the geometrically frustrated lattice in vesignieite will only add further complexity to this already exotic physics.

The spin-wave spectra of vesignieite reveal a transition to a complicated magnetic structure. The spectra below T_{N} are dominated by an intense flat mode at 4 meV and spin-wave-like branches below 4 meV. These two features have different temperature dependencies that suggest they may have different origins (Figure 7.7d): the spin-waves persist above T_{N} albeit becoming broader and weaker, however the intense flat mode abruptly disappears at T_{N}. The spin-waves are characteristic of an ordered antiferromagnetic structure with $k \neq 0$ and their persistence above T_{N}, often termed 'sloppy spin waves', is common in other materials and indicative of spin relaxation processes. The different behaviour of the 4 meV mode is more similar to that expected for conventional spin-waves, however it may also suggest that it is not an excitation related to the antiferromagnetic structure. Further work is required to confirm this, but one possible origin is from a spin-phonon coupling induced by the magnetic order, such as the excitation found in the dynamic JT material $FeSc_2S_4$ which the Q- and E-dependence of the flat mode in vesignieite resembles [29].

With regards to the magnetic structure in vesignieite, it is important to determine this as no long-

range ordered non-coplanar magnetic structures have been observed before in quantum kagome magnets. This would be an important step in helping to define the phase diagram of the $S = \frac{1}{2}$ KAFM.

7.6 Future work

Initially, an important step is to construct a spin-wave model of vesignieite for comparison with the experimental inelastic neutron scattering data. Firstly, this will help determine the origin of the flat 4 meV band in the inelastic neutron scattering data. Moreover, from fits with the experimental data this can determine the number of superexchange terms required, *i.e.* whether further-neighbour terms are present, and the magnitude of these. Knowledge of these values will significantly aid comparisons with theoretical predictions of $S = \frac{1}{2}$ KAFMs, for instance in the exchange phase diagram proposed by Messio *et al.* for the kagome lattice [22].

Beyond this, further characterisation of the low temperature magnetic and nuclear structure would be invaluable. Observing magnetic Bragg peaks in powder neutron diffraction is inherently difficult in $S = \frac{1}{2}$ systems, however with the large sample sizes of vesignieite available this may be possible on an instrument such as WISH at ISIS. It would be more beneficial to combine such an experiment with a high-resolution neutron or synchrotron diffraction study at several temperatures from below T_2 to above T_{N}. The lattice parameter dependence would be a useful and easy parameter to extract from this and any evidence of orbital ordering would be evident.

The ability to synthesise 100 % Zn^{2+} doped vesignieite, *i.e.* $BaZn_3V_2O_8(OH)_2$ described in Chapter 6, raises the possibility of using this sample as a phonon blank for specific heat measurements. Thus, the purely magnetic specific heat, C_{mag}, could be accurately extracted from data collected on vesignieite. Accurate C_{mag} data would be particularly useful for characterising the transition in χ at T_2, which little is known of, and the orbital physics at low temperatures.

7.7 Conclusions

This chapter deals with magnetic characterisation of a high quality vesignieite sample, synthesised using a method adapted from 'Sr-vesignieite' described in Chapter 6, Section 6.4.1. The magnetic properties of this material share many similarities with other vesignieite samples, such as strong antiferromagnetic interactions, $\theta_{\mathrm{W}} \sim -80\,\mathrm{K}$, and a magnetic transition at $T_{\mathrm{N}} \sim 9\,\mathrm{K}$. The latter is well defined in χ and is consistent with long-range antiferromagnetic order. This is confirmed from the inelastic neutron scattering data, which shows clear spin-waves below T_{N} that originate from an ordered antiferromagnetic structure and the corresponding magnetic Bragg peaks index with the $k = \frac{1}{2}, 0, 0$ propagation vector. Through comparisons with predicted classical magnetic orders on the kagome lattice, the determined propagation vector and the observed magnetic Bragg peaks suggest that the material adopts an exotic non-coplanar octahedral magnetic structure not previously observed experimentally.

In addition to characterising the magnetic structure below T_{N}, a further magnetic transition is observed in χ that has not previously been reported in the literature. The behaviour of χ at T_2 when the sample is cooled in high field suggests this feature is ferromagnetic and the field dependence of M confirms the presence of a small ferromagnetic component at $T = 2\,\mathrm{K}$, with such behaviour often associated

with Dzyaloshinskii-Moriya exchange. The low-E excitation gap in the neutron scattering data is also consistent with this picture and its temperature dependence suggests the T_2 transition may introduce this component. However, further work is required to fully characterise this low temperature transition.

Compared to other model $S = \frac{1}{2}$ KAFMs the magnetic properties of vesignieite are quite unique. Neither volborthite nor herbertsmithite enter magnetic long-range order at any temperature despite their structures being remarkably similar to vesignieite. Hopefully with the results presented in this chapter and the acknowledgment of the importance of orbital physics we can gain a better understanding of how the magnetic frustration is relieved in vesignieite.

Bibliography

[1] Y. Okamoto, H. Yoshida and Z. Hiroi, *J. Phys. Soc. Japan*, 2009, **78**, 033701.

[2] M. Yoshida, Y. Okamoto and H. Yoshida, *J. Phys. Soc. Japan*, 2013, **82**, 013702.

[3] R. H. Colman, F. Bert, D. Boldrin, A. Hillier, P. Manuel, P. Mendels and A. S. Wills, *Phys. Rev. B*, 2011, **83**, 180416.

[4] D. Boldrin, *M. Sci.*, University College London, 2010.

[5] H. Yoshida, Y. Michiue, E. Takayama-Muromachi and M. Isobe, *J. Mater. Chem.*, 2012, **22**, 18793.

[6] Z. Hiroi, H. Yoshida, Y. Okamoto and M. Takigawa, *J. Phys. Conf. Ser.*, 2009, **145**, 012002.

[7] J. Quilliam, F. Bert, R. H. Colman, D. Boldrin, A. S. Wills and P. Mendels, *Phys. Rev. B*, 2011, **84**, 180401.

[8] D. Wulferding, P. Lemmens, H. Yoshida, Y. Okamoto and Z. Hiroi, *J. Phys. Condens. Matter*, 2012, **24**, 185602.

[9] T.-H. Han, J. S. Helton, S. Chu, D. G. Nocera, J. A. Rodriguez-Rivera, C. Broholm and Y. S. Lee, *Nature*, 2012, **492**, 406–410.

[10] M. Zhesheng, H. Ruilin and Z. Xiaoling, *Acta Geol. Sin.*, 1991, **4**, 145–151.

[11] A. Zorko, F. Bert, A. Ozarowski, J. van Tol, D. Boldrin, A. S. Wills and P. Mendels, *Phys. Rev. B*, 2013, **88**, 144419.

[12] M. Elhajal, B. Canals and C. Lacroix, *Phys. Rev. B*, 2002, **66**, 014422.

[13] I. Rousochatzakis, S. Manmana, A. Läuchli, B. Normand and F. Mila, *Phys. Rev. B*, 2009, **79**, 214415.

[14] H. Yoshida, Y. Muraoka, T. Sörgel, M. Jansen and Z. Hiroi, *Phys. Rev. B*, 2006, **73**, 020408.

[15] B. Fåk, E. Kermarrec, L. Messio, B. Bernu, C. Lhuillier, F. Bert, P. Mendels, B. Koteswararao, F. Bouquet, J. Ollivier, A. D. Hillier, A. Amato, R. H. Colman and A. S. Wills, *Phys. Rev. Lett.*, 2012, **109**, 037208.

[16] G. J. Nilsen, F. C. Coomer, M. A. de Vries, J. R. Stewart, P. P. Deen, A. Harrison and H. M. Rönnow, *Phys. Rev. B*, 2011, **84**, 172401.

[17] T. Yildirim and A. B. Harris, *Phys. Rev. B*, 2006, **73**, 214446.

[18] J. Park, J.-G. Park, G. Jeon, H.-Y. Choi, C. Lee, W. Jo, R. Bewley, K. McEwen and T. Perring, *Phys. Rev. B*, 2003, **68**, 104426.

[19] H. Nakamura, T. Yamasaki, S. Giri, H. Imai, M. Shiga, K. Kojima, M. Nishi, K. Kakurai and N. Metoki, *J. Phys. Soc. Japan*, 2000, **69**, 2763–2766.

[20] A. Krimmel, M. Mücksch, V. Tsurkan, M. Koza, H. Mutka and A. Loidl, *Phys. Rev. Lett.*, 2005, **94**, 237402.

[21] K. Kawasaki, *Prog. Theor. Phys.*, 1968, **39**, 285–311.

[22] L. Messio, C. Lhuillier and G. Misguich, *Phys. Rev. B*, 2011, **83**, 184401.

[23] E. Dagotto, T. Hotta and A. Moreo, *Phys. Rep.*, 2001, **344**, 1–153.

[24] P. Bonville, A. Gukasov, I. Mirebeau and S. Petit, *Phys. Rev. B*, 2014, **89**, 085115.

[25] Y. Ishiguro, K. Kimura, S. Nakatsuji, S. Tsutsui, A. Q. R. Baron, T. Kimura and Y. Wakabayashi, *Nat. Commun.*, 2013, **4**, 2022.

[26] J. Bertinshaw, C. Ulrich, A. Günther, F. Schrettle, M. Wohlauer, S. Krohns, M. Reehuis, A. J. Studer, M. Avdeev, D. V. Quach, J. R. Groza, V. Tsurkan, A. Loidl and J. Deisenhofer, *Sci. Rep.*, 2014, **4**, 6079.

[27] T. Moriya, *Phys. Rev.*, 1960, **120**, 91–98.

[28] B. Binz and A. Vishwanath, *Phys. B Condens. Matter*, 2008, **403**, 1336–1340.

[29] N. Büttgen, J. Hemberger, V. Fritsch, A. Krimmel, M. Mücksch, H.-A. K. V. Nidda, P. Lunkenheimer, R. Fichtl, V. Tsurkan and A. Loidl, *New J. Phys.*, 2004, **6**, 191–191.

Chapter 8

Haydeeite, α-$MgCu_3(OH)_6Cl_2$, a geometrically perfect $S = \frac{1}{2}$ kagome magnet

8.1 Introduction

The mineral haydeeite, α-$MgCu_3(OH)_6Cl_2$, is a crystallographic polymorph of the well studied $S = \frac{1}{2}$ kagome mineral herbertsmithite [1] and the Mg-analogue of kapellasite, α-$ZnCu_3(OH)_6Cl_2$ [2]. As discussed in previous chapters herbertsmithite and kapellasite provide two of the best model $S = \frac{1}{2}$ KAFMs to explore quantum spin liquid behaviour, characterised by the absence of long-range magnetic order as $T \rightarrow 0\,\text{K}$ along with exotic spin excitations [3, 4]. Given the crystallographic similarities of haydeeite to these materials, particularly kapellasite, it would logically be expected to have a similar magnetic response. However, previous work has shown haydeeite to undergo a magnetic transition to long-range order at low temperatures which appears to involve competing ferromagnetic and antiferromagnetic components [5]. This surprising finding demonstrates the delicate nature of the ground state in these materials and haydeeite provides a unique example through which to study the long-range ordered side of the $S = \frac{1}{2}$ kagome phase diagram.

8.2 Background on the (Mg,Zn)$Cu_3(OH)_6Cl_2$ family of materials

8.2.1 Crystal structures

Haydeeite crystallises in the trigonal $P\bar{3}m1$ space group with lattice parameters $a = 6.2885(1)\,\text{Å}$ and $c = 5.7271(1)\,\text{Å}$. These are similar to those of the isostructural kapellasite ($a = 6.3468(1)\,\text{Å}$ and $c = 5.6823(2)\,\text{Å}$) [2]. An important feature of both materials is the 'construction' of the kagome lattice. Concentrating on haydeeite, the Cu/Mg sublattice is a 2-dimensional triangular lattice with Mg^{2+} occupying the $1b$ site with $\bar{3}m$ symmetry and Cu^{2+} the $3f$ site with $2/m$ symmetry. Consequently, Mg^{2+} ions form a vertex sharing triangular sublattice, leaving the Cu^{2+} ions in a kagome lattice with Mg^{2+} at the centre of the kagome hexagons (Figure 8.1b). Both ions coordinate in octahedral geometry, however that of the Jahn-Teller active d^9 Cu^{2+} is axially elongated, thus lowering the $3f$ site symmetry compared to the $1b$ site. The Zn^{2+} ion forms an equilateral ZnO_6 octahedra on the higher symmetry $1b$ site. Despite this site preference for each ion, significant amounts of antisite disorder is apparent in haydeeite.

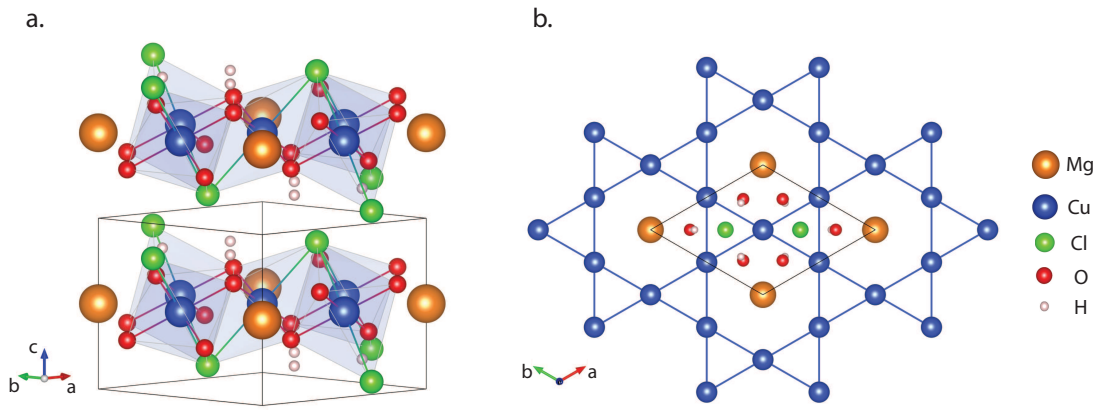

Figure 8.1: Views of the crystal structure of haydeeite, α-MgCu$_3$(OH)$_6$Cl$_2$. **a.** The lack of any Cu^{2+} or Mg^{2+} sites between the kagome planes makes haydeeite remarkably 2-dimensional. The kagome planes are linked by weak hydrogen bonding of the Cl–H–O link thus minimising any magnetic coupling of the layers. **b.** A view along the c-axis highlighting the regular doping of the Cu^{2+} kagome triangular lattice with Mg^{2+} ions to leave a kagome sublattice.

Refinement of powder neutron diffraction gives the $3f$ site with $\sim 16\,\%$ Mg^{2+} occupation and a Cu:Zn ratio of 1.68 [5]. This is less disorder than is found in kapellasite with $\sim 11\,\%$ occupation of the $1b$ site with Cu^{2+} in addition to $\sim 27\,\%$ of Zn^{2+} on the $3f$ site (Cu:Zn $= 1.37$) [5].

In both materials, the Cu–μ_3O(H)–Cu link mediates the magnetic superexchange with similar bond angles of 104.7° in haydeeite and 104.4° in kapellasite [5]. With respect to the Goodenough-Kanamori rules, the superexchange angle in both materials is close to the changeover in sign of J found in similar materials [6]. However, further-neighbour interactions must also be taken into account. Electronic structure calculations have predicted that 4 distinct exchange pathways should have a significant effect, these are termed J_1, J_2, J_3 and J_d (Figure 8.2a) [7].

8.2.2 Magnetism in the isoelectronic mineral kapellasite, α-ZnCu$_3$(OH)$_6$Cl$_2$

In order to get a better understanding of the magnetism in haydeeite, it is first useful to look at the isoelectronic $S = \frac{1}{2}$ kagome material kapellasite, α-ZnCu$_3$(OH)$_6$Cl$_2$. As discussed in section 8.2, kapellasite is the Zn-analogue of haydeeite and thus both have very similar crystal structures. The only marked difference is the increase in Cu^{2+}/Zn^{2+} site disorder in kapellasite [5].

Kapellasite does not enter a magnetically long-range ordered state down to the lowest measured temperatures, $T = 20\,$mK [4]. Instead the magnetic susceptibility shows a gradual increase below $T \sim 100\,$K. Local susceptibility data, measured using ^{35}Cl NMR, matches the bulk susceptibility across the whole temperature range confirming the Curie-like low-T upturn to be an intrinsic contribution (Figure 8.3a). The bulk susceptibility is also characterised by a significant collapse in the effective moment below $T \approx 25\,$K, which can be understood as the condensation of spins into $S = 0$ singlets [5].

Given the lack of long-range order in kapellasite, characterising its magnetic properties with common techniques, such as neutron scattering, is challenging. A clearer understanding is gained from looking at the possible exchange pathways on the kagome lattice (Figure 8.2a). Theoretical calculations

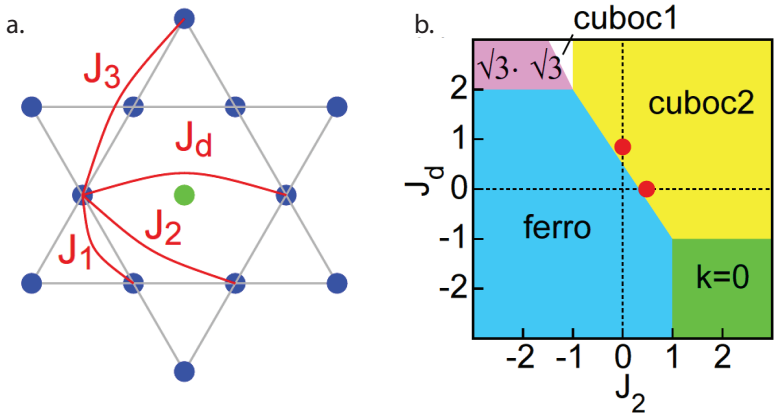

Figure 8.2: **a.** Part of the kagome lattice of haydeeite showing the 4 significant and distinct exchange pathways between the blue Cu^{2+} ions. The green circle represents the diamagnetic Mg^{2+} ion. **b.** Phase diagram of the J_2-J_d model with a ferromagnetic $J_1 = -1$ and $J_3 = 0$. The cuboc2 state is a chiral 12 sublattice structure with spins pointing towards the corners of a cuboctahedron and the best fits to high temperature series analysis of susceptibility data lie in this region (red circles). Adapted from [4]

have shown that the $S = \frac{1}{2}$ KAFM with competing interactions has a rich phase diagram with various different magnetic long-range and short-range ordering [8, 7, 9]. Whilst some of these have quite regular structures such as the ferromagnetic (F) state, the cuboc1 and cuboc2 states are chiral and non-coplanar [10]. Assuming ferromagnetic nearest-neighbour interaction, these chiral states define large areas of the phase diagram for small values of J_2, J_3 and J_d. Moreover, values for these exchange integrals in kapellasite obtained from high-temperature series analysis of the static magnetic susceptibility ($J_1 = -12$, $J_2 = -4$ and $J_\mathrm{d} = 15.6\,\mathrm{K}$) place it in the cuboc2 domain [11].

The analysis of the inelastic powder neutron scattering data on kapellasite agrees well with results from the static magnetic susceptibility [4]. $S(Q,\omega)_{T=0.1\,\mathrm{K}}$ is dominated by a broad, gapless continuum of excitations centred at $Q \approx 0.5\,\mathrm{\AA}^{-1}$ (Figure 8.3b). The position and relative intensity of this peak is in agreement with that predicted for the cuboc2 structure [9]. Comparing the experimental $S(Q)$ with calculations using a bosonic approach of the Hamiltonian in the cuboc2 structure adds further weight to the suitability of this model.

The spin dynamics in the low-T state is further characterised by a deviation in the behaviour of the dynamic magnetic susceptibility $\chi''(E)$ below $T \approx 5\,\mathrm{K}$ [4]. Any spin freezing in this temperature regime is ruled out through the μSR response [12]. Instead, the spin fluctuations slow down, indicating an enhancement in the correlations, but they remain wholly dynamic down to $T = 20\,\mathrm{mK}$ putting an upper bound of a spin-gap to $10^{-3}\,J_1$. It is worth noting that bosonic based calculations predict spin-waves at higher energy transfers that would be visible in the neutron scattering data [4]. The absence of such features highlights the limitations with the approach, and in these cases a fermionic approach should be more appropriate for further investigation of the quantum spin liquid state of kapellasite [13].

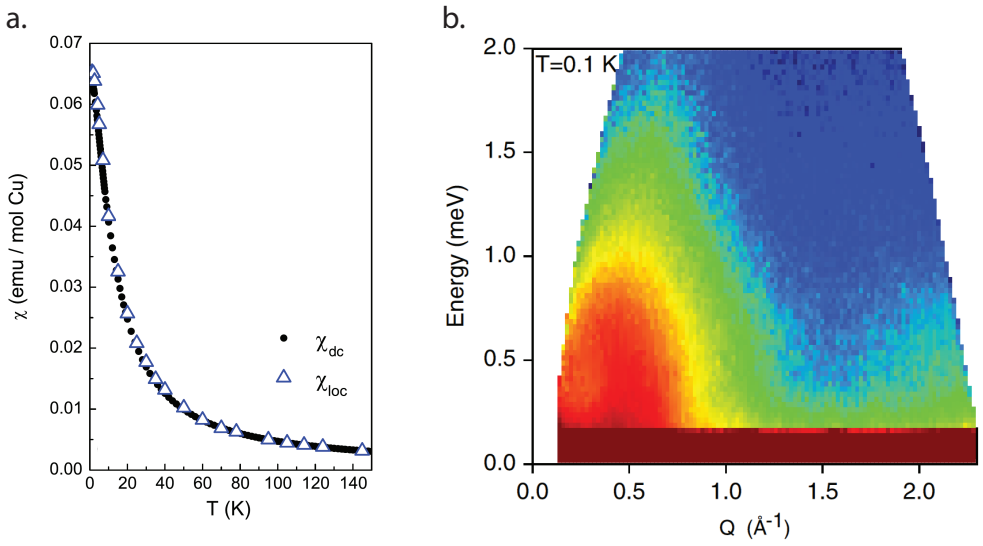

Figure 8.3: **a.** A plot of the bulk, $\chi_{\rm dc}$, and local susceptibility, $\chi_{\rm loc}$, of kapellasite. The close agreement across the whole temperature range measured suggests the Curie-like upturn at low-T is intrinsic in nature. **b.** $S(Q,\omega)$ of kapellasite at $T = 0.1$ K measured on the inelastic neutron scattering spectrometer IN5, ILL. The position of the gapless continuum of excitations in Q agrees well with that expected for a cuboc2 short-range ordered structure. Both taken from [4].

8.2.3 Magnetism in haydeeite, α-MgCu$_3$(OH)$_6$Cl$_2$

Whilst the magnetic characteristics of haydeeite are not as well studied as kapellasite, it is clear that they behave very differently. The high temperature magnetic suscpetibility of haydeeite is well described by the Curie-Weiss law, with $\theta_{\rm w} = 0$ K, $C = 0.445$ emu mol-Cu^{-1} and $\mu_{\rm eff} = 1.89\,\mu_{\rm B}$ Cu^{-1} [5]. The effective moment is larger than that expected from the spin-only formula, but this is often observed in similar Cu^{2+}-based kagome materials due to an enhancement of the Landé g-factor. Below $T \approx 100$ K, χ deviates slightly from Curie-Weiss behaviour, likely signalling the build-up of short-range correlations as in kapellasite, before a clear ferromagnetic transition occurs at $T_{\rm C} = 4.2$ K. Upon further cooling, χT reaches a maximum before decreasing down to the lowest measured temperature, revealing an additional antiferromagnetic component. Field dependent $\mu_{\rm eff}$ measurements at $T = 3$ K shows a hysteresis associated with the magnetic transition and a small spontaneous moment of $0.02\,\mu_{\rm B}$ Cu^{-1}. The small sign of this moment makes it is unsurprising that no magnetic Bragg peaks are observed in the powder neutron diffraction experiment on the high-resolution D2B diffractometer.

Electronic structure calculations have suggested a weaker nearest-neighbour exchange coupling (J_1) compared to kapellasite, resulting in $|J_1| \approx |J_{\rm d}|$ [7]. Considering the importance in further neighbour exchange in defining the magnetic ground state, this difference should not have such a drastic effect. However, these calculations are limited by the unknown H(D) position in haydeeite, which has a large influence on the exchange values and may explain the incorrect prediction of antiferromagnetic J_1. Experimentally, static magnetic susceptibility and specific heat data is best reproduced with values: $J_1 = -12.4$ K, $J_2 = 1.2$ K and $J_{\rm d} = 2.1$ K [12]. This places haydeeite in the ferromagnetically ordered region of the phase diagram, thus agreeing with the transition observed in χ. The large difference in

J_{d} compared to kapellasite is perhaps unsurprising given that it is mediated by the diamagnetic ion in both materials. It remains to be seen whether the reduced cation site disorder in haydeeite affects the exchange energies, although this is likely to induce spin singlet freezing along the J_{d} path and should not effect the exchange integrals [11]. A note should be made that all the models presented thus far have neglected any anisotropic exchange *via.* the DM interaction, which is allowed on the kagome lattice, and all its possible consequences are not understood.

The close link between theoretical and experimental studies in these materials requires advancements to be made in both camps. The rest of this chapter deals with magnetic characterisation of haydeeite to determine the magnetic structure and exchange constants.

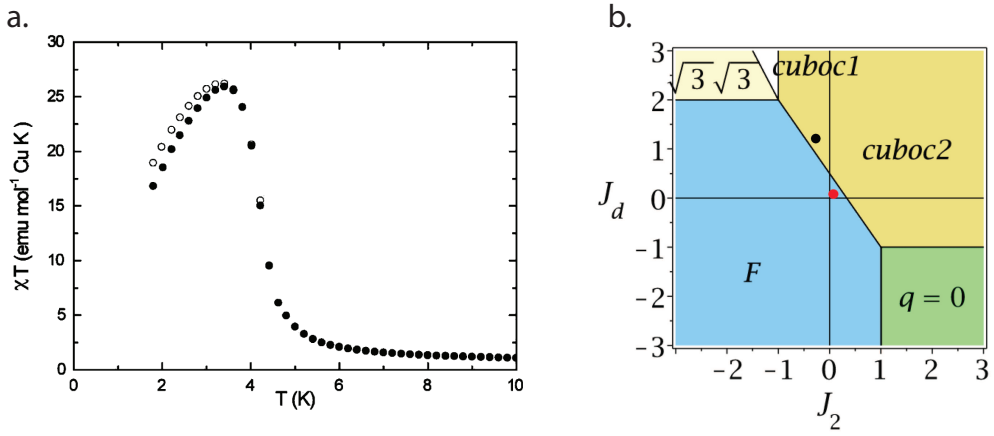

Figure 8.4: **a.** Temperature dependence of χT measured using a SQUID magnetometer. A ferromagnetic transition occurs at $T_{\mathrm{C}} = 4.2\,\mathrm{K}$ followed by a subsequent downturn indicating an additional antiferromagnetic component [5]. **b.** A J_1-J_2 phase diagram, with J_1 = 1 (FM), taken from [12]. The red point represents the values of J that best model experimental bulk χ and specific heat data. This places haydeeite in the ferromagnetic region of the phase diagram, whilst kapellasite (black point) sits in the cuboc2 region.

8.3 Synthesis and initial characterisation

For this project, synthesis of powdered haydeeite was performed with the main aim of characterising the magnetic contribution in neutron scattering experiments. Given that Cu^{2+} d^9 is $S = \frac{1}{2}$, the magnetic scattering has relatively low intensity and large sample sizes are required to observe it. Previous synthesis of haydeeite was limited by a low yield ($\sim 200\,\mathrm{mg}$) and this section describes a modified method used to produce larger yields of deuterated material [5, 14].

The scaled-up synthesis is based on that previously reported for haydeeite [5]. This consists of a gentle reflux reaction of copper powder in a highly concentrated aqueous $MgCl_2$ solution. However, in the scaled-up reactions, a few peculiarities not previously reported were found. Stirring the reaction ceased the production of any haydeeite or paratacamite phases whatsoever. Instead, the product 'grew' on the surface of the copper powder at the bottom of the flask over a period of several days (> 1 week). Interestingly, introducing an initial stirring phase at the start of the reaction, before allowing the copper to settle, sped up the subsequent growth phase to $\sim$ 2 days. Presumably this allows dissolution of

the copper in solution, thus promoting a faster precipitation of the product once the stirring is stopped. Additionally, the reaction slowed once the copper sediment was covered with blue haydeeite powder and so intermittant stirring further sped up the reaction.

As noted in the literature, lower $MgCl_2$ concentrations encouraged the growth of minor paratacamite impurites. For the deuterated reactions, yet higher [$MgCl_2$] was needed compared to the protonated equivalent in order to prevent any impurity phases. This may be due to the slightly lower pH of D_2O compared to H_2O. Post-synthesis preparation is complicated by any unreacted Cu powder which remains at the end of the reaction. Luckily, the Cu agglomerates into ~ 0.1 mm particles, allowing most of the product to be decanted out of the flask leaving the dense Cu powder behind. The product can then be further purified by sonicating, leaving to stand and pipetting off the product suspended in solution.

8.3.1 Refined synthetic method

Anhydrous $MgCl_2$ (190.422 g, 1.596 mol) was dissolved in D_2O (500 ml) in a 3-neck, 1 l round-bottomed flask. The solution was magnetically stirred and the flask held in an ice bath during the addition of $MgCl_2$, as the dissolution is very exothermic. Copper powder (2.22 g, 35 mmol) was subsequently added along with 4 glass beads ($\varnothing$ 2 mm) and the flask placed in an oil bath, which was set to heat to reflux the solution. Two of the flask necks were sealed with superseals and oxygen gas was bubbled gently through these using needles into solution. An air condenser was attached to the final neck to avoid losing any D_2O.

The solution was stirred initially for $\sim$ 12 h at 300 rpm. Once the stirring is stopped, blue powder was visible within a few hours. The solution was stirred at $\sim$ 12 h intervals for 5 mins until the reaction was complete, $i.e.$ when there is no change in the amount of copper powder which settles after each stirring. Upon completion, the reaction solution is decanted off whilst hot, leaving the product behind. The product is then washed with D_2O and decanted into a 50 ml centrifuge tube leaving any large copper particulates behind. This centrifuged tube is then sonicated for 5 mins and left to settle for another 5 mins. The top 40 ml of solution, containing pure haydeeite powder in suspension, can then be collected using a pipette. The pure product is then washed once with 50 ml D_2O and thrice with 30 ml acetone before being dried on a rotary evaporator. A typical yield was on the order of ~ 1.5 g.

8.3.2 Nuclear structure refinement

Powder neutron diffraction was performed on the WISH diffractometer at ISIS, UK. A standard vanadium can of 10 mm diameter was loaded with 1.756 g of deuterated powdered haydeeite and placed in a standard 'orange' cryostat. Rietveld refinement was performed on data collected at $T = 1.5$ K for a total of 2 hours using banks 5 and 3 ($2\theta = 153$ and $90\,^\circ$respectively) with the main aim of determining the Mg^{2+}/Cu^{2+} site mixing ratio. Atomic positions on all sites were stably refined together along with anisotropic displacements on the Mg, O, Cl and D sites, whilst the Cu site was only stable with an isotropic displacement. Refinements were performed using the TOPAS software suite [15].

The refined lattice parameters at $T = 1.5$ K are $a = b = 6.2633(2)$ and $c = 5.7025(2)$ Å which are in good agreement with published results and give the first indication of similar anti-site disorder in this sample [5]. The atomic positions, occupancies and displacement parameters are listed in Table 8.1.

Site	Wyckoff site	x	y	z	Occupation	B_{iso} (Å^2)
Mg	$1b$	0	0	$\frac{1}{2}$	1	
Cu	$3f$	$\frac{1}{2}$	0	$\frac{1}{2}$	0.78(2)	0.550(70)
Mg	$3f$	$\frac{1}{2}$	0	$\frac{1}{2}$	0.22(2)	0.550(70)
O	$6i$	0.3510(5)	0.1755(5)	0.3453(4)	1	
Cl	$2d$	$\frac{1}{3}$	$\frac{2}{3}$	0.1492(6)	1	
D	$6i$	0.3907(4)	0.1954(4)	0.1746(6)	1	
Site	B_{11} (Å^2)	B_{22} (Å^2)	B_{33} (Å^2)	B_{12} (Å^2)	B_{13} (Å^2)	B_{23} (Å^2)
Mg	0.96(20)	0.96(20)	3.99(50)	0.47(20)	0	0
O	0.75(19)	0.39(19)	1.21(16)	0.38(19)	-0.44(17)	-0.23(17)
Cl	0.74(17)	0.74(17)	2.12(14)	0.36(17)	0	0
D	2.62(20)	2.42(19)	3.33(16)	1.20(20)	0.31(17)	0.16(17)

Table 8.1: Table of refined crystallographic data of deuterated haydeeite obtained from Rietveld refinement of powder neutron diffraction data. The final $R_{\mathrm{wp}} = 6.32$ for 37 parameters.

Again, these parameters are in good agreement with the literature. The main interest in these results is the cation disorder: the triangular $1b$ Mg^{2+} site refined to full occupancy, as has previously been found [5], whilst the kagome $3b$ Cu^{2+} site is occupied with $\sim 22(2)\,\%$ Mg^{2+}. This latter figure is slightly larger than the 16 % found in the literature [5]. However, the previous study was performed on the high-resolution D2b diffractometer, whereas WISH is not a dedicated high-resolution diffractometer and has a limited high-Q range. The errors on the occupation is evidence of the poor Q-range on WISH and it is unsurprising that the values are slightly different from previous studies.

IN6		IN5		
$\lambda = 5.12$ Å	$\lambda = 4.14$ Å	$\lambda = 3.60$ Å	$\lambda = 4.14$ Å	$\lambda = 4.80$ Å
1.5 K	1.5 K	1.5 K	1.5 K	1.5 K
3.0 K	6.0 K	$\geq$ 10 K		8.0 K
6.0 K		$\geq$ 25 K		
12.0 K				

Table 8.2: Table of measurements taken on the IN6 and IN5 neutron spectrometers.

8.4 Determination of exchange interactions from inelastic neutron scattering

The ferromagnetic transition in haydeeite presents the opportunity of observing spin-wave excitations using inelastic neutron scattering. This allows extraction of magnetic superexchange couplings and gives a valuable comparison to those determined from high-temperature series expansions and electronic structure calculations [7, 12]. To this end, experiments were performed on three time-of-flight inelastic instruments to measure the excitations spectrum in various different energy ranges.

For the first two experiments on IN6 and IN5, a 0.78 g powdered haydeeite sample was loaded into an aluminium can with annular geometry of 15 mm outside diameter, 13 mm inside diameter and 50 mm height. Various measurements were taken on both instruments and these are summarised in Table 8.2.

8.4.1 Preliminary experiment - IN6

The measurements taken at smaller wavelength featured strong spurious scattering from the sample environment which could not be fully removed through the data reduction. As such, the data analysis here will focus on the $\lambda = 5.12$ Å data. The fully reduced $S(Q, \omega)$ for temperatures above and below T_C measured at this wavelength can be seen in Figure 8.5.

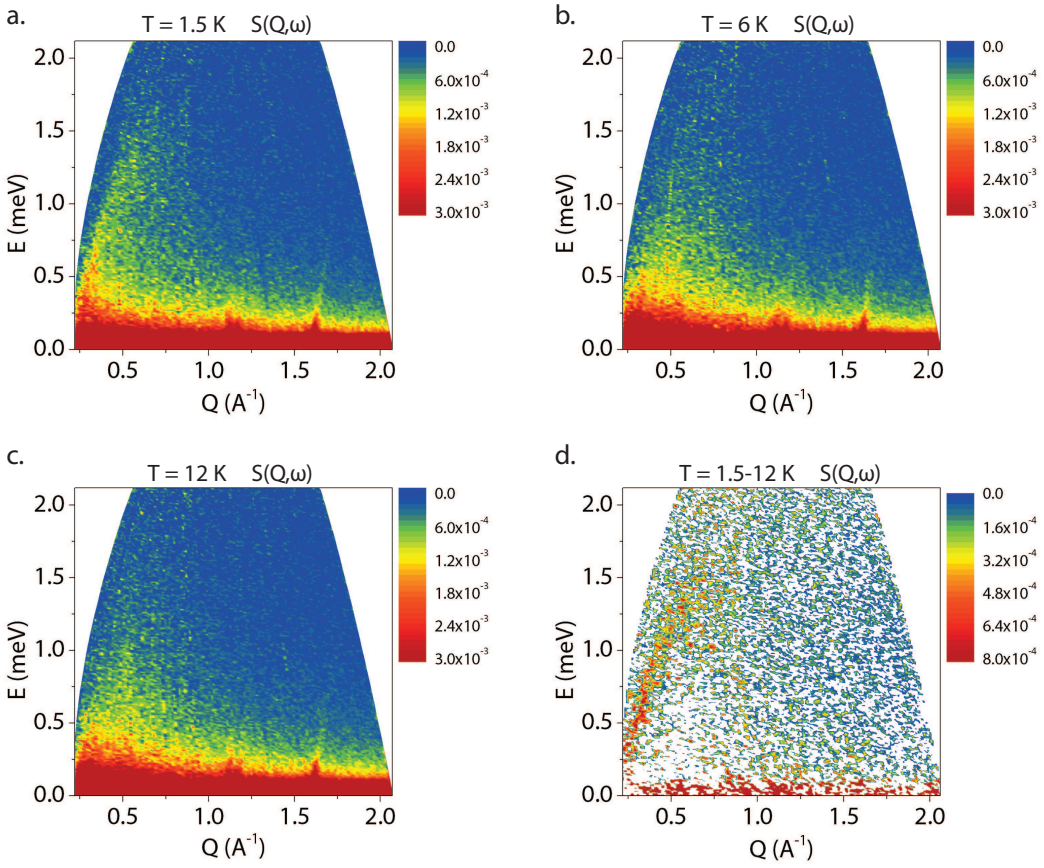

Figure 8.5: $S(Q, \omega)$ measured on IN6 at **a.** $T = 1.5$ K, **b.** $T = 6$ K, **c.** $T = 12$ K and **d.** $T = 1.5 - 12$ K with neutrons of $\lambda = 5.12$ Å. Above $T_C = 4.2$ K, excitations form a broad peak centred at low-Q. Below T_C, a spin-wave with what appears to be a linear dispersion at low-E appears, in addition to the excitations apparent above T_C. The low-T-high-T subtraction shows the spin-wave as well as an over subtraction in the area of the low-E excitations, the latter indicating a reduction of their intensity. The poor statistics hinder a quantitative analysis of the spin-wave dispersion.

The temperature dependence of $S(Q, \omega)$ above T_C shows similar behaviour to that of kapellasite. The broad hump at low-Q, which persists up to 12 K, is a result of magnetic excitations of a short-range order, although it is centred slightly lower in Q than kapellasite. However, below T_C the behaviour drastically changes as a clear spin-wave dispersion develops as well as a weakening of the short-range-

ordered signal. A difference plot between $T = 6$ and 1.5 K on the right of Figure 8.5 produces a clearer picture of the spin-wave dispersion and confirms an over-subtraction in the area of the short-range excitations. In these data, the spin-wave appears to emanate linearly from $Q \neq 0$, which would result from antiferromagnetic long-range order, however it will be shown later that it has the quadratic dispersion expected for ferromagnetic order.

The data collected at $\lambda = 4.14$ Å was unusable due to spurious scattering in the energy region of interest. As this data would have given better resolution and flux in the region of the spin-wave, it was necessary to take more measurements on another instrument. The time-of-flight spectrometer IN5 provides much better flux at this E_i and thus provides the ideal instrument to explore the magnetic scattering observed on IN6.

8.4.2 Low energy excitations – IN5

The exact same sample and aluminium can from IN6 was measured on IN5. Runs of ~ 10 h were performed at $\lambda = 4.8$ Å at temperatures of $T = 1.5$ and 8 K. Shorter measurements were also performed on cooling at $\lambda = 3.6$ Å and $\lambda = 4.1$ Å however no vanadium normalisation was possible for these wavelengths. Data reduction was performed in LAMP and the fully reduced $S(Q,\omega)$ for $\lambda = 4.8$ Å is shown in Figure 8.6.

The improved statistics on IN5 give a clearer view of the dispersion of both the spin-wave and short-range excitations. Above T_C, broad peaks at $Q \approx 0.4$ Å^{-1} and 2.3 Å^{-1} have dispersion similar to that seen for kapellasite, shifting to higher Q with increased energy transfer. Dividing $S(Q,\omega)$ by $1 - \exp(-E/k_\mathrm{B}T)$ to obtain the imaginary part of the dynamic susceptibility, $\chi''(Q,\omega)$, highlights this strange dispersion (Figure 8.7b). This cannot be modelled with a quasielastic Lorentzian line-shape, as is possible in kapellasite at $T > 5$ K, and understanding this feature remains problematic.

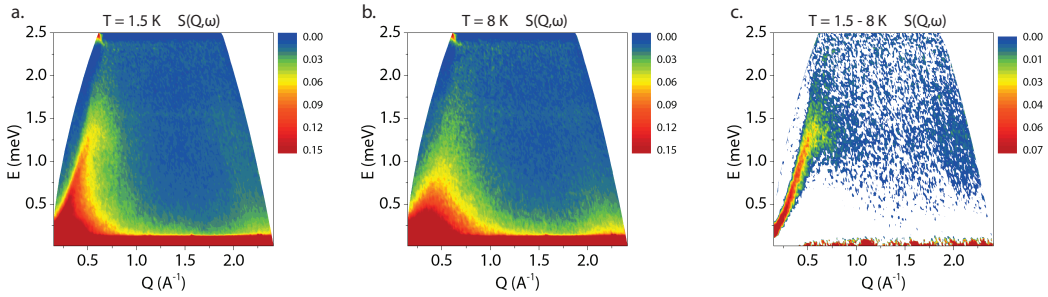

Figure 8.6: $S(Q,\omega)$ of haydeeite measured on IN5 at **a.** $T = 1.5$ K, **b.** $T = 8$ K and **c.** low-T-high-T subtraction. The quadratic dispersion of the spin-wave at low-Q proves it be ferromagnetic in origin. A second peak of excitations can be seen at higher Q above T_C.

Below T_C the spin-wave is again clearly observed. A quadratic dispersion of the spin-wave at low-Q is seen in the low-T high-T subtraction, which confirms that it originates from ferromagnetic order as expected from the bulk susceptibility data. The low-energy excitations are still present below T_C, although an over-subtraction in the low-Q, low-E area shows they have reduced intensity. Coexistence of static and dynamic spins is also observed in μSR measurements where 2 contributions are needed to

model the μ^+ relaxation [12]. Rather than a coalescence of the two states, as seen in vesignieite [16], this can be understood to be a phase separation with 'pockets' of dynamic and static spins [17].

The spin-wave dispersion is determined by the magnitude and structure of the superexchange interactions between the magnetic ions. To extract this information, integrations of $\chi''(\phi, \omega)$ were taken at various Q and E values so as to follow the maximum intensity of the spin wave. At low-Q, integrations were taken at fixed E values, whilst the peak of the spin wave was better determined using integrations at fixed Q values (Figures 8.7d and 8.7e). At constant E, the position of the peak was measured using the maximum intensity of the peak, rather than trying to model the peak with a function. At $E > 1.0$ meV the peaks are quite asymmetric due to diffuse scattering around the peak of the spin-wave and, as such, their positions are ill-defined. However, from the constant Q strips, the spin-wave peaks at $E \approx 1.3$ meV.

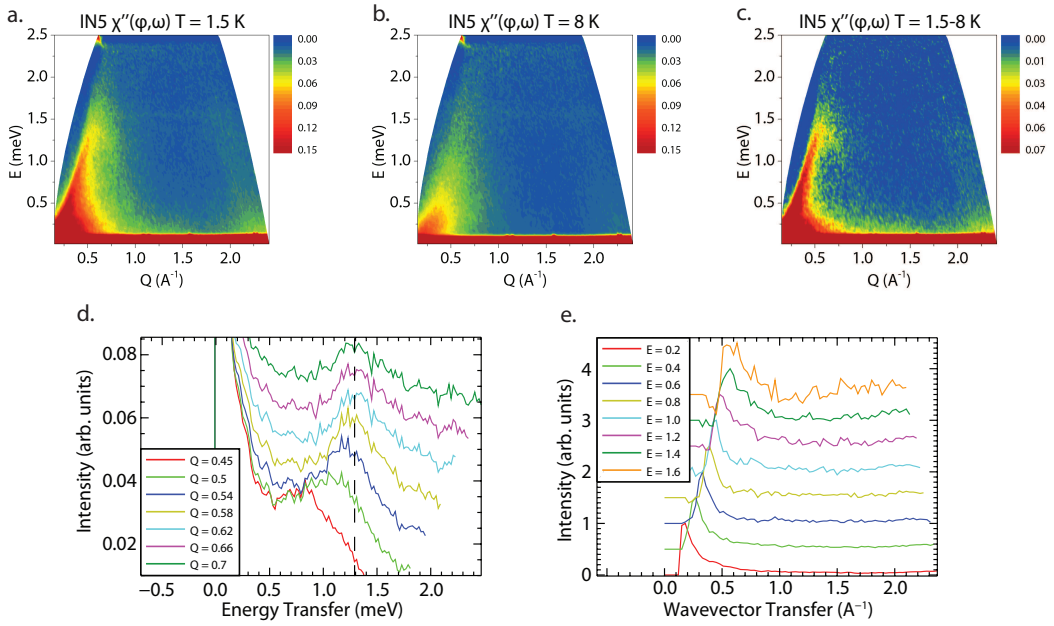

Figure 8.7: Top. Plots of $\chi''(Q, \omega)$ at **a.** $T = 1.5$ K, **b.** $T = 8$ K and **c.** low-T-high-T subtraction. The dispersion of the excitations above T_C cannot be modelled with any standard peak-shape. **Bottom.** Constant Q and E cuts of the temperature subtracted $\chi''(\phi, E)$ were used to map the spin-wave dispersion. **d.** Integrations at constant Q were used to determine the peak maximum (≈ 1.3 meV). The dotted line is a guide to the eye. **e.** Integrations at constant E were used to follow the dispersion to low-Q values. The peak maximum was taken to be the position of the peak.

To analyse the experimental excitation spectra a model based on a J_1, J_2, J_3 and J_d exchange system, as described earlier in the chapter, was developed to predict the magnetic excitations spectra. The three Cu atoms in the unit cell of haydeeite, produced from the symmetry operations on the single crystallographic Cu site, results in three excitation branches. By expanding the calculations to higher energies, and averaging over all directions as occurs in powder scattering, it becomes clear that the higher energy excitation bands are important for uniquely defining the exchange parameter. Figure 8.7 shows powder averaged magnetic excitation spectra for the $J_1 = -0.65$ meV and $J_1 = -1.07$, $J_2 = 0.1$ and $J_d = 0.18$ meV models, respectively. Whilst both models give qualitatively similar spectra at lower

energies, the higher energy branches are very different. Unfortunately, the energy range measured on IN5 is insufficient to measure the other excitation branches and therefore further measurements were required to determine the exchange energies.

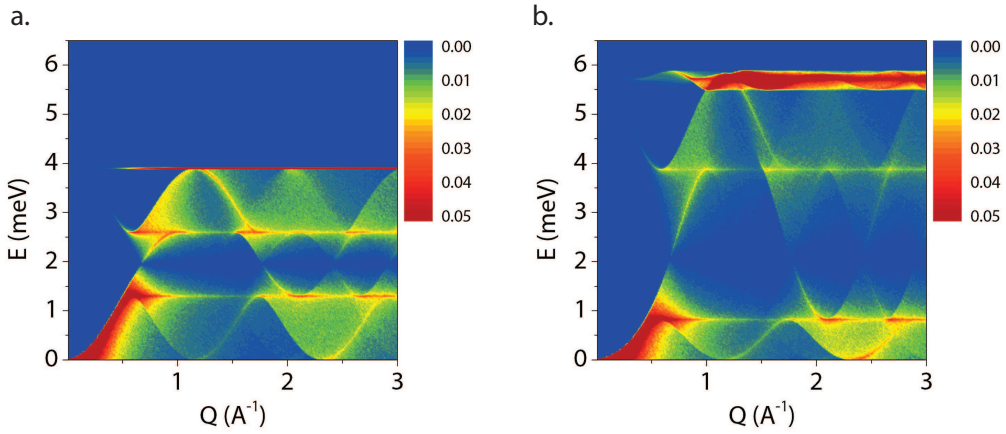

Figure 8.8: a. Calculated powder averaged magnetic excitation spectrum of haydeeite for a $J_1 = -0.65$ meV model. **b.** The same as **a.** but with exchange values $J_1 = -1.07$, $J_2 = 0.1$ and $J_\mathrm{d} = 0.18$ meV obtained from the fits to experimental bulk susceptibility and specific heat data [12].

8.4.3 High energy excitations – IN4

To observe the higher energy magnetic excitations of haydeeite, measurements were taken on the thermal time-of-flight spectrometer IN4 at the ILL. A larger deuterated sample mass of 1.75 g, prepared using the same synthetic method as before, was loaded into a flat sample holder with a 2×4 cm window. Spectra were collected with an incoming energy $E_i = 16.6$ meV ($\lambda = 2.22$ Å) with the background choppers at 3000 rpm and the Fermi chopper at 12000 rpm. Several data runs were collected above the transition temperature $T_\mathrm{C} = 4.2$ K between 30 and 78 K, an average temperature of $T \approx 60$ K confirmed by detailed balance, for a total of 10.5 hours. Below the transition, a spectrum was collected at $T = 2.1$ K for 2.5 hours. A vanadium spectrum was collected for normalisation at the same incoming energy.

Figure 8.9a-b shows $S(Q,\omega)$ for the two measured temperatures. At low temperature significant additional scattering occurs at low-Q and $E \sim 8$ meV compared to at high temperature, which does not appear to extend far out in Q suggesting it is magnetic in origin. The temperature subtractions shown in Figure 8.9c-d for $S(Q,\omega)$ and $\chi''(Q,\omega)$, respectively, clearly show this band of scattering and its magnetic-like Q-dependence. The simple J_1 model calculation in Figure 8.8a has a completely flat highest energy band with a narrow width in energy, however the scattering in the experimental data does not look flat and occurs in a broad energy range between $7 \leq E(\mathrm{meV}) \leq 10$. Thus, the magnetic dispersion is similar to the J_1-J_2-J_d model in Figure 8.8b and a simple J_1 model can be ruled out.

The powder-averaging of $S(Q,\omega)$ causes bands to occur flat in E at the extrema of the dispersion. For a J_1-J_d model, the relationship between the energy of the flat bands and the exchange interactions is simple to determine and are given by $E_\mathrm{high} = -6J_1 - 3J_\mathrm{d}$ for the highest energy band and $E_\mathrm{low} = -2J_1 - 4J_\mathrm{d}$ for the lowest energy band. The calculated spectra are very sensitive to J_2 which

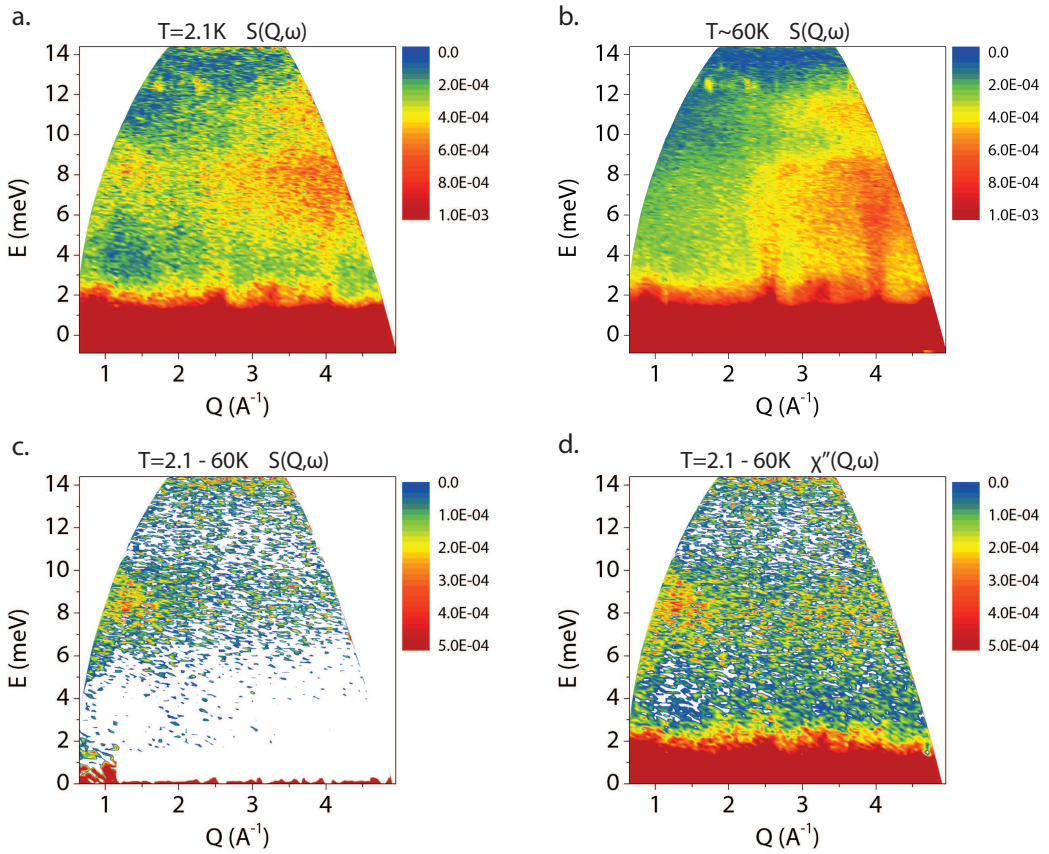

Figure 8.9: Top: $S(Q,\omega)$ for haydeeite collected on IN4 at temperatures of **a.** $T = 2.1\,\mathrm{K}$ and **b.** $T \approx 60\,\mathrm{K}$. **Bottom:** Temperature subtractions performed for **c.** $S(Q,\omega)$ and **d.** $\chi''(Q,\omega)$. A broad band of magnetic excitations occur at low-Q and $E \sim 8\,\mathrm{meV}$ that suggests a simple J_1 exchange model is insufficient.

causes dispersion of the flat bands at even small values (Appendix D, Figure D.1 and also discussed later with Figure 8.12). These relationships make it easy to determine the rough J values that match the experimental data.

A cut at constant $Q = 1.5\,\mathrm{Å}^{-1}$ on $\chi''(\phi,\omega)$ from IN4 is shown in Figure 8.10a and gives the peak intensity of the magnetic excitations at $8 \leq E(\mathrm{meV}) \leq 8.5$. Another peak is seen at $E \sim 6.5\,\mathrm{meV}$ which likely corresponds to the middle flat band that is significantly weaker. Taking the higher energy peak as $E_{\mathrm{high}} = 8.25\,\mathrm{meV}$ and the lower energy peak, from the IN5 data, as $E_{\mathrm{low}} = -1.3\,\mathrm{meV}$, the relationship described in the previous paragraph gives $J_1 = -1.62$ and $J_{\mathrm{d}} = 0.48\,\mathrm{meV}$.

The calculated excitation spectrum for the model $J_1 = -1.62$ and $J_{\mathrm{d}} = 0.48\,\mathrm{meV}$ is shown in Figure 8.10b. The higher energy excitations are a much better match to the IN4 data than both the J_1 only model and the values from bulk susceptibility fits. The calculations also puts the peak of the middle flat branch at $E \sim 6.5\,\mathrm{meV}$, again in agreement with the IN4 data. Furthermore, the low energy excitations still closely resemble the IN5 data. However, in order to quantify the match between experiment and theory, constant E and Q-cuts are required for the calculated data. To do this, the calculated data for the $J_1 = -1.62$ and $J_{\mathrm{d}} = 0.48\,\mathrm{meV}$ model was read into LAMP [18] and the same manipulation techniques were used as for the experimental data.

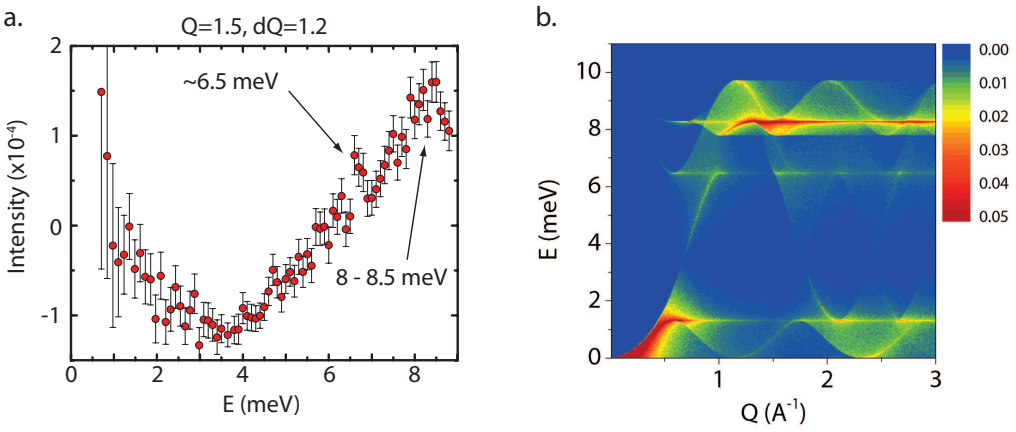

Figure 8.10: **a.** A cut at constant $Q = 1.5$ and d$Q = 1.2$ of $\chi''(\phi, \omega)$ for the temperature subtracted data from IN4. The peak in the magnetic excitations at $E \sim 8.25$ meV allows a more accurate determination of the exchange values than the IN5 data alone. **b.** Calculated excitation spectra for the model $J_1 = -1.62$ and $J_\mathrm{d} = 0.48$ meV, where the J values have been estimated from the IN4 and IN5 data. The calculation from these values is in much better agreement with experiment than the J_1 only model or the values obtained from bulk susceptibility fits.

Comparisons between the $J_1 = -1.62$ and $J_\mathrm{d} = 0.48$ meV model and the experimental data are shown in Figure 8.11a-f. For all plots, the same constant E cuts were performed on both the calculated and experimental data. At energies lower than $E = 0.8$ meV, the agreement between data sets is significantly worse due to diffuse scattering in the experimental data. However, above this energy both the position and width of the peak matches the calculated data extremely well. At the higher energies from the IN4 data the statistics of the experimental data are clearly worse despite a large dE integration, yet the fit remains excellent and confirms the suitability of the $J_1 = -1.62$ and $J_\mathrm{d} = 0.48$ meV model.

It is now important to discuss how J_2 affects the excitation spectrum and its agreement with experimental data, as bulk susceptibility fits predict it has a similar magnitude to J_d [12]. Including a non-zero J_2 exchange interaction shifts the position of the low-energy branch, E_low discussed earlier, however does not alter the most intense point at the high energy branch, E_high. Therefore, the relationship of E_low to the experimental energy branches attained earlier can be altered to take account of J_2 giving $E_\mathrm{low} = -2J_1 - 4J_\mathrm{d} - 6J_2$, whereas E_high remains the same.

Figure 8.12a-b shows calculated patterns where the J_1 and J_d values are obtained using the E_high and E_low relationships for $J_2 = 0.1$ and -0.1 meV. Whilst the dispersion of the top energy branch changes with J_2 the most intense band remains at the same energy. Aside from those changes, the most noticeable difference is the shift in E of the middle branch, E_middle. The position in energy of this branch thus gives an excellent parameter to determine the value of J_2 and Figure 8.12c compares constant Q strips of calculated data with $-0.1 < J_2 < 0.1$. This graph confirms that $J_2 = 0$ is a good model as $E_\mathrm{middle} \sim 6.5$ meV is in excellent agreement with the experimental data (Figure 8.10a). Furthermore, the large shift of E_middle with a value of $J_2 = 0.1 = 0.07J_1$ means that any error in J_2 will be insignificant in determining the final position of haydeeite in the exchange interaction phase diagram.

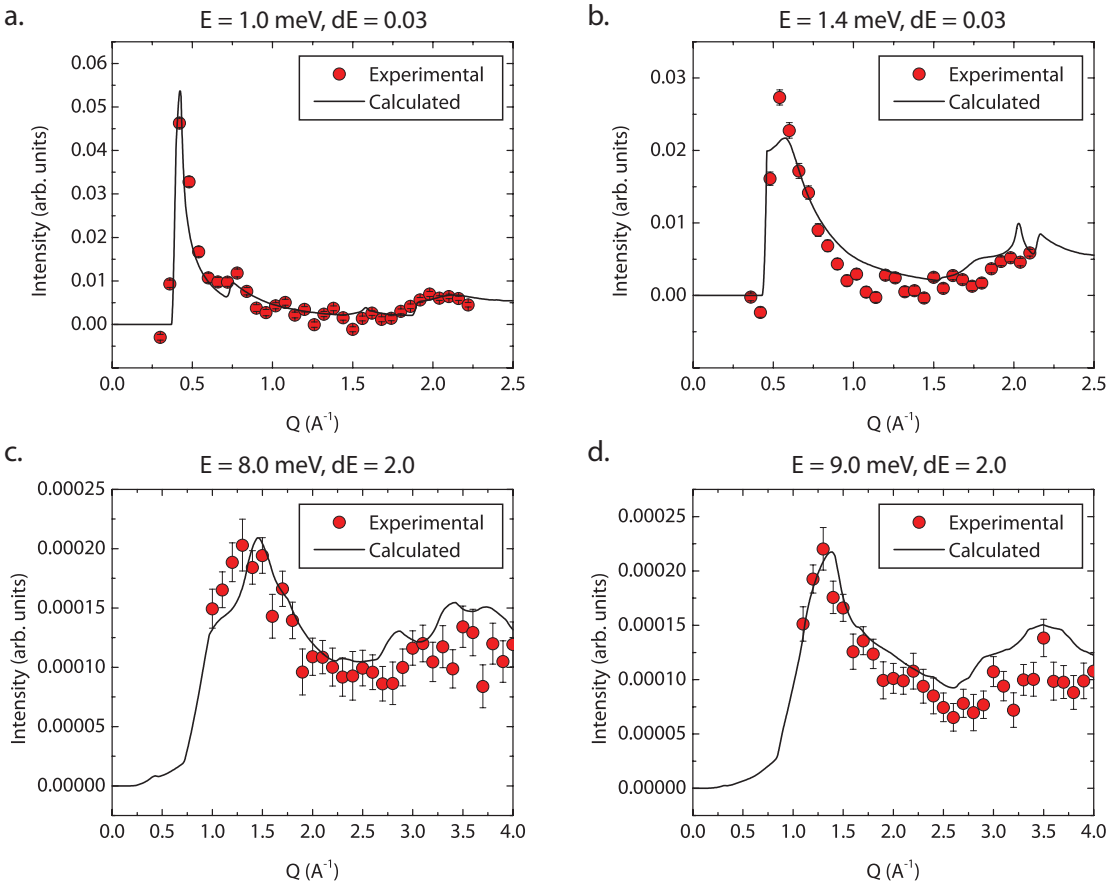

Figure 8.11: Constant E cuts on both the calculated $J_1 = -1.62$ and $J_\mathrm{d} = 0.48\,\mathrm{meV}$ model and the experimental $\chi''(\phi,\omega)$ data from IN5 (**a. - c.**) and IN4 (**d. - f.**). The excellent agreement between experimental and calculated data quantitatively confirms the suitability of the J_1-J_d model.

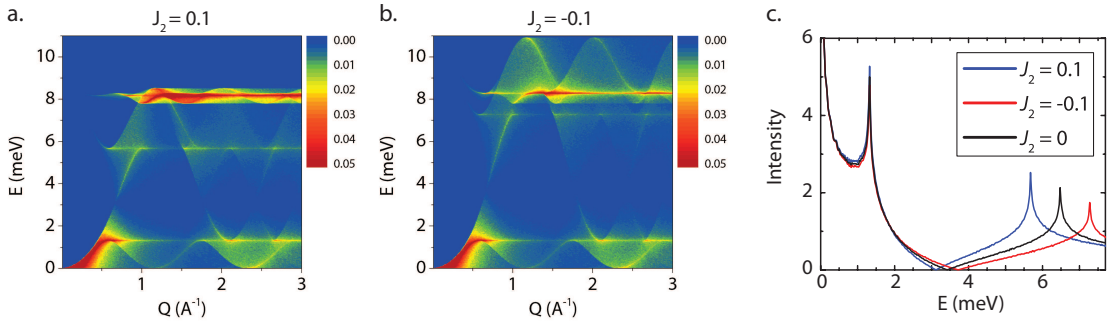

Figure 8.12: Calculated excitation spectra for haydeeite with **a.** $J_1 = -1.52$, $J_2 = 0.1$ and $J_\mathrm{d} = 0.28\,\mathrm{meV}$ and **b.** $J_1 = -1.72$, $J_2 = -0.1$ and $J_\mathrm{d} = 0.68\,\mathrm{meV}$. Including a non-zero J_2 shifts the energy of the middle flat mode, E_middle. **c.** Constant Q cuts of the calculated spectra in **a** and **b**. The value of E_middle for $J_2 = 0$ is in good agreement with the experimental data, whilst the large change in E_middle with $J_2 = \pm 0.1 = \pm 0.07 J_1$ shows that any error in J_2 is insignificant with respect to the exchange interaction phase diagram.

8.5 Magnetic structure refinement

The time-of-flight IN5 spectrometer is the ideal instrument for observing low energy spin wave excitations in frustrated magnets but the poor Q-resolution compared to a dedicated diffractometer makes

analysis of the elastic line and magnetic Bragg peaks difficult. However, the advantages IN5 has over a dedicated diffractometer are (i) the increased neutron flux, which can reveal small magnetic Bragg peaks, particularly for $k = 0$ structures where the nuclear and magnetic peaks overlay and (ii) the ability to remove any quasi- or inelastic scattering from integrations on the elastic line.

Constant $E = 0$ cuts of the elastic line are shown in Figure 8.13. In the temperature subtracted data, peaks occur at the same Q values as the nuclear structure and their relative intensities have a magnetic-like form factor Q-dependence, indicating (i) they are magnetic Bragg peaks and (ii) they are indexed with a $k = 0$ propagation vector. This is in agreement with the ferromagnetic characteristics of the spin waves and the transition in the magnetic susceptibility data.

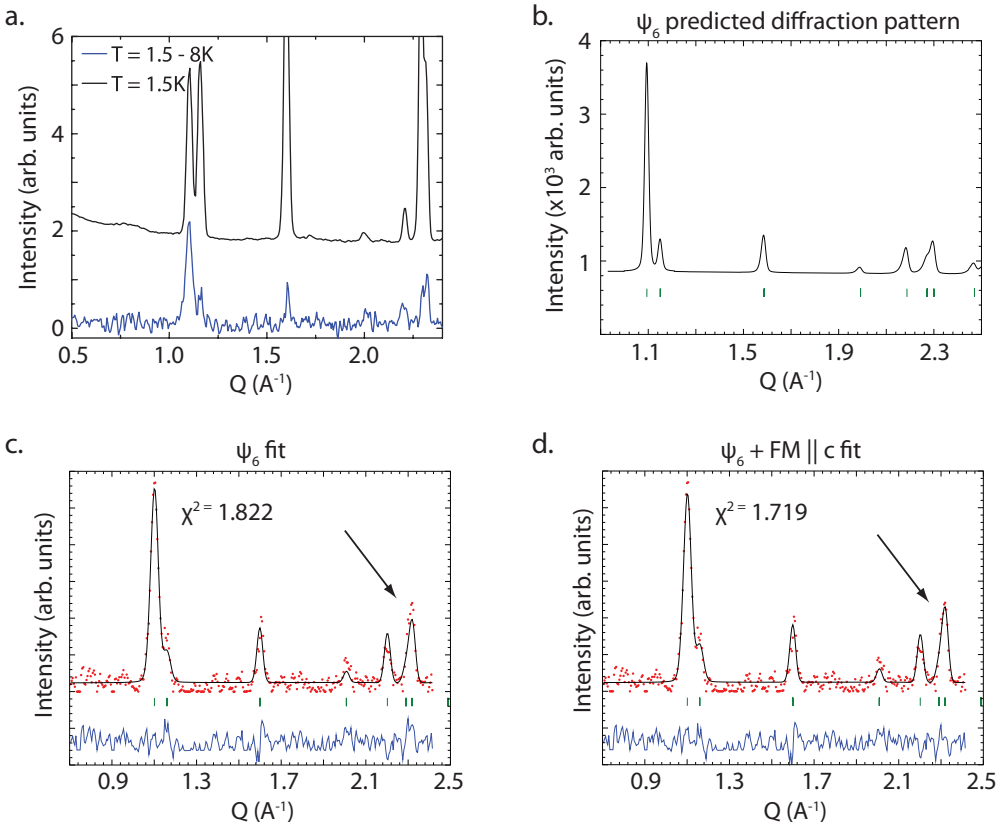

Figure 8.13: **a.** A comparison of constant $E = 0$ meV strips with d$E = 0.05$ meV of $T = 1.5 - 8$ K and $T = 1.5$ K data collected on IN5. The magnetic Bragg peaks in the temperature subtracted data are centred on the nuclear Bragg peaks and are therefore indexed with $k = 0$. **b.** Predicted powder diffraction pattern for the ferromagnetic along b ψ_6 magnetic structure. The relative peak intensities closely resembles the magnetic Bragg peaks observed on IN5. **c.** Rietveld refinement of the magnetic Bragg peaks in the elastic line from IN5 with a magnetic structure defined by ψ_6 only. The black arrow indicates the poor fit. **d.** Rietveld refinement of the IN5 data using ψ_6 plus an additional ferromagnetic component along c. This model lowers χ^2 due to an improvement in the fit at the peak indicated and is strong evidence for a DM interaction in haydeeite.

Knowledge of the magnetic propagation vector and the positions of the Cu atoms in the unit cell allows calculation of the symmetry allowed magnetic structures *via.* representational analysis with the program SARAh [19]. The decomposition of the magnetic representation in the notation of Kovalev [20]

is $\Gamma_{Mag} = 1\Gamma_1^1 + 0\Gamma_2^1 + 3\Gamma_3^1 + 0\Gamma_4^1 + 3\Gamma_5^2 + 0\Gamma_6^2$ and the real basis vector components are given in Appendix D, Table D.1. The regular collinear ferromagnetic structure along b is ψ_6, and ferromagnetic along c, whilst not obvious, is found within Γ_3 and can be constructed from combinations of two of ψ_2, ψ_3 and ψ_4. Through comparison of the predicted magnetic Bragg peaks for each basis vector with the experimental data, it is clear that the latter closely resembles the predicted pattern for a ferromagnetic along b magnetic structure, *i.e.* ψ_6 (Figure 8.13). Figure 8.13c shows a magnetic refinement of the temperature subtracted IN5 elastic line data where the ψ_6 coefficient was allowed to refine and this gives a good fit to the data.

It has been well documented that the Dzyaloshinskii-Moriya (DM) interaction is allowed on the kagome lattice and can perturb the magnetic ground state [21, 22, 23]. The DM interaction often causes a canting of the moments in a magnetic structure, therefore it is useful to investigate whether such a model fits with the IN5 data. Figure 8.13d shows a fit to the same data with ϕ_6 plus an additional ferromagnetic contribution along c. The black arrow in the figure highlights the most significant improvement in the fit which lowers χ^2 from 1.822 to 1.719 and provides strong evidence for a DM interaction in haydeeite. It is often stated that the inclusion of two irreps to describe a magnetic structure is not allowed from Landau theory for second-order phase transitions. However, rather than being unphysical, the requirement of two irreps instead suggests that the transition is weakly first-order. Specific heat data collected on haydeeite show a sharp peak at T_C that is characteristic of a first-order transition and therefore adds further weight behind the legitimacy of using two irreps in the magnetic refinement [12]. It is important to note that IN5 is not a dedicated diffractometer and therefore there may be issues with Lorentz polarisation and absorption corrections. To unambiguously confirm the findings from this refinement further experiments are required on a more suitable instrument.

8.6 Analysis of magnetic scattering from neutron diffraction - WISH

The measurements at WISH were performed on the same sample used on IN4. A standard vanadium can of diameter 10 mm was loaded with 2.74 g of powdered haydeeite and placed in a standard orange cryostat. Measurements were made at 8 temperatures, $T = 1.5, 2.0, 2.5, 3, 3.5, 4, 6$ and 10 K for a total of 80 μAh each (2 hours).

Data collected on bank 2, which extends down to $Q \sim 0.5\,\text{Å}^{-1}$, either side of $T_C = 4.2$ K are shown in Figure 8.14. The data at the two temperatures look very similar and no clear magnetic Bragg peaks are visible at $T = 1.5$ K. In the low-Q region (Figure 8.14b) the background is visibly lower in the raw data at low temperature, likely due to a reduction in the paramagnetic scattering below the magnetic transition. Despite this reduction in the background, the peak intensity of the first peak (001) at $Q \sim 1.10\,\text{Å}^{-1}$ does not reduce accordingly which suggests there is some magnetic scattering contributing to the Bragg peak at $T = 1.5$ K (Figure 8.14b inset).

The high flux at the highest angle bank 1 on WISH makes it ideal for observing weak magnetic signals. Figure 8.14c shows the integrated area of the (001) peak compared with the local background

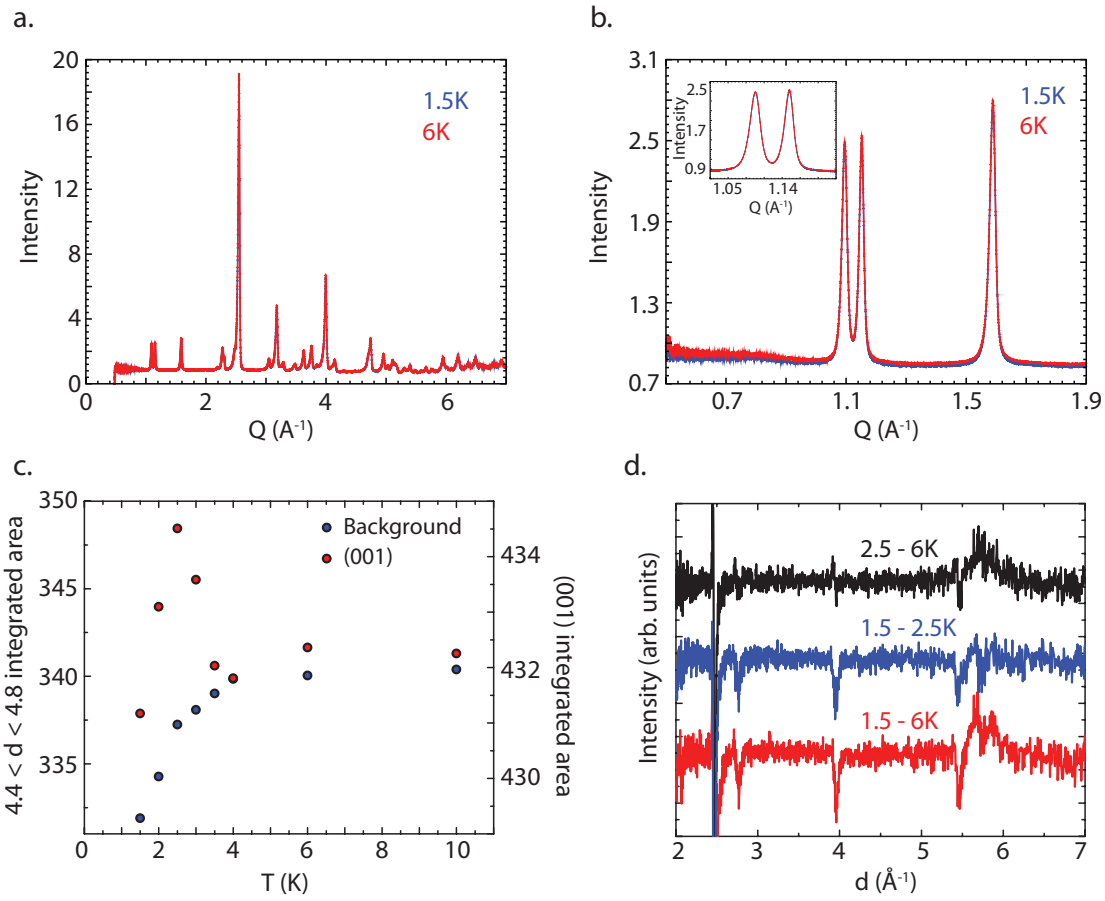

Figure 8.14: **a.** A comparison of the diffraction patterns collected on bank 2 at WISH either side of T_{C} at $T = 1.5$ and 6 K. **b.** The low-Q region showing a reduction in the background at $T = 1.5$ K due to less paramagnetic scattering in the magnetically ordered phase. **inset** Despite the background reduction, very little change in the intensity of the first peak between the two temperatures suggests a magnetic contribution. **c.** Integrated area of the (001) peak and the local background from data collected on bank 1. The increase in the area below $T_{\mathrm{C}} = 4.2$ K indicates a magnetic contribution, however a sudden change in the background occurs below $T = 2.5$ K. **d.** Temperature subtractions of the data on bank 1 showing the appearance of a magnetic peak centred on the (001) peak between 6 and 2.5 K before a large change in background below $T = 2.5$ K.

on bank 1. Below T_{C} an increase in the (001) peak area compared to the background indicates magnetic Bragg scattering, however below $T = 2.5$ K the area decreases again due to a large change in the background which swamps any intensity increase of the Bragg peak. The raw data temperature subtractions in Figure 8.14d shows a broad magnetic peak centred on the (001) peak appears between 2.5 and 6 K with little change in the background. Below $T = 2.5$ K, the intensity of this magnetic peak does not grow further, however the background has clearly reduced as shown by the negative peaks centred on the nuclear Bragg peaks.

Bank 1 on WISH measures down to $Q \sim 0.12$ Å^{-1} and therefore gives access to features originating from short-range interactions. Figure 8.15a shows the low-Q scattering on bank for the $10 - 6$ K and $10 - 1.5$ K temperature subtractions. In the $10 - 1.5$ K subtraction a broad hump centred at $Q \sim 0$ Å^{-1} is visible that is not present above T_{C}. As the shape of this low temperature scattering is not that expected

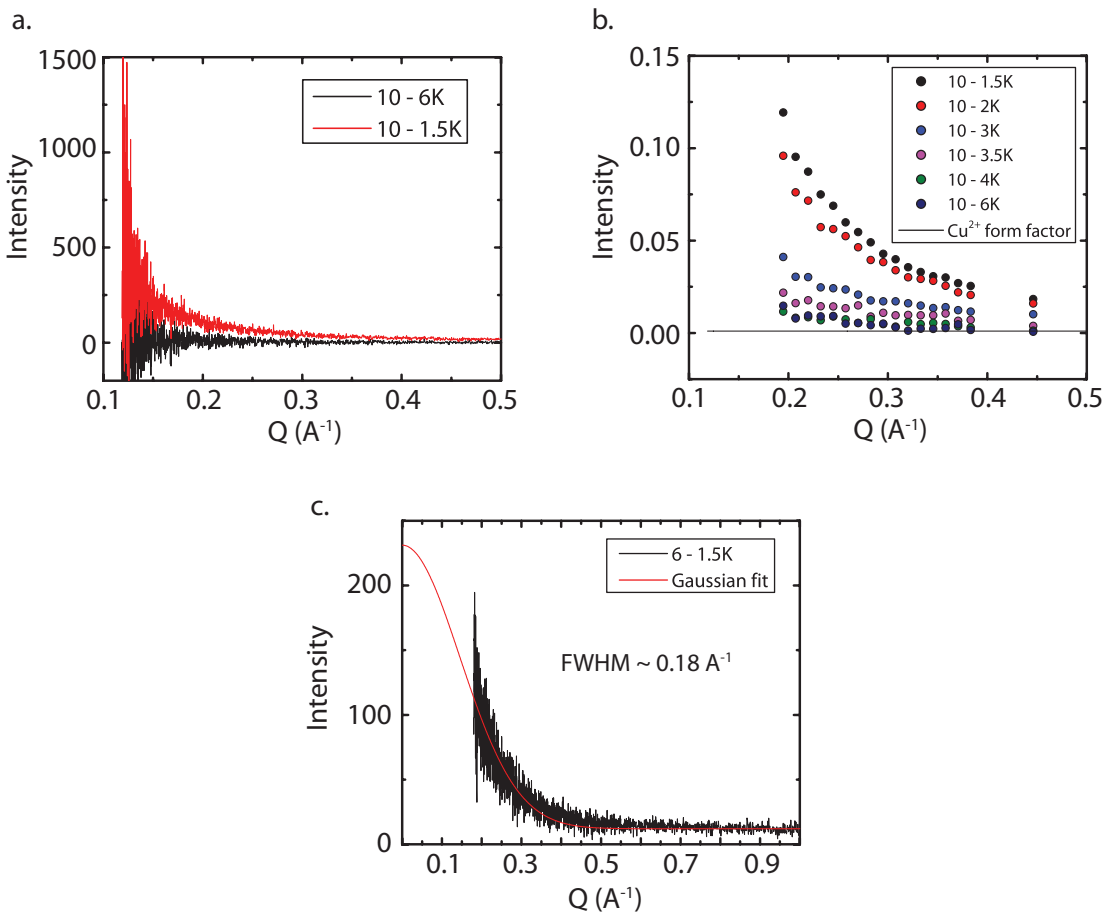

Figure 8.15: **a.** Temperature subtractions of the low-Q scattering measured on bank 1, WISH. The peak at low-T centred on $Q = 0\,\text{Å}^{-1}$ indicates a decrease in short-range ferromagnetic correlations below T_C. **b.** The temperature dependence of the low-Q peak. It increases sharply below $T = 3\,\text{K}$ which occurs at the same temperature as the sudden drop in the background discussed in the text. The Cu^{2+} form factor is relatively flat in this Q region **c.** A fit of the low-Q peak with a Gaussian function fixed at $Q = 0\,\text{Å}^{-1}$ gives the length scale of the correlations as $Q \sim 0.18\,\text{Å}^{-1}$ or $d \sim 34.9\,\text{Å}$.

from the Cu^{2+} form factor, this feature originates from short-range correlations that can be assumed to be ferromagnetic as they are centred at $Q = 0\,\text{Å}^{-1}$. The short-range correlations persist well below T_C and only decrease below $T = 3\,\text{K}$, as shown by the temperature dependence of the low-Q peak in Figure 8.15b. The reduction in short-range correlations coincides with (i) the sudden change in background discussed earlier and (ii) the zero-field-cooled/field-cooled splitting seen in bulk magnetic susceptibility [5]. The Gaussian-like peakshape gives information on the form of these short-range interactions: the FWHM is equal to the length scale of the correlations. Fitting the peak with a Gaussian function fixed at $Q = 0\,\text{Å}^{-1}$ gives a FWHM $\sim 0.18\,\text{Å}^{-1}$, therefore the length-scale of the correlations are 34.9 Å in d-spacing (~ 3 kagome hexagons).

8.7 Magnetic susceptibility

Several studies in the literature have characterised the magnetic susceptibility of haydeeite, thus $\chi(T)$ plots are omitted here but are found in Appendix D, Figure D.2 for completeness. This chapter will focus on an analysis of the magnetisation as a function of magnetic field to reveal the partially ordered magnetic ground state and provide complementary information to the elastic and inelastic neutron scattering studies already discussed. Furthermore, the results here provide evidence for sample consistency by comparing measurements on two different samples. Sample **1** was measured on IN6 and IN5, whilst Sample **2** on IN4 and WISH.

A comparison of χ^{-1} *vs.* T for the two samples discussed in this chapter are shown in Figure 8.16. Both samples have a similar temperature dependence of the susceptibility and fits between $150 < T < 300$ give values of θ_{W} within 5 K of each other, which when considering errors in the sample mass, SQUID reading and fitting procedure does not represent a significant difference. The main structural difference likely to occur between samples that would alter their magnetic properties is the Cu/Mg site mixing. Significant changes in this ratio would affect the Curie constant, which effectively measures the number of spins, and for the two samples these are 0.3517(9) and 0.3480(9) emu mol K Cu^{-1}. Again, these are remarkably similar and therefore the comparisons made between these samples in this chapter are legitimate.

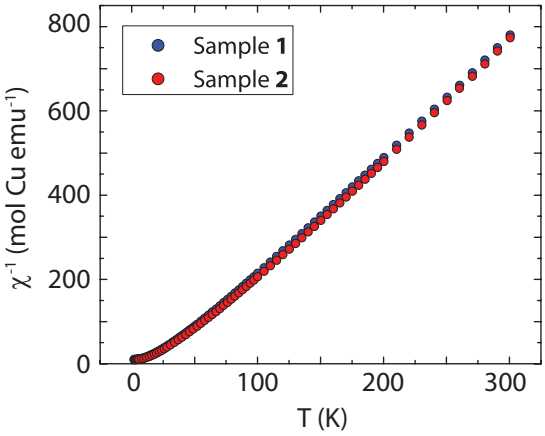

Figure 8.16: χ^{-1} as a function of temperature measured in a 5 T field for the two haydeeite samples discussed in this chapter. Fitting the $150 < T < 300$ K region for both samples gives similar values for both θ_{W} and C, as discussed in the text.

A plot of magnetisation, M, as a function of field at $T = 2$ K for both haydeeite samples is shown in Figure 8.17a. A cursory look at the plot shows that both samples saturate at similar values of $\sim 0.83\,\mu_{\mathrm{B}}$ mol^{-1} Cu^{-1} however there is a slight difference in the curvature, particularly between $0 < H(T) < 1$. Despite being measured well below $T_{\mathrm{C}} = 4.2$ K, the shape of the response neither resembles a paramagnetic nor a ferromagnetic Brillouin function and previous analysis of the haydeeite M *vs.* H response has been modelled by a combination of both paramagnetic and ferromagnetic components [12]. A similar analysis is performed here for the two samples to determine the heterogeneity of the samples and to compare with the results from the neutron diffraction and inelastic scattering experiments.

The large initial increase of μ in the M *vs.* H plots of haydeeite indicates that the magnetisation saturates quickly with applied field. As haydeeite has a heterogeneous state of ferromagnetic and paramagnetic components, the high field data can be fitted with a paramagnetic Brillouin function plus a constant term to account for the saturated ferromagnetic signal [12]. The model used was:

$$M(H)/M_{\mathrm{sat}} = (1 - f)B_{\mathrm{J,PM}}(H) + f \tag{8.1}$$

where f is the constant ferromagnetic component, M_{sat} is the saturated magnetisation at high field and the paramagnetic Brillouin function, $B_{\mathrm{J,PM}}(H)$, is given by:

$$B_{\mathrm{J,PM}}(H) = \tanh(g\mu_{\mathrm{B}}JH/k_{\mathrm{B}}T) \tag{8.2}$$

The Landé g-factor was allowed to refine freely along with f, but the total angular momentum quantum number was fixed to $J = S = 0.5$. A fit to the region $0.8 \leq H(T) \leq 8$ is shown in Figure 8.17b and models the high field data well giving a refined g-factor of 1.73, very close to that expected for a $S = \frac{1}{2}$ system. The refined ferromagnetic component $f = 0.63$ gives a saturated ferromagnetic moment of $\sim 0.55\,\mu_{\mathrm{B}}$ mol^{-1} Cu^{-1} as $M_{\mathrm{sat}} \sim 0.88\,\mu_{\mathrm{B}}$ mol^{-1} Cu^{-1}. Thus, the remaining paramagnetic moment of $\sim 0.33\,\mu_{\mathrm{B}}$ mol^{-1} Cu^{-1} shows that a significant portion of the spins remain fluctuating even at $T = 2 < \frac{T_{\mathrm{C}}}{2}$ K. The same analysis performed on Sample **2** gives $g = 1.73$ and $f = 0.69$ again showing the similarities between the samples.

Subtracting the paramagnetic Brillouin function from the M *vs.* H data should then give the ferromagnetic component of the magnetisation, shown in Figure 8.17c. To model this, the paramagnetic Brillouin function is adapted to take into account the effective Weiss molecular field. Assuming the Weiss field is proportional to the applied field, one can replace H with $\lambda(H + H_{\mathrm{C}})$ where H_{C} is the coercive field at the given temperature and λ is the Weiss molecular field ($H_{\mathrm{C}} = 13$ Oe at $T = 2$ K) [24]. With this we can create an approximate ferromagnetic Brillouin function, $B_{\mathrm{J,FM}}$:

$$B_{\mathrm{J,FM}}(H) = \tanh(g\mu_{\mathrm{B}}J\lambda(H + H_{\mathrm{C}})/k_{\mathrm{B}}T) \tag{8.3}$$

Using this function to fit the ferromagnetic component shown in Figure 8.17c did not work as the parameters refined to unphysical values and the large number of points in the $H < 0.1$ T region skewed the process. However, fixing the g value to that refined from the paramagnetic fit and λ to the value of the Weiss constant, $\theta_{\mathrm{W}} = 28.1$ K, allows a reasonable fit to the low field region. It is noteworthy that the experimental data saturates much more smoothly than the model, which may hint at the complexity of the heterogeneous magnetic state. For instance, the paramagnetic component in haydeeite below T_{C} may act more like a superparamagnet, with interactions between paramagnetic clusters, whilst more complex interactions with the ferromagnetic regions will also occur. Consequently, the paramagnetic region may be incorrectly modelled, due to these additional interactions, therefore a purely ferromagnetic component cannot be extracted. These results add further evidence towards the complexity of the ground state of haydeeite, despite the seemingly simple ferromagnetic transition in χ.

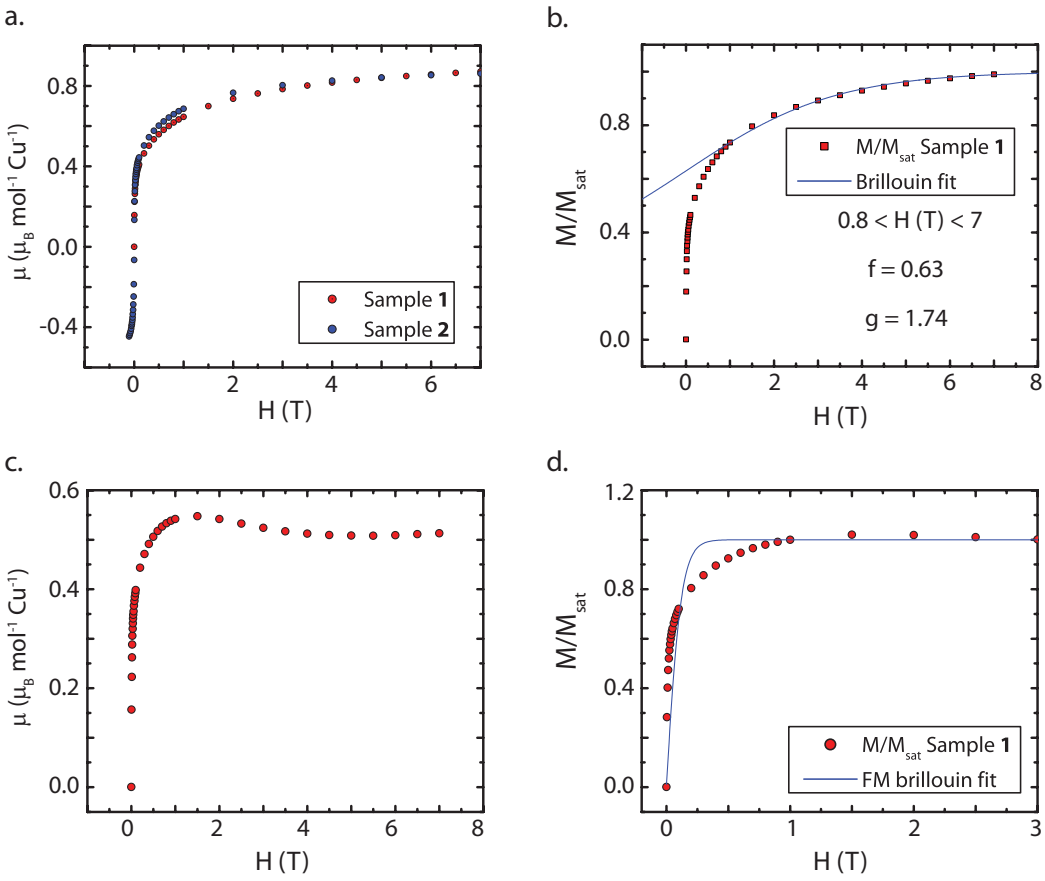

Figure 8.17: **a.** Magnetisation as a function of field, $M(H)$, at $T = 2\,\mathrm{K}$ for haydeeite Samples **1** and **2** (explained in the text). The shape of the $M(H)$ curve does not resemble either a ferromagnetic or paramagnetic response. **b.** A fit to the $0.8 < H(T) < 7$ region with a paramagnetic Brillouin functions described in the text. The fit gives a ferromagnetic component of 63 %. **c.** The purely ferromagnetic component of $M(H)$ from subtraction of the raw data with the fitted paramagnetic component, which saturates at $\sim 0.53\,\mu_\mathrm{B}$. **d.** A fit to the ferromagnetic component of $M(H)$ with a ferromagnetic Brillouin function described in the text. The poor fit is likely a problem with the paramagnetic subtraction.

8.8 Discussion

Haydeeite has quite different magnetic properties to those of the closely related minerals in the $S = \frac{1}{2}$ paratacamite group of minerals. Its closest relative, kapellasite, contains multiple exchange terms between Cu^{2+} however remains disordered down to the lowest temperatures measured [4]. The other similar materials herbertsmithite and 'Mg-herbertsmithite' have strong antiferromagnetic interactions yet do not magnetically order [4, 3, 25]. Further afield, the monoclinic $CdCu_3(OH)_6Cl_2$ again shows strong antiferromagnetic interactions and no order to $T = 2\,\mathrm{K}$ [26], whilst the $S = \frac{3}{2}$ $MgCo_3(OH)_6Cl_2$ displays a spin glass transition at $T = 2.75\,\mathrm{K}$ [27]. Haydeeite, on the other hand, has weakly ferromagnetic interactions and enters a long-range ordered magnetic state at $T_\mathrm{C} = 4.2\,\mathrm{K}$ [2]. The origins of these very different magnetic properties are currently unexplained.

8.8.1 Haydeeite in the J_1-J_d kagome phase diagram

When discussing the magnetic properties of haydeeite with respect to other $S = \frac{1}{2}$ kagome magnets, kapellasite is the most interesting and useful comparison as it shares the same crystal structure, although with Mg^{2+} replaced by Zn^{2+}. The predicted magnetic orders in classical frustrated antiferromagnets correctly places kapellasite in the cuboc2 region of the phase diagram based on a multiple exchange model [9, 4]. The best fits to high-temperature susceptibility of kapellasite give the exchange values as $J_1 = -1.03$, $J_2 = -0.34$ and $J_d = 1.34$ meV (ferromagnetic is negative), thus the across hexagon term is of similar magnitude to the nearest-neighbour interaction [11].

From the inelastic neutron scattering data presented in this chapter, the haydeeite magnetic structure is defined by the exchange interactions $J_1 = -1.62$ and $J_d = 0.48$ meV and therefore, aside from J_2, of similar magnitude to kapellasite. This puts haydeeite in the ferromagnetic region of the phase diagram predicted in [9], as shown in Figure 8.18a, very close to the phase boundary with cuboc2. The ferromagnetic ordering agrees with the transition in the SQUID data and, more conclusively, the magnetic Bragg peaks observed in the elastic line of the IN5 data. From these classical calculations, it is evident that a slightly increased J_d exchange for haydeeite would push it into cuboc2 magnetic order.

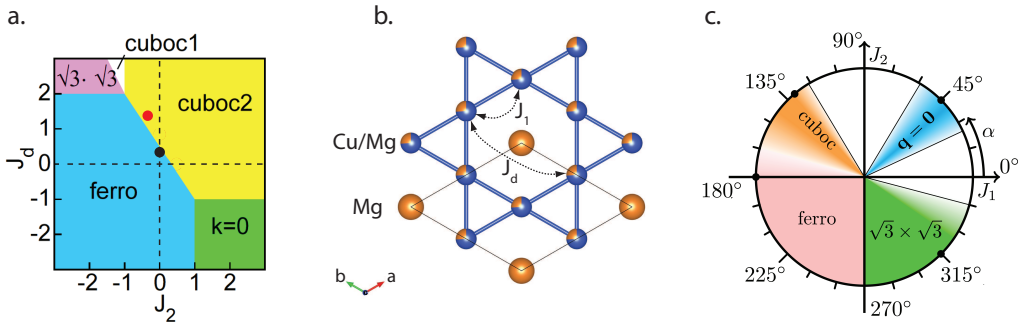

Figure 8.18: **a.** Classical J_1-J_2-J_d phase diagram on the kagome lattice. The red dot is the best fit to high-temperature susceptibility and specific heat data of kapellasite [11]. The black dot is the exchange values for haydeeite from the inelastic neutron scattering data in this chapter. **b.** The J_1 and J_d exchange paths in haydeeite. The J_d exchange path is mediated by the $1b$ Mg site. The small J_d in haydeeite compared to kapellasite is likely due to full occupation of the $1b$ site with Mg in the former. **c.** Magnetic quantum phase diagram for a J_1-J_2 model on the kagome lattice [28].

The J_d exchange path for haydeeite is across the kagome hexagon, likely mediated *via*. the $1b$ Mg site. It is noteworthy that the $1b$ Mg^{2+} site is fully occupied on haydeeite, as shown from neutron diffraction in this chapter and in the literature [5], however kapellasite has 11.6 % Cu^{2+} on this site [5]. Furthermore, the valence band contribution from Mg^{2+} in haydeeite is negligible whilst that from Zn^{2+} in kapellasite is significant [7]. Therefore, J_d should be smaller in haydeeite compared to kapellasite due to (i) negligible contribution of Mg s- or p-states to the Cu–O–Mg–O–Cu path and (ii) no Cu occupation on the $1b$ Mg site, which if present would produce favourable Cu $3d$–O$2p$ overlap. The results presented in this chapter agree with these predictions and explain the different magnetic structures in the two materials.

Recent calculations of magnetic quantum order using a fermionic approach for a J_1-J_2 model have predicted a phase diagram with four stable regions in addition to several disordered phases induced by quantum fluctuations, as shown in Figure 8.18c [28]. The cuboc state, which is identical to the cuboc2 state of kapellasite, occurs with ferromagnetic J_1 and a significant antiferromagnetic J_2 in agreement with experimental findings [4, 11]. Of particular interest are the enhanced quantum fluctuations in the cuboc phase which may destabilise long-range magnetic order and therefore explain the disordered state in kapellasite. Furthermore, a destabilised region may exist between the ferromagnetic and cuboc regimes ($\alpha \approx 161\,^{\circ}$), *i.e* with small J_2, which is in close proximity to the predicted exchange values of kapellasite.

Expanding quantum calculations to the J_1-J_2-J_{d} model that describes haydeeite suggests a new chiral spin liquid phase exists that neighbours both the ordered ferromagnetic and cuboc2 regions [29]. This elegantly explains the different magnetic states found in haydeeite and kapellasite. Quantum fluctuations do not destabilise the ferromagnetic regime that haydeeite occupies, however they open up a chiral spin liquid phase (CSL-A in [29]), close to cuboc2, that kapellasite likely sits in and explains its disordered ground state.

8.8.2 A candidate for the magnon Hall effect

The magnetic transition at $T_{\mathrm{C}} = 4.2\,\mathrm{K}$ in haydeeite makes it the only $S = \frac{1}{2}$ kagome magnet to enter long-range ferromagnetic order, although vesignieite has now been shown to enter long-range antiferromagnetic order (Chapter 7). The magnetic structure refined from the IN5 data confirms the ferromagnetic structure and provides strong evidence for a Dzyaloshinskii-Moriya (DM) interaction. Insulating ferromagnets on highly frustrated lattices are excellent candidates for hosting topologically protected magnon states and the magnon equivalent of the anomalous Hall effect: the magnon Hall effect [30, 31]. The insulating collinear ferromagnet $Lu_2V_2O_7$ has experimentally verified the magnon Hall effect, opening up possibilities for its use in spintronics devices [32].

The Dzyaloshinskii-Moriya interaction opens band gaps in the spin wave, or magnon, dispersion and it is these avoided crossings that give a non-zero Berry curvature producing a transverse thermal conductivity, κ^{xy}, *i.e.* the magnon Hall effect [33]. In the spin wave spectra of haydeeite, the most obvious region of $S(Q,\omega)$ to observe a band gap would be between the two higher energy bands between $6.5 < E\,(\mathrm{meV}) < 8$ (Figure 8.19). Unfortunately, the inelastic neutron scattering results presented in this chapter do not give evidence of a gap in the spin wave excitations due to the poor resolution of the higher energy excitation data. This is not surprising if the size of the DM interaction is similar to herbertsmithite, *i.e.* on the order of $\frac{D}{J} \approx 0.1\,\mathrm{meV}$ [34].

A ferromagnetic insulating DM state on the kagome lattice adds further intrigue to the magnon Hall state. Calculations of the topological phase diagram of the transverse thermal conductivity κ^{xy} in the D, J_{N} (nearest-neighbour) and J_{NN} (next-nearest-neighbour) space predict it to be strongly temperature dependent and to change sign with temperature. Haydeeite is currently the only experimental example of a ferromagnetic kagome system and, whilst similar calculations for J_1-J_{d}-D would be useful, it provides an excellent opportunity to study and better understand the magnon Hall effect, a very new branch of

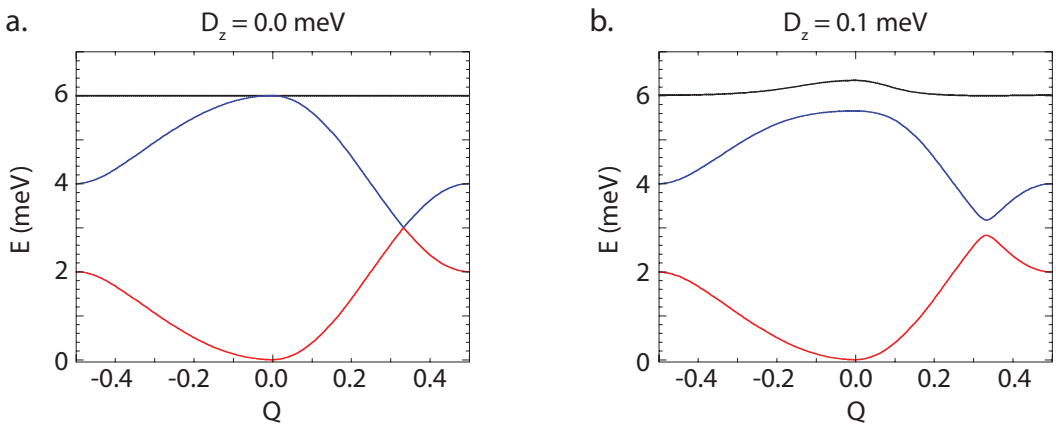

Figure 8.19: Spin-wave excitation spectra of preliminary models **a.** without and **b.** with a DM interaction. The splitting of the two higher energy branches would be the easiest to see in inelastic neutron scattering data, however the poor resolution of the IN4 data made any gap impossible to determine.

solid state physics.

8.9 Future work

Minor changes in further-neighbour interactions between haydeeite and kapellasite give rise to contrasting magnetic properties and so create the opportunity for further exploring the $S = \frac{1}{2}$ KAFM phase diagram with respect to competing interactions. Experimentally, the most logical method to achieve this would be to change the [$MgCl_2$] concentration in the reaction with the hope that samples with different stoichiometries could be synthesised. If possible, this would add valuable understanding to all other model $S = \frac{1}{2}$ KAFMs, as they all possess further neighbour correlations to various degrees.

8.10 Conclusions

Haydeeite, along with vesignieite, is one of only two model $S = \frac{1}{2}$ KAFMs that enters long-range magnetic order. This is somewhat surprising, given that the isoelectronic mineral kapellasite does not order and shows hallmarks of QSL behaviour. The inelastic neutron scattering data presented in this chapter confirms the magnetically ordered ground state of haydeeite with the superexchange parameters $J_1 = -1.62$ and $J_\mathrm{d} = 0.48$ meV. These values place the material in the ferromagnetically ordered regime of the $J_1 - J_2 - J_\mathrm{d}$ phase diagram for the kagome lattice proposed by Messio *et al.*, therefore adding support to the legitimacy of this theoretical approach. Kapellasite, however, is in the cuboc2 regime of the phase diagram due to a significantly larger J_d exchange, likely due to differences in the Cu^{2+}/Zn^{2+} site disorder between the materials. The ability to manipulate the exchange parameters during synthesis would allow further exploration of the kagome phase diagram and give access to other exotic ground states.

From the results in this chapter it is also evident that the magnetic structure of haydeeite is not solely a collinear ferromagnet. The diffuse scattering from the neutron diffraction data show short-range ordered correlations that persist to below T_C and this is corroborated by the continuum of excitations in

the inelastic data as well as the field dependence of the magnetisation. Moreover, the magnetic Bragg peaks are consistent with a DM interaction which rotates the spins of the ordered ferromagnetic structure out of the kagome plane, although further work on a dedicated diffractometer is required to confirm this finding. Recent predictions of exotic physics have been predicted in ferromagnetic insulating DM systems, such as the magnon Hall effect, and haydeeite provides an exciting opportunity to explore this unique phenomena and the first of which on the frustrated kagome lattice. This warrants attempts at some challenging future experiments, such as low temperature thermal conductivity measurements.

Bibliography

[1] M. P. Shores, E. A. Nytko, B. M. Bartlett and D. G. Nocera, *J. Am. Chem. Soc.*, 2005, **127**, 13462–3.

[2] R. H. Colman, C. Ritter and A. S. Wills, *Chem. Mater.*, 2008, **20**, 6897–6899.

[3] T.-H. Han, J. S. Helton, S. Chu, D. G. Nocera, J. A. Rodriguez-Rivera, C. Broholm and Y. S. Lee, *Nature*, 2012, **492**, 406–410.

[4] B. Fåk, E. Kermarrec, L. Messio, B. Bernu, C. Lhuillier, F. Bert, P. Mendels, B. Koteswararao, F. Bouquet, J. Ollivier, A. D. Hillier, A. Amato, R. H. Colman and A. S. Wills, *Phys. Rev. Lett.*, 2012, **109**, 037208.

[5] R. H. Colman, A. Sinclair and A. S. Wills, *Chem. Mater.*, 2010, **22**, 5774–5779.

[6] X. Rocquefelte, K. Schwarz and P. Blaha, *Sci. Rep.*, 2012, **2**, 759.

[7] O. Janson, J. Richter and H. Rosner, *Phys. Rev. Lett.*, 2008, **101**, 106403.

[8] J.-C. Domenge, P. Sindzingre, C. Lhuillier and L. Pierre, *Phys. Rev. B*, 2005, **72**, 024433.

[9] L. Messio, C. Lhuillier and G. Misguich, *Phys. Rev. B*, 2011, **83**, 184401.

[10] L. Messio, B. Bernu and C. Lhuillier, *Phys. Rev. Lett.*, 2012, **108**, 207204.

[11] B. Bernu, C. Lhuillier, E. Kermarrec, F. Bert, P. Mendels, R. H. Colman and A. S. Wills, *Phys. Rev. B*, 2013, **87**, 155107.

[12] E. Kermarrec, *Ph.D. thesis*, 2012.

[13] Y. Ran, M. Hermele, P. A. Lee and X.-G. Wen, *Phys. Rev. Lett.*, 2007, **98**, 117205.

[14] R. H. Colman, *Ph.D. thesis*, University College London, 2010.

[15] Bruker AXS, *TOPAS V4: General profile and structure analysis software for powder diffraction data*, 2008.

[16] J. Quilliam, F. Bert, R. H. Colman, D. Boldrin, A. S. Wills and P. Mendels, *Phys. Rev. B*, 2011, **84**, 180401.

[17] O. Cépas and B. Canals, *Phys. Rev. B*, 2012, **86**, 024434.

[18] D. Richard, M. Ferrand and G. J. Kearley, *J. Neutron Res.*, 1996, **4**, 33–39.

[19] A. S. Wills, *Phys. B*, 2000, **278**, 680–681.

[20] O. V. Kovalev, *Irreducible representations of the space groups*, Gordon and Breach, New York, 1965.

[21] O. Cépas, C. Fong, P. Leung and C. Lhuillier, *Phys. Rev. B*, 2008, **78**, 140405.

[22] T. Yildirim and A. B. Harris, *Phys. Rev. B*, 2006, **73**, 214446.

[23] I. Rousochatzakis, S. Manmana, A. Läuchli, B. Normand and F. Mila, *Phys. Rev. B*, 2009, **79**, 214415.

[24] L. Chen, L. Guo, Z. Li, H. Zhang, J. Lin, J. Huang, S. Jin and X. Chen, *Sci. Rep.*, 2013, **3**, 2599.

[25] R. H. Colman, A. Sinclair and A. S. Wills, *Chem. Mater.*, 2011, **23**, 1811–1817.

[26] T. McQueen, T. Han, D. Freedman, P. Stephens, Y. Lee and D. Nocera, *J. Solid State Chem.*, 2011, **184**, 3319–3323.

[27] M. Fujihala, X. G. Zheng, Y. Oohara, H. Morodomi, T. Kawae, A. Matsuo and K. Kindo, *Phys. Rev. B*, 2012, **85**, 012402.

[28] R. Suttner, C. Platt, J. Reuther and R. Thomale, *Phys. Rev. B*, 2014, **89**, 020408.

[29] S. Bieri, L. Messio, B. Bernu and C. Lhuillier, *arXiv*, 2014, **arXiv:1411**, 1–6.

[30] L. Zhang, J. Ren, J.-S. Wang and B. Li, *Phys. Rev. B*, 2013, **87**, 144101.

[31] H. Katsura, N. Nagaosa and P. A. Lee, *Phys. Rev. Lett.*, 2010, **104**, 066403.

[32] Y. Onose, T. Ideue, H. Katsura, Y. Shiomi, N. Nagaosa and Y. Tokura, *Science*, 2010, **329**, 297–9.

[33] R. Matsumoto and S. Murakami, *Phys. Rev. Lett.*, 2011, **106**, 197202.

[34] A. Zorko, S. Nellutla, J. van Tol, L. Brunel, F. Bert, F. Duc, J.-C. Trombe, M. de Vries, A. Harrison and P. Mendels, *Phys. Rev. Lett.*, 2008, **101**, 25–28.

Chapter 9

Conclusions

$S = \frac{1}{2}$ KAFMs are at the forefront of research in frustrated magnetism, yet experimentalists are currently limited to only a handful of synthetic examples. They provide the most promising models for observing QSLs in 2-dimensions, a new state of magnetism in addition to Néel, as recently shown by the discovery of fractionalised excitations in herbertsmithite. QSLs are a new form of magnetism, such as ferromagnetism, that are proposed to underpin the theory behind unconventional high-T_{C} superconductivity as well as give rise to exotic quantum entangled states with potential applications in computing. This thesis investigates the synthesis and study of three different $S = \frac{1}{2}$ KAFMs that are some of the best models available to experimentalists. Through crystallographic and magnetic characterisation techniques the results presented in this thesis exemplify the variety of exotic states that can occur in $S = \frac{1}{2}$ KAFMs alongside QSLs. Moreover, the materials studied expand our library of experimental models through which our theoretical understanding of quantum effects in frustrated magnets can be improved.

Crystallographic and magnetic studies of 'Sr-vesignieite', $SrCu_3V_2O_8(OH)_2$, are detailed in Chapter 5. This material is a new $S = \frac{1}{2}$ KAFM, not previously reported in the literature, characterised by a kagome network built from CuO_6 octahedra whose distorted geometries are consistent with dynamic JT fluctuations. A transition at $T_{\mathrm{JT}} \sim 230\,\mathrm{K}$ observed in magnetic and structural data indicates a transition to a heterogenous state of static and dynamic JT Cu sites, whilst no magnetic order occurs until $T_{\mathrm{N}} \sim 10\,\mathrm{K}$, well below the strength of the antiferromagnetic interactions, $\Theta_{\mathrm{W}} \sim -100\,\mathrm{K}$. The results suggest both spin and orbital frustration and, by comparing the structure of 'Sr-vesignieite' with related minerals in the literature, evidence for dynamic Jahn-Teller effects is also found in other $S = \frac{1}{2}$ KAFMs. Consequently, further work is warranted to determine the importance of orbital degrees of freedom in the magnetic properties of these model materials.

High-quality samples of vesignieite, prepared using a hydrothermal method adapted from that used for 'Sr-vesignieite', are crystallographically and magnetically characterised in Chapters 6 and 7, respectively. Neutron and synchrotron diffraction reveal that these samples also crystallise with a trigonal structure similar to that of their Sr^{2+}-analogue. Close inspection of structural data from vesignieite samples prepared *via.* different methods, and also with samples studied in the literature, confirm that the trigonal structure is adopted by all samples but when poorly crystalline thew structure is disordered and easily misidentified. Crystallographic strain analysis suggests the disorder is related to the JT states of

the CuO_6 and that there is an incomplete transition to the static JT distortion of the Cu sublattice. At low temperatures, evidence of dynamic JT fluctuations persist below the magnetic ordering temperature, $T_N \sim 9\,K$, although a previously unobserved small anomaly in the magnetic susceptibility at $T \sim 4\,K$ may indicate the onset of orbital order. The persistence of orbital disorder to such low temperatures indicates a large orbital frustration concomitant with the spin frustration.

The long-range antiferromagnetic structure of vesignieite below T_N is characterised by a $k = (\frac{1}{2}, 0, 0)$ propagation vector and the magnetic Bragg peaks are consistent with a unique non-coplanar octahedral structure not previously observed experimentally. Long-range magnetic order at this relatively high temperature is surprising given how close the structure is to an ideal $S = \frac{1}{2}$ KAFM and further work is required to determine the role orbital ordering may play in this. Along with vesignieite, haydeeite also has a transition to long-range magnetic order, as characterised in Chapter 8, which is unexpected considering the QSL ground states of its Zn^{2+}-analogue kapellasite and the isoelectronic mineral herbertsmithite. Inelastic neutron scattering data reveal the presence of further neighbour exchange interactions that place haydeeite in the ferromagnetic region of the phase diagram, as predicted from classical calculations on the kagome lattice, and explain the ordered ground state. The refined ferromagnetic structure is in excellent agreement with this theoretical prediction, however a significant fraction of the spins remain in a paramagnetic-like state, indicative of short-range fluctuations, and this latter mismatch between theory and experiment may arise from the omission of quantum correlations or a Dzyaloshinskii-Moriya interaction in the current theoretical model.

Originally promoted as QSL candidates, these three materials highlight the broad variety of exotic states that can arise in $S = \frac{1}{2}$ KAFMs. In the vesignieite family it is clear that the orbital degree of freedom is not quenched and undoubtedly interacts to some extent with the spin, which perhaps explains the surprising magnetic ground state and leaves open the possibility of a unique orbital liquid. Moreover, these findings force reconsideration of orbital effects in several related $S = \frac{1}{2}$ KAFMs, such as the extensively studied volborthite. Further variety is found in haydeeite, where the unique mix of ferromagnetic order on a geometrically perfect kagome lattice make it a candidate material for observing the magnon Hall effect, whilst the experimentally determined superexchange parameters add confidence to the classical calculations used for theoretical comparisons with other kagome magnets. Finally, not only do these results encourage future research on these specific materials but they open routes to the synthesis of new materials in the vesignieite family or changes in site-mixing in haydeeite to explore different regions of the multi-exchange $S = \frac{1}{2}$ KAFM phase diagram.

Appendix A

Appendix for Chapter 5

Atom	Wyckoff Site	Oxidation state	x	y	z	Occupation	B_{iso} (Å^2)
Sr1	3a	2+	0.6759(4)	0.0166(7)	0.3316(3)	1	1.141(22)
Cu1	3a	2+	0.6934(5)	0.5084(7)	0.8373(4)	1	0.337(64)
Cu1_2	3a	2+	0.5013(10)	0.6858(7)	0.1666(5)	1	1.176(77)
Cu2	3a	2+	0.0000(10)	0.1977(4)	0.1669(14)	1	0.305(35)
O11_1	3a	2-	0.1679(82)	0.9835(51)	0.5600(13)	1	2.891
O11_2	3a	2-	0.9855(54)	0.1754(86)	0.4360(13)	1	2.891
O12_1	3a	2-	0.5440(80)	0.7439(31)	0.9165(11)	1	2.891
O12_2	3a	2-	0.7193(34)	0.5354(86)	0.0866(12)	1	2.891
O13_1	3a	2-	0.8294(79)	0.3622(44)	0.2306(15)	1	2.891
O13_2	3a	2-	0.3461(50)	0.8150(81)	0.7708(13)	1	2.891
O21_1	3a	2-	0.6686(28)	0.0245(27)	0.1198(5)	1	2.891
O21_2	3a	2-	0.0172(41)	0.6587(34)	0.8696(5)	1	2.891
O31_1	3a	2-	0.7707(34)	0.1061(41)	0.0074(9)	1	3.181
O31_2	3a	2-	0.1125(40)	0.7736(37)	1.0013(9)	1	3.181
V1	3a	5+	0.7205(9)	0.0502(9)	0.9240(3)	1	0.151(21)
V2	3a	5+	0.0418(9)	0.7081(10)	0.0704(3)	1	0.151(21)
H1	3a	1+	$\frac{2}{3}$	0	0.0719	1	0.790
H2	3a	1+	0	$\frac{2}{3}$	0.9281	1	0.790

Table A.1: Refined atomic information of 'Sr-vesignieite' from synchrotron powder diffraction data. The starting model was a $P3_1$ structure adapted from the β-vesignieite structure. The refined lattice parameters are $a = b = 5.89577(2)$ and $c = 20.4126(1)$ Å.

Appendix B

Appendix for Chapter 6

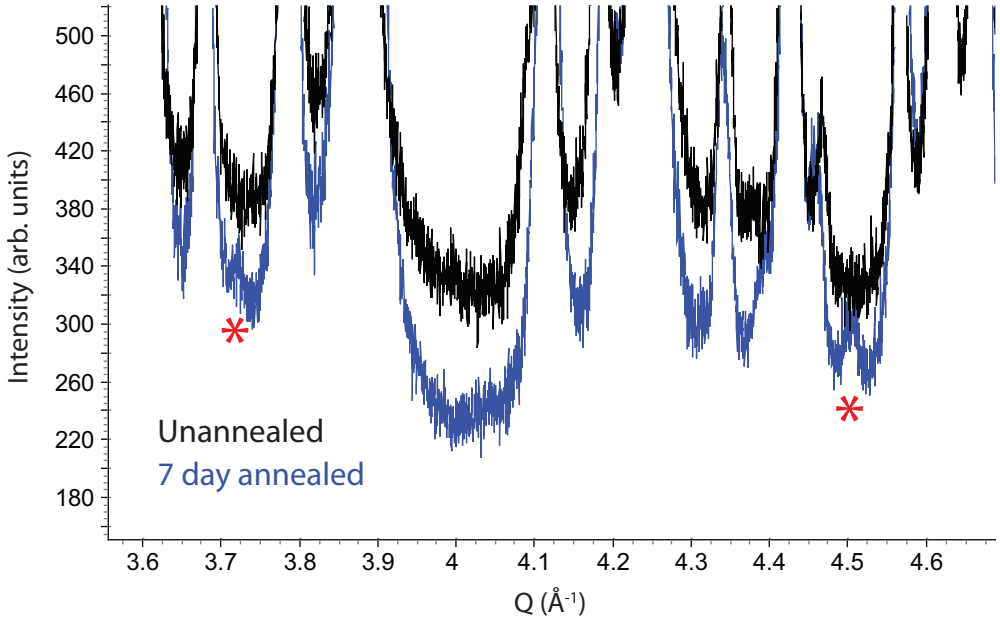

Figure B.1: Synchrotron diffraction data collected on vesignieite samples that have been left unannealed and hydrothermally annealed for 7 days, described in Chapter 6, Section 6.3. The red stars indicate new peaks that appear with annealing that index with the trigonal $P3_1$ related structure.

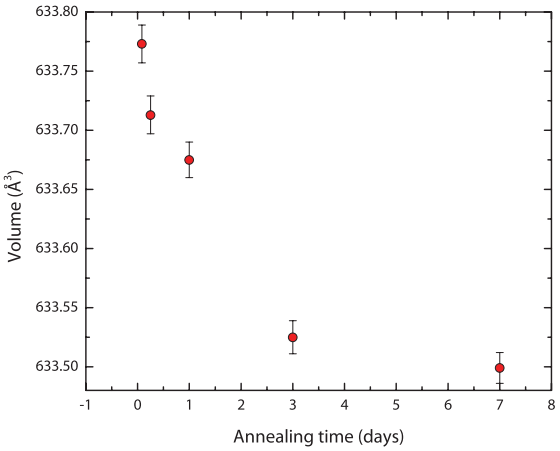

Figure B.2: Refined cell volume as a function of hydrothermal annealing time for vesignieite samples prepared by a reflux method (Method 2 in Chapter 6). The unannealed sample is not shown and has a significantly smaller lattice than shown here (632.012(14) $Å^3$).

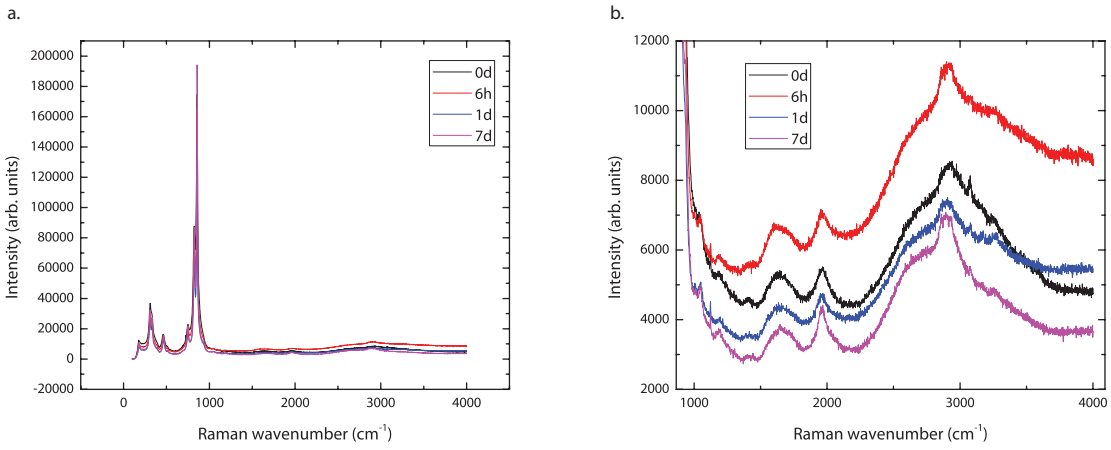

Figure B.3: Raman scattering data collected on vesignieite samples prepared using a reflux reaction and subsequently hydrothermally annealed for the number of days indicated (Method 2 in Chapter 6). **a.** The full spectrum and **b.** the high wavenumber region.

Atom	Wyckoff Site	Oxidation state	x	y	z	Occupation	B_{iso} (Å^2)
Ba1	3b	2+	0.6890(20)	0	$\frac{1}{3}$	1	0.087(120)
Cu1	6a	2+	0.6836(17)	0.5054(21)	0.8352(8)	1	0.156(269)
Cu2	3b	2+	0	0.1940(69)	$\frac{1}{6}$	1	0.821(528)
O11	6a	2-	0.1732(60)	0.9892(17)	0.5574(9)	1	0.714(148)
O12	6a	2-	0.5425(56)	0.7052(17)	0.9092(27)	1	0.714(148)
O13	6a	2-	0.8200(23)	0.3543(36)	0.2271(11)	1	0.714(148)
O21	6a	2-	0.6740(16)	0.0236(36)	0.1273(5)	1	0.401(262)
O31	6a	2-	0.7379(34)	0.0792(11)	0.0022(2)	1	1.168(141)
V1	6a	5+	0.7154	0.0454	0.9167	1	0.151
D1	6a	1+	0.6744(18)	0.0299(17)	0.0770(2)	1	1.328(277)

Table B.1: Refined atomic information of vesignieite from neutron powder diffraction data. The starting model was taken from the $P3_121$ structure of 'Sr-vesignieite' described in Chapter 5 with Ba^{2+} substituted for Sr^{2+}. The refined lattice parameters are $a = b = 5.91780(4)$ and $c = 20.7596(4)$ Å. The final goodness-of-fit parameters were $R_{\mathrm{wp}} = 3.732$ and $\chi^2 = 0.062$ for 76 parameters.

Atom	Wyckoff Site	Oxidation state	x	y	z	Occupation	B_{iso} (Å^2)
Ba1	3b	2+	0.6879(19)	0	$\frac{1}{3}$	1	0.349(80)
Cu1	6a	2+	0.6857(31)	0.4924(31)	0.8344(10)	1	0.545(50)
Cu2	3b	2+	0	0.1758(24)	$\frac{1}{6}$	1	0.297(214)
O11_1	6a	2-	0.1935(97)	1.0150(73)	0.5617(10)	1	0.084(34)
O11_2	6a	2-	0.1417(108)	0.9661(27)	0.5559(29)	1	0.084(34)
O12_1	6a	2-	0.5340(46)	0.6945(115)	0.8958(7)	1	0.084(34)
O12_2	6a	2-	0.5390(37)	0.7467(28)	0.9174(6)	1	0.084(34)
O13_1	6a	2-	0.8401(41)	0.3543(91)	0.2176(7)	1	0.084(34)
O13_2	6a	2-	0.8064(34)	0.6536(100)	0.2383(9)	1	0.084(34)
O21	6a	2-	0.6747(16)	0.0234(35)	0.1268(2)	1	0.288(145)
O31	6a	2-	0.7390(12)	0.0799(9)	0.0017(5)	1	1.010(96)
V1	6a	5+	0.7154	0.0454	0.9167	1	0.151
D1	6a	1+	0.6854(17)	0.0318(17)	0.0767(2)	1	1.256(69)

Table B.2: Refined atomic information of vesignieite from neutron powder diffraction data. The starting model was taken from the refined parameters in Table B.2 the O11, O12 and O13 sites split and their positions allowed to freely refine. The refined lattice parameters are $a = b = 5.91786(4)$ and $c = 20.7599(4)$ Å. The final goodness-of-fit parameters were $R_{\mathrm{wp}} = 3.615$ and $\chi^2 = 0.060$ for 82 parameters.

x	V_2O_5		$Cu(NO_3)_2 \cdot H_2O$		NaOH		$Zn(CH_3COO)_2 \cdot 2H_2O$		NaOH	
	Mass (g)	Moles (mol)	Mass (g)	Moles (mol)	Mass (g)	Moles (mol)	Mass (g)	Moles (mol)	Mass (g)	Moles (mol)
0.15	0.7760	0.004212	2.4677	0.01200	0.9602	0.02401	0.1210	0.0006318	0.0505	0.001264
0.2	0.7659	0.004211	2.4240	0.01179	0.9431	0.02358	0.1612	0.0008422	0.0674	0.001685
0.3	0.7656	0.004210	2.3365	0.01137	0.9091	0.02273	0.2418	0.001263	0.1010	0.002526
0.6	0.7647	0.004205	2.0745	0.01009	0.8071	0.02018	0.4830	0.002523	0.2018	0.005046
1.0	0.7635	0.004198	1.7261	0.008396	0.6716	0.01679	0.8038	0.004198	0.3358	0.008396
2.0	0.7606	0.004182	0.8597	0.004182	0.3345	0.004182	1.6014	0.008364	0.6690	0.01673

Table B.3: Reagent amounts for the synthesis of Zn^{2+} doped vesignieite calculated from the reaction equations given in Section 6.5.1.

Appendix C

Appendix for Chapter 7

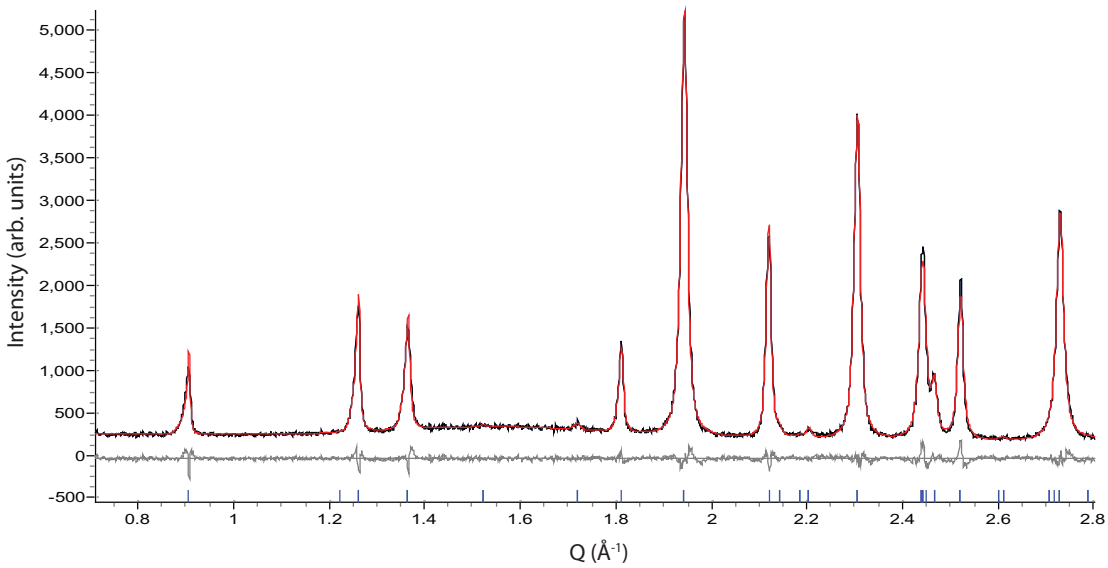

Figure C.1: Pawley refinement of data collected with a STOE STADI-P, described in Chapter 4, on a deuterated vesignieite sample prepared for inelastic neutron scattering experiments, described in Chapter 7. The refined lattice parameters are $a = b = 5.9283(4)$ and $c = 20.8163(13)$ Å.

Appendix D

Appendix for Chapter 8

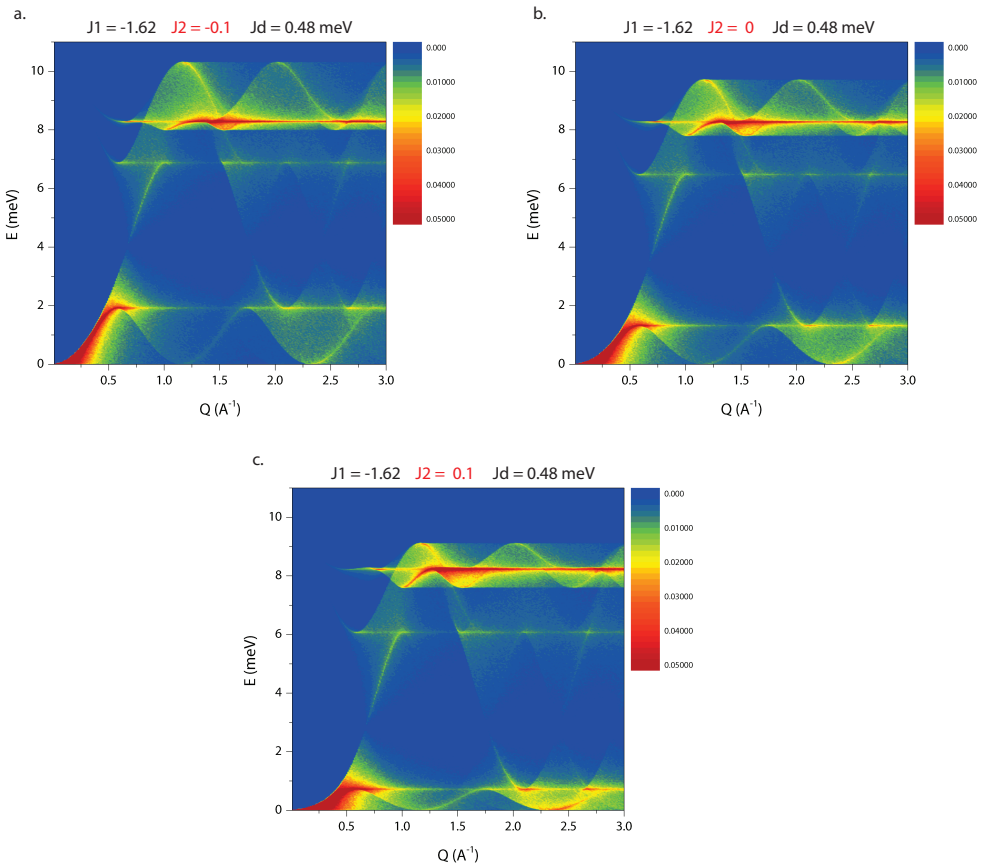

Figure D.1: Calculated spin-wave excitation spectra for haydeeite with $J_1 = -1.62$, $J_\mathrm{d} = 0.48\,\mathrm{meV}$ and **a.** $J_2 = -0.1$, **b.** $J_2 = 0$ or **c.** $J_2 = 0.1\,\mathrm{meV}$.

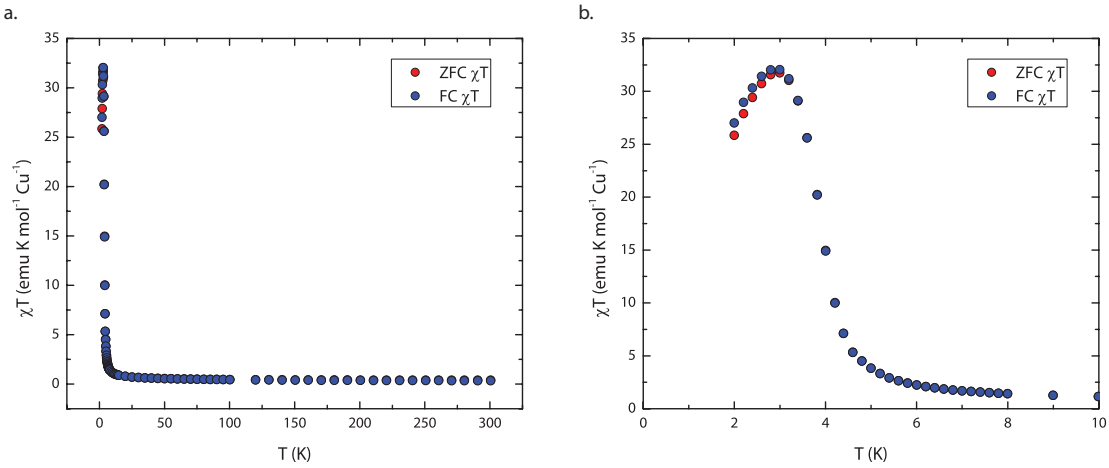

Figure D.2: Magnetic susceptibility measurements as a function of temperature in a field of 100 Oe for deuterated haydeeite (Sample **1**), discussed in Chapter 8. **a.** χT as a function of T in the whole temperature range. **b.** χT as a function of T for the low temperature regime showing the transition and ZFC-FC splitting.

IR	BV	Atom	BV components			IR	BV	Atom	BV components		
			$m_{\|a}$	$m_{\|b}$	$m_{\|c}$				$m_{\|a}$	$m_{\|b}$	$m_{\|c}$
Γ_1	ψ_1	1	2	0	0	Γ_5	ψ_5	1	2	3	3
		2	0	2	0			2	0	-1	0
		3	-2	-2	0			3	-2	1	-3
Γ_3	ψ_2	1	2	4	4		ψ_6	1	0	-3	0
		2	-4	-2	4			2	0	-3	0
		3	2	-2	4			3	0	-3	0
	ψ_3	1	-2	-4	0		ψ_7	1	2	3	-6
		2	4	2	0			2	0	-1	0
		3	-2	2	0			3	-2	1	6
	ψ_4	1	2	4	-8		ψ_8	1	0	1.732	1.732
		2	-4	-2	-8			2	0	1.732	0
		3	2	-2	-8			3	0	1.732	-1.732
							ψ_9	1	-3.464	-1.732	0
								2	0	5.196	0
								3	3.464	1.732	0
							ψ_{10}	1	0	1.732	-3.464
								2	0	1.732	0
								3	0	1.732	3.464

Table D.1: Basis vectors for the space group $P\bar{3}m1$ with $\mathbf{k}_{16} = (0,\ 0,\ 0)$. The decomposition of the magnetic representation for the Cu site $(.5,\ 0,\ .5)$ is $\Gamma_{Mag} = 1\Gamma_1^1 + 0\Gamma_2^1 + 3\Gamma_3^1 + 0\Gamma_4^1 + 3\Gamma_5^2 + 0\Gamma_6^2$. The atoms of the nonprimitive basis are defined according to 1: $(.5,\ 0,\ .5)$, 2: $(0,\ .5,\ .5)$, 3: $(.5,\ .5,\ .5)$.